

# **FIBRE-OPTIC SENSOR DEVELOPMENT FOR PROCESS MONITORING OF EPOXY RESINS**



**David Gareth King**

**A thesis submitted to the  
University of Birmingham  
for the degree of  
DOCTOR OF PHILOSOPHY**

School of Metallurgy and Materials  
College of Engineering and Physical Sciences  
University of Birmingham  
October 2018

UNIVERSITY OF  
BIRMINGHAM

**University of Birmingham Research Archive**

**e-theses repository**

This unpublished thesis/dissertation is copyright of the author and/or third parties. The intellectual property rights of the author or third parties in respect of this work are as defined by The Copyright Designs and Patents Act 1988 or as modified by any successor legislation.

Any use made of information contained in this thesis/dissertation must be in accordance with that legislation and must be properly acknowledged. Further distribution or reproduction in any format is prohibited without the permission of the copyright holder.

## ABSTRACT

Thermosetting resin systems are widely used in fibre-reinforced carbon-fibre composites and a range of characterisation techniques are available to monitor the cross-linking reaction. However, many of these are completed in laboratory settings and cross-correlation between different techniques becomes challenging due to the differing thermal environments. A range of optical-fibre based sensing systems have been developed which can be embedded within composite structures, to enable in-situ cross-linking monitoring. The Fresnel reflection sensor (FRS) is a refractive index sensor, which is relatively straightforward to prepare and has been shown to track the cross-linking of epoxy resin systems.

In this research, the performance of the FRS to track the cross-linking of epoxy resins was investigated by incorporating the sensor into a differential scanning calorimeter (DSC). The initial design used a micrometer translation stage to lower the FRS through an orifice in the DSC platinum lids and into the pan containing the sample. During exothermic cross-linking experiments, the resin refractive index and the heat evolved were measured simultaneously, allowing for direct comparison between the data.

Combining the two measurement techniques produced a powerful hyphenated analytical procedure that demonstrated the feasibility of using the FRS for in-situ cross-linking monitoring of epoxy resin systems. During the cross-linking of specified resins, the sensor revealed optical phenomena throughout the later stages and was shown to be sensitive to the glass transition, nano-particulate movement, nano-

particulate concentration and phase separation. Therefore, the introduction of the FRS to the DSC provided valuable additional cross-linking information.

A second modification to the DSC permitted the accommodation of an optical fibre probe, which facilitated simultaneous DSC/FRS/Fourier transform infrared spectroscopy (FTIRS) analysis. The DSC platinum lid was drilled out to allow for the insertion of the probe into the DSC. A good correlation between the cross-linking kinetics of an epoxy resin system was demonstrated using the hyphenated techniques and hence alleviated the issues of cross-correlation between individual experiments.

Due to the good correlation of the FRS with both the DSC and FTIRS data, it can be concluded that the FRS can be used as a low-cost option to provide in-situ cross-linking information. Additionally, the introduction of the FRS with conventional analytical techniques provides valuable data concerning optical phenomena.



## **ACKNOWLEDGEMENTS**

I would like to take this opportunity to thank Professor Gerard Fernando for his continued supervision and support in the pursuit of this research. The regular discussions with him and subsequent guidance have been invaluable in providing me with the tools to undertake the research design, experimentation and analysis in order to complete this thesis.

In addition, I would also like to thank the support from Dr Claude Billaud and Dr Peter Mills from Cytec/Solvay for their technical expertise and funding necessary to undertake this PhD research. The School of Metallurgy and Materials within the university has provided me with the facilities and an enthusiastic research atmosphere to promote and facilitate exploratory investigation.

I am also grateful to the advice and support of Dr Surya Pandita, Frank Biddlestone, Dr James Talbot, Dr Raj Machavaram and Dr Francisco Nieves.

Finally, I would like to thank my parents for all their love and support.

# CONTENTS

	Page
<b>1. INTRODUCTION</b>	<b>1</b>
1.1 Background	1
1.2 Aims and Objectives	6
1.3 Outline of the Thesis	7
<b>2. LITERATURE REVIEW</b>	<b>9</b>
2.1 Epoxy Resins	9
2.2 Cross-linking of Epoxy Resins	13
2.2.1 Evolution of the Refractive Index during Cross-linking	15
2.3 Monitoring the Cross-linking of Epoxy Resins	18
2.3.1 Differential Scanning Calorimetry	18
2.3.1.1 Calibrating a Differential Scanning Calorimeter	19
2.3.1.2 Analysis of Cross-linking Reactions Using Differential Scanning Calorimetry	21
2.3.1.2.1 Non-isothermal Enthalpy Determination	22
2.3.1.2.2 Isothermal Enthalpy Determination	25
2.3.1.3 Detecting the Glass Transition Temperature	27
2.3.1.4 Cross-linking Kinetics	29
2.3.2 Fourier Transform Infrared Spectroscopy	34
2.3.2.1 Mid-infrared Spectroscopy	35
2.3.2.2 Near-infrared Spectroscopy	37
2.3.2.3 Comparison of Mid-infrared and Near-infrared Spectroscopy for Epoxy Conversion	41
2.3.2.4 Parallel Plate Rheology	42
2.3.2.5 Detection of Gelation	43
2.3.2.6 Detection of Vitrification	49
2.3.2.7 Impact of Carbon-based Additives on the Cross-linking of Epoxy Resins	52

2.3.3	Impact of Graphene Nano-particles on the Cross-linking of Epoxy Resins	58
2.4	Optical Fibres	61
2.4.1	Introduction	61
2.4.2	Structure of Optical Fibres	62
2.4.3	Numerical Aperture and Acceptance Angle	63
2.4.4	Total Internal Reflection	64
2.4.5	Reflections at Normal Incidence	65
2.5	Process Monitoring using Optical Fibre Sensors	66
2.5.1	Refractive Index Monitoring	67
2.5.2	The Abbe Refractometer	67
2.5.3	Monitoring the Cross-linking using the Abbe Refractometer	69
2.5.4	Stripped Optical Fibre Refractometer	71
2.5.5	Optical Fibre Based Fresnel Reflection Sensor	74
2.5.5.1	Sensing System Instrumentation	75
2.5.5.2	Capability of the Fresnel Reflection Sensor to Detect Refractive Index	77
2.5.5.3	Tracking Isothermal Cross-linking	78
2.5.5.4	Non-isothermal Heating Regimes using Fresnel Reflection Sensor	80
2.5.5.5	Effect of Power Fluctuations from the Light Source	82
2.5.5.6	Multiplexing Fresnel Reflection Sensors	83
2.5.5.7	Deployment of the Fresnel Reflection Sensor with Resin Containing Particulates	84
2.5.5.8	Summary	85
2.5.6	Fibre Optic Fourier Transform Infrared Spectroscopy	86
2.5.6.1	Optical Fibre-based Transmission Spectroscopy	87
2.5.6.2	Evanescent Wave Spectroscopy	88

2.5.6.3	Reflection/Transmission Spectroscopy	89
2.5.7	Hyphenated Optical Fibre-based Differential Scanning Calorimetry and Fourier Transform Infrared Spectroscopy	90
2.6	Conclusion	94
<b>3.</b>	<b>MATERIALS AND EXPERIMENTAL METHODS</b>	<b>96</b>
3.1	Introduction	96
3.2	Materials	96
3.2.1	LY3505/XB3403	96
3.2.2	LY3505/XB3403 containing Graphene Nano-particles	97
3.2.3	Cytec/Solvay Resins	98
3.3	Conventional Analytical Techniques	98
3.3.1	Differential Scanning Calorimetry	98
3.3.1.1	Calibration	99
3.3.1.2	Non-isothermal Cross-linking	99
3.3.1.3	Isothermal Cross-linking	99
3.3.2	Fourier Transform Infrared Spectroscopy	100
3.3.2.1	Temperature Distribution within the Cuvette	102
3.3.2.2	Fourier Transform Infrared Spectroscopy from within the Cuvette Holder	103
3.3.3	Parallel-plate Rheometry	104
3.4	Fresnel Reflection Sensor	104
3.4.1	Experimental Setup for the Fresnel Reflection Sensor	104
3.4.2	Calibration of the Fresnel Reflection Sensor	106
3.5	Integrating the Fresnel Reflection Sensor within a Differential Scanning Calorimeter	107
3.5.1	Investigation into Reflectivity of Differential Scanning Calorimetry Pans	108

3.5.1.1	Cross-linking of LY3505/XB3403 Resin System with and without Graphene Nanoparticles	109
3.5.1.2	Cross-linking of Cytec/Solvay Resin	110
3.6	Integration of the Fresnel Reflection Sensor within the Rheometer	111
3.7	Hyphenated Differential Scanning Calorimetry /Fourier Transform Infrared Spectroscopy /Fresnel Reflection Sensor	112
3.7.1	Construction of the Fibre Optic Probe	112
3.7.2	Modification of the Differential Scanning Calorimeter Pans to Enable Simultaneous Fourier Transform Infrared Spectroscopy / Fresnel Reflection Sensor	114
3.7.3	Simultaneous Fourier Transform Infrared Spectroscopy and Fresnel Reflection Sensor-based Monitoring of the Cross-linking of LY3505/XB3403	115
3.7.4	Simultaneous Differential Scanning Calorimetry /Fourier Transform Infrared Spectroscopy and Fresnel Reflection-based Monitoring of the Cross-linking of the LY3505/XB3403 Resin System	117
<b>4.</b>	<b>RESULTS, ANALYSIS AND DISCUSSION: MONITORING CROSS-LINKING USING CONVENTIONAL ANALYTICAL TECHNIQUES</b>	<b>120</b>
4.1	Differential Scanning Calorimetry	122
4.1.1	Calibration of the Differential Scanning Calorimeter	122
4.1.2	Non-isothermal cross-linking in the Differential Scanning Calorimeter	123

4.1.3	Isothermal Cross-linking in the Differential Scanning Calorimeter	125
4.1.4	Ramped Heating in the Differential Scanning Calorimeter	133
4.1.5	Modelling the Cross-linking Kinetics of the Resin System	136
4.2	Fourier Transform Infrared Spectroscopy	141
4.2.1	Temperature Distribution within the Cuvette Holder	141
4.2.2	Identification of Absorbance Peaks for the LY3505/XB3403 Resin System	143
4.2.3	Baseline Construction of the Absorption Peak Areas during the Cross-linking of LY3505/XB3403.	145
4.2.4	Impact of Deconvolution on the Degree of Cross-linking	149
4.3	Comparison between Independent Cross-linking Data obtained using Differential Scanning Calorimetry Fourier Transform Infrared Spectroscopy	156
4.4	Rheology	160
4.5	Summary of Conventional Methods for Characterising Cross-linking Reactions	170
<b>5.</b>	<b>CURE MONITORING USING SIMULTANEOUS DIFFERENTIAL SCANNING CALORIMETRY AND FRESNEL REFLECTION SENSOR</b>	<b>171</b>
5.1	Development of the Hyphenated Technique for the Differential Scanning Calorimeter	171
5.1.1	Calibration of the Fresnel Reflection Sensor using Standard Refractive Index Oils	171
5.1.2	Stability of the Light Source and Detector	176

5.1.3	Interaction between the Fresnel Reflection Sensor and the Differential Scanning Calorimeter Sample Pan	177
5.1.4	Calibration of the Differential Scanning Calorimeter	179
5.1.5	Impact of Light source on the Differential Scanning Calorimeter	180
5.2	Hyphenated Differential Scanning Calorimetry /Fresnel using the LY3505/XB3403 Resin System	184
5.2.1	Isothermal Cross-linking	184
5.2.2	Isothermal Cross-linking Kinetics	192
5.2.3	Detecting the Glass Transition Temperature Subsequent to Isothermal Cross-linking	199
5.2.4	Detecting the Glass Transition Temperature for a Stoichiometrically Un-Balanced Resin System	203
5.3	Isothermal Cross-linking of Cytec/Solvay Phase Separating Resins	207
5.4	Summary	215
<b>6.</b>	<b>EVALUATION OF THE FRESNEL REFLECTION SENSOR WITH LY3505/XB3403 CONTAINING GRAPHENE NANO-PARTICLES</b>	<b>217</b>
6.1	Simultaneous Differential Scanning Calorimetry /Fresnel Reflection Sensor	217
6.1.1	Isothermal Cross-linking	218
6.2	Impact of Ultrasonic Mixing of Resin on the Fresnel Reflection Sensor Signal	229
6.3	Effect of Freezing Resin System on the Output from the Fresnel Reflection Sensor	231
6.4	Hyphenated Rheology/Fresnel Reflection Sensor	237
6.4.1	LY3505/XB3403	237
6.4.2	Rheological Characteristics of the LY3505/XB3403 Resin System with GNPs	239

6.5	Summary	243
<b>7.</b>	<b>HYPHENATED DIFFERENTIAL SCANNING CALORIMETRY, FRESNEL REFLECTION SENSOR AND FOURIER TRANSFORM INFRARED SPECTROSCOPY</b>	<b>245</b>
7.1	Development of the Differential Scanning Calorimetry /Fresnel Reflection Sensor /Fourier Transform Infrared Spectroscopy Technique	245
7.1.1	Reflectivity of the Differential Scanning Calorimeter Pans	245
7.1.2	Cure Monitoring outside the Differential Scanning Calorimeter	248
7.1.3	Calibration of the Differential Scanning Calorimeter with the Fresnel Reflection Sensor /Fourier Transform Infrared Spectroscopy Probe	250
7.2	Isothermal Cross-linking	251
7.2.1	Differential Scanning Calorimetry Data Obtained via the Fresnel Reflection Sensor /Fourier Transform Infrared Spectroscopy Probe	251
7.2.2	Fourier Transform Infrared Spectroscopy Data	257
7.2.3	Fresnel Reflection Sensor Data	261
7.2.4	Kinetic Data	268
7.2.5	Correlation of Isothermal Differential Scanning Calorimetry, Fourier Transform Infrared Spectroscopy and Fresnel Reflection Sensor Data	273
7.3	Non-isothermal Differential Scanning Calorimetry Experiments	279
7.4	Summary	282
<b>8.</b>	<b>CONCLUSIONS AND RECOMMENDATIONS FOR FUTURE RESEARCH</b>	<b>284</b>
8.1	Conclusion	284
8.1.1	Conventional Analytical Techniques	284



8.1.2	Differential Scanning Calorimetry /Fresnel Reflection Sensor	285
8.1.3	LY3505/XB3403 Resin system with Graphene Nano-particles	286
8.1.4	First Demonstration of Simultaneous Differential Scanning Calorimetry /Fresnel Reflection Sensor /Fourier Transform Infrared Spectroscopy	287
8.2	Recommendations for Future Research	288
	<b>LIST OF REFERENCES</b>	<b>289</b>

## LIST OF FIGURES

		Page
<b>Figure 2.1</b>	Oxirane ring.	9
<b>Figure 2.2</b>	Generalised reaction scheme for an epoxy/amine resin system.	13
<b>Figure 2.3</b>	Schematic illustration of power-compensation DSC technique developed by Perkin-Elmer.	19
<b>Figure 2.4</b>	Baseline construction to allow integration of exothermic reaction.	22
<b>Figure 2.5</b>	Cross-linking reaction at 190 °C before and after baseline construction.	26
<b>Figure 2.6</b>	Assignment of glass transition.	28
<b>Figure 2.7</b>	Conversion of DGEBA hexaanhdro-4-methylphthalicanhydride system as a function of time at various temperatures for the cure of an epoxy resin (DGEBA/MDA) alongside theoretical predictions using Equation 2.12.	32
<b>Figure 2.8</b>	Tan $\delta$ evolution with time at 130 °C for a DGEBA/epichlorohydrin system.	48
<b>Figure 2.9</b>	Schematic of illustration of an optical fibre showing different components.	62
<b>Figure 2.10</b>	The acceptance angle when launching light into an optical fibre.	63
<b>Figure 2.11</b>	Schematic of the operating principles of an Abbe refractometer.	68
<b>Figure 2.12</b>	Schematic of optical fibre core with section of cured resin.	71
<b>Figure 2.13</b>	Schematic of the fibre optic sensor entering and exiting a prepreg.	73
<b>Figure 2.14</b>	Schematic illustration showing reflection at normal incidence.	75
<b>Figure 2.15</b>	Plot of theoretical and experimental Fresnel reflection as a function of refractive index.	77
<b>Figure 2.16</b>	Fresnel reflection signal as a function of temperature during the cross-linking of an epoxy resin.	81
<b>Figure 2.17</b>	Comparison of refractive index and degree of cure during isothermal cross-linking for phase separating epoxy at 180 °C.	85
<b>Figure 2.18</b>	Evanescent wave phenomena at the core-cladding interface.	88
<b>Figure 2.19</b>	Trans-reflection interaction of light with resin.	89
<b>Figure 2.20</b>	Probe design for simultaneous DSC/FTIRS/TMA.	93
<b>Figure 3.1</b>	Schematic illustration of temperature controlled cuvette used for transmission FTIRS.	101
<b>Figure 3.2</b>	Schematic illustration of the demountable cuvette with a 1 mm path length used during transmission FTIRS.	101

<b>Figure 3.3</b>	Schematic illustrations showing the relative positions of the thermocouples on one face of the demountable cuvette to determine the temperature.	<b>102</b>
<b>Figure 3.4</b>	Schematic illustration of the experimental set-up for the simultaneous DSC and Fresnel experiments.	<b>105</b>
<b>Figure 3.5</b>	(a) Photograph and (b) Schematic illustration show the key components of the custom-modified Perkin Elmer Diamond DSC top-cover.	<b>108</b>
<b>Figure 3.6</b>	(a) Photograph and (b) schematic illustration of hyphenated FRS/rheometer.	<b>111</b>
<b>Figure 3.7</b>	Schematic illustration of the FRS/FTIRS probe.	<b>113</b>
<b>Figure 3.8</b>	(a) Photograph and (b) schematic of Fresnel/FTIR probe.	<b>114</b>
<b>Figure 3.9</b>	Image of a modified aluminium DSC pan showing the reflective and non-reflective sections.	<b>115</b>
<b>Figure 3.10</b>	Schematic illustration of translation stage, lowering probe into orifice of insulation brick.	<b>116</b>
<b>Figure 3.11</b>	(a) Schematic illustration and (b) photograph of the key components of the custom-modified Perkin-Elmer Diamond differential scanning calorimeter top cover.	<b>119</b>
<b>Figure 4.1</b>	DSC calibration trace for indium where the sample was heated at 10 K/minute in air using and open-top aluminium pan.	<b>121</b>
<b>Figure 4.2</b>	Thermograms for the LY3505/XB3403 resin system at specified heating rates.	<b>123</b>
<b>Figure 4.3</b>	Heating up and stabilisation periods from 30 °C to the desired isothermal cross-linking temperature when the samples were heated at 40 K/minute.	<b>126</b>
<b>Figure 4.4</b>	Isothermal cross-linking data for the LY3505/XB3403 resin system for isothermal experiments at 50, 60 and 70 °C. The method for constructing the baseline and calculating the enthalpy of cross-linking is also presented: (a) Experiment 1; and (b) Experiment 2.	<b>127</b>
<b>Figure 4.5</b>	Degree of cross-linking under isothermal conditions at 50, 60 and 70 °C for the LY3505/XB3403 resin system.	<b>130</b>
<b>Figure 4.6</b>	Rate of reaction of LY3505/XB3403 as a function of the rate of cure for isothermal processing at 50, 60 and 70 °C.	<b>132</b>
<b>Figure 4.7</b>	Expanded view of the glass transition region for the LY3505/XB3403 resin system that was initially cross-linked isothermally at 70 °C for 600 minutes followed by three	<b>133</b>

	consecutive ramped heating at 10 K/minute: (a) Experiment 1; and (b) Experiment 2.	
<b>Figure 4.8</b>	Comparison between DSC experimental data and autocatalytic model at: (a) 50 °C; (b) 60 °C; and (c) 70 °C.	<b>137</b>
<b>Figure 4.9</b>	Arrhenius plot for the cross-linking of the LY3505/XB3403 resin system.	<b>139</b>
<b>Figure 4.10</b>	Temperature measurements at specified locations within the demountable quartz cuvette filled with silicone oil between 20-70 °C as a function of: (a) Time; and (b) Temperature.	<b>141</b>
<b>Figure 4.11</b>	Spectra of LY3505/XB3403 resin system at the beginning of cross-linking and after 600 minutes at 70°C.	<b>142</b>
<b>Figure 4.12</b>	Integration of the absorbance spectra peak area during cross-linking of LY3505/XB3403 at 70 °C for specified times.	<b>145</b>
<b>Figure 4.13</b>	Integration of the absorbance spectra of the LY3505/XB3403 resin system cross-linked at 70 °C after 600 minutes.	<b>146</b>
<b>Figure 4.14</b>	Deconvoluted spectra of Figure 4.13 using the Fourier self-deconvolution routine in the OPUS software at: the start of reaction, after 60 minutes and 120 minutes.	<b>148</b>
<b>Figure 4.15</b>	Degree of cross-linking calculated using Equation 2.4 for LY3505/XB3403 at 70 °C using raw spectra and de-convoluted spectra.	<b>149</b>
<b>Figure 4.16</b>	Degree of cure for the LY3505/XB3403 resin system at 50, 60 and 70 °C. The data was generated using conventional FTIR spectroscopy: (a) Experiment 1, and (b) Experiment 2.	<b>152</b>
<b>Figure 4.17</b>	Comparison between transmission FTIR experimental data that were generated isothermally at: (a) 50 °C; (b) 60 °C; (c) 70 °C; and simulated data using Equation 4.1 with the average rate constant for each specified temperature.	<b>153</b>
<b>Figure 4.18</b>	Comparison of the Degree of Cross-linking for the LY3505/XB3403 resin system from isothermal FTIRS and DSC: (a) Experiment 1; and (b) Experiment 2.	<b>156</b>
<b>Figure 4.19</b>	Degree of cross-linking of the LY3505/XB3403 resin system studied by conventional DSC, conventional FTIR and using a hyphenated simultaneous DSC/FTIR technique.	<b>159</b>
<b>Figure 4.20</b>	Evolution of G' and G'' during isothermal cross-linking of the resin system LY3505/XB3403 at 70 °C: (a) Experiment 1; (b) Experiment 2; and (c) Experiment 3.	<b>160</b>

<b>Figure 4.21</b>	Evolution of $G'$ and $G''$ during isothermal cross-linking of the resin system LY3505/XB3403 at 70 °C following the removal of data: (a) Experiment 1; (b) Experiment 2; and (c) Experiment 3.	<b>162</b>
<b>Figure 4.22</b>	Evolution of $G'$ and $G''$ during the cross-linking of LY3505/XB3403 at specified isothermal temperatures: (a) Experiment 1; and (b) Experiment 2.	<b>166</b>
<b>Figure 4.23</b>	Typical plot of the evolution of the complex viscosity during the cross-linking of LY3505/XB3403 at 70 °C.	<b>169</b>
<b>Figure 5.1</b>	Simultaneous data acquisition from the Abbe refractometer and a FRS for standard refractive index oils between 25 to 40 °C. Five repeat readings are shown at each temperature	<b>173</b>
<b>Figure 5.2</b>	Comparison of theoretical Fresnel reflection alongside the experimentally-derived FRS data using standard refractive index oils between 25 to 40 °C.	<b>176</b>
<b>Figure 5.3</b>	Fresnel reflection data obtained in air at 30 °C using hyphenated DSC/Fresnel.	<b>177</b>
<b>Figure 5.4</b>	Response of FRS as a function of height from the base of DSC pan types.	<b>177</b>
<b>Figure 5.5</b>	Summary of the enthalpy and melt onset for indium using the DSC/Fresnel system. The effect of the light source is also included. The data are derived from six independent experiments.	<b>180</b>
<b>Figure 5.6</b>	Impact of the Fresnel light source on DSC when the cleave-end of the optical fibre was in contact with base of empty alumina pan.	<b>182</b>
<b>Figure 5.7</b>	Magnitude of the FRS upon the DSC for each on/off cycle for (a) an empty alumina pan and (b) an alumina pan containing LY3505 resin.	<b>183</b>
<b>Figure 5.8</b>	DSC traces of cross-linking of LY3505/XB3403 obtained using the hyphenated DSC/Fresnel and conventional techniques at specified isothermal cross-linking temperatures. Showing (a) Experiment 1 (b) Experiment 2.	<b>185</b>
<b>Figure 5.9</b>	Simultaneous FRS/DSC data acquisition showing the degree of cross-linking using DSC and the normalised Fresnel reflection at isothermal cross-linking temperatures of 50, 60 and 70 °C: (a) Experiment 1; and (b) Experiment 2.	<b>189</b>
<b>Figure 5.10</b>	Time to reach points A, B and C during the cross-linking of LY3505/XB3403 at 50, 60 and 70 °C during DSC/FRS. A =	<b>190</b>

Deviation from initial linear region; B = Intersection of extrapolation of initial and final linear regions; and C = Deviation of from final linear region.

<b>Figure 5.11</b>	Magnitude of gradient of the FRS and DSC signal at the beginning and end of the cross-linking experiments.	<b>191</b>
<b>Figure 5.12</b>	FRS and DSC data from isothermal cross-linking experiments during simultaneous DSC/Fresnel at 50 °C: (a) Experiment 1; and (b) Experiment 2.	<b>193</b>
<b>Figure 5.13</b>	FRS and DSC data from isothermal cross-linking experiments during simultaneous DSC/Fresnel at 60 °C: (a) Experiment 1; and (b) Experiment 2.	<b>194</b>
<b>Figure 5.14</b>	FRS and DSC data from isothermal cross-linking experiments during simultaneous DSC/Fresnel at 70 °C: (a) Experiment 1; and (b) Experiment 2.	<b>195</b>
<b>Figure 5.15</b>	Arrhenius plot for the cross-linking LY3505/XB3403 during FRS/DSC.	<b>197</b>
<b>Figure 5.16</b>	Thermogram obtained from DSC during a non-isothermal scan through the glass transition for the LY3505/XB3403 resin system along with data obtained from the Fresnel reflection sensor: (a) First non-isothermal heating ramp;( b) Temperature ramp 2; and (c) Temperature ramp 3.	<b>201</b>
<b>Figure 5.17</b>	Graphic representation of variation in glass transition temperature with stoichiometry change following isothermal cross-linking at 70 °C:(a) Temperature ramp 1; (b) Temperature ramp 2; and (c) Temperature ramp 3.	<b>205</b>
<b>Figure 5.18</b>	Histogram showing variation in the $T_g$ following isothermal cross-linking at 70 °C.	<b>206</b>
<b>Figure 5.19</b>	Isothermal cross-linking of Cytec/Solvay resin system without a thermoplastic additive: (a) Experiment 1; and (b) Experiment 2.	<b>207</b>
<b>Figure 5.20</b>	Isothermal cross-linking of Cytec/Solvay resin system with specified quantities of thermoplastic additive: (a) 10 wt%; (b) 20 wt%; and (c) 30 wt%.	<b>210</b>
<b>Figure 5.21</b>	SEM micrographs of cryo-fracture surfaces of Cytec/Solvay resins containing specified concentration of thermoplastic: (a) 0%; (b) 10%; (c) 20%; and (d) 30%.	<b>213</b>
<b>Figure 6.1</b>	Isothermal cross-linking of LY3505/XB3403 with: (a) 0%; (b) 0.01 wt%; (c) 0.1 wt%; (d) 0.5 wt%; (e) 1 wt%; and (f) 2 wt% GNP.	<b>219</b>

<b>Figure 6.2</b>	Magnitude of enthalpy during cross-linking at 70 °C of LY3505/XB3403 containing specified wt% of GNP.	<b>223</b>
<b>Figure 6.3</b>	Response of the FRS during isothermal cross-linking of LY3505/XB3403 at 70 °C containing specified wt% of GNP: (a) Over 600 minutes; (b) An expanded view from 0-40 minutes	<b>224</b>
<b>Figure 6.4</b>	FRS signal emanating from LY3505 containing 0.1 wt% GNP at 30 and 70 °C using hyphenated DSC/FRS.	<b>227</b>
<b>Figure 6.5</b>	FRS signal emanating from the LY3505 resin containing 0.1 wt% GNP at room temperature using an increased acquisition rate of 10 Hz. A schematic representation of the cause of the fluctuations is also shown.	<b>229</b>
<b>Figure 6.6</b>	Impact of sonication of the resin/GPN on the FRS signal for LY3505 containing 2% GNP (no hardener) after various times, using an amplitude of 12 kHz.	<b>230</b>
<b>Figure 6.7</b>	FRS of LY3505 resin upon cooling in a bath of liquid nitrogen	<b>232</b>
<b>Figure 6.8</b>	FRS of LY3505 containing 2% GNP upon repeated cooling within a bath of liquid nitrogen.	<b>236</b>
<b>Figure 6.9</b>	Simultaneous rheology/FRS and conventional rheology during cross-linking of LY3505/XB3403 at 70 °C: (a) Experiment 1; and (b) Experiment 2.	<b>238</b>
<b>Figure 6.10</b>	Hyphenated rheology/FRS during cross-linking of LY3505/XB3403/2wt %GNP at: (a) 50 °C; (b) 60 °C; and (c) 70 °C	<b>241</b>
<b>Figure 6.11</b>	Comparison of the G'/G'' crossover and the onset of linearity during hyphenated rheology/FRS of LY3505/XB3403/2 wt% GNP.	<b>242</b>
<b>Figure 7.1</b>	Epoxy and amine peak areas as a function of the height of the probe from the surface of the DSC pan.	<b>246</b>
<b>Figure 7.2</b>	Spectra of freshly mixed LY3505/XB3403 at 70 °C from a conventional transmission cell and the FTIR/Fresnel probe.	<b>247</b>
<b>Figure 7.3</b>	Thermocouple reading in air during cross-linking at 70 °C.	<b>249</b>
<b>Figure 7.4</b>	Simultaneous FTIRS and Fresnel acquisition during curing of LY3505/XB3403 using a partially reflective DSC pan. These experiments were conducted on a hot-plate using a thermally insulated enclosure.	<b>250</b>
<b>Figure 7.5</b>	Thermograms for indium after calibration with FRS/FTIRS probe inserted in the DSC.	<b>251</b>

<b>Figure 7.6</b>	Typical DSC data obtained during cure of the LY3505/XB3403 resin system at 70 °C using the simultaneous DSC/Fresnel/FTIRS technique.	<b>252</b>
<b>Figure 7.7</b>	Magnitude of the isothermal cross-linking reaction during DSC/FRS/FTIRS and conventional DSC at specified temperatures.	<b>254</b>
<b>Figure 7.8</b>	Degree of cross-linking obtained from DSC during isothermal DSC and DSC/FRS/FTIRS experiments completed at: (a) 50; (b) 60; and (c) 70 °C.	<b>255</b>
<b>Figure 7.9</b>	Spectra taken at various stages of cure of LY3505/XB3403 at 70 °C using simultaneous DSC/Fresnel/FTIRS technique.	<b>258</b>
<b>Figure 7.10</b>	Degree of cross-linking of LY3505/XB3403 using spectral data during simultaneous DSC/Fresnel/FTIRS and conventional FTIRS at: (a) 50 °C; (b) 60 °C; and (c) 70 °C.	<b>259</b>
<b>Figure 7.11</b>	Degree of cure after 600 minutes of cross-linking of LY3505/XB3403 using DSC/FRS/FTIRS and conventional FTIRS at specified temperatures.	<b>261</b>
<b>Figure 7.12</b>	FRS signal during isothermal cross-linking of LY3505/XB3403 at 50, 60 and 70 °C: (a) Experiment 1; and (b) Experiment 2.	<b>262</b>
<b>Figure 7.13</b>	Time to reach points A, B and C during the cross-linking of LY3505/XB3403 at 50, 60 and 70 °C during DSC/FRS and DSC/FRS/FTIRS.	<b>264</b>
<b>Figure 7.14</b>	Degree of cure obtained from DSC and FTIRS alongside normalised Fresnel reflection during hyphenated DSC/FRS/FTIRS at 50 °C: (a) Experiment 1; (b) Experiment 2.	<b>265</b>
<b>Figure 7.15</b>	Degree of cure obtained from DSC and FTIRS alongside normalized Fresnel reflection during hyphenated DSC/FTIRS/FRS at 60 °C: (a) Experiment 1; (b) Experiment 2.	<b>266</b>
<b>Figure 7.16</b>	Degree of cure obtained from DSC and FTIRS alongside normalised Fresnel reflection during hyphenated DSC/FTIRS/FRS at 70 °C: (a) Experiment 1; (b) Experiment 2.	<b>267</b>
<b>Figure 7.17</b>	Comparison between the degree of cross-linking and the autocatalytic model at 50 °C: (a) DSC data; and (b) FTIRS data.	<b>269</b>
<b>Figure 7.18</b>	Comparison between the degree of cross-linking and the autocatalytic model at 60 °C: (a) DSC data; and (b) FTIRS data.	<b>270</b>
<b>Figure 7.19</b>	Comparison between the degree of cross-linking and the autocatalytic model at 70 °C during simultaneous DSC/FRS/FTIRS: (a) DSC data; and b) FTIRS data.	<b>271</b>



<b>Figure 7.20</b>	Histogram showing the average rate constant obtained for the autocatalytic model during DSC, FTIRS. DSC/FRS and DSC/FRS/FTIRS at 50, 60 and 70 °C.	<b>272</b>
<b>Figure 7.21</b>	DSC, FRS and FTIRS data alongside the autocatalytic model during simultaneous DSC/FRS/FTIRS of LY3505/XB3403 at 50 °C: (a) Experiment 1; and (b) Experiment 2.	<b>276</b>
<b>Figure 7.22</b>	DSC, FRS and FTIRS data alongside the autocatalytic model during simultaneous DSC/FRS/FTIRS of LY3505/XB3403 at 60 °C: (a) Experiment 1; and (b) Experiment 2.	<b>277</b>
<b>Figure 7.23</b>	DSC, FRS and FTIRS data alongside the autocatalytic model during simultaneous DSC/FRS/FTIRS of LY3505/XB3403 at 70 °C: (a) Experiment 1; and (b) Experiment 2.	<b>278</b>
<b>Figure 7.24</b>	Thermogram obtained from DSC during a non-isothermal scan through the glass transition for the LY3505/XB3403 resin system along with data obtained from the Fresnel reflection sensor during DSC/FRS/FTIR: (a) Temperature ramp 1; (b) Temperature ramp 2; and (c) Temperature ramp 3.	<b>280</b>

## LIST OF TABLES

		Page
<b>Table 1.1</b>	Selection of common epoxy resins.	2
<b>Table 1.2</b>	Selection of common hardeners for epoxy resin systems.	3
<b>Table 2.1</b>	Effect of repeat unit upon viscosity and softening point of cross-linked resin systems.	10
<b>Table 2.2</b>	Molar refractivities for bonds involved in the cross-linking of epoxy resins.	17
<b>Table 2.3</b>	Summary of practices for DSC calibration.	20
<b>Table 2.4</b>	Relative errors of the enthalpy of the melting of ice due to different baseline constructions.	24
<b>Table 2.5</b>	Examples of autocatalytic model correlated with DSC data for cross-linking of epoxy resin systems.	31
<b>Table 2.6</b>	Examples of the autocatalytic model containing diffusion factor being modelled alongside DSC data.	33
<b>Table 2.7</b>	Band assignments for epoxy/amine resin systems in the MIR range.	35
<b>Table 2.8</b>	Summary of the main NIR absorbance bands for an epoxy/amine resin and their associated peak assignments.	38
<b>Table 2.9</b>	Summary of criteria used to determine gelation of epoxy resin systems using parallel plate rheology.	44
<b>Table 2.10</b>	Examples of research aimed at the detection of vitrification detection through parallel-plate rheology.	50
<b>Table 2.11</b>	Properties of graphene.	53
<b>Table 2.12</b>	Summary of Experiments using GNPs in thermosetting resins.	54
<b>Table 2.13</b>	A summary of investigations into the impact of functionalised graphene on the mechanical strength of epoxy resin nanocomposites.	56
<b>Table 2.14</b>	A summary of the impact of graphene, GO and functionalised graphene particulates on the cure kinetics of epoxy resin system	59
<b>Table 3.1</b>	Chemical structure of LY3505 (resin) and XB3403 (hardener).	97
<b>Table 4.1</b>	Summary of the heating rates and the corresponding enthalpy of cross-linking and peak exothermic temperatures for the LY3505/XB3403 resin system.	124
<b>Table 4.2</b>	Values obtained from DSC experiments during isothermal and non-isothermal scans.	128

<b>Table 4.3</b>	Summary of relevant cure data for the LY3505/XB3403 resin system.	<b>131</b>
<b>Table 4.4</b>	Rate constants and activation energy for the LY3505/XB3403 resin system using Equation 4.1 and isothermal data generated using the DSC.	<b>139</b>
<b>Table 4.5</b>	Near-infrared peak assignments identified for the LY3505/XB34 resin system.	<b>143</b>
<b>Table 4.6</b>	Reported conversions during the cross-linking of LY3505/XB3403 at 70 °C using FTIRS	<b>150</b>
<b>Table 4.7</b>	Rate constants and activation energy for the LY3505/XB3403 resin system using FTIRS data and Equation 4.1.	<b>154</b>
<b>Table 4.8</b>	Initial rate of reaction during the cross-linking of LY3505/XB3403 at specified isothermal temperatures using DSC and FTIRS experiments.	<b>157</b>
<b>Table 4.9</b>	Repeatability of gelation times during the cross-linking of LY3505/XB3403 at 70 °C.	<b>165</b>
<b>Table 4.10</b>	Gelation times at various isothermal temperatures and the corresponding degree of cure (DoC) when cross-correlating with the FTIRS and DSC data.	<b>167</b>
<b>Table 5.1</b>	Refractive indices and thermo-optic coefficients quoted by the manufacturer (Cargille, USA) and those obtained experimentally via the Abbe refractometer.	<b>174</b>
<b>Table 5.2</b>	Summary of the enthalpy of crosslinking and other relevant parameters from the conventional and hyphenated DSC/FRS experiments during isothermal experiments.	<b>186</b>
<b>Table 5.3</b>	Normalised Fresnel reflection readings during cross-linking experiments	<b>187</b>
<b>Table 5.4</b>	Initial rate of cross-linking during the cross-linking of LY3505/XB3403 as detected by the FRS and DSC.	<b>190</b>
<b>Table 5.5</b>	Rate of cross-linking of LY3505/XB3403 toward the end of the isothermal heating as detected by the FRS and DSC.	<b>191</b>
<b>Table 5.6</b>	Rate constants and activation energy for the LY3505/XB3403 resin system obtained using hyphenated DSC techniques.	<b>198</b>
<b>Table 5.7</b>	Previously reported activation energies for LY3505/XB3403.	<b>198</b>
<b>Table 5.8</b>	Glass transitions of LY3505/XB3403 after cross-linking using the simultaneous DSC/Fresnel technique and using conventional DSC.	<b>203</b>

<b>Table 5.9</b>	Glass transition temperatures of LY3505/XB3403 systems with specified stoichiometric ratios following isothermal cross-linking at 70 °C for 600 minutes.	<b>204</b>
<b>Table 5.10</b>	Relevant data from DSC/FRS experiments during the isothermal cross-linking of the Cytec/Solvay resins systems at 180 °C.	<b>211</b>
<b>Table 5.11</b>	Literature citing the effect of thermoplastics upon the cross-linking of epoxy resin systems.	<b>215</b>
<b>Table 6.1</b>	A summary of the times at which the fluctuations are detected in the FRS signal during the cross-linking of LY3505/XB3403 with specified wt% of GNP.	<b>225</b>
<b>Table 7.1</b>	Degree of cure and initial rate of reaction of LY3505/XB3403 during isothermal DSC/FRS/FTIRS and conventional DSC experiments.	<b>256</b>
<b>Table 7.2</b>	Degree of cure and initial rate of reaction of LY3505/XB3403 during isothermal DSC/FRS/FTIRS and conventional FTIRS experiments.	<b>259</b>
<b>Table 7.3</b>	Values from FRS at various points during cross-linking during hyphenated DSC/FRS/FTIRS.	<b>263</b>
<b>Table 7.4</b>	Average rate constants for autocatalytic model from conventional methods compared to hyphenated DSC/FTIRS/FRS.	<b>272</b>
<b>Table 7.5</b>	Glass transition values during ramped scans from 30-100 °C following isothermal cross-linking of LY3505/XB3403.	<b>281</b>

## LIST OF ABBREVIATIONS

CNT	Carbon nano tubes
CNF	Carbon nano fibres
DDA	Dicyandiamide
DDM	Dichlorophenyl methane
DDS	Diamino diphenyl sulphone
DETA	Diethylene triamine
DGEB A	Diglycidyl ether of bisphenol-A
DGEB F	Diglycidyl ether of bisphenol-F
DMA	Dynamic mechanical analysis
DMAP	4-( <i>N,N</i> -Dimethylamino)pyridine
DMTA	Dynamic mechanical thermal analysis
DoC	Degree of cure
DSC	Differential scanning calorimetry
EDA	Ethylene diamine
FBG	Fibre Bragg Grating
FOS	Fibre optic sensor
FRS	Fresnel reflection sensor
FTIRS	Fourier transform infrared spectroscopy
G'	Storage modulus
G''	Loss modulus
G*	Complex modulus
GNP	Graphene nano-particles
GO	Graphene Oxide
MCDEA	Methylene chlorodiethyl aniline
MDA	Methylene dianiline
MDEA	Methylene diethylaniline
MHHPA	Methyl hexahydrophthalic anhydride

MIR	Mid-infrared
NIR	Near-infrared
PDMS	Polydimethyl siloxane
PC	Polycarbonate
PS	Polysulphone
PES	Polyethersulphone
SEM	Scanning electron microscopy
Tan $\delta$	Damping factor
TETA	Triethylene tetramine
T <sub>g</sub>	Glass transition temperature
TGDDM	Tetraglycidyl diamino diphenyl methane
TMA	Thermal mechanical analysis
TMDSC	Temperature modulated DSC
TRGO	Thermally reduced graphene oxide

# 1. INTRODUCTION

## 1.1 Background

Epoxy resins are a class of thermosetting materials that are used widely as the matrix in fibre-reinforced composites. Epoxy-based resin systems are also used in a wide range of applications, including adhesives and coatings, and are generally cross-linked (cured) with a hardener, such as an amine or anhydride. The cross-linking (or curing) reactions can be activated by, for example, heat, light, and microwaves, and result in the conversion of monomers into a highly cross-linked structure that cannot be dissolved by solvents. Repeat unit structures for selected classes of epoxy resins and hardeners are presented in Tables 1.1 and 1.2, respectively. Accordingly, cross-linked resins with the desired properties can be obtained by the appropriate selection of resins and hardeners (Brostow *et al.*, 2014).

A variety of conventional analytical techniques are used currently to monitor specific parameters during the cross-linking process. Differential scanning calorimetry (DSC) (Lee *et al.*, 2000), Fourier transform infrared spectroscopy (FTIRS) (Fraga *et al.*, 2001) and dynamic mechanical analysis (DMA) (Stark, 2013) enable the acquisition of information regarding the enthalpy of the reactions, the infrared absorbance characteristics of specific chemical functional groups and the thermo-mechanical properties, respectively. However, these laboratory-based techniques may not necessarily simulate the exact environments experienced during processing of the thermoset. Additionally, each of the above-mentioned analytical techniques has its own unique thermal environment and this can affect the rate and extent of cross-linking. Thus, the cross-correlation of data between different analytical techniques

can be difficult. Moreover, the substrate used to contain the resin systems also differs. For example, FTIRS requires optically transparent materials, whereas aluminium and alumina pans are used in differential scanning calorimeters. The development of techniques to enable the remote monitoring of cross-linking reactions in real time will help to overcome issues related to difficulties in cross-correlating data from different instruments. The ability to monitor cross-linking reactions within the processing equipment will permit monitoring and optimisation of the process (Fernando and Degamber, 2006).

Table 1.1 Selection of common epoxy resins (Brostow *et al.*, 2014).

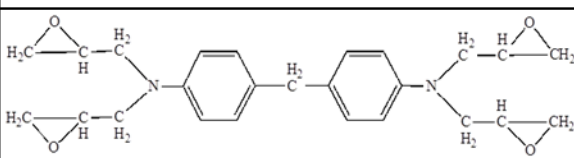
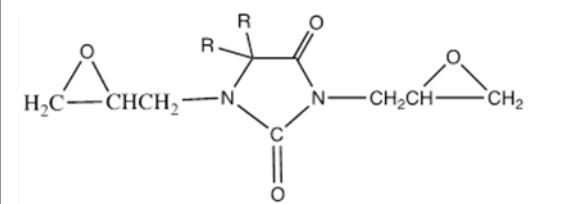
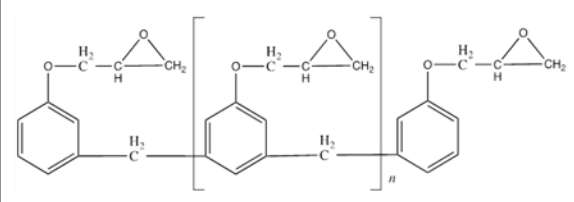
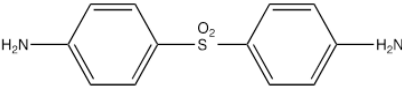
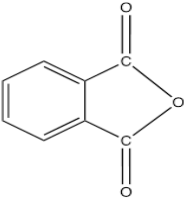
Resin Type	Structure	Comments
Diglycidyl Ether Resins	 <p style="text-align: center;">DGEBA</p>	- Most widely used epoxy resin
Hydatonin Resins	 <p style="text-align: center;">Hydatonin resin</p>	<ul style="list-style-type: none"> <li>- UV resistance due to lack of presence of aromatic rings</li> <li>- Long cure times</li> <li>- Low viscosity allowing for good wettability with fibres</li> </ul>
Novolac Resins	 <p style="text-align: center;">Novolac resin</p>	<ul style="list-style-type: none"> <li>- High functionality</li> <li>- Excellent adhesion properties</li> <li>- Excellent chemical and temperature resistance</li> <li>- Strengths of over 6.9 MPa can be maintained up to 150 °C</li> </ul>



Table 1.2 Selection of common hardeners for epoxy resin systems  
(Brostow *et al.*, 2014).

Hardener	Structure	Comments
Aliphatic Amine	$\text{H}_2\text{N}-(\text{CH}_2)_2-\overset{\text{H}}{\underset{ }{\text{N}}}-\text{H}-(\text{CH}_2)_2-\overset{\text{H}}{\underset{ }{\text{N}}}-\text{H}-(\text{CH}_2)_2-\text{NH}_2$ <p style="text-align: center;">Triethylenetetramine</p>	<ul style="list-style-type: none"> <li>- Most widely used hardeners</li> <li>- Tightly cross-linked network</li> <li>- Room temperature cure</li> <li>- Tensile strength up to 78.6 MPa</li> <li>- Heat deflection temperature up to 107 °C</li> </ul>
Aromatic Amine	 <p style="text-align: center;">44DDS</p>	<ul style="list-style-type: none"> <li>- Elevated cure temperature required for long curing times and large exotherms.</li> <li>- Improved thermal and chemical resistance when compared to aliphatic amine cured systems.</li> <li>- Tensile strength up to 73.1 MPa</li> <li>- Heat deflection temperature up to 190 °C</li> </ul>
Acid Anhydrides	 <p style="text-align: center;">Phthalic Anhydride</p>	<ul style="list-style-type: none"> <li>- Second largest widely used hardener class.</li> <li>- Elevated cure temperatures for long periods but with low exotherms.</li> <li>- Low shrinkage during cure in stress free environment</li> <li>- Tensile strength up to 82.7 MPa</li> <li>- Heat deflection temperature up to 190 °C</li> </ul>

With reference to the remote monitoring of cross-linking reactions, dielectric (Kim, 1996) and fibre-optic sensors (Crosby *et al.*, 1996a) have demonstrated capability in the laboratory and in service. Dielectric sensors are generally based on inter-digitated electrodes, and the mobility of ions in the resin system is monitored as a function of processing time and temperature. These ions are impurities from the production of the resin system. As cross-linking proceeds, the mobility of these ions is impeded by increasing viscosity of the resin (Dealy and Wissbrun, 2012). The dielectric sensors have an area of 2 cm<sup>2</sup>, with a thickness of 150 µm (Boll *et al.*, 2014). For instances where quantitative information is required to describe the cross-linking kinetics, a number of fibre-optic-based techniques have been developed and demonstrated (Crosby *et al.*, 1996b; Liu and Fernando,

2001; Pandita, *et al.*, 2012). The diameter of conventional telecommunications single-mode optical fibres is 125  $\mu\text{m}$ . Thus, these fibres can easily be integrated into processing machinery (Wang *et al.*, 2012), civil structures (Schubel *et al.*, 2013) and analytical equipment (Harris and Fernando, 2009).

The advantages of optical fibres include their immunity to electromagnetic interference, lower density relative to that of copper and chemical resistance towards common solvents. A wide range of intensity and spectral-based sensors have been designed from optical fibres. The measurands that can be monitored include temperature (Degamber *et al.*, 2004a), strain (Tsuda and Lee, 2007), refractive index (Kuang-An *et al.*, 2002) and specified chemical functional groups (Nair *et al.*, 2015). The sensors can also be integrated within conventional analytical instrumentation (Pandita *et al.*, 2012; Harris, 2011).

The small dimensions of the sensors allow for integration within composite structures to enable *in-situ* and real-time data acquisition, during and after the manufacturing process. These embedded sensors can also be multiplexed to allow placement throughout a component and parameters of interest to be mapped spatially (Machavaram *et al.*, 2014).

Spectral-based sensing requires a spectrometer, the cost of which can be expensive and may be prohibitive for routine implementation for the process monitoring of thermosets. On the other hand, intensity-based fibre-optic sensors can be assembled inexpensively. If precautions are taken to minimise drift in the light source and detector, as well as bend-induced losses in the optical fibre, intensity-

based sensors can provide a cost-effective technique for process monitoring.

Intensity-based sensors also require prior calibration.

A simple intensity-based optical fibre sensor is the Fresnel reflection sensor (FRS), which is effectively the cleaved-end of an optical fibre. The mode of operation of the FRS is described in the Chapter 3.

Prior to the deployment of intensity-based sensors for monitoring cross-linking reactions, it is necessary to demonstrate that the output from these sensors is meaningful, repeatable and quantifiable. This can be demonstrated by integrating the intensity-based fibre-optic sensor into common analytical equipment used to characterise thermosetting resins. In the current project, an intensity-based fibre-optic sensor was integrated into a differential scanning calorimeter to demonstrate, for the first time, direct correlation between the two outputs.

In addition to the integration of the FRS in a differential scanning calorimeter, a fibre-optic probe was also integrated into the equipment to show correlation between the outputs from the three devices, during the cross-linking of thermosetting resins. At the time of writing, the author was not aware of any previous demonstration of simultaneous acquisition of Fourier transform infrared spectra and refractive index from within DSC.

## 1.2 Aims and Objectives

The aims and objectives of this study were as follows:

- (i) To calibrate the output from a FRS using an Abbe refractometer.  
This was achieved by using reference refractive-index oils at specified temperatures and wavelength.
- (ii) To develop a methodology to integrate a FRS into a custom-modified differential scanning calorimeter.  
Accordingly, a series of experiments were undertaken to develop this methodology. This involved accurate positioning of the sensors within the chamber of the sample and reference compartment of the calorimeter. The influence of the light source on the output of the DSC was also studied by using reference refractive-index oils.
- (iii) To investigate the versatility of the FRS for monitoring the cross-linking kinetics of commercially available epoxy resin systems, with and without specified classes of additives.  
For this purpose, a common epoxy/amine resin system was used. The additives used were graphene and phase-separating thermosets.
- (iv) To investigate the feasibility of integrating a FRS and a fibre-optic probe to acquire near-infrared spectra within the differential scanning calorimeter.  
A fibre-optic probe was designed and integrated into the DSC alongside the FRS. The outputs from the three devices were compared and correlated.

### **1.3 Outline of the Thesis**

Chapter 2 provides a literature review of conventional analytical techniques used to monitor the cross-linking kinetics of epoxy resin systems. This is followed by a review on optical fibres and sensors, with a focus on the FRS. Other hyphenated techniques involving the differential scanning calorimeter are also considered.

Chapter 3 presents details of the experimental methodology associated with conventional and custom-modified differential scanning calorimeters, as well as calibration of the FRS. This chapter also includes details of the experimental procedures used to study the role of additives on the cross-linking behaviour of commercially available epoxy/amine resins.

Chapter 4 provides a discussion of the results obtained from the use of conventional analytical techniques, including DSC, FTIRS and rheometry, on the LY3505/XB3403 resin system.

Chapter 5 discusses the development of a novel hyphenated DSC/FRS technique. Experiments to demonstrate the performance of the system are presented before a discussion of cross-linking data for LY3505/XB3403. Results obtained from a resin system displaying phase separation are also discussed.

Chapter 6 contains an investigation into the impact of graphene nanoparticles (GNPs) upon the cross-linking kinetics of LY3505/XB3403 using the hyphenated DSC/FRS technique. Further experiments are then presented to investigate the effect of GNPs on the FRS signal.

In Chapter 7, a novel hyphenated DSC/FRS/FTIRS technique is demonstrated. Calibration of the system is first verified. Cross-linking kinetics of LY3505/XB3403 are then presented and compared with previous data on the resin system.

Chapter 8 provides a conclusion of the results obtained in each chapter and suggestions for further research.

## 2. LITERATURE REVIEW

### 2.1 Epoxy Resins

The term 'epoxy resin' refers to pre-polymers containing an epoxy functional group, or oxirane ring, as shown in Figure 2.1. This term is also used colloquially to describe resin systems after they have been cross-linked with a specified hardener.

With reference to Figure 2.1, the differing electro-negativities of the carbon and oxygen atoms allow for ring opening by nucleophilic reaction. A large variety of reactions can take place, depending on the hardener used (Fernando and Degamber, 2006; Ellis, 2015).

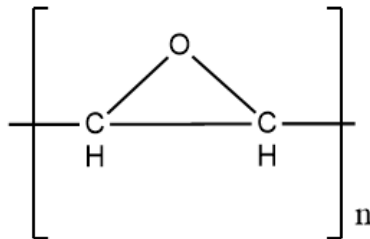


Figure 2.1 Oxirane ring (Ellis, 2015).

The diglycidyl ether of bisphenol A (DGEBA) is a commonly used epoxy resin. The value of the repeat unit ( $n$ ) allows for a variety of resin viscosities (Fernando and Degamber, 2006), as well as cross-link densities, temperature and chemical resistances in the cured system (Lee, 1989). Table 2.1 lists the increase in viscosity observed with increasing  $n$ . Liquid resins with low viscosities are suitable for use as matrices because they can impregnate the fibres (Bauer, 1995).

Resins are commonly characterised by their epoxy equivalent weight/weight per epoxide, which is defined as the molecular weight required to produce one molar equivalent of epoxide (Brock *et al.*, 2000). This value increases with increasing  $n$ , as shown in Table 2.1 (Weatherhead, 2012).

Table 2.1 Effect of repeat unit upon viscosity and softening point of cross-linked DGEBA resin systems (Lee, 1989; Campbell, 2010).

Repeat Unit $n$	State	Viscosity/Softening Point	Weight per epoxide
0	Liquid	0.004–0.006 Pa-s	170–178
0.07	Liquid	0.007–10Pa-s	180–190
0.14	Liquid	0.01–16 Pa-s	190–200
1	Semi-solid	40 °C	310
2	Solid	70 °C	475
3	Solid	100 °C	875

A disadvantage of using DGEBA is a lack of UV resistance. Hydantoin resins (Table 1.1) do not contain aromatic rings, and thus, provide UV resistance (Fiore and Valenza, 2013) that enables them to be widely used for structural composites (Brostow *et al.*, 2014). The resins have long curing times and low viscosity, which allows for good wettability with different fibres, whilst maintaining equivalent mechanical properties to those of DGEBA (Elias and Vohwinkel, 1986). The system, however, presents toxicity problems (Brostow *et al.*, 2014).



Novolac resins are characterised by high functionality that leads to a densely cross-linked structure with excellent adhesion properties (Ellis, 2015), temperature resistance and chemical resistance (Park, 2014). Depending upon the cross-linking agent, strengths of over 6.8 MPa can be maintained from room temperature to 150 °C (Panda, 2016).

Table 1.2 lists some common hardeners used with epoxy systems. Aliphatic amines are the most widely used hardeners and are characterised by large exotherms and short pot-lives. The resins are highly reactive, to produce a 'tightly' cross-linked network, due to the small distance between reactive sites, resulting in excellent solvent resistance and mechanical strength (Ellis, 2015). The most commonly used aliphatic amines, such as diethylenetriamine (DETA) and triethylenetetramine (TETA), produce systems that exhibit tensile strengths of up to 78 MPa, with heat-deflection temperatures of up to 107 °C. The epoxy systems can be cured at room temperature, although the final properties can be improved by post-curing (Brostow *et al.*, 2014).

Aromatic amine cured systems provide improved thermal and chemical resistance and longer pot-lives than those of aliphatic amine cured systems.

4,4'-Diaminodiphenyl sulfone (DDS) systems can allow for a heat-deflection temperature of 190 °C, although long cross-linking times are required at elevated temperatures with large exotherms (Fiore and Valenza, 2013). Tensile strengths range from 7000 to 10600 psi (Brostow *et al.*, 2014).

Acid anhydrides are the second largest group of hardeners used with epoxy resins; of these, cyclic anhydrides are widely used due to their low exotherms. Although the systems require long times (8–16 hours) before cross-linking at elevated

temperatures (150–200 °C) (Delawa, 1990), the cross-linked product shows low shrinkage in a stress-free system that provides excellent electrical insulation (Ellis, 2015). The systems have a range of heat-deflection temperatures from 70 to 190 °C, with tensile strengths ranging from 55 MPa to 82 MPa. The temperature resistance is superior to that of aliphatic amines, but not as good as that of some aromatic amines. Combined with electrical resistance, the hardener is widely used in the electrical coating industry (Delawa, 1990).

Epoxy resins have been widely used as surface coating materials due to their good mechanical properties, electrical insulation, adhesion and chemical resistance. Whilst epoxy resins may be more expensive than some other materials, they are used for electrical protection with electrical circuit board panels, for corrosive protection of pipelines and coating protection for the inside of drum containers (Hamerton, 1996).

Epoxy resins have outstanding adhesive properties and will bond to many surfaces. Resins can therefore be used to bond a wide variety of materials including steel and aluminium for use in aircraft structures (Panda, 2016).

When used with composite materials, epoxy resins contribute strength, durability and chemical resistance. This allows the composite to operate at elevated temperatures of up to 120 °C. During the initial mixing, the low viscosity of the resin facilitates good impregnation of the fibres and, due to the excellent adhesion properties, permits load transfer to the fibres (Hamerton, 1996).

## 2.2 Cross-Linking of Epoxy Resins

During the cross-linking reaction, the epoxy interacts with a hardener, such as a primary or secondary amine, through the generalised reaction scheme shown in Figure 2.2. Stage (i) involves nucleophilic attack of the carbon in the epoxide ring by the nitrogen atom of the amine. The nitrogen then bonds to the carbon of the epoxy group to form a secondary amine; a hydroxyl group is also formed (Ehlers *et al.*, 2007).

During stage (ii) of the reaction, the secondary amine produced during stage (i) can react with another epoxy molecule to form a tertiary amine. This mechanism allows for two different epoxy molecules to bond and cross-link (Fernando and Degamber, 2006). The cross-linking process is autocatalytic because the presence of the hydroxyl group during stage (ii) of the reaction protonates the oxygen atom, which facilitates ring opening of the epoxy group (McAdams, 1986; Vyazovkin and Sbirrazzuoli, 1996a).

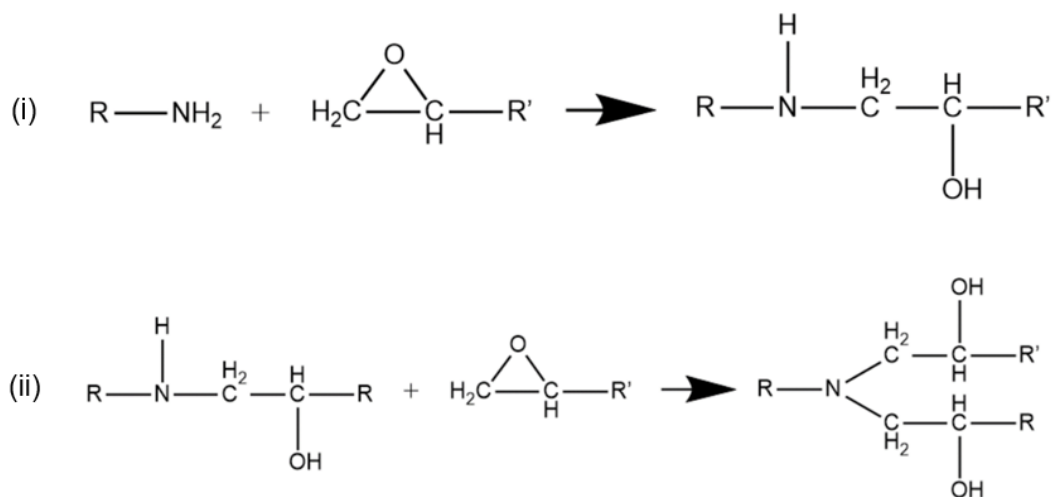


Figure 2.2 Generalised reaction scheme for an epoxy/amine resin system.

The cross-linking process is an irreversible transformation of a low-molecular-weight liquid into a highly cross-linked, hard and insoluble material (Hamerton, 1996). Upon mixing an epoxy resin and, for example, an amine hardener, the reactions lead to the formation of oligomers, which continue to react to form increasingly larger molecules (Kelly and Zweben, 2000). The reaction can be initiated by a number of methods, including thermal and electromagnetic means (Degamber and Fernando, 2004).

The glass transition temperature ( $T_g$ ) is a temperature range over which an amorphous polymer transitions from a glass into a rubbery state. Below  $T_g$ , the translational and rotational motions of polymer chains are restricted. As the material is heated through the transition, these motions become active (Menczel and Prime, 2014). During cross-linking,  $T_g$  increases with the extent of curing. As the molecular weight increases, mobility becomes more difficult and requires more energy to activate rotational and translational movement (Daniels, 1989).

As the resin system undergoes cross-linking, a stage is reached at which gelation is said to occur. This is represented by a significant change in the rheological properties, and the average molecular weight increases rapidly. The point of gelation is of particular interest because the increase in viscosity, accompanied by the formation of an infinite network, prevents the material from flowing, and thus, affects how it can be processed. The increase in viscosity is also accompanied by an increase in the modulus of the material; the macroscopic effects of gelation can be seen through DMA (Teil *et al.*, 2004).

Vitrification describes the process through which a cross-linking resin system becomes a glass. The  $T_g$  of a cross-linking resin system increases as the reaction proceeds. As the  $T_g$  reaches a value equivalent to the curing temperature, the

material undergoes vitrification. This process is reversible, unlike gelation. Vitrification leads to a rapid decrease in the rate of reaction because molecular motions are restricted. The cross-linking reactions can continue through a diffusion-controlled reaction mechanism (Gillham, 1986). Vitrification is often undesirable during processing because a large increase in viscosity is associated with the transition. Vitrification can be reversed by increasing the temperature of the resin above the  $T_g$  of the cross-linking resin system (Van Assche *et al.*, 1997).

### 2.2.1 Evolution of the Refractive Index during Cross-Linking

The refractive index,  $n$ , is an optical property that describes the propagation of light through a material. It is a dimensionless number and defined as the ratio of the velocity of light in a vacuum to that of light in the medium of interest, as shown in Equation 2.1

$$n = \frac{\text{Velocity of light in vacuum}}{\text{Velocity of light in the medium}} \dots\dots\dots \text{Equation 2.1}$$

The Debye equation (Equation 2.2) relates the dielectric constant, polarisability and dipole of a molecule.

$$N \left( \alpha + \frac{\mu^2}{3\varepsilon_0 kT} \right) = 3(K_r - 1)/(K_r + 2) \dots\dots\dots \text{Equation 2.2}$$

where

$N$  = number of molecules per unit volume,

$\alpha$  = polarisability,

$\mu$  = dipole,

$\varepsilon_0$  = permittivity of a vacuum,

$K_r$  = relative permittivity,

$k$  = Boltzmann constant.

At optical frequencies, the terms corresponding to molecular alignment do not influence the dielectric coefficient, and thus, Equation 2.2 can be simplified to Equation 2.3 (Bialkowski, 1996).

$$N\alpha = 3(K_r - 1)/(K_r + 2) \dots\dots\dots\text{Equation 2.3}$$

The term for  $N$  can then be replaced with a term for density to give Equation 2.4.

$$\alpha = 3M/L\rho(K_r - 1)/(K_r + 2)\dots\dots\dots\text{Equation 2.4}$$

where

$\rho$  = density,

$L$  = Avogadro's number,

$M$  = molar mass.

Also, at optical frequencies, the term for relative permittivity can be replaced by the square of the refractive index to give Equation 2.5 (Fulay & Lee, 2016).

$$\alpha = 3M/L\rho(n_r - 1)/(n_r + 2)\dots\dots\dots\text{Equation 2.5}$$

Equation 2.5 is a version of the Lorentz–Lorenz equation and shows that the refractive index is a function of the density and mean molar refractivity (Born & Wolf, 2013).

During cross-linking, shrinkage causes an increase in density and contributes to an increase in the refractive index. Polarisability is a measure of the rigidity of electrons within a molecule as light passes through it, and also changes during cross-linking (Zhou, 1993). Polarisability can be described by Equation 2.6.

$$\alpha = 3R_M/L \dots \dots \dots \text{Equation 2.6}$$

where

$R_M$  = molar refractivity.

Molar refractivity can then be derived from Equation 2.7.

$$R_M = \frac{M}{\rho} (n_r^2 - 1) / (n_r^2 + 2) \dots \dots \dots \text{Equation 2.7}$$

The molar refractivity is the total polarisability of a mole of a substance (Born & Wolf, 2013). Different bonds have characteristic molar refractivities, and Table 2.2 lists values relevant to the cross-linking of epoxy resins (Atkins *et al.*, 2014). As cross-linking proceeds, the C-O-C group of the epoxy becomes depleted and becomes replaced by hydroxide and tertiary amines. Thus, the increased polarisability contributes to the increase in refractive index.

Table 2.2 Molar refractivities of bonds involved in the cross-linking of epoxy resins (Atkins *et al.*, 2014; Zhou, 1993).

<b>Group</b>	<b>Molar Refractivity (cm<sup>3</sup>/mol) at 589 nm</b>
C-O-C	2.85
C-O-H	3.23

By taking Equation 2.7 and replacing  $M/\rho$  with the molar volume,  $V_M$ , Equation 2.8 can be obtained, which is an expression for refractive index in terms of composition through molar refractivities.

$$n_r = \{(V_M + 2R_M)/(V_M - R_M)\}^{\frac{1}{2}} \dots \dots \dots \text{Equation 2.8}$$

By dividing Equation 2.8 by  $V_M$ , Equation 2.9 can be obtained.

$$n_r = \left\{ \left( 1 + \frac{2R_M}{V_M} \right) / \left( 1 - \frac{R_M}{V_M} \right) \right\}^{\frac{1}{2}} \dots\dots\dots \text{Equation 2.9}$$

From the binomial theorem, the denominator term,  $1/(1-R_M/V_M)$ , tends to  $(1+R_M/V_M)$  and Equation 2.9 approximates to a linear expression. Thus, a linear relationship between refractive index and molar refractivity exists for small changes in refractive index. The refractive index should only depend upon the chemical nature of the molecules and the molar volume.

## 2.3 Monitoring the Cross-Linking of Epoxy Resins

### 2.3.1 Differential Scanning Calorimetry

Differential scanning calorimetry (DSC) is a common and frequently used technique to study cross-linking reactions. The cross-linking reactions shown in Figure 2.2 are exothermic and DSC is used to quantify the enthalpy of the reactions, which can be used to determine the degree of curing. Second-order transitions, such as  $T_g$ , can also be detected through DSC (Höhne *et al.*, 1996; Brown, 2012).

Power-compensated DSC was introduced by Perkin-Elmer in 1963. This method involves heating a sample and reference container in separate chambers, as shown in Figure 2.3. Two identical chambers are controlled to remain at the same temperature during cross-linking. Platinum thermocouples are located below the sample and reference chambers, so any difference in energy required to maintain thermal equilibrium is recorded. In this way, if heat is liberated by the sample, less



energy will be required to maintain the temperature and an exothermic output will be recorded. The energy difference dictates the magnitude of the exo- or endothermic process taking place. The differential scanning calorimeter can be used for non-isothermal heating/cooling or isothermal experiments (Menczel and Prime, 2014).

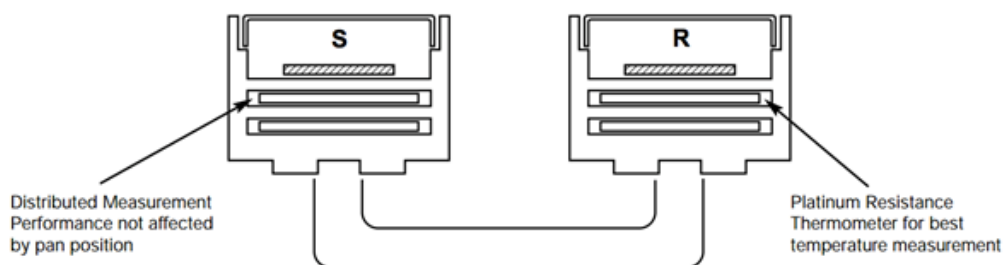


Figure 2.3 Schematic illustration of the power compensation DSC technique developed by Perkin-Elmer (Perkin-Elmer, 2016).

### 2.3.1.1 Calibrating of a Differential Scanning Calorimeter

A calibration procedure, involving the use of high-purity reference standard materials, allows for the alignment of the temperature sensors of the differential scanning calorimeter with known thermal properties such as the melting and freezing points (Menczel and Prime, 2014). Similarly, the power output also has to be calibrated by using standards with well-defined enthalpies (Haines, 2002).

Sarge *et al.* (1997) summarised test conditions and calibrants for temperature and heat-flow calibration. A summary of the test conditions used to obtain the calibration values are listed in Table 2.3. Many of the calibrants available exhibit well-defined transition temperatures and enthalpies of transition, to allow both types of calibration to be completed simultaneously (Sarge *et al.*, 1997).

Table 2.3 Summary of practices for DSC calibration  
(ASTM-E967 2014; ASTM-E968 2014).

	<b>Temperature Calibration</b>	<b>Enthalpy Calibration</b>
<b>Measurement</b>	Onset of melting	Endothermic melting peak area
<b>Choice of Calibrants</b>	Those exhibiting melting within a temperature range of interest	Those exhibiting melting within a temperature range of interest
<b>Sample Mass</b>	5-15 mg	5-10 mg
<b>Heating Rate</b>	10 K/minute	10 K/minute
<b>Containers</b>	Inert pans or crucibles	Inert pans or crucibles
<b>Repeatability</b>	95% Confidence	95% Confidence

Metals and polymer reference standards are recommended for temperature and heat-flow calibration procedures. Charsley *et al.* (2010) compared the differences between using organic (diphenyl acetic acid) and metallic (indium) standards for DSC calibration. Excellent correlations between the materials certificate, experimental heat flow and enthalpy of melts were obtained with observed differences in repeatability. An increased heat-capacity change during heating of the polymer standard caused a decrease in reproducibility during repeated scans. Thus, metallic standards are recommended for high-precision calibration. Polymer standards are useful if their transition temperatures are close to the desired application range.

### 2.3.1.2 Analysis of Cross-Linking Reactions Using Differential Scanning Calorimetry

When determining the degree of cross-linking of a thermosetting resin, an assumption is made that the total heat evolved is proportional to the degree of cross-linking (Lam and Afromowitz, 1995a). Cross-linking kinetics can be obtained under isothermal or non-isothermal heating conditions.

Non-isothermal heating is used to define the total enthalpy of exothermic reactions that occur during cross-linking (Zhang and Zhao, 2016). This can then be used to determine the degree of curing at time,  $t$ , under either non-isothermal or isothermal heating regimes. This relationship is given as Equation 2.10 (Garschke *et al.*, 2013).

$$\alpha = \frac{\Delta H_t}{\Delta H_{total}} \dots \dots \dots \text{Equation 2.10}$$

where

$\alpha$  = extent of reaction,

$\Delta H_t$  = reaction enthalpy at time  $t$ ,

$\Delta H_{total}$  = total enthalpy of reaction.

Uncertainties can arise upon determining the enthalpy of the reaction in both isothermal and non-isothermal modes of operation due to uncertainties in the geometry of the baseline and integration limits. These issues are discussed in Sections 2.3.1.2.1 and 2.3.1.2.2.

### 2.3.1.2.1 Non-isothermal Enthalpy Determination

Non-isothermal curing experiments monitored by DSC can provide information on cross-linking kinetics through the enthalpy of the reaction and evolution of the glass transition temperature. These experiments can take less time to complete than isothermal scans and avoid the loss of data experienced during the 'heat-up' period of isothermal experiments (Bilyeu *et al.*, 2000). However, the constant temperature change can create thermal gradients across a sample, giving non-equilibrium conditions (Mettler-Toledo, 2001). Results are also dependent on the heating rate, whereby the enthalpy, onset of the reaction and the peak are affected (Roşu *et al.*, 2002; Kim *et al.*, 2012; Xia *et al.*, 2014).

When conducting cross-linking kinetic studies using non-isothermal heating, the following method is recommended in ASTM-E537-12 (2012). A horizontal baseline is drawn between the onset and end of the exothermic reaction, as illustrated in Figure 2.4. The area under the reaction exotherm is integrated to obtain the enthalpy of the reaction. The situation described is an ideal case if a horizontal baseline is present.

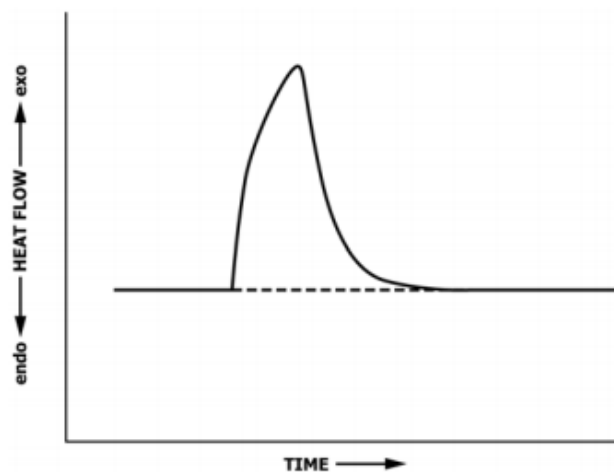



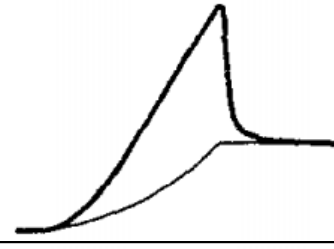



Figure 2.4 Baseline construction to allow integration of an exothermic reaction.

However, in most samples, the ideal scenario is not present. Significant deviations in the baseline can be present as a result of the changing heat capacity during cross-linking, in addition to thermal degradation. Construction of a baseline during the reaction can become difficult due to an absence of clear start and end points. The geometry of the baseline is also not straightforward because a linear baseline does not take into account the contribution of heat capacity to shifts in the baseline (Hemminger and Sarge, 1991).

Hemminger and Sarge (1991) investigated errors associated with different baseline constructions, against an assumed true baseline for the melting of ice. Table 2.4 shows these baseline constructions and their error relative to the 'true' value. The determination of the baseline limits was not discussed. It can be seen that each method introduces errors into the calculation. Höhne *et al.* (2013) stated that no 'correct' baseline construction method existed and that various construction methods should be investigated.

Table 2.4 Relative errors of the enthalpy of the melting of ice due to different baseline constructions (Hemminger and Sarge, 1991).

Method	Representation	Real Error
True Baseline		0.000
Straight Line		0.008
Step		0.020
Parabola		0.003
Proportional to the degree of conversion		0.016

### 2.3.1.2.2 Isothermal Enthalpy Determination

Isothermal cross-linking has increased repeatability over non-isothermal scans due to the presence of a thermal equilibrium (Fava, 1968). However, part of the curing data is lost during the initial heat-up period and this source of inaccuracy is exacerbated at higher temperatures. During rapid cross-linking regimes, the initial heating and stabilisation period of DSC accounts for a large proportion of the overall curing, and hence, isothermal analysis may be unsuitable (Bernath *et al.*, 2016).

Two methods for sample loading during isothermal experiments are present and seek to minimise the 'heat-up' period.

Method 1 (Fava, 1968): Introduce the sample to the calorimeter at room temperature and ramped it rapidly to the desired isothermal cross-linking temperature.

Method 2 (Sourour and Kamal, 1976): Introduce a sample into a preheated calorimeter.

Method 1 allows for a reproducible thermal history of the sample, although data was lost in the heat-up and equilibration stage. Method 2 is designed to minimise the heat-up period, but the time to insert the sample and allow for equilibration will vary (Cheng, 2002). The enthalpy during isothermal curing for both methods was compared by Miller and Oebser (1980) during the curing of a bisphenol-based epoxy system. No significant differences in enthalpy were observed after a 20-minute

cross-linking schedule, although the instrument was able to reach equilibrium quicker using the Method 2.

A period of instrument instability exists immediately after reaching the desired temperature and appears as a spike in the trace. The system reaches equilibrium once temperature control is re-established by the instrument (Barton, 1983). The heat-up period and this period of instability are removed by drawing a horizontal baseline from the end of the reaction to intersect with the heat-up period (ASTM-D3418, 2015). This approach is illustrated in Figure 2.5. This method for constructing the baseline has been adopted as the standard procedure for calculating  $\Delta H$  under isothermal conditions (ASTM-D3418, 2015).

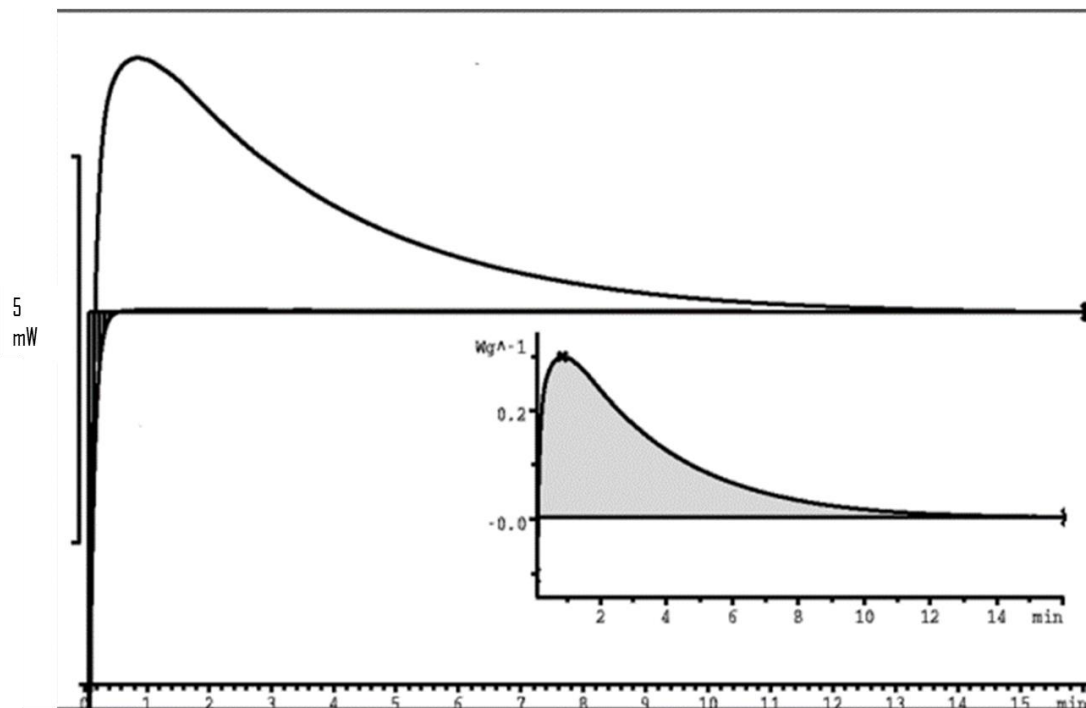


Figure 2.5 Cross-linking reaction at 190 °C before and after baseline construction (Mettler-Toledo, 2001).

Barton (1983) aimed to improve this approach by developing a method that produced a non-linear baseline, which did not remove data during heat-up. A



second scan was completed on a fully cured sample under identical conditions to obtain a 'true' baseline that could be deducted from the cross-linking data. Improved repeatability was achieved when the 'true' baseline method was used instead of a horizontal baseline. The method, however, does not account for the changing heat capacity of the sample due to cross-linking; a constant heat capacity of the fully cross-linked sample is assumed. The second scan can also be time-consuming, especially under long cross-linking schedules. The success of the 'true' baseline method has been absorbed into all DSC instrumentation software, whereby the user is able to subtract the desired baseline (Turi, 1997). Despite success, a horizontal baseline remains the standard procedure.

### **2.3.1.3 Detecting the Glass Transition Temperature**

Although the manifestation of the  $T_g$  occurs over a temperature range, a single value is often quoted. The methodology described (ASTM-E1356 2014) for defining  $T_g$  is illustrated in Figure 2.6 (Bilyeu *et al.*, 2000). The  $T_g$  is effectively the midpoint temperature of the step change in the baseline or heat-capacity trace (ASTM-E1356, 2014). Heating rate affects the width and range of  $T_g$ , and thus, the rate must be stated (Bair, 1981).

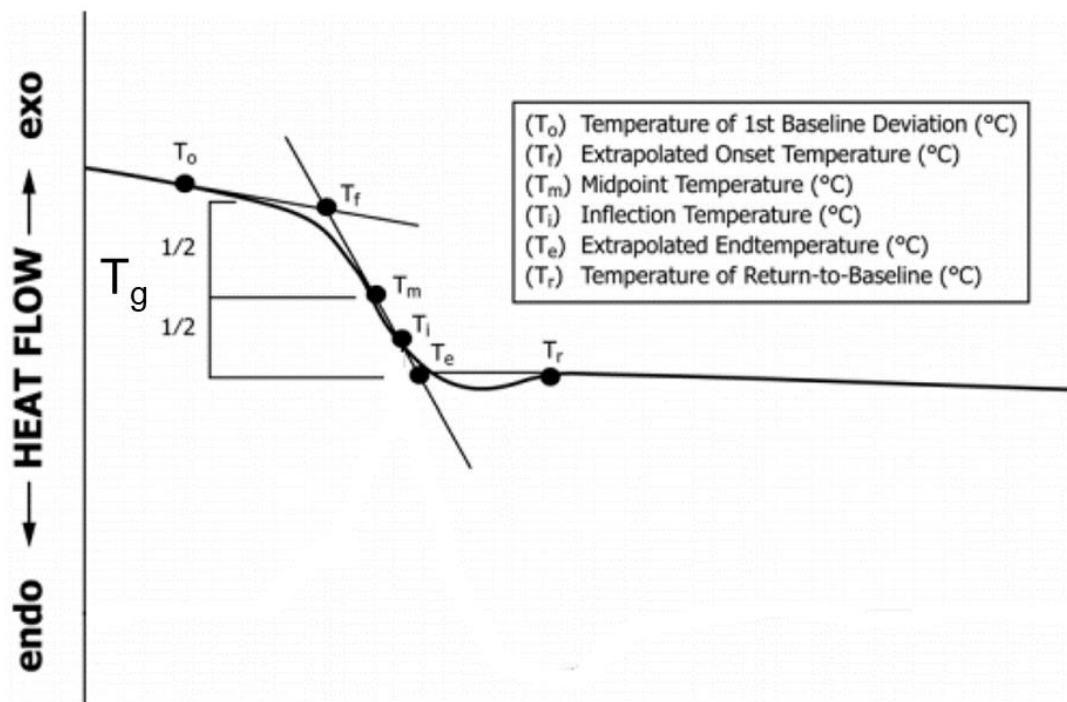


Figure 2.6 Assignment of the glass transition (ASTM-E1356, 2014).

The thermogram of the glass transition region can be affected by annealing of an amorphous resin below its  $T_g$ , causing enthalpic relaxation. The enthalpic relaxation can be observed as an endothermic event immediately after heating through the glass transition region (Hay, 1995). This is applicable to thermoplastic (Hay, 1995) and thermoset (Montserrat, 2000) materials. Richardson and Savill (1975) suggested the use of an extrapolated baseline to determine  $T_g$  if enthalpic relaxation was observed. The  $T_g$  of annealed samples remained within  $\pm 1$  K of non-annealed samples, despite the presence of large enthalpic events. An example of an extrapolated baseline is shown in Figure 2.6 between points  $T_e$  and  $T_f$ . This approach has been adopted by TA instruments (Sichina, 2000) and Mettler-Toledo (2001), in addition to ASTM-E1356 (2014).

The glass transition temperature of a partially cross-linked system can be distorted and perhaps masked by the presence of residual exotherms. Fava (1968) investigated the glass transitions of a partially cross-linked DGEBA system. Due to residual cross-linking, the end temperature of the glass transition temperature was not obtainable and so the onset temperature was quoted. Bilyeu *et al.* (2000) agreed upon this approach under such circumstances but insisted that the value must be clearly defined as the onset.

#### **2.3.1.4 Cross-Linking Kinetics**

The cross-linking kinetics of thermosetting resins can be described by mechanistic (Blanco *et al.*, 2005) or phenomenological models (Liu *et al.*, 2012b). Mechanistic models require information regarding the mass-balance and relative concentrations of chemical species involved in the reactions. Complex reactions taking place during cross-linking can result in the need for information on many parameters, creating a complicated and complex model. Although this approach is time-consuming, it can provide realistic predictions of cross-linking (Rabearison *et al.*, 2011). Due to the complexity of the mechanistic models, phenomenological predictions are used more widely. These models predict the main features of the reaction, whilst ignoring details related to the individual chemical species (Ruiz *et al.*, 2006).

Phenomenological models can then be used to describe two reaction types of thermosetting materials, known as  $n^{\text{th}}$  order or autocatalytic kinetics. As described in Equation 2.11, the  $n^{\text{th}}$  order (or catalytic) kinetics state that the rate of the reaction is proportional to the amount of unreacted material in the system. The peak reaction

rate during isothermal curing is at  $t = 0$  (Montserrat and Cima, 1999; Janković, 2010; Boyard, 2016; Wang *et al.*, 2016).

$$\frac{d\alpha}{dt} = k(1 - \alpha)^n \dots\dots\dots\text{Equation 2.11}$$

where

$\frac{d\alpha}{dt}$  = rate of reaction,

$\alpha$  = degree of cross-linking,

$k$  = rate constant,

$t$  = time,

$n$  = reaction order.

Autocatalytic kinetics describes a curing process in which an increase in the reaction rate is seen during cross-linking. Figure 2.8 depicts an example thereof, showing a maximum rate of reaction part-way through cross-linking of an epoxy resin (Lee *et al.*, 2000). Fraga *et al.* (2001), Billaud *et al.* (2002), and Yamasaki and Morita (2012) have used FTIRS to show the reaction rate increase that occurs with an increase in hydroxyl content during the first step of the reaction shown in Figure 2.2. McAdams (1986), Buist *et al.* (1996) and Vyazovkin and Sbirrazzuoli (1996a) stated that the inclusion of the hydroxyl group acted to partially protonate the oxygen atom of the epoxy group; thus facilitating ring opening and acting as a catalyst. The formation of secondary and tertiary amines is then accelerated (McAdams, 1986; Buist *et al.*, 1996; Billaud *et al.*, 2002). The autocatalytic equation is described by Equation 2.12 (Kamal, 1972; Prime, 1981; Boyard, 2016).

$$\frac{d\alpha}{dt} = k\alpha^m(1 - \alpha)^n \dots\dots\dots\text{Equation 2.12}$$

where

$m$  and  $n$  = reaction orders.

Table 2.5 lists examples in which the autocatalytic model has been plotted alongside the degree of cross-linking obtained by DSC for various DGEBA systems. In each case, good agreement between the model and experimental data was present until the later stages of cross-linking, as shown in Figure 2.7. Discrepancies during the later stages of cross-linking occur when the rate of reaction changes from being chemically controlled to diffusion controlled (Vyazovkin and Sbirrazzuoli, 1996b; Ruiz *et al.*, 2006; Rabearison *et al.*, 2011).

Table 2.5 Examples of autocatalytic model (Equation 2.12) correlated with DSC data for the cross-linking of epoxy resin systems. DMAP: 4-(*N,N*-dimethylamino)pyridine.

Material	$\ln k$	$m$	$n$	Comments	Reference
DGEBA/ triamine of polyoxypropylene	12.2	0.23	1.61	Good agreement until later stages of cross-linking at 80 °C.	Montserrat and Cima, 1999
DGEBA with diaminodiphenyl methane	6.8	0.76	2.33	Good agreement, but deviations observed in later stages of cross-linking at 80 °C.	Janković, 2010
DGEBA/DMAP	21.2	1	2.4	Good agreement up to about 70% at 80°C isothermal cross-linking.	Román <i>et al.</i> , 2013
DGEBA/ polyoxypropylene diamine	-8.29 to -6.31	0.35	1.65	Cross-linking at 35-65 °C. A good correlation was observed up to 80% conversion	Wang <i>et al.</i> , 2016

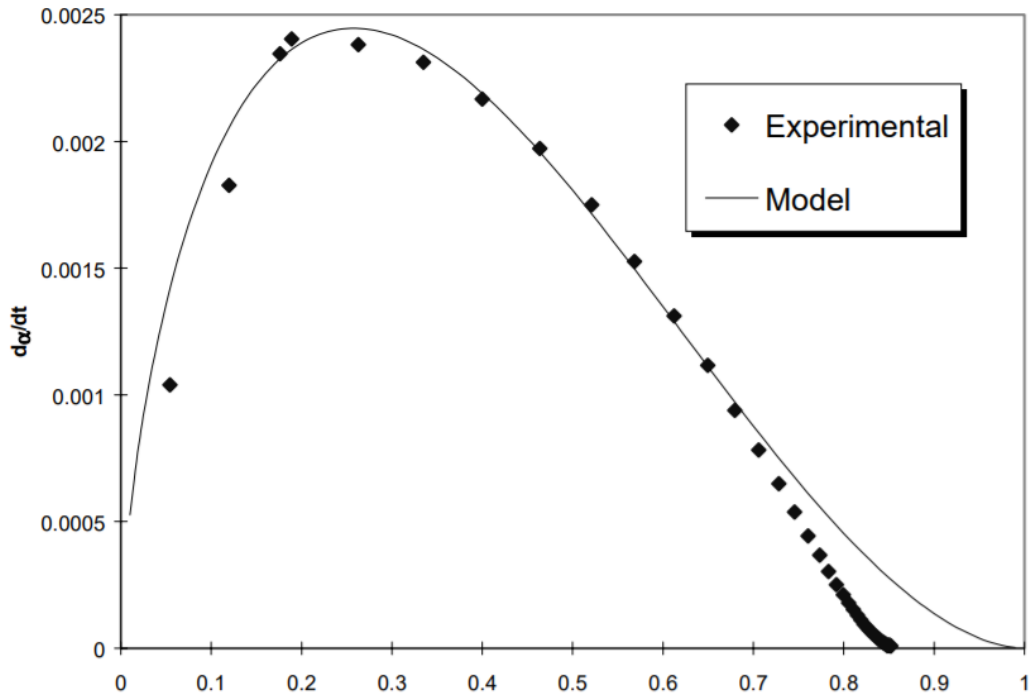


Figure 2.7 Conversion of a DGEBA hexanhydro-4-methylphthalic anhydride system as a function of time at various temperatures for the curing of an epoxy resin (DGEBA/methylene dianiline (MDA)), alongside theoretical predictions obtained by using Equation 2.12 (Boey and Qiang, 2000).

Kamal (1974) introduced a diffusion factor into Equation 2.12 to account for vitrification and produced Equation 2.13.

$$\frac{d\alpha}{dt} = (k_1 + k_2\alpha^m)(1 - \alpha)^n \dots\dots\dots\text{Equation 2.13}$$

where

$k_1$  and  $k_2$  = rate constants.

Table 2.6 provides a summary of examples for which the model has been compared with DSC data. Conflicting results are present, whereby Min *et al.* (1993b) and Garschke *et al.* (2013) observed excellent correlations across the whole cross-linking regime, whilst Sourour and Kamal (1976) and Ryan and Dutta (1979) still observed discrepancies during the later stages of cross-linking.

Table 2.6 Examples of the autocatalytic model containing a diffusion factor and modelled alongside DSC data.

Material	$k_1$	$k_2$	$n$	$m$	Comment	Reference
DGEBA/ MPD - bisphenol A/ <i>m</i> - phenylene diamine	From $0.02 \times 10^3$ to $8 \times 10^3$	$2.5 \times 10^3$ to $60 \times 10^3$	1	1	Good correlation with DSC data from 50–150 °C, although discrepancies remain during diffusion control.	Sourour and Kamal, 1976
DGEBA with <i>m</i> - phenylene diamine	From 0.002 to 0.2	0.05–1	0.9– 1.3	0.7– 1.1	Close correlation across the whole reaction scheme from isothermal cross-linking at 70–170 °C.	Ryan and Dutta, 1979
DGEBA with DDS	$2.41 \times 10^3$	$9.91 \times 10^3$	2	1	Deviation from the model after approximately 40–60% conversion at 220 °C. Performed worse than the $n^{\text{th}}$ order model	Barton <i>et al.</i> , 1992
DGEBA/ DDS	$6.5 \times 10^3$	$1.3 \times 10^3$	1	1	Upon comparison with the $n^{\text{th}}$ order model, improved correlations were observed during the later stages of cross-linking at 130 °C.	Min <i>et al.</i> , 1993b
TGMDA/ DDS	From $2.7 \times 10^{-3}$ to $87.6 \times 10^{-3}$	From $1.94 \times 10^{-3}$ to $12.17 \times 10^{-3}$	2.62– 2.35	1.23 – 1.77	An excellent correlation with the experimental data from 150–210 °C.	Garschke <i>et al.</i> , 2013

### 2.3.2 Fourier Transform Infrared Spectroscopy

Fourier transform infrared spectroscopy (FTIRS) is another widely used technique for characterising the curing of thermosetting resins, by determining the functional groups present and their concentration. Specific functional groups absorb radiation in the mid-infrared (MIR) and near-infrared (NIR) regions from 400 to 4000 and 4000 to 14000  $\text{cm}^{-1}$ , respectively (Smith, 2011). A Fourier transform infrared (FTIR) spectrometer launches infrared radiation through a sample and measures the absorption of light over a range of wavelengths (Mosiewicki *et al.*, 2011). The absorbance bands are related to functional groups in the sample; changes in their intensity are related to functional group depletion and formation (Fernando and Degamber, 2006). Cross-linking kinetics can be monitored by tracking the relative absorbance bands associated with specific functional groups that participate in the cross-linking reaction (Bartolomeo *et al.*, 2001).

The degree of cross-linking can be calculated using Equation 2.14 and it has been used widely for tracking the cross-linking of epoxy resins using NIR or MIR FTIRS (Wang and Gillham 1991; Bartolomeo *et al.*, 2001; Billaud *et al.*, 2002).

$$\alpha = \left[ \frac{(A_{\text{reactive band}}/A_{\text{reference band}})_t}{(A_{\text{reactive band}}/A_{\text{reference band}})_{t=0}} \right] \dots\dots\dots \text{Equation 2.14}$$

where

$\alpha$  = degree of curing,

$A_{\text{reference band}}$  = area of a reference absorbance band,

$A_{\text{reactive band}}$  = area of a reactive absorbance band,

$t$  = time after the start of the reaction,

$t_0$  = start of the reaction.



Normalisation of the reactive absorbance band allows for (i) changes in the path length, and (ii) an increase in the baseline of the spectra as a result of the increasing refractive index of the resin during cross-linking.

### 2.3.2.1 Mid-Infrared Spectroscopy

MIR spectroscopy (400–4000  $\text{cm}^{-1}$ ) is used to identify organic compounds (Poisson *et al.*, 1996). In this region, the fundamental frequencies are observed, and hence, show their strongest absorptions. The area is well researched and libraries are available to identify spectral bands. Table 2.7 lists the main absorbance bands associated with epoxy/amine resin systems.

Table 2.7 Band assignments for epoxy/amine resin systems in the MIR range.

Group	Wavelength ( $\text{cm}^{-1}$ )	Reference
Epoxy	915, 1345, 1430, 3056	Poisson <i>et al.</i> , 1996; Don and Bell, 1998; Fraga <i>et al.</i> , 2001; Rigail-Cedeño and Sung, 2005; Pritchard, 2012; Yamasaki and Morita, 2014; McCoy <i>et al.</i> , 2016
Hydroxyl	1914, 3450	Fraga <i>et al.</i> , 2001; Yamasaki and Morita, 2014; Cysne Barbosa <i>et al.</i> , 2017
CH	830, 1180, 1510, 1607	Poisson <i>et al.</i> , 1996; Fraga <i>et al.</i> , 2001; Rigail-Cedeño and Sung, 2005; Pritchard, 2012; Cysne Barbosa <i>et al.</i> , 2017
Primary amine	1624, 2025, 3370, 3460	Mijović and Andjelić, 1996; Don and Bell, 1998; Yamasaki and Morita, 2014

Fraga *et al.* (2001) obtained isothermal curing kinetics at 60, 70, 80 and 90 °C for a DGEBA/1,2 diamine cyclohexane system using MIR spectroscopy and DSC. The authors used the terminal epoxy band at 915  $\text{cm}^{-1}$ , which was referenced to an inert phenylene group at 830  $\text{cm}^{-1}$ . The spectral and thermal degrees of curing gave similar results, although a slight increase was observed for the FTIRS data at each temperature. Additionally, both methods showed a good correlation to the autocatalytic model (Equation 2.13). A possible cause of the discrepancy is the presence of an unassigned band reported by Dannenberg and Harp (1956), which was observed during the curing of two epoxy resin systems. An increase in the hydroxyl group at 3450  $\text{cm}^{-1}$  was observed throughout cross-linking, concurrent with reports by Lee *et al.* (2000), Fraga *et al.* (2001) and Yamasaki and Morita (2012), during which the increasing OH content accompanied an increase in the rate of reaction.

Don and Bell (1998) used MIR spectroscopy to monitor the curing of a DGEBA/4,4'-diaminodiphenyl methane (DDM) system modified by the introduction of polycarbonate. They tracked the depletion of the primary amine at 1624  $\text{cm}^{-1}$  and the epoxy at 915  $\text{cm}^{-1}$  during cross-linking at 90 °C. The primary amine band at 3460  $\text{cm}^{-1}$  could not be used due to overlap with the secondary amine and hydroxyl groups. The presence of the unassigned band reported by Dannenberg and Harp (1956) and the normalisation band were not discussed. The authors concluded that FTIRS could be used for blended systems.

Nikolic *et al.* (2010) investigated the curing of DGEBA with an aliphatic amine hardener at 30 °C through FTIRS in the MIR region. Depletion of the epoxy intensity at 915  $\text{cm}^{-1}$  was referenced to an inert band at 1182  $\text{cm}^{-1}$  due to C–O stretching of

the aromatic ring of DGEBA. The results appeared to correlate with a decrease in the absorption of a secondary epoxy band at  $3056\text{ cm}^{-1}$ , although the absorbance band was of low intensity and close to that of strong OH absorptions.

The use of MIR spectroscopy for quantifying the depletion of the epoxy functional group using the band at  $915\text{ cm}^{-1}$  has also been demonstrated by Xu *et al.* (1994), Mijovic and Andjelic (1995), Poisson *et al.* (1996) and Yamasaki and Morita (2012). Each of the authors noted the presence of the unassigned band overlapping with the epoxy band at  $915\text{ cm}^{-1}$ . Don and Bell (1998), Fraga *et al.* (2001) and Nikolic *et al.* (2010) all reported cross-linking data of epoxy resins using MIR spectroscopy, but they observed overlapping spectra and did not quantify the contribution of the unassigned band close to that of the epoxy. This may lead to erroneous conclusions. Discrepancies can be seen upon comparing the data with the NIR data, as discussed in Section 2.3.2.3.

### **2.3.2.2 Near-Infrared Spectroscopy**

NIR spectroscopy operates between  $4000$  and  $10000\text{ cm}^{-1}$  (Xu *et al.*, 1994). The strong and isolated observed bands are overtones of the vibrations in the MIR region. In the NIR region, a strong band at  $4530\text{ cm}^{-1}$  is designated as a combination of the second overtone of the epoxy stretching with CH stretching (González *et al.*, 2012). The bands in the NIR range have been used to track the cross-linking of epoxy resins (Gillham, 1991; Poisson *et al.*, 1996; Nikolic *et al.*, 2010; Mosiewicki *et al.*, 2011; Pritchard, 2012; Wang *et al.*, 2016). A summary of the main absorbance bands for an epoxy/amine resin system is given in Table 2.8 (Pandita *et al.*, 2012).

Table 2.8 Summary of the main NIR absorbance peaks for an epoxy/amine resin and their associated assignments.

Group	Wavelength (cm <sup>-1</sup> )	Reference
Epoxy	4535, 6060	Strehmel and Scherzer, 1994; Xu <i>et al.</i> , 1994; Mijović and Andjelić, 1996; Poisson <i>et al.</i> , 1996; Norris, 2000; Billaud <i>et al.</i> , 2002; Pandita <i>et al.</i> , 2012
Hydroxyl	4784, 4878, 5449, 7000	Strehmel and Scherzer, 1994; Xu <i>et al.</i> , 1994; Mijović and Andjelić, 1996; Norris, 2000; Billaud <i>et al.</i> , 2002; Pandita <i>et al.</i> , 2012; Dümichen <i>et al.</i> , 2015
CH	4680, 4620, 5969	Strehmel and Scherzer, 1994; Mijovic and Andjelic, 1995; Poisson <i>et al.</i> , 1996; Norris, 2000; Billaud <i>et al.</i> , 2002; Pandita <i>et al.</i> , 2012
Primary amine	5045	Strehmel and Scherzer, 1994; Mijovic and Andjelic, 1995; Norris, 2000; Billaud <i>et al.</i> , 2002; Dümichen <i>et al.</i> , 2015
Primary and secondary amine	6660	St John and George, 1992; Billaud <i>et al.</i> , 2002; Dümichen <i>et al.</i> , 2015

Xu *et al.* (1994) monitored the cross-linking of a phenyl glycidyl ether with *N*-methylaniline. They observed changes in the intensity of the epoxide group at 4535 cm<sup>-1</sup>, the primary and secondary amines at 6660 cm<sup>-1</sup> and the hydroxyl group at 7000 cm<sup>-1</sup>. Absorbance bands were referenced to aromatic CH stretching at 5969 cm<sup>-1</sup>. During isothermal curing at 140 °C, depletion of the epoxide conversion was determined using the well-separated peak at 4530 cm<sup>-1</sup>. An increase in the hydroxyl group was observed throughout cross-linking; the authors suggested that the autocatalytic reaction scheme was caused by the catalytic effect of the hydroxyl

group. The results showed excellent correlation with a mechanistic model proposed by the authors.

Min *et al.* (1993c) investigated the kinetics of a DGEBA and 4,4'-diaminodiphenyl sulfone (DDS) system at various intervals during cross-linking at 130 and 205 °C. Quantitative analysis of cross-linking was obtained over a period of 600 minutes using the epoxy band at 4535 cm<sup>-1</sup>. The authors used the inert band at 4620 cm<sup>-1</sup> (aromatic CH bond) as a reference. Additionally, the authors tracked the conversions of primary and secondary amines by subtracting the primary amine band at 4935 cm<sup>-1</sup> from the combined primary and secondary amine absorption at 6635 cm<sup>-1</sup>. In a subsequent paper by Min *et al.* (1993a), the authors compared the degree of cross-linking derived from FTIRS analysis with that of DSC data. The degree of cure was analysed through the evolution of the glass transition temperature after various cross-linking periods and correlated closely with the FTIRS data. The authors provided further corroboration by showing a close correlation between the autocatalytic model (Equation 2.13) and the degree of cross-linking observed by FTIRS (Min *et al.*, 1993b).

Billaud *et al.* (2002) quantified the cross-linking reaction of the diglycidyl ether of bisphenol F (DGEBF) with 4,4'-methylenebis(2,6-diethylaniline) (MDEA) at 72 and 160 °C. They encountered overlaps of the epoxy and aromatic C–H bands between 5900 and 6100 cm<sup>-1</sup> and the secondary and primary amines between 6600 and 6700 cm<sup>-1</sup>. They referenced the bands using the aromatic CH at 4620 cm<sup>-1</sup>. The authors used a method previously reported by St John and George (1992) and Min *et al.* (1993b) to determine the secondary amine concentration by subtracting the primary amine band from that of the combined primary and secondary band at

6600  $\text{cm}^{-1}$ . The degree of curing between the epoxy bands at 4530 and 6060  $\text{cm}^{-1}$  was compared upon normalisation to the band at 4620  $\text{cm}^{-1}$ . Similar trends were observed, although the band at 6060  $\text{cm}^{-1}$  gave an increased final degree of conversion by 6%. The reasons for the discrepancies were given as follows:

- (i) possible solvent evaporation during initial cross-linking that might overlap with the epoxy band at 4530  $\text{cm}^{-1}$ ,
- (ii) observed retardation of the spectra between 7650 and 6350  $\text{cm}^{-1}$  after approximately 80% conversion.

The authors noted the presence of a band close to the epoxy region at 4530  $\text{cm}^{-1}$  that became apparent towards the end of cross-linking.

The presence of a relatively small band close to the epoxy band at 4530  $\text{cm}^{-1}$  has also been reported during the cross-linking of an epoxy resin/amine hardener system by Strehmel and Scherzer (1994), Mijovic and Andjelic (1995), Mijovic *et al.* (1996) and Pandita *et al.* (2012). Pandita *et al.* (2012) investigated the cross-linking of the LY3505/XB3403 resin system and assessed the significance of the unassigned band. Following cross-linking for 600 minutes, the area of the unassigned band was estimated to be less than 5% of the initial epoxy peak area. The authors used a Fourier self-deconvolution routine to resolve the contribution of the unresolved band to the epoxy band. The results showed an excellent correlation to results obtained through DSC experiments.

NIR spectroscopic analysis reveals a clear epoxy band at 4530  $\text{cm}^{-1}$ , which makes it useful for quantifying the degree of cross-linking. Clear absorbance bands for the primary amine and the combined primary and secondary amine band allow additional cross-linking information to be obtained upon comparison with the results of MIR

spectroscopy. Additionally, the presence of hydroxyl groups allows the reported catalytic effect on the reaction rate to be quantified.

### **2.3.2.3 Comparison of Mid-infrared and Near-infrared Spectroscopy for Epoxy Conversion**

Mijovic and Andjelic (1995) investigated the cross-linking of a DGEBF and 4,4'-methylenedianiline (MDA) system at 110 and 120 °C through MIR spectroscopy. They also used the band at 915 cm<sup>-1</sup>, which was normalised to the inert CH<sub>2</sub> group at 2920 cm<sup>-1</sup>. Similar to the study by Dannenberg and Harp (1956), the researchers found an unassigned band at 905 cm<sup>-1</sup>, close to the epoxy band. This unassigned band affected their quantitative analysis. The authors compared the degree of cross-linking to that obtained by NIR spectroscopy and found discrepancies of approximately 10% after 150 min. The MIR data also showed an increased initial rate of reaction. This study quantifies the significant contribution of the unassigned band at 915 cm<sup>-1</sup>.

Large discrepancies between MIR and NIR conversions due to the contribution of the unassigned band at 915 cm<sup>-1</sup> have also been reported by Poisson *et al.* (1996). They investigated the curing kinetics of a DGEBA and dicyandiamide (DDA) system at 80 °C using the band at 915 cm<sup>-1</sup> referenced to the benzene ring at 830 cm<sup>-1</sup>. The appearance of the unassigned band became apparent during the later stages of curing and contributed to discrepancies of up to 35%.

Comparisons between data obtained through NIR and MIR spectroscopy during cross-linking of epoxy resins have also been reported by Lachenal (1995), Mijović and Andjelić (1996), Yu *et al.* (2009) and González *et al.* (2012). The authors

reported discrepancies and cited the unassigned band at  $905\text{ cm}^{-1}$  as a source of error. The authors recommended NIR as the spectroscopic technique of choice for analysing epoxy conversion due to the strong, isolated band at  $4530\text{ cm}^{-1}$ .

#### **2.3.2.4 Parallel-Plate Rheology**

Rheology is associated with testing viscous liquids. A commonly used assembly involves identical parallel plates with resin contained between them. An oscillating force is applied in a shearing motion to one plate, whilst the other is stationary (Gupta, 2000). The ability of the material to return imparted energy is denoted as  $G'$ , the ability to lose energy is denoted as  $G''$  and the ratio of these values is known as the damping factor ( $\tan \delta$ ). The summation of these values gives a complex shear modulus known as  $G^*$  (Menard, 2008).

Rheology is unique from DSC and FTIRS because it can provide physical properties of a cross-linking material, which imparts important information regarding the processability of an epoxy (Hamerton, 1996). The gelation time is an important parameter for processing thermosetting resins because of the significant increase in viscosity as the cross-linking reactions proceed (Wissbrun, 2013).

During the cross-linking of an epoxy resin, typically, three distinct stages can be observed (Barton & Wright, 1985; Matějka, 1991; Cheng *et al.*, 1994):

- (i) The  $G''$  value is dominant during initial cross-linking as the viscosity increases. In this region,  $\tan \delta$  is larger than one.
- (ii) A dramatic increase in  $G'$  and  $G''$  is observed as the gel forms. In this region,  $G'$  becomes dominant and  $\tan \delta$  becomes lower than one.



- (iii) A slower rate of reaction during which the increase in  $G'$  and  $G''$  decreases and levels off.  $G'$  is dominant throughout.

The critical conversion at which gelation occurs can be estimated using Equation 2.15 (Flory, 1941; Cadenato *et al.*, 1997; Sbirrazzuoli *et al.*, 2003; Pascault and Williams, 2009; Li *et al.*, 2012; Menczel and Prime, 2014):

$$\alpha_{gel} = \left[ \frac{1}{(f_A-1)(f_E-1)} \right]^{1/2} \dots\dots\dots \text{Equation 2.15}$$

where

$f_A$  = functionality of the amine,

$f_E$  = functionality of the epoxy.

The following sections discuss cross-linking using parallel-plate rheology and the methods used to determine the points of gelation and vitrification.

### 2.3.2.5 Detection of Gelation

As mentioned previously, gelation is the point during the cross-linking process at which an infinite network is formed and the liquid resin becomes a semi-solid gel. Various criteria have been used to give an estimate of gelation using rheology and are listed in Table 2.9.

Table 2.9 Summary of criteria used to determine gelation of epoxy resin systems through parallel-plate rheology.

Reference	Criteria Used	Materials	Comments
Tung & Dynes, 1982	$G'/G''$ , steady-state rheology	DGEBA-based resins	Compared their results to steady-state rheology and observed a good correlation. This was the first instance of using $G'/G''$ crossover.
Chambon, 1987	$G'/G''$ , multi-frequency $\tan \delta$ crossover	polydimethyl siloxane (PDMS) system	$G'/G''$ gave delayed times compared with the $\tan \delta$ crossover.
Cheng <i>et al.</i> , 1994	Intersection of extrapolated baseline and tangent to rapid increase of viscosity profile, $G'/G''$ crossover, $G''$ max, $G'$ , intersection of rapidly rising section of $G'$ with time axis, peak of $\tan \delta$	DGEBA with tertiary amine	Similar results were obtained from each method upon cross-linking at 50, 60 and 70°C. Each criterion changed with testing frequency.
Ampudia <i>et al.</i> , 1999	$G'/G''$ crossover, baseline/tangent intersection of $G'$ curve	DGEBA/tri (dimethyl aminoethyl) phenol	Good correlation between the criteria at cross-linking temperatures of 70, 80, 90 and 100 °C.
Lange <i>et al.</i> , 2000	Multi-frequency $\tan \delta$ crossover	DGEBF/4,4'-diaminodiphenyl methane	Not possible to define the gel point below 80°C because it appeared to merge with vitrification.
Fernandez <i>et al.</i> , 2001	Tan $\delta$ peak	tetraglycidyl diaminodiphenylmethane (TGDDM)/DDS	Multi-frequency tests are required for accurate determination, but the peak in $\tan \delta$ is used for arbitrary reasons.
O'Brien <i>et al.</i> , 2001	$G'/G''$ crossover	DGEBF/diethyl toluene diamine	Good consistency of degree of conversion upon comparison with DSC results within 2%.

Table 2.9 (continued) Summary of criteria used to determine gelation of epoxy resin systems through parallel-plate rheology.

Reference	Criteria used	Material	Comments
Bilyeu and Brostow, 2002	Peak in $\tan \delta$ , single frequency	TGDDM/ DDS	$G'/G''$ was clearly observed. Data was compared with that from three-point bend tests and parallel-plate rheology.
Calabrese and Valenza, 2003	$G'/G''$ , max $\tan \delta$	DGEBA/ DGEBAF and anhydride hardener	Linear relationship with isothermal curing temperature.
Teil <i>et al.</i> , 2004	Multi-frequency $\tan \delta$ crossover	DGEBA/ methylhexahydro phthalic anhydride (MHHPA) hardener	Clear crossover point is observed.
Yu <i>et al.</i> , 2005	$G'/G''$ , extrapolation of the steady-state viscosity to infinite viscosity, novel thermo-mechanical analysis (TMA) method	DGEBA/ amine system	Approximately 10% variation in $G'/G''$ , and divergence of viscosity. The order of gelation was $G'/G''$ /viscosity divergence, curing shrinkage inflection.
Abdalla <i>et al.</i> , 2008	$G'/G''$	DGEBA/ diethyltoluene diamine	Observed a reduction in gel time upon modification with carbon nanotubes (CNTs).
Rusli <i>et al.</i> , 2014	Tan $\delta$ crossover	DGEBA/ methylene chlorodiethyl aniline (MCDEA)	Cross-linked at 180 °C. In some samples, the crossover of five frequencies was over a range not a single point.

Tung and Dynes (1982) conducted rheological experiments on nine different thermosetting resin systems, including four epoxy systems. They measured the time to gelation through steady-state rheometry using the conditions specified in ASTM

D2471-99. That method could only measure the properties in the liquid state and extrapolation was required to obtain the time to gelation. The results were compared with the crossover of  $G'/G''$  from parallel-plate rheology and an excellent correlation was reported. The authors noted, however, that the criterion was dependent upon experimental frequency, despite gelation being a material constant that was independent of frequency.

Yu *et al.* (2005) determined gelation through thermo-mechanical analysis (TMA) and compared their results to those of the  $G'/G''$  crossover obtained by parallel-plate rheology, in addition to a divergence of the viscosity profile near gelation. They cured samples under isothermal experimental conditions at 90, 100 and 110 °C, and observed a deflection in the cross-linking shrinkage near gelation, which correlated with rheological measurements. At 90°C, the data revealed values of  $G'/G'' = 339$  s, divergence of viscosity = 390 s and curing shrinkage inflection = 420 s. The rheological criteria estimated gelation before the observed cross-linking shrinkage inflection; a similar trend was observed at higher temperatures. This work demonstrated the correlation of rheological  $G'/G''$  crossover and divergence of viscosity with a mechanical phenomenon near gelation.

The  $G'/G''$  crossover also has close correlations to the gelation time when determined by fibre Bragg grating (FBG) strain sensors. Harsch *et al.* (2008) incorporated FBG strain sensors within a carbon fibre composite and observed an increase in compressive strain at gelation. The resin was a DGEBA/anhydride system. The  $G'/G''$  value obtained from parallel-plate rheology experiments performed under the same heating conditions correlated within 10% to an increase in compressive strain at gelation times of approximately 3 hours.

Winter (1987) dismissed the proposal of using the  $G'/G''$  crossover, calling it “a widely believed myth”. He developed a 'gel equation', which stated that the gel point could only be equal to the  $G'/G''$  crossover at temperatures much greater than that of the glass transition. A method for detecting the gelation was later reported (Chambon, 1987). The cross-linking of a stoichiometrically balanced PDMS system was halted at various time intervals during single-frequency isothermal tests close to the  $G'/G''$  crossover; multi-frequency testing was then completed at each interval. A time at which the log plot of  $G'$  and  $G''$  displayed parallel lines during the multi-frequency test was reported. This frequency-independent event occurred in each sample and was assumed to be the gel point. Solubility tests later confirmed that the system was liquid before the frequency-independent event and solid afterwards. The authors found that the frequency-independent event occurred before  $G'/G''$  crossover and could be used as a new frequency-independent gelation criterion.

Matějka (1991) also observed a frequency-independent event during multiple single-frequency tests using an epoxy system of DGEBA/poly(oxypropylene)diamine. In these results, unlike those from Chambon (1987), the position of frequency independence came after the  $G'/G''$  crossover. The authors obtained data in stoichiometrically balanced and unbalanced systems.

Smith and Ishida (1999) studied the gelation behaviour of a DGEBA/epichlorohydrin system. They used a technique; wherein multiple test frequencies were analysed within a 30 second interval. This allowed the authors to obtain the crossover of multi-frequency  $\tan \delta$  plots in one experiment. They termed the  $G'/G''$  crossover as 'mechanical gelation' and the crossover of  $\tan \delta$  plots as 'critical gelation'. Critical gelation occurred before mechanical gelation, as shown in Figure 2.8. The intersection

of  $\tan \delta = 1$  with each testing frequency illustrates the variability of the  $G'/G''$  criterion reported by Tung and Dynes (1982). The authors voiced concerns over the possibility of gel damage and non-linear viscoelastic effects at high frequencies.

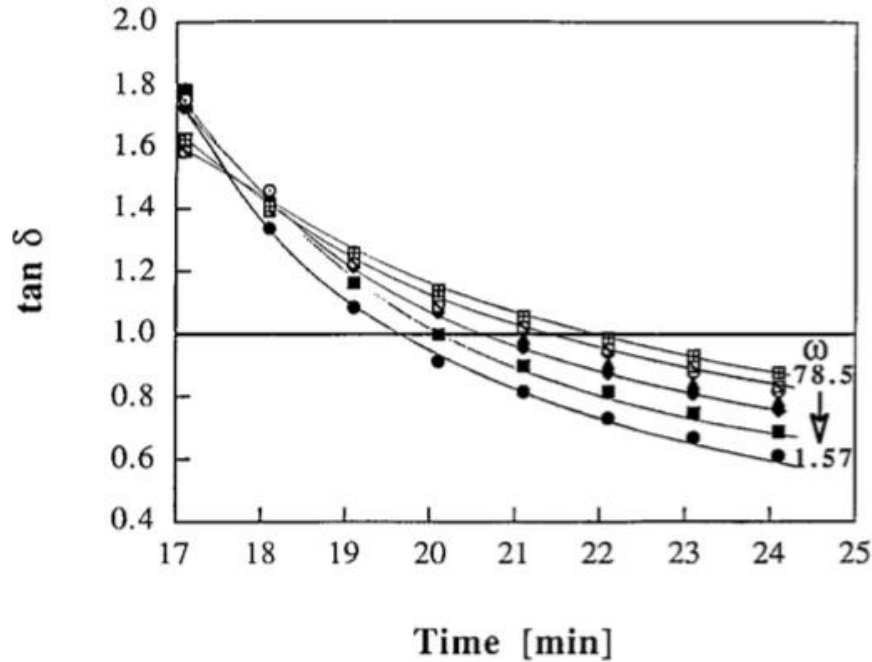


Figure 2.8  $\tan \delta$  evolution with time at 130 °C for a DGEBA/epichlorohydrin system  
Smith and Ishida (1999).

A number of authors refer to critical gelation as being the most precise method of gelation detection, due to the frequency-independent nature of the criterion (Lange *et al.*, 1999b; Teil *et al.*, 2004; Stark, 2013). Despite this, the results in Table 2.9 demonstrate that this method has not been adopted exclusively. The application of multiple frequencies often requires multiple, time-consuming experiments that exhibit variation in cross-linking times (Ishida and Agag, 2011). Thus,  $G'/G''$  has been used regularly as a quickly obtainable estimation that correlates with steady-state viscosity extrapolations, mechanical phenomena during gelation and frequency independence.

### 2.3.2.6 Detection of Vitrification

Vitrification is another important processing parameter that occurs during the cross-linking of a thermosetting resin. It is the transformation of a liquid or rubber into a glass. The  $T_g$  of a curing system increases as the cross-linking reactions proceed. Once the evolving  $T_g$  reaches a value that is equivalent to the cross-linking temperature, the material undergoes vitrification (Tung and Dynes., 1992; Teil *et al.*, 2004; Yu *et al.*, 2009). This process is reversible, unlike gelation, and is dependent on frequency. The transformation from a liquid or rubber into an amorphous glass leads to a rapid decrease in the rate of reaction because molecular motions are frozen and mobility is reduced (Turi, 1997; Yu *et al.*, 2009; McHugh *et al.*, 2010). The cure reactions can continue, although now through a diffusion-based mechanism, which leads to a significantly reduced reaction rate (Gillham, 1986; Turi, 1997). Vitrification is a process that is often undesirable because the increase in viscosity, seen from the transition, leads to a reduction in the processability of the material (Van Assche *et al.*, 1997).

The point at which vitrification is detected is very much dependent upon the technique and criteria used; the process occurs over a temperature range, and thus, issues arise in attempts to define a specific point (Van Assche *et al.*, 1997; Lange *et al.*, 2000). Estimations of the vitrification time can be determined through DMA (Stark, 2013), parallel-plate rheology (Lange *et al.*, 2000), thermo-mechanical analysis (Yu *et al.*, 2009) and temperature-modulated differential scanning calorimetry (TMDSC) (Bilyeu *et al.*, 1999). A summary of criterion used during parallel-plate rheometry with epoxy resins is shown in Table 2.10.

Table 2.10 Examples of research aimed at the detection of vitrification through parallel-plate rheology.

Reference	Criteria	Material	Comments
Lange <i>et al.</i> , 1999a	Onset of frequency dependence in $G'$ , peak in $\tan \delta$ at 1 Hz, peak in $G''$ at 1 Hz, end of frequency dependence in $G'$ , TMDSC	DGEBF/DDS	Rheological criteria were spread over a range, but each showed an increase with cross-linking temperature. TMDSC results fell within the range of the rheological values. The $G'$ peak lay closest to the TMDSC values.
Velazquez <i>et al.</i> , 2000	Peak in $G''$	DGEBA/ethylenediamine (EDA)	$G''$ peak clearly observed for a stoichiometrically balanced system.
Teil <i>et al.</i> , 2004	Peak in $\tan \delta$	DGEBA/MHHPA	Time to vitrification decreased with isothermal cross-linking temperature.
Yu <i>et al.</i> , 2005	Tan $\delta$ peak, $G''$ peak, curing shrinkage inflection	DGEBA/amine system	Strong correlation between each measurement. A strong correlation was observed between $G''$ and the cross-linking induced shrinkage point of inflection.
Mravljak and Sernek, 2011	Peak in $G''$	DGEBA/ <i>N</i> -(3-aminopropyl)- <i>N,N</i> -dimethylpropane-1,3-diamine	Decrease in vitrification time with isothermal cross-linking temperature. A clear $G''$ peak was observed.

Lange *et al.* (2000) conducted a thorough investigation into the vitrification time using parallel-plate rheology on a DGEBF/DDM system. Several criteria were listed for the location of the point of vitrification (Table 2.10). As expected, the time to vitrification decreased as the isothermal cross-linking temperature increased from



40 to 120 °C; experiments were completed at 10 °C intervals. The onset of frequency dependence could not be determined below 100 °C and the authors did not suggest a reason for these results. The peak in  $G''$ , peak in  $\tan \delta$  and end of the frequency dependence in  $G'$  were observable at all temperatures, although the times varied by up to 50%. The authors attributed this to the nature of vitrification being a gradual process that extended over a large part of the cross-linking reactions.

The previously mentioned work by Yu *et al.* (2005) correlated the changes in an epoxy/amine system during isothermal curing using TMA and rheology. An inflection in the cure induced shrinkage during vitrification, in addition to gelation, was observed. In a similar manner to their gelation investigation, the authors compared the rheological-based vitrification times to the cure shrinkage at the inflection point. At 90 °C, the data were as follows:  $\tan \delta$  peak = 567 seconds, peak in  $G''$  = 697 seconds and cure induced shrinkage at inflection = 663 seconds. The change in cure shrinkage lay within the spread of values obtained by the peak in  $G''$  and the peak in  $\tan \delta$  observed during vitrification. Similarly to Lange *et al.* (2000), a spread of data emphasised the issues of trying to define vitrification as a single point.

A TGDDM/DDS system was investigated by Bilyeu and Brostow (2002) using parallel-plate rheology and TMDSC. A modulated temperature ramp was used with TMDSC to determine the heat capacity of a sample. Vitrification could be observed using this method by the presence of a stepwise shift in the baseline of the specific heat capacity, similar to the glass transition temperature. These values were compared with that obtained using the peak in  $\tan \delta$ . At an isothermal curing temperature of 160 °C, the vitrification times were within approximately 10%. Exact

values at each temperature were not stated, but the authors commented on how the vitrification point determined from  $\tan \delta$  was consistently higher than those recorded for TMDSC. The differing thermal environments, sample sizes and superior temperature management of TMDSC may have contributed to the differing vitrification times.

Previously, no generally accepted criterion had been used (Cadenato *et al.*, 1997; Lange *et al.*, 2000; Teil *et al.*, 2004; Yu *et al.*, 2005), but the introduction of TMDSC in the 1990s has led to this becoming the most widely used method (Fraga *et al.*, 2008). Despite there being no generally accepted criteria of vitrification, the peak in  $G''$  during parallel-plate rheology has shown close correlation to TMDSC and TMA data.

### **2.3.2.7 Impact of Carbon-Based Additives on the Cross-linking of Epoxy Resins**

Epoxy resins used in composites that are deployed in demanding applications may require improvements to the desired properties. The use of fillers can help to achieve this goal by improving the mechanical properties, as well as the thermal and electrical conductivity of a composite (Yue *et al.*, 2014). Recently, the use of CNTs (Martin-Gallego *et al.*, 2013; Yue *et al.*, 2014) carbon nanofibres (CNFs) (Xie *et al.*, 2005) and graphene nanoparticles (GNPs) (King *et al.*, 2013; Ma *et al.*, 2014; Prolongo *et al.*, 2014) has received much attention due to their excellent physical, electrical and chemical properties. The additives exhibit small dimensions that allow them to be incorporated into the resin. This has led to an enhancement in the desired material properties of the resulting composite, but high costs of the fillers

and dispersion problems have limited their applications (Qiu *et al.*, 2011; King *et al.*, 2013; Ma *et al.*, 2014; Prolongo *et al.*, 2014).

Graphene consists of an atomically thick layer of sp<sup>2</sup>-hybridised carbon in a honeycomb structure (Stankovich *et al.*, 2006). This material has been reported to have a Young's modulus of 1 TPa (Liu *et al.*, 2007). The large specific area and high mechanical, electrical and thermal properties of graphene make the material an attractive reinforcing nanofiller, as shown in Table 2.11.

Table 2.11 Selected properties of graphene.

Property	Reported Values	Reference
Surface area	2600 m <sup>2</sup> /g	Stankovich <i>et al.</i> , 2006; Kim <i>et al.</i> , 2010
Mechanical properties	Young's modulus = 1000 GPa Breaking strength = 130 GPa	Kim <i>et al.</i> , 2010; Bertolazzi <i>et al.</i> , 2013
Electrical conductivity	3000 mW <sup>-1</sup> /K	Stankovich <i>et al.</i> , 2006
Thermal conductivity	5300 W/m/K	Balandin <i>et al.</i> , 2008; Kim <i>et al.</i> , 2010

Prolongo *et al.* (2014) completed an in-depth characterisation of the impact of GNPs on an epoxy resin system. They saw an increase in the storage modulus of the samples with graphene; the maximum stiffening was 28% with 8 wt % GNP. The tensile modulus also slightly increased by 15% with 3 wt % GNP. However, the increased stiffness led to decreases of up to 23% in the tensile strength. Table 2.12 summarises findings from similar experiments, and thus, shows a consensus in a stiffening effect being induced by GNPs, whilst reducing the strength of epoxy resin systems.

Table 2.12 Summary of selected experiments with GNPs in thermosetting resins.

Reference	Resin	Additive	Dispersion Comments	Impact on Mechanical Properties
Zaman <i>et al.</i> , 2012	DGEBA/ DDS	1% GNPs of approximately 3.57 nm thick.	Sonication and high-speed stirring. Uniformly dispersed GNPs under 1 $\mu\text{m}$ in diameter, as viewed by SEM, with a 3.57 nm thickness.	Tensile modulus = 5% increase tensile strength = 37% decrease fracture toughness = 167% increase critical strain energy release rate = 573% increase
Li <i>et al.</i> , 2013	Novolac-based resin system.	0.5 wt% of 10–15 $\mu\text{m}$ long CNTs and 3–4 $\mu\text{m}$ long GNPs.	A three-roll mill was used and SEM images showed excellent dispersion.	For 0.5 wt%: tensile modulus = 40% increase
King <i>et al.</i> , 2013	DGEBF diethyl toluene diamine	1 wt% GNPs. 15 $\mu\text{m}$ average particle size of 7 nm thick	GNPs were dispersed through mechanical stirring (40 min) and sonication (30–60 min). SEM images revealed good particle dispersion, despite some agglomerations.	At 1 wt%: tensile modulus = 3% increase ultimate tensile strength = 28% decrease
Ma <i>et al.</i> , 2014	DGEBA/ Jeffamine D230	1% GNPs	Sonication produced well-dispersed particles, as observed by SEM.	Young's modulus = 9% increase tensile strength = 38% decrease fracture toughness = 160% increase
Prolongo <i>et al.</i> , 2014	DGEBA/ aromatic amine	1 wt% of 25 $\mu\text{m}$ GNPs	45 min ultrasonication at 400 W at 50% amplitude. Then three-roll milling was completed four times. SEM images revealed a good dispersion.	Storage modulus = 10% increase tensile modulus = constant flexural modulus = constant tensile strength = 24% decrease

Several authors have reported SEM micrographs of fracture surfaces of resin systems containing GNPs. All indicated toughening due to coarser surfaces than those of the neat resin systems (Rafiee *et al.*, 2009; Zaman *et al.*, 2012; Chandrasekaran *et al.*, 2014; Prolongo *et al.*, 2014; Raza *et al.*, 2016). The following methods through which GNPs can increase the fracture energy have been reported:

- (i) GNPs act as obstacles to a growing crack, which causes the crack to deflect around the particle (Rafiee *et al.*, 2009; Zaman *et al.*, 2012; Qin and Ye, 2015).
- (ii) GNPs cause the crack tip to blunt and reduce local stress concentrations (Zaman *et al.*, 2012; Qin and Ye, 2015).
- (iii) De-bonding of the matrix–GNP interface (Zaman *et al.*, 2012; Qin and Ye 2015).

Various sources cite the following reasons as contributions towards the reduced failure strength:

- (i) A weak interface between the GNPs and the matrix, which prevents load transfer.
- (ii) Sliding between agglomerations of GNPs, which leads to crack initiation (Zaman *et al.*, 2012; Chandrasekaran *et al.*, 2014; Prolongo *et al.*, 2014).

It has been well reported that the strengthening properties of pristine GNPs are limited by the tendency of the particles to agglomerate and their weak interactions with the matrix (King *et al.*, 2013; Chandrasekaran *et al.*, 2014; Wan *et al.*, 2014a). This has led to interest in oxidising graphene (Zhu *et al.*, 2010). Graphene oxide (GO) can be functionalised to alter the van der Waals forces between particles, reduce the tendency to agglomerate and produce stronger interactions with the epoxy (Stankovich *et al.*, 2006; Liu *et al.*, 2012a; Ryu *et al.*, 2014). A summary of investigations into the impact of functionalised graphene upon the mechanical strength of epoxy resin nanocomposites is presented in Table 2.13.

Table 2.13 A summary of investigations into the impact of functionalised graphene on the mechanical strength of epoxy resin nanocomposites.

Reference	Resin	Additive	Dispersion Comments	Impact on Mechanical Properties
Yang <i>et al.</i> , 2009	DGEBA/ amine hardener	0.0375 wt % GO	Samples were stirred for 4 hours at 50 °C. Well-dispersed 500 nm flakes were observed under SEM.	Compressive failure strength = 48.3% increase compressive failure toughness = 1185% increase
Chatterjee <i>et al.</i> , 2012	DGEBA/ aromatic diamine	0.1 wt % amine-functionalised graphene	Mechanical mixing and roll-mill calendaring. Uniform dispersion for up to 0.5 wt % loading. Beyond this, agglomerations are present.	Fracture toughness = 61% increase flexural modulus = 8% increase
Chandrasekaran <i>et al.</i> , 2014	DGEBA/ anhydride hardener carbon fibre composite	1 wt % thermally reduced graphene oxide (TRGO)	Preparation of the composite by roll milling, which applied high pressure to the resin. A fairly good dispersion of agglomerates was observed, although TRGO appeared better dispersed than GNPs.	Fracture toughness = 40% increase
Guan <i>et al.</i> , 2014	DGEBA/ anhydride hardener	0.5 wt % poly etheramine-functionalised GO	6 hours sonication. Fairly good dispersion was achieved, but agglomeration remained.	Storage modulus = 33% increase tensile strength = 51% increase elastic modulus = 10% increase toughness = 119% increase
Wan <i>et al.</i> , 2014b	DGEBA/ MHHPA	0.5 wt % GO sheets	Planetary ball milling for 30 minutes and mechanical mixing. TEM results showed highly dispersed sheets.	Tensile modulus = 7% increase tensile strength = 35% increase fracture toughness = 26% increase
Wan <i>et al.</i> , 2014b	DGEBA/ MHHPA	0.25 wt % graphene sheets functionalised with DGEBA	Planetary ball milling for 30 minutes and mechanical mixing. TEM results showed highly dispersed sheets.	Tensile modulus = 13% increase tensile strength = 75% increase fracture toughness = 41% Increase

Chandrasekaran *et al.* (2014) investigated the impact of introducing GNPs and thermally reduced graphene oxide (TRGO) into an epoxy resin system on the fracture toughness. The thermal treatment of graphene aimed to functionalise the sheets with a mixture of hydroxyl and carboxylic acid groups on the surfaces and edges. The introduction of 1wt % GNPs resulted in a 25% increase in fracture toughness, whilst 0.5wt % TRGO produced a 40% increase. Rough fracture surfaces were observed using SEM in both cases, although the TRGO samples showed increased toughening due to increased crack-tip bifurcations into smaller cracks. TRGO also showed less agglomeration than that of the GNP reinforced materials. The authors concluded that the presence of functionalisation in the graphene sheets increased interactions with the matrix to allow the formation of covalent bonds.

Reductions of tensile strength due to weak interactions of pristine graphene with the matrix have been circumvented by the appropriate functionalisation of graphene. The introduction of 0.5wt % GO produced increases in the tensile modulus, tensile strength and fracture toughness of 7%, 35% and 26%, respectively. However, improved strengthening was observed with the addition of 0.25 wt % DGEBA-functionalised graphene; this resulted in increases in the tensile modulus, tensile strength and fracture toughness of 13%, 75% and 41%, respectively. SEM fracture surfaces revealed smaller and more numerous dimples in the DGEBA-functionalised system. In the GO fracture surface, agglomerations of 5–10  $\mu\text{m}$  were observed, which implied a non-uniform distribution. The authors reported on the compatibility of the DGEBA-functionalised particles with the matrix and revealed that strong chemical bonds could be formed due to participation of the functionalised groups in the cross-linking process. This also promoted dispersion of the sheets. The study

demonstrates how appropriate functionalisation can solve dispersion and matrix interaction issues associated with pristine GNPs.

A number of authors have reported the increased interaction of GO/functionalised graphene with epoxy resin systems to allow covalent bonding (Yang *et al.*, 2009; Chatterjee *et al.*, 2012; Wan *et al.*, 2014b; Galpaya *et al.*, 2015a). Additionally, an improved dispersion of particles has been widely reported. These two factors have resulted in improved mechanical properties, relative to those of pristine graphene nanocomposites (Yang *et al.*, 2009).

### **2.3.3 Impact of Graphene Nanoparticles on the Cross-Linking of Epoxy Resins**

Table 2.14 presents a summary of the impact of graphene, GO and functionalised graphene particles on the curing kinetics of epoxy resin systems. The results indicate that there is no consensus in the literature on the effect of graphene particles on the curing kinetics of epoxy resins. Galpaya *et al.* (2015b) stated that the variation in results was likely to arise from the complex chemistry involved between different resins, hardeners and functionalised graphene particles.



Table 2.14 A summary of the impact of graphene, GO and functionalised graphene particulates on the curing kinetics of epoxy resin systems.

Reference	Resin	Additive	Dispersion Comments	Impact on Curing Kinetics
Teng <i>et al.</i> , 2011	DGEBA/ DDS	0.5% graphene nanosheets (9x7 $\mu\text{m}$ )	Ultrasonic bath for 10 minutes. No comment on distribution.	The addition of graphene reduced $\Delta H$ from 128.95 to 93.24 J/g and the peak temperature shifted from 205.4 to 211.3 °C. Overall retarding effect.
Qiu <i>et al.</i> , 2011	TGDDM/ DDS	2% GO	Mechanical stirring for 10 minutes. SEM fracture surfaces revealed a fine dispersion of GO; however, some agglomerations existed.	The reaction onset was lowered from 162 to 142 °C, which indicated a catalytic effect on the reaction. The overall enthalpy reduced from 659 J/g to 654 J/g.
Ryu <i>et al.</i> , 2014	DGEBA/ amine hardener	1 wt% GO flakes (0.2 $\mu\text{m}$ maximum size)	High-speed mechanical stirring. Uniform distribution was observed, but with some irregularities.	Non-isothermal DSC showed a slight retardation effect by reducing the enthalpy of reaction by 8%.
Ryu <i>et al.</i> , 2014	DGEBA/ amine hardener	1 wt% amine-functionalised GO flakes (0.2 $\mu\text{m}$ maximum size)	High-speed mechanical stirring. Uniform distribution was observed.	Non-isothermal DSC revealed a catalytic effect on the reaction rate and increased the enthalpy of reaction by 5%.
Galpaya <i>et al.</i> , 2015a	DGEBA/ DDM	0.3 wt% GO flakes (250 $\mu\text{m}$ maximum size)	Sonication for 1 hour. Well-dispersed sheets, but agglomerations observed by TEM.	During non-isothermal DSC, the GO flakes induced an increased degree of conversion from 89% to 92% after 20 minutes.
Galpaya <i>et al.</i> , 2015a	DGEBA/ DDM	0.3 wt% GO flakes heat-treated at 180 °C for 12 hours (250 $\mu\text{m}$ maximum size)	Sonication for 1 hour. Slightly improved dispersion compared with GO flakes.	During non-isothermal DSC, the heat-treated GO flakes induced a decreased degree of conversion from 89% to 80% after 20 minutes.
Li <i>et al.</i> 2015	DGEBA/ DDM	0.5 wt % GO flakes and amine-functionalised GO flakes	Sonication at room temperature for 1 hour. Molecular-level dispersion reported.	No significant change in the total heat of reaction, onset temperature or peak temperature during non-isothermal DSC for either additive.
Prolongo <i>et al.</i> , 2016	DGEBA/ DDM	1% GNPs	Mechanical stirring for 30 minutes followed by sonication for 60 minutes at 400 W. Good dispersion observed.	The enthalpy of reaction was reduced by 8%, although the peak of reaction was delayed from 143 to 146 °C during non-isothermal DSC.

Ryu *et al.* (2014) used DSC to demonstrate the impact of surface functionalisation of graphene on the curing kinetics of an epoxy resin. They introduced 1 wt% GO and an amine-modified GO into a DGEBA/amine system. The GO flakes delayed the onset of reaction by 8 °C during non-isothermal testing at 10 K/minute, relative to the neat resin. The functionalisation of graphene, however, had the opposite effect, causing a decreased onset of reaction and an increase in the rate of reaction. The authors reported that cross-linking went to completion in each case, although the value of the total enthalpy was not stated.

Conversely, Qiu *et al.* (2011) observed a reduction in the onset and peak reaction temperatures upon introducing 1 wt% GO into a TGDDM/DDS system. The authors investigated percentages of up to 5 wt% and found that the catalytic effect increased with GO content. The total enthalpy of the reaction was reduced. The work is in contrast to that of Ryu *et al.* (2014) and highlights the inconsistent outcomes of the effects of graphene-based particulates on cross-linking.

Galpaya *et al.* (2015a) studied the effect of 0.3 wt% GO on the curing kinetics of a DGEBA/DDM system. Using non-isothermal DSC, it was observed that GO increased the onset temperature and reduced the rate of reaction. Using FTIRS, it was revealed that the retardation effect was predominantly on the reaction of the secondary amine with epoxide. It had previously been reported that the introduction of low-molecular-weight material onto the reactive sites of GO during manufacturing influenced the catalytic behaviour of GO. The authors heat-treated GO using an autoclave at 180 °C for 12 hours, then, upon removal from the autoclave, X-ray photoelectron spectroscopy revealed a large decrease in oxygen content. It was believed that this heat treatment removed oxidative debris. Non-isothermal DSC results then revealed that the autoclave-treated samples had a catalytic effect on the

resin system. This work highlights the importance of oxidised debris on curing kinetics.

The introduction of pristine graphene particles can induce significant toughening in epoxy resin systems, although a reduction in strength was observed. Weak interactions between the particles and resin, in addition to dispersion problems, limit improvements to the mechanical properties. Functionalisation of the particulates can diminish the limitations observed with pristine graphene to improve both strength and stiffness.

No consensus has been achieved in the literature with respect to the impact of pristine graphene on the cross-linking regime of epoxy resin systems. Catalytic and retarding effects have been reported; these are dependent upon the interactions between particles, resins and hardeners. Appropriate functionalisation has been demonstrated to have a catalytic effect on the cross-linking regime.

## **2.4 Optical Fibres**

### **2.4.1 Introduction**

Optical fibre sensors have been shown to provide unique advantages over conventional thermal analysis techniques for investigating and monitoring the curing of thermosetting resins (Crosby *et al.*, 1996; Powell., 1998; Fernando and Degamber, 2013; Schubel *et al.*, 2013). The sensors are immune to electromagnetic radiation, small in dimensions (125  $\mu\text{m}$  in diameter), can be multiplexed, and their inclusion within composites does not adversely affect quasi-static tensile mechanical

properties. These sensors can allow *in-situ* monitoring during production to facilitate increased control of the cross-linking material (Fernando and Degamber, 2006).

## 2.4.2 Structure of Optical Fibres

Optical fibres are made of dielectric materials, often silica, and have been utilised as a method of light transportation in telecommunications. Although other fibre types do exist, herein the focus is on silica-based fibres. The fibres consist of a buffer coating, core and cladding; the refractive index of the core is higher than that of the cladding (Daly, 1984; Hecht, 1984). The fibre in Figure 2.9 is described as a step-index fibre, due to the abrupt change in refractive index at the core/cladding interface (Naidu and Mani, 2009). The cladding is then surrounded by a protective buffer coating, which is often a polyimide or polyacrylate (Daly, 1984; Hecht, 1984; Crosby, 1996; Al-Azzawi, 2006; Fernando and Degamber, 2006).

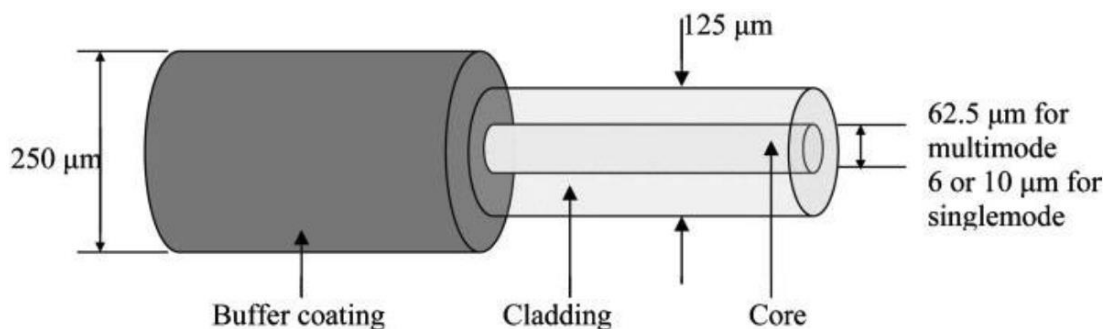


Figure 2.9 Schematic illustration of an optical fibre showing different components (Fernando and Degamber, 2006).

### 2.4.3 Numerical Aperture and Acceptance Angle

The magnitude of the refractive-index dissimilarity between the core and the cladding determines the acceptance angle of a cleaved optical fibre. This property describes the ability of the fibre to collect incoming light, and is shown in Figure 2.10 (Downing, 2004; Bagad, 2007). Light travelling along pathway A lies within the acceptance angle and can therefore enter the fibre and propagate along the core. Pathway B, however, lies outside of the acceptance angle and light will be attenuated into the cladding material. The acceptance angle can be determined by Equation 2.16 (Avadhanulu, 1992; Bagad, 2007; Raghuvanshi, 2011).

$$\phi_a = \sin^{-1} \left( \frac{\sqrt{n_1^2 - n_2^2}}{n_0} \right) \dots \dots \dots \text{Equation 2.16}$$

where

$\phi_a$  = acceptance angle,

$n_1$  = refractive index of the fibre core,

$n_2$  = refractive index of the fibre cladding,

$n_0$  = refractive index of the medium surrounding the fibre distal end.

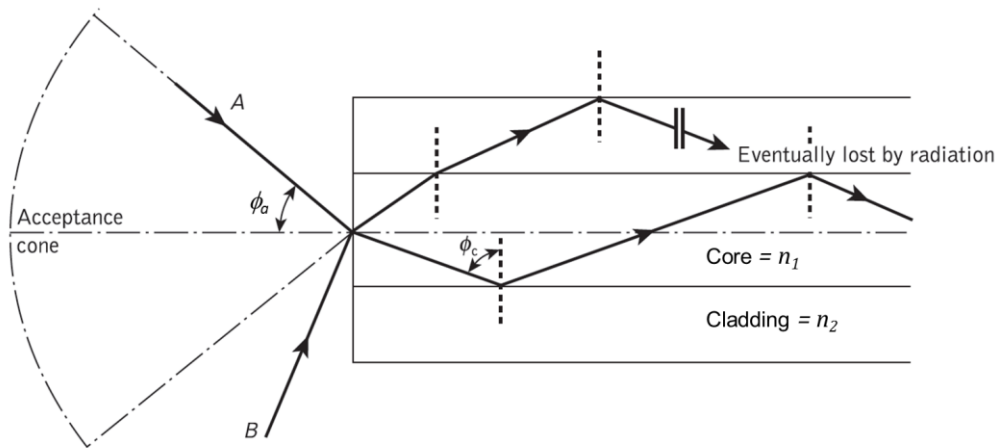


Figure 2.10 The acceptance angle upon launching light into an optical fibre (Senior, 2009).

The numerical aperture (N.A.), which can be calculated using Equation 2.17 (Weik, 1989; Avadhanulu, 1992; Bagad, 2007; Senior, 2009), is a commonly used unit that describes the light-gathering capability of a system. A large value is indicative that an increased amount of light can be accepted by the fibre.

$$N.A. = \left( \frac{\sqrt{n_1^2 - n_2^2}}{n_0} \right) \dots \dots \dots \text{Equation 2.17}$$

The dimension of the core dictates how many modes can be transmitted through the fibre. A single-mode fibre core has a diameter of 5–10 μm, through which only one mode of light can propagate. Multi-mode cores have diameters in the range of 50–100 μm and allow many modes to propagate (Avadhanulu, 1992; Chomycz, 2000).

#### 2.4.4 Total Internal Reflection

Cladding in optical fibres causes light to be confined to the core of the fibre by total internal reflection. The critical angle is the smallest angle of incidence for which the light rays are totally reflected at the interface between the cladding and the core. The critical angle is calculated using Equation 2.18 (Senior, 2009; Lalauze, 2012; Weik, 2013).

$$\theta_c = \sin^{-1} \frac{n_c}{n_f} \dots \dots \dots \text{Equation 2.18}$$

where

$\theta_c$  = critical angle,

$n_f$  = refractive index of the fibre core,

$n_c$  = refractive index of the fibre cladding.

At angles greater than the critical angle, light is propagated in the core by total internal reflection.

### 2.4.5 Reflections at Normal Incidence

When light travels between two homogenous transmission media, with differing refractive indices, both reflection and refraction can occur (Fernando and Degamber, 2006; Singh, 2015; Weik, 2013). Equations deduced by Fresnel (Equations 2.19 and 2.20) can describe the behaviour of reflected light in the parallel and perpendicular directions (Spiller, 1994; Gillen *et al.*, 2013; Sampath *et al.*, 2015).

$$r_p = \frac{n_m \cos \theta_1 - n_f \cos \theta_2}{n_m \cos \theta_1 + n_f \cos \theta_2} \dots \dots \dots \text{Equation 2.19}$$

$$r_n = \frac{n_f \cos \theta_1 - n_m \cos \theta_2}{n_f \cos \theta_1 + n_m \cos \theta_2} \dots \dots \dots \text{Equation 2.20}$$

where

$\theta_1$  = angle of incidence,

$\theta_2$  = angle of transmitted light,

$n_m$  = refractive index of resin,

$n_f$  = refractive index of the fibre core,

$r_p$  = parallel polarisation,

$r_n$  = perpendicular polarisation.

If reflection occurs under normal incidence,  $\theta_1 = \theta_2 = 0$ , so the Fresnel equations can be expressed as Equation 2.21 (Crosby *et al.*, 1996a; Sampath *et al.*, 2015, Singh

2015; Goldstein, 2016). This equation has been used for the cure monitoring of epoxy resins wherein changes in  $n_s$  are detected by an increasing Fresnel reflection (Crosby *et al.*, 1996; Powell *et al.*, 1998).

$$R = \left( \frac{n_f - n_s}{n_f + n_s} \right)^2 \dots\dots\dots \text{Equation 2.21}$$

where

$n_f$  = refractive index of fibre core,

$n_s$  = refractive index of sample,

$R$  = Fresnel reflection at normal incidence.

## 2.5 Process Monitoring Using Optical Fibre Sensors

The most widely used conventional analytical methods discussed previously for monitoring cross-linking reactions include DSC, FTIRS and DMA. These methods are well established and provide valuable information on cross-linking in a laboratory environment. When processing a component, variations exist in the distribution of temperature due to the dimensions of the mould, the characteristics of the curing oven and the intensity of the exothermic reaction (Pandita *et al.*, 2012; Nair *et al.*, 2015). Thus, different locations within a component will show varying properties for which conventional thermal analysis techniques cannot account (Lam and Afromowitz, 1995a).

The small dimensions of optical fibre sensors allow for them to be embedded within a composite to provide *in-situ* data at multiple points. The sensors are immune to electromagnetic radiation and can be used in a microwave environment (Degamber and Fernando, 2004). The sensors are also chemically inert and relatively



inexpensive. A range of sensors are available to detect temperature, strain, refractive index and functional-group strengths (Degamber and Fernando, 2002; Nair *et al.*, 2015). The current research will focus on optical refractive-index sensors based on Fresnel reflection and the integration of optical sensors within a differential scanning calorimeter.

### **2.5.1 Refractive-Index Monitoring**

As an epoxy resin cross-links, the refractive index can increase by 2–3%; optical refractometers are capable of tracking this change to give qualitative information about the degree of curing (Afromowitz and Lam, 1990). These sensors are inexpensive due to their quick preparation and the low cost of the light source, because only a single wavelength of light is used (Crosby *et al.*, 1996a; Machavaram *et al.*, 2014). This section describes the principles of a conventional Abbe refractometer and the development of optical refractometers as methods for monitoring the curing of epoxy resins.

### **2.5.2 The Abbe Refractometer**

The Abbe refractometer is a conventional method for measuring the refractive index of liquids and solids. The refractive index is the ratio of the velocity of light in a vacuum to the velocity of light in a specific medium (Keirl and Christie, 2007).

A schematic illustration of the mode of operation of an Abbe refractometer is shown in Figure 2.11 (Boyes, 2002). The liquid sample is dispensed between two prisms of a known refractive index using a pipette; light is launched through prism A and the sample. The refractive index of the sample determines the critical angle up to which

light can refract. Incident light at, and above, the critical angle can then enter prism B (Simmons and Potter, 2000). The critical angle provides a sharp contrast between an illuminated area and a dark area, as observed under a microscope. Cross-hairs are aligned with this boundary to determine the angle of incidence required for total internal reflection. The refractive index can then be calculated using Equation 2.21 (Boyes, 2002). The refractive index varies with wavelength, and hence, the wavelength of light must be specified when quoting the index of refraction; the sodiumD line at 589.3 nm is often used (Räty *et al.*, 2013). The refractive index also varies with temperature, and therefore, the temperature must also be stated. One technique to control the temperature of the refractometer is to circulate water at a specified temperature around the prisms (Harris and Fernando, 2009; Kenkel, 2010). Modern Abbe refractometers can reach an accuracy of  $\pm 0.0001$  (Stanley, 2017).

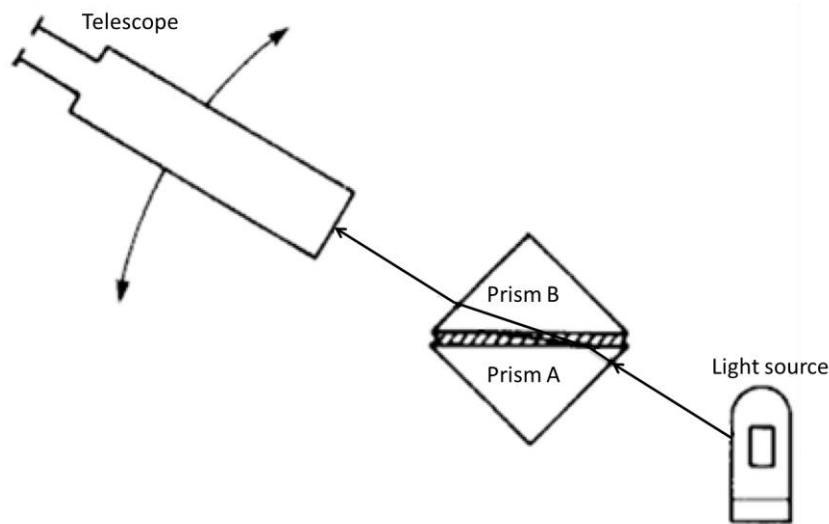


Figure 2.11 Schematic illustration of the operating principles of an Abbe refractometer (Boyes, 2002).

### 2.5.3 Monitoring Cross-Linking Using the Abbe Refractometer

The Abbe refractometer can have limited practicality when assessing the refractive index during the cross-linking of epoxy resins because the cross-linking material can bond to the prism. Additionally, the temperature is often controlled by a water bath, which limits the range and stability. Despite these restrictions, modifications can be made to the refractometer.

Crosby *et al.* (1996) cross-linked an epoxy resin within an Abbe refractometer and used a laser diode operating at 1310 nm to illuminate a fibre optic Fresnel reflection sensor. The refractometer temperature was set to 50 °C and the refractive index was measured every 2 minutes. The refractive index showed an initial decrease, upon heating, before increasing by 0.04 over the curing period. A release agent was used on the surface of the prism to allow for the removal of the resin upon cross-linking. Further experiments (Crosby *et al.*, 1996b) showed that the temperature increased as the rate of the refractive index increased, in addition to the overall change in refractive index.

Harris and Fernando (2009), modified an Abbe refractometer to enable the cross-linking of an epoxy resin, without bonding to the surface of the prism. A custom-built cell was made with the same refractive index as that of the glass prism ( $n = 1.76$ ). The cell consisted of top and bottom glass slides placed on the two prisms. A contact liquid was placed between the bottom prism and the glass slide to ensure good optical transmission. The release agent was then used on the glass slides before cross-linking. Similar to the work undertaken by Crosby *et al.* (1996b), an initial decrease in the refractive index was observed, upon heating to the desired

isothermal temperature, before a gradual increase over the curing period. In this work, the results showed close correlation to the optical refractive-index data and FTIRS data.

Philipp *et al.* (2008) investigated the impact of the mixing sequence of an epoxy resin, amine hardener and alumina nanoparticles. They modified a refractometer sample chamber and observed an increase in the refractive index as cross-linking progressed. They found that the order in which the nanoparticles were introduced into their resin system had little effect on the curing behaviour but did have an impact on the initial and final refractive-indices. Introducing nanoparticles into the resin, before mixing with the hardener, produced a system with an increased refractive index over that in which the nanoparticles were introduced into the hardener before mixing with the resin. The authors suggested that interactions between the particles and constituents allowed for improved dispersion. This demonstrated the significant impact of the mixing sequence on the optical properties of a resin system.

The evolution of the refractive index during curing, as measured using a conventional Abbe refractometer, has shown close correlation to the degree of curing obtained from spectral data. Thus, refractive-index monitoring allows for qualitative information to be obtained during the cross-linking of epoxy resins. Refractive-index monitoring can detect additional effects, when considering nanocomposites, that conventional detection methods have not revealed. The development of refractometers based on fibre optics is discussed in the next sections. The two most prominent designs for an optical refractometer involve an optical fibre section, in which the cladding has been removed, and the use of a cleaved optical fibre.

## 2.5.4 Stripped Optical Fibre Refractometer

Afromowitz (1988) designed a refractometer that consisted of a light source and a detector with light travelling through a fibre-optic cable. The optical fibre contained a region of a small diameter polymer fibre, which was made from a cured sample of epoxy resin, as shown in Figure 2.12. This region was surrounded by an uncured sample of the same epoxy resin. The intensity of light travelling through the fibre was recorded. At the start of the cross-linking reactions, the sample had a lower refractive index than that of the fibre; this allowed for total internal reflection of the light to occur. As the epoxy became cross-linked, the refractive index increased, until it reached the same value as that of the section of the epoxy resin based optical fibre. From this point onwards, the propagation of light through total internal reflection was not possible. The epoxy took only 5 minutes to cross-link and a decrease in the light output occurred throughout curing.

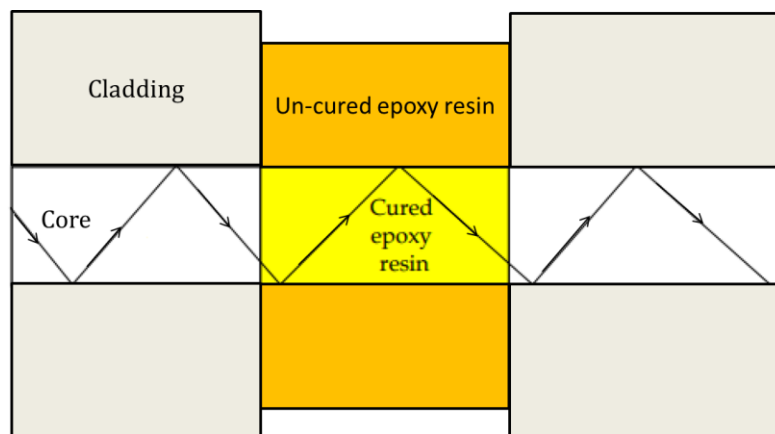


Figure 2.12 Schematic illustration of an optical fibre core with a section of cured resin. Figure adapted from Vodicka (1997).

Afromowitz and Lam (1990), followed up this investigation by using the same optical fibre refractometer on an aerospace resin, which took over 400 minutes to cross-

link. They compared the evolution of the refractive index to the degree of curing obtained from DSC; a close correlation between the two results was observed (Afromowitz and Lam, 1990). The authors continued their investigation in 1995 and observed that, before the gelling point during curing, a linear relationship existed between the degree of cross-linking and the refractive index. They illustrated the capability of the sensor to work in non-stoichiometric epoxy systems over a longer curing period than had previously been illustrated (Lam and Afromowitz 1995b).

Crosby *et al.* (1996b) used a polymer-clad optical fibre sensor, in which a section of the cladding was removed using sulfuric acid. The exposed core was then immersed in an epoxy/amine resin. The sensing region had a diameter of 60  $\mu\text{m}$ , which was smaller than the 1 mm diameter sensing region used by Afromowitz (1988) and Afromowitz and Lam (1990). For total internal reflection to occur, the refractive index of the core must be higher than that of the surrounding medium. Therefore, a fibre containing a high refractive index (1.7) was used. The sensor showed a decrease in signal strength, and hence, an increase in refractive index, with cross-linking time. The rate of the reaction increased with an increase in curing temperature from 25 to 50  $^{\circ}\text{C}$ . These results showed a good correlation with those obtained from a single-ended refractometer, an optical evanescent wave sensor and conventional FTIRS data.

Liu *et al.* (1997) used a similar sensor configuration to that of Crosby *et al.* (1996b), but used a different fibre with a core refractive index of 1.62. The diameter of the fibre in this case was 100  $\mu\text{m}$ . The sensor was inserted into prepregs containing a thermosetting resin, as shown in Figure 2.13. Curing of the samples was then completed using a hot-press and an autoclave at elevated temperature and pressure.

Each experiment showed an initial decrease in attenuation due to the drop in refractive index associated with an increase in temperature. Subsequently, an increase in attenuation was observed as the refractive index of the resin increased due to cross-linking. Here the results reflected those reported previously, whilst demonstrating the performance of the sensor in a manufacturing environment to obtain *in-situ* information.

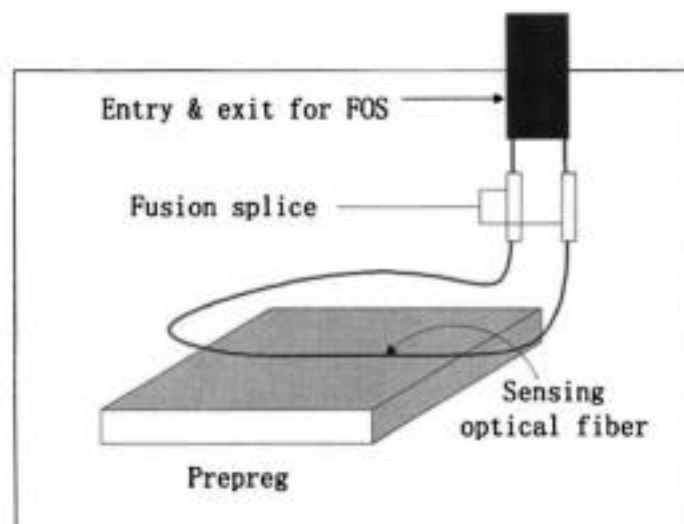


Figure 2.13 Schematic illustration of the fibre-optic sensor (FOS) entering and exiting a prepreg (Liu *et al.*, 1997).

Powell *et al.* (1998) used an optical fibre containing a high-refractive-index core; in this design, a 20 mm section of the cladding was removed. The curing of an epoxy/amine resin was observed isothermally between 30 and 60 °C using a refractive-index sensor, in addition to an evanescent wave sensor and an optical fibre transmission spectroscopy sensor. An excellent correlation was observed between the refractive-index and transmission spectroscopy sensors. The authors noted the advantages and disadvantages of each sensor system. They observed that, whilst a high-refractive-index core was required for the sensor, it had

advantages over other optical sensors due to its ease of preparation, small sensing region, inexpensive light source and excellent signal-to-noise ratio.

The optical refractive-index sensors mentioned here consisted of optical fibres containing a sensing area of either a pre-cured polymer or stripped regions of fibre to expose the core. This approach has enabled a method of introducing on-line process monitoring during cross-linking. In the following sections, subsequent studies have shown a shift towards using a single-ended Fresnel reflection sensor (FRS), which requires less preparation.

### **2.5.5 Optical Fibre Based Fresnel Reflection Sensor**

The single-ended FRS requires little preparation, in comparison to the stripped-cladding fibre sensor, which requires chemical etching. A FRS is prepared by stripping the buffer (or jacket) using a pair of mechanical strippers to expose the cladding. The fibre is cleaved using a conventional optical fibre cleaver to obtain a  $(90\pm 0.5)^\circ$  cleaved optical fibre-end (Crosby *et al.*, 1996; Powell *et al.*, 1998; Machavaram *et al.*, 2014). At normal incidence, the reflected light intensity is described by Equation 2.21. In this scenario, a larger difference in the refractive index between  $n_f$  (fibre core) and  $n_s$  (sample surrounding cleaved fibre) results in a larger reflected Fresnel signal as shown in Figure 2.14.



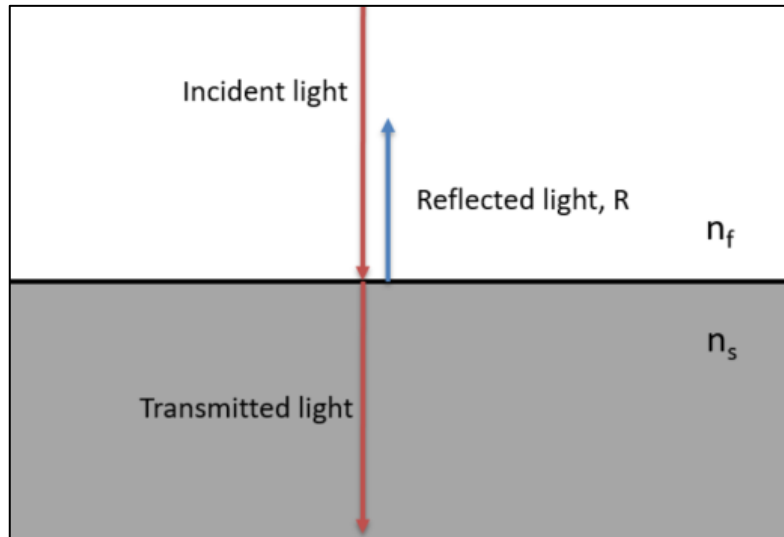


Figure 2.14 Schematic illustration showing reflection at normal incidence.

### 2.5.5.1 Sensing System Instrumentation

Crosby *et al.* (1996b) first demonstrated a single-ended FRS system using a y-coupler. The branched ends were attached to a 1310 nm laser diode and a photodiode detector, while the other end was connected to the FRS. Upon immersion in an epoxy resin, during cross-linking, the resin exhibited significant fluctuations. The low sensitivity was believed to be due to the similarity of the refractive index of the fibre core and the resin system. Higher sensitivity can be achieved if a greater mismatch is present. Similar sensing systems, using a y-coupler with a light source and photodiode detector, have been used by Cusano *et al.* (2003), Antonucci *et al.* (2006) and Aduriz *et al.* (2007).

A 2x2 single-mode fibre coupler with a 50:50 split ratio was used by Kuang-An *et al.* (2002) to connect a laser diode and a detector to an FRS and a fibre spool. The laser operating at 1300 nm was coupled to the FRS and fibre spool, which were of different lengths. The returning pulses, due to Fresnel reflections, were then

temporarily separated by approximately 40  $\mu\text{s}$ . Any light-source fluctuations could then be normalised by the signal from the spool. An accuracy of  $2 \times 10^{-5}$  refractive-index units was then demonstrated by observing NaCl concentrations in water. In a later publication, the authors used the same sensing system to demonstrate that the measurement resolution applied when using methanol, acetone, isopropanol and a Cargille-index liquid (Chang-Bong & Chin, 2004).

Zhang *et al.* (2012) also used a 2x2 coupler to connect a photodiode detector and a diode laser, operating at 1550 nm to an FRS and a second detector. This enabled the input and output powers to be detected, which allowed normalisation of any power fluctuations. The system was used to demonstrate the cross-linking of an epoxy resin.

Robert and Dusserre (2014) designed a simpler system without a secondary sensor for normalisation. A high-stability laser source operating at 1550 nm was connected to an optical circulator. The circulator was also connected to the FRS and a high-resolution power meter. The circulator allowed the input light to be separated from the Fresnel-reflected light and was then measured using the power meter. The sensing system was shown to track the refractive index during cross-linking of an epoxy resin under non-isothermal and isothermal conditions. Each of the FRS systems discussed herein consisted of a light source and a detector, although laser stability could affect the quality of the signal. Normalisation procedures have been demonstrated using a second detector and sensor head for increased stability. Recent research has demonstrated that lasers with improved stability produced a more stable signal without the need for reference sensors. Modifications that allow multiplexing of the FRS are discussed in Section 2.5.5.6.

### 2.5.5.2 Capability of the Fresnel Reflection Sensor to Detect Refractive Index

The previously mentioned work of Crosby *et al.* (1996b) used a single-ended FRS, in addition to a stripped fibre sensor to investigate the cross-linking of an epoxy resin. The response of the sensor over a range of refractive indices was investigated. Theoretical predictions of the magnitude of the reflected light ( $R$ ) were made using Equation 2.21 by assuming that the refractive index of the fibre,  $n_f$ , was 1.458. The experimental response of the fibre was obtained using various standard refractive-index oils with a light source at 1550 nm and 25 °C. A parabolic relationship centring on 1.458 (Figure 2.15) was obtained in both cases, and an excellent correlation between the two data sets were observed. The same investigation was carried out by Hewa-Gamage and Chu (2002), who also observed an excellent correlation.

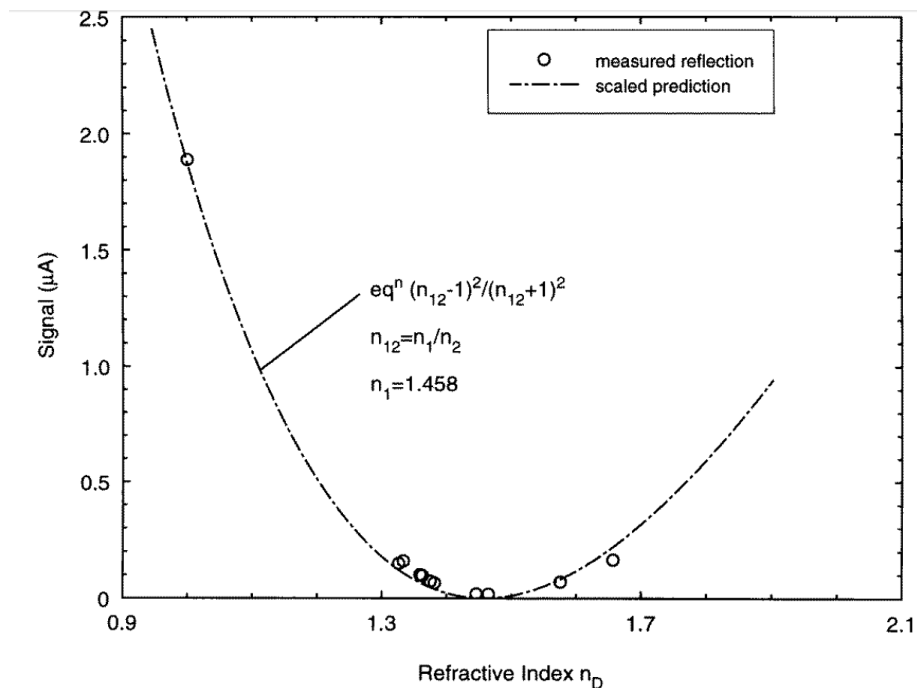


Figure 2.15 Plot of theoretical and experimental Fresnel reflections as a function of refractive index (Crosby *et al.*, 1996b).

Harris and Fernando (2009) incorporated two single-ended FRSs into a custom-modified Abbe refractometer; one was a single-mode fibre and the other was a multimode fibre. The refractive index of an epoxy resin was recorded using both sensors, in addition to the Abbe refractometer. An excellent correlation between the three refractometers was observed throughout the cross-linking reactions. An initial drop in the refractive index was observed upon reaching the desired isothermal temperature, before there was an increase over the cross-linking period. The authors observed that the single-mode fibre sensor had improved reproducibility and stability.

### **2.5.5.3 Tracking Isothermal Cross-Linking**

Giordano *et al.* (2000) used a single-mode, single-ended sensor with an epoxy resin system to measure the Fresnel reflection increase over a two-hour curing period at temperatures between 40 and 60 °C. The sensor consisted of a laser diode, operating at 1310 nm, connected to a y-coupler, the single end of which was immersed in the epoxy. The third connection was to a photodiode amplifier, a lock-in amplifier and a data acquisition system. The cross-linking temperature was controlled by a Peltier heater with a sample temperature accuracy of 0.1%, although no thermocouple data were provided. Comparisons of the sensor output were made with the degree of curing, as obtained independently through DSC. The DSC results showed higher conversion during the early stages of curing, but this discrepancy decreased as cross-linking commenced. Overall, a good correlation was observed and the sensor demonstrated the ability to track isothermal cross-linking.

Cusano *et al.* (2001) extended the work of Giordano *et al.* (2000) by proposing a relationship between the refractive index and the degree of curing, using the Lorentz–Lorenz equation, which linked the molecular weight, refractive index, density and polarisability of a material (Equation 2.22).

$$\frac{n^2-1}{n^2+1} = \frac{N}{3M\varepsilon} \rho\beta \dots\dots\dots \text{Equation 2.22}$$

where

$n$  = refractive index,

$N$  = Avogadro's number,

$M$  = molecular weight,

$\varepsilon$  = permittivity of free space,

$\rho$  = density,

$\beta$  = polarisability.

Experimental data from de Boer *et al.* (1992) indicated that there was a negligible change to polarisability during curing, and thus, it was assumed to be constant.

Using the simplified version of Equation 2.22, the authors assumed a linear relationship between the refractive index and density during cross-linking.

Equation 2.23 was used for predicting the degree of curing.

$$\alpha_1 = \frac{n_p(t) - n_p(t_0)}{n_p(t_\infty) - n_p(t_0)} \dots\dots\dots \text{Equation 2.23}$$

where

$n_p(t)$  = refractive index of the epoxy at time  $t$ ,

$n_p(t_0)$  = initial refractive index of the epoxy,

$n_p(t_\infty)$  = final refractive index of the epoxy.

Equation 2.23 showed a good correlation with degree of curing data obtained from DSC results. Discrepancies were observed during the early stages of cross-linking and appeared to increase at lower cross-linking temperatures.

Cusano *et al.* (2001) assumed that the degree of curing had a linear relationship with the refractive index. To make this assumption, the authors used Equation 2.23 and assumed that density reductions were proportional to the degree of curing. Aduriz *et al.* (2007) sought to validate this assumption by investigating simultaneously, the evolution of the refractive index, the specific volume and the degree of curing of an epoxy resin during resin transfer moulding. The refractive index was tracked using FRSs operating at 1550 nm; the degree of cure was obtained from heat-flux sensors and shrinkage was measured by a displacement sensor. The authors observed a linear relationship between the degree of curing and shrinkage (and hence, density); thus verifying the assumptions made by Cusano *et al.* (2001). The authors also compared the refractive index as a function of the degree of curing and observed a linear relationship. This work demonstrated the linearity of the refractive index increase with the evolution of degree of curing and the capability of the sensor to operate in an industrial environment.

#### **2.5.5.4 Non-Isothermal Heating Regimes Using Fresnel Reflection Sensor**

Much of the work associated with monitoring curing through the refractive index, using optical techniques, has been completed using isothermal heating regimes. Under non-isothermal conditions, because of changes in temperature, the refractive index changes in the fibre core, cladding and sample. This is in addition to the

increase in optical density associated with cross-linking. Quantifying the impact of each of these variables upon the overall Fresnel reflection to determine cross-linking kinetics has not yet been completed (Schubel *et al.*, 2013).

During dynamic heating regimes, a change in the thermo-optic coefficient of a cross-linked resin has been reported by several authors (Giordano *et al.*, 2000; Machavaram *et al.*, 2014; Robert and Dusserre 2014). Figure 2.16 displays the Fresnel reflection signal of an epoxy resin during heat-up, isothermal cross-linking at 140 °C and subsequent cooling. A change in the gradient of the signal upon cooling is expected due to the resin passing through the glass transition region. Previous research has suggested that  $T_g$  can be determined by the intersection of horizontal lines constructed on either side of the region, as shown in Figure 2.16 (Giordano *et al.*, 2000; Machavaram *et al.*, 2014; Robert and Dusserre, 2014).

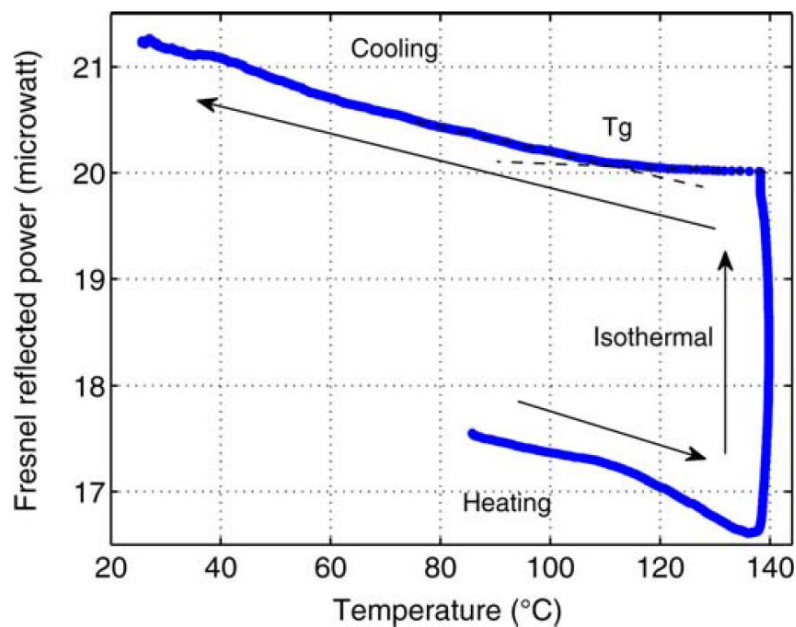


Figure 2.16 Fresnel reflection signal as a function of temperature during the cross-linking of an epoxy resin (Robert and Dusserre, 2014).

### 2.5.5.5 Effect of Power Fluctuations from the Light Source

Chang-Bong and Chin (2004) used a sensing system with a 2x2 coupler. Light was coupled into the coupler and split 50/50 between a short fibre with a FRS and a longer spool of fibre, left in air, which acted as a reference. Reflected light then returned to the coupler, where signals from the sensor and reference fibre were then decoupled and detected. The combination of different fibre lengths and the pulsed laser system allowed for this decoupling. Any variation in the laser power was used to normalise the Fresnel reflection. This arrangement does, however, require an expensive pulsed laser system and a 200 m long reference fibre. Multiplexing the system also becomes complex using this assembly.

Using a similar normalisation technique, Buggy *et al.* (2007) used a coupler to split light from a laser source into a sensing arm and a reference arm. Each arm had a secondary coupler to incorporate a sensor and a photodiode detector. The sensing arm was immersed in an epoxy resin, whilst the reference arm, left in air, measured fluctuations in the power supply. The signal from the reference arm was used to normalise the sensing arm. The sensor was then used to track the cross-linking of an epoxy resin over a period of 3 hours under UV light.

Xu *et al.* (2013) demonstrated a Fresnel refractometer that could reach resolutions of  $8.4 \times 10^{-6}$  when using analytical grades of water, ethanol and benzene. The system contained only one photodiode detector, with an optical switch, leading to a reference arm in air and sample sensor, both made from a single-mode fibre. The optical switch allowed for the photodetector to switch between the two sensors every 10 milliseconds; this accounted for any variations in intensities of the light source.



The sensor displayed good resolution and the use of an optical switch allowed for multiplexing of the system. The sensor system was limited by the assumption that the thermal environment of the reference sensor was identical to that of the sample sensor.

#### **2.5.5.6 Multiplexing Fresnel Reflection Sensors**

Using multiple FRSs can allow mapping of the extent of cross-linking in a composite structure. This can produce real-time, *in-situ*, detailed information on the state of curing at various locations in the preform. Liu *et al.* (1997) used multiple single-ended FRSs within a heated sample container. A pulsed laser, operating at 904 nm, was used, along with optical fibres of specified lengths. This allowed for the separation of the signal from each sensor, by measuring the time taken for light to reach the detector. Three sensors were immersed in neat resin (no hardener) and three within the mixed epoxy resin. A good correlation was observed between the sensors during heating; small mismatches in data were present and this was attributed to the thermal gradient in the heating bath. The magnitude of the reflected Fresnel signal decreased for the sensors immersed in the curing epoxy resins, during initial heating, as a result of a decrease in the refractive index caused by an increase in temperature. The effect of curing then dominated the signal because an increase in the reflected light intensity was observed due to cross-linking. Isothermal curing was also investigated and an increase in the optical signal, over time, correlated closely with the degree of curing determined independently from DSC data.

Chen *et al.* (2011) proposed a sensing system that used a broadband light source, in combination with an arrayed waveguide gratings, which split the light source into a specified number beams with specified wavelengths. Each beam was then connected to a sensing system containing an FRS and a photodiode detector. The ends of the sensors were immersed within an epoxy resin surrounded by a heated cell; the response of the sensors was shown to change with temperature.

Machavaram *et al.* (2014) deployed multiple single-ended FRSs using SMF-28 fibres with a 1550 nm light source. Multiplexing was achieved using an automatic optical channel selector. The optical channel selector allowed for the light to be directed and reflected from each sensor sequentially, whilst using a single photodetector. Six sensors were placed in separate vials containing epoxy resin, in addition to a sensor in neat resin. The samples were placed in an oven at room temperature, heated to 70 °C and cured for 7 hours. The Fresnel signals of each sample initially dropped upon heating to the isothermal temperature due to a reduction in density. Subsequently, an increase in Fresnel reflection was observed as cross-linking progressed. The curing kinetics was tracked at six separate locations simultaneously.

#### **2.5.5.7 Deployment of the Fresnel Reflection Sensor with Resin Containing Particulates**

Previous studies have investigated the evolution of the refractive index during curing using single-ended FRSs with epoxy resins (Crosby *et al.*, 1996a; Powell *et al.*, 1998; Machavaram *et al.*, 2014). Although little has been reported on resins containing fillers, Dimopoulos *et al.* (2009) investigated the curing behaviour of two different epoxy resins; one of which displayed phase separation. The curing

behaviour of each resin was investigated through DSC and refractive-index monitoring using an FRS. Close correlation between the data were observed in each resin. The phase-separating resin showed small fluctuations in its Fresnel signal during the early stages of cross-linking, as shown in Figure 2.17. These fluctuations were not seen for the resin that did not exhibit phase separation.

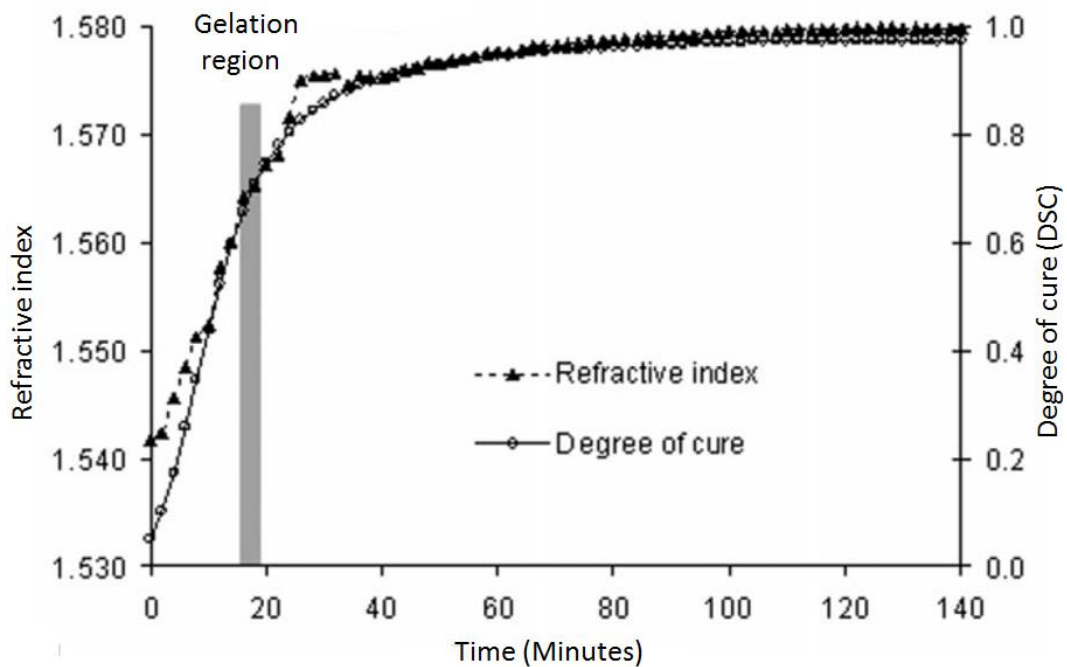


Figure 2.17 Comparison of the refractive index and degree of curing during isothermal cross-linking for phase-separating epoxy at 180 °C (Dimopoulos *et al.*, 2009).

Up to 1 wt% CNTs were introduced into the resins to observe the impact of particulates on curing. The particulates introduced fluctuations during the early stages of curing for the non-phase-separating resin. The existing fluctuations were exacerbated in the phase-separating resin system at early curing times. These fluctuations dissipated soon after gelation for both Fresnel signals and a good correlation was observed between DSC and refractive-index data. The authors suggested that localised

movement around the 8  $\mu\text{m}$  fibre core led to the fluctuations. Dimopoulos *et al.* (2009) stated that possible movements in this region occurred for the following reasons:

- (i) The presence and movement of small air bubbles that were not removed during degassing of the viscous mixtures.
- (ii) Cure-induced phase separation that led to the creation and movement of thermoset-rich regions.
- (iii) The movement of CNT clusters.

The results demonstrated the feasibility of using FRSs to track the curing of resins containing nanoparticles. Research indicated that the sensor was sensitive to phase separation and the presence of particulates, although further work would be required to confirm this sensitivity. The point at which noise was removed from the Fresnel reading could also be utilised to estimate the gelation time.

#### **2.5.5.8 Summary**

The capability of FRSs to monitor isothermal cross-linking of epoxy resins in an industrial environment has been demonstrated, due to the linear relationship between refractive index and the degree of curing. Issues of power fluctuations have been resolved and multiplexing demonstrated. Identification of the glass appears to be possible but has not been quantified conclusively.

#### **2.5.6 Fibre-Optic Fourier Transform Infrared Spectroscopy**

Conventional spectroscopic techniques are undertaken in a laboratory, where the thermal environment will differ from that during manufacturing. Various sensor

configurations exist to obtain *in-situ* quantitative information of functional groups at desired positions.

### **2.5.6.1 Optical Fibre Based Transmission Spectroscopy**

Doyle *et al.* (1998b) demonstrated a fibre-optic transmission sensor using two 50/125  $\mu\text{m}$  fibres. One fibre delivered light from a quartz-halogen source, whilst the other collected light and guided it towards a photodiode detector. The fibres were cleaved and aligned with a gap of 1.25 mm. An epoxy resin system was inserted within the cavity. The resin was cross-linked at 42 °C, with spectral data collected in the range of 6900–6000  $\text{cm}^{-1}$ . Depletion of the epoxy band at 6060  $\text{cm}^{-1}$  was observed throughout cross-linking.

Powell *et al.* (1998) extended this research using a larger 200/240  $\mu\text{m}$  fibre and reduced the path length to 0.5 mm. A monochromatic source and detector were attached to the non-sensing ends of the fibres. Light was collected from 4450 to 4800  $\text{cm}^{-1}$ . The degree of curing was determined using the epoxy band at 4530  $\text{cm}^{-1}$  and showed a good correlation to conventional FTIRS results at 40, 50 and 60 °C, although discrepancies were observed at 30 °C. Research demonstrated the performance of the sensor alongside conventional spectroscopy results for the epoxy band at 4530  $\text{cm}^{-1}$ , which, as discussed in Section 2.3.2.2, is a strong and isolated absorption band.

### 2.5.6.2 Evanescent Wave Spectroscopy

During total internal reflection within an optical fibre, light is not instantaneously reflected at the interface. A standing electromagnetic wave is formed, which decays exponentially with penetration depth ( $d_p$ ), as shown in Figure 2.18. Evanescent wave spectroscopy operates on a section of the fibre where the core is exposed to the resin. The resin acts as an absorbing fluid, which causes power to be lost from the fibre core with each reflection at the interface. The light emanating from this sensing region reveals absorption characteristics of the surrounding medium surrounding (Gupta and Gupta, 2006). The sensor is a single-use device.

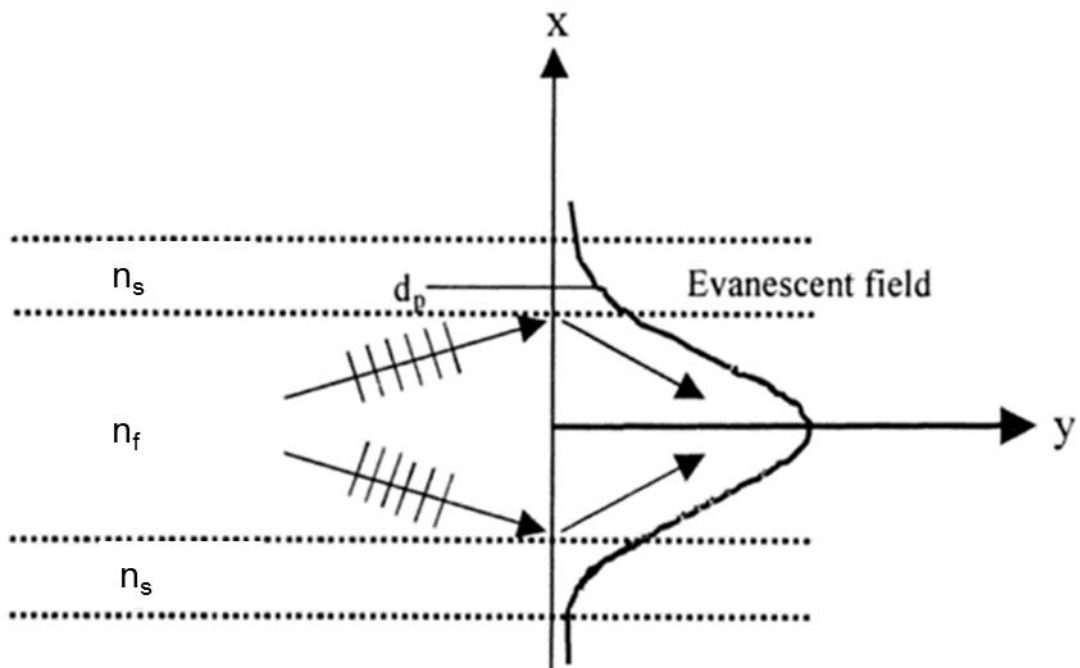


Figure 2.18 Evanescent wave phenomena at the core–cladding interface.

$n_f$  = refractive index of fibre core,  $n_s$  = refractive index of sample

(Gupta and Gupta, 2006).

### 2.5.6.3 Reflection/Transmission Spectroscopy

Multiple low-OH optical fibres can be bundled together to form a probe that can transmit and receive infrared light. Light is launched towards a sample contained in a vessel with a reflective surface. The light transmits through the sample before reflecting off the surface, and the reflected light can be directed to a detector. This interaction has been termed trans-reflection and is depicted in Figure 2.19. The sensor is attractive because it is non-contact and reusable (Fernando and Degamber, 2006).

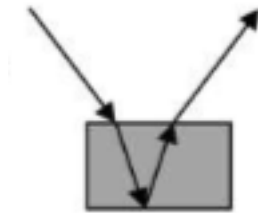


Figure 2.19 Trans-reflection interaction of light with resin  
(Fernando and Degamber, 2006).

Yu and Sung (1995) used trans-reflection spectroscopy to monitor the curing kinetics of epoxy resin for a sample cross-linked within a metal heating element. Reflected light was collected by a fibre-optic probe and directed to a spectrometer. The epoxy group concentration was recorded during cross-linking at 160, 200 and 250 °C. This work demonstrated a new technique of using fibre optics for a non-contact, cost-effective testing method that required little sample preparation.

## **2.5.7 Hyphenated Optical Fibre Based Differential Scanning Calorimetry and Fourier Transform Infrared Spectroscopy**

The non-contact nature of trans-reflection spectroscopy has enabled the technique to be introduced into a differential scanning calorimeter sample chamber to combine the two curing characterisation techniques. This combination has attracted interest because the technique ensures identical thermal and chemical environments for both data sets to allow direct correlation between thermal and spectral events. Simultaneous DSC/FTIRS techniques have been demonstrated, although their application is limited by a combination of complex light-transmission methods, using non-conventional DSC pans and lengthy sample preparation procedures (de Bakker *et al.*, 1993; George *et al.*, 1996). This section investigates the introduction of optical fibres into the differential scanning calorimeter for simultaneous data acquisition with FTIRS.

Frushour and Sabatelli (1988) first reported the introduction of a fibre-optic probe into a differential scanning calorimeter. They accommodated the probes into the calorimeter by drilling holes above the sample and reference compartments. Their probe consisted of an array of randomly distributed fibres that were split equally into sample and reference probes housed in brass cylinders. Within each probe, half of the fibres were for illumination and they were attached to an infrared light source operating at 880 nm; the other half were used for acquiring the reflected light and connected to a photodiode detector. During the experiments, only the sample side was illuminated; the presence of the reference probe was to balance the thermal environment in both chambers. Light was launched towards the sample compartment, transmitted through the samples, reflected off the aluminium sample



pans and back towards the probe, where it was detected. The optical signal obtained is simply an intensity that changes with transparency of the sample. The authors demonstrated the ability of the sensing technique to track thermal and optical properties during melting, crystallisation and the glass transition temperature of common thermoplastics. Despite modification to the differential scanning calorimeter, calibration did not impact on the accuracy or resolution of DSC significantly.

The pioneering work of Frushour and Sabatelli (1988) has subsequently enabled multiple parameters to be acquired simultaneously and exploited excellent temperature control supplied by DSC. Modifications of DSC have been accomplished using microscopic lenses (Haines and Skinner, 1982) and conventional FTIRS (Mirabella, 1986; de Bakker *et al.*, 1993), but the methods require elaborate optical alignment and glass pans, which exhibit poor thermal conductivity.

Dumitrescu (2003) used the reflection/transmission spectroscopy design of Yu and Sung (1995) to introduce fibre-optic probes into a differential scanning calorimeter. A bifurcated fibre-optic bundle was used that consisted of 98 optical fibres. The fibres were split evenly between the light source and detector arms, where they were distributed randomly. The two arms terminated in sub-miniature adaptor A (SMA) connectors, whilst the sensing region was housed in steel tubing. An epoxy resin was used to secure the fibre in place at each end. The probe was polished to obtain maximum light transmission and collection. The top lid of the differential scanning calorimeter was drilled into to accommodate the probes. To maintain thermal stability within the differential scanning calorimeter, conventional platinum lids were replaced with custom-made, optically transparent glass lids. The customised DSC

was re-calibrated; the onset of melting and heating of indium were compared closely to conventional DSC results.

Cross-linking of an epoxy resin (LY3505/XB3403) was completed at 60, 70, 80 and 85 °C. The degree of curing results obtained from conventional DSC and FTIRS correlated closely to those obtained using the simultaneous acquisition technique. Some common trends were observed. DSC showed an advanced degree of curing up until approximately 80% conversion. After this point, the degree of curing obtained through FTIRS advanced further until the end of curing. This could be accounted for by small amounts of exothermic cross-linking below the minimum sensitivity of the differential scanning calorimeter.

The work demonstrated a thorough investigation, in which the calibration of the differential scanning calorimeter was considered and results closely compared with those of conventional data obtained in both isothermal and non-isothermal modes. Whilst a dummy probe was present in the reference compartment of the differential scanning calorimeter, it was not illuminated and did not impact on the thermal equilibrium required during DSC. The steel housing containing the probes reduced the insulation of the system due to the high thermal conductivity of the material.

Degamber *et al.* (2004b) demonstrated a probe design to obtain simultaneous DSC/FTIRS/TMA data. The probe was a bifurcated fibre bundle made using 172 low-OH fibres, split evenly between the arms. Two arms were connected to an FTIR light source and detector through SMA connectors. The opposite two arms were housed in steel tubes bonded together by epoxy resin and polished to allow for maximum light transmission and collection. As illustrated in Figure 2.20, the central diameter of the probe contained 10 single-mode fibres operating at 1550 nm, which

were housed in a 3 mm outer-diameter tube that served as the TMA sensor. The end of the TMA probe was also polished.

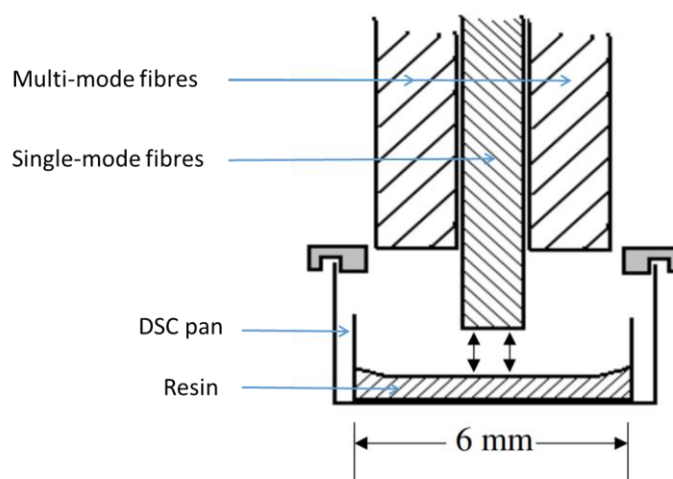


Figure 2.20 Probe design for simultaneous DSC/FTIRS/TMA data acquisition (Degamber and Fernando, 2006).

The probe was used to characterise a polypropylene film by providing thermal, spectral and dilatometric data as the polymer was heated through its melting transition. An increase in sample volume was observed with increasing temperature, until the onset of melting. The onset of melt correlated with conventional thermo-mechanical analysis results.

With thermosetting resins, the technique has the potential to determine curing shrinkage alongside thermal and spectral information. Illumination of the reference probe produced a light intensity equal to that of the sample probe; a feature that was absent from previous work. The ends of the probe were encased in low-conductive glass capillaries to minimise the impact of the environment on the thermal stability.

Pandita *et al.* (2012) developed a probe that consisted of 150 low-OH optical fibres, which were split evenly between the sample and reference probe ends. The probes

were held over samples in a conventional aluminium pan; the platinum lids of the differential scanning calorimeter were removed for optical access. The curing of an epoxy resin was conducted over a ten-hour period at 50 and 70 °C, and curing data was compared for simultaneous measurements and those of conventional measurements; an excellent correlation was observed. Small discrepancies were observed in comparison with the results obtained through conventional techniques; these were attributed to differing thermal environments and sample sizes.

This study expanded on work reported by Dumitrescu (2003) by inserting equal power into the sample and reference compartments. An excellent correlation between the thermal and spectral degree of cross-linking was observed. The fibres were again encased in glass capillaries to reduce the impact on the thermal environment of the sample. Removal of the platinum lids would have a detrimental effect on insulation within the sample and reference compartments; this could limit the operating temperatures to avoid extreme thermal gradients.

## **2.6 Conclusion**

Analytical approaches to track the cross-linking of epoxy resin systems reported in the literature were reviewed. The use of conventional DSC, FTIRS and rheology techniques were discussed. The impact of graphene on the outcome of these techniques was then discussed before optical fibre-based sensors were reviewed.

Cross-linking analysis of epoxy resins using DSC and FTIRS has been reported widely, and models have been developed to predict the cross-linking kinetics, although discrepancies were frequently seen in the data. Sources of error emanate

from differing thermal environments, sample sizes, temperature-control systems and conversion calculations.

Strengthening effects upon the introduction of pristine graphene particulates within an epoxy system have been limited by the tendency of graphene to agglomerate, in addition to weak interactions with the resin system. Appropriate functionalisation of graphene, however, has circumvented these issues to allow for improvements in resin strength, toughness and shorter cross-linking times.

A range of optical fibre sensors have been developed that can be used to obtain qualitative and quantitative data during cross-linking. This thesis has focused upon the deployment of a refractive-index sensor, known as the FRS and spectral sensors.

It has been shown that the increase in the refractive index during cross-linking of an epoxy resin is proportional to the degree of conversion. The feasibility of using the FRS to obtain qualitative information has been demonstrated by comparison with FTIRS and DSC data. Multiplexing the FRS system has been demonstrated successfully; thus, making it an attractive prospect for on-line process monitoring at multiple points. The FRS has also been reported to be capable of identifying the glass transition due to a change in the thermo-optic coefficient.

Spectral-based optical sensors also provide an attractive option for on-line process monitoring. Transmission/reflection and transmission sensors have demonstrated correlation with results obtained through conventional analytical techniques. Interest in developing hyphenated techniques, wherein optical fibres are incorporated into a differential scanning calorimeter, have also proved to be powerful analytical techniques with which direct correlation of data sets can be undertaken.

## **3. MATERIALS AND EXPERIMENTAL METHODS**

### **3.1 Introduction**

The materials, equipment and development of hyphenated analytical techniques are discussed in this chapter. Experimental details concerning the use of specified equipment are also described.

### **3.2 Materials**

This research focused primarily on the use of an epoxy/amine resin. The epoxy resin and hardener were coded as LY3505 and XB3403, respectively. The resin was also blended with GNPs by the Gwent Group, using high-speed shear mixing. An aerospace-grade epoxy resin system was prepared in collaboration with Cytec/Solvay; this system was formulated to undergo phase separation during cross-linking.

#### **3.2.1 LY3505/XB3403**

An epoxy resin, LY3505, and hardener, XB3403, were used throughout the course of the current project. The resin was a mixture of DGEBA and DGEBF. The hardener, XB3403, was polyoxypropylene diamine. Table 3.1 displays the chemical structures of the resin and hardener used in this current study.

Table 3.1 Chemical structure of LY3505 (resin) and XB3403 (hardener).

Name	Structure
LY3505 - Bisphenol A	
LY3505 - Bisphenol F	
XB3403	

The resins and hardener were mixed in the recommended stoichiometric ratio of 100:35 (parts by weight), respectively. Approximately 5 g of resin was mixed with 1.75 g of hardener for each experiment. A five-digit analytical balance (Analytical Plus, Ohaus, UK) was used to measure the individual components into aluminium dishes before mixing. Manual mixing was undertaken using a wooden spatula for 5 minutes and the sample was visually inspected to ensure homogeneity. The mixed system was placed into a vacuum chamber for 20 minutes to allow degassing. The resin system was used immediately after the degassing phase. A fresh batch of the resin system was used for each experiment.

### 3.2.2 LY3505/XB3403 Containing Graphene Nano-particles

High-shear mixing was used by Gwent Group (UK) to blend GNPs into the LY3505 resin. Concentrations of 0.01, 0.1, 0.5, 1, 2 wt% GNP resins were prepared. The resin was mixed with hardener (XB3403), as described in Section 3.2.1.

### **3.2.3 Cytec/Solvay Resins**

A set of aerospace resin formulations were prepared at the Cytec/Solvay research laboratory in Wilton, UK. The materials consisted of epoxy resins, a hardener and a thermoplastic. The compositions of the materials are proprietary, and hence, they are not disclosed. Six formulations were prepared with increasing quantities of thermoplastic, ranging from 0 to 30 wt% in 10 wt% increments. The formulations were heated using an oil bath set at 80 °C and mixed using a mechanical stirrer. After 30 minutes of mixing, the blends were degassed, sealed and transported to The University of Birmingham in a container that was maintained at sub-ambient temperature. The samples were stored in air-tight containers at –17 °C until required. Prior to the cross-linking experiments, each sample was allowed to thaw to room temperature in a desiccator.

## **3.3 Conventional Analytical Techniques**

The conventional analytical techniques used to characterise the LY3505/XB3403 resin system were DSC, FTIRS and parallel-plate rheometry.

### **3.3.1 Differential Scanning Calorimetry**

A Perkin-Elmer Diamond differential scanning calorimeter was used for the DSC experiments.



### **3.3.1.1 Calibration**

The differential scanning calorimeter was calibrated in the conventional manner using pure indium and tin, the melting points of which were 156.6 and 231.9 °C, respectively. The samples were placed in open-top aluminium pans (product code 02190041, Perkin Elmer, USA) and the onset of melting and the enthalpy of fusion were determined for each sample at a heating rate of 10 K/minute. Following the above-mentioned calibration procedure, an indium sample was heated from 30 to 180 °C at 10 K/minute to establish that the onset of melting and the enthalpy of fusion were within recommended tolerances of  $\pm 0.3$  °C and  $\pm 0.6$  J/g, respectively. The calorimeter was calibrated at regular intervals using indium.

### **3.3.1.2 Non-Isothermal Cross-Linking**

Approximately 20 mg of the resin system (LY3505/XB3403) was dispensed into the centre of an aluminium pan using a micro-pipette (product code 725020, Biohit, UK). The open DSC pan with the resin system was positioned in the differential scanning calorimeter chamber at 30 °C. The sample was permitted to equilibrate for 1 minute prior to subjecting it to a temperature ramp. The calorimeter was programmed to heat the sample and reference compartments from 30 to 300 °C at 1, 10, 20 and 40 K/minute.

### **3.3.1.3 Isothermal Cross-Linking**

Approximately 20 mg of the resin system (LY3505/XB3403) was dispensed into the centre of an aluminium pan using a micro-pipette (product code 725020, Biohit, UK).

The open-top DSC pan containing the resin was positioned in the centre of the differential scanning calorimeter chamber at 30 °C. The sample was permitted to equilibrate for 1 minute prior to heating to the desired isothermal cross-linking temperature at 40 K/minute. The calorimeter was heated to the isothermal cross-linking temperatures and maintained for 10 hours. The isothermal temperatures used were of 50, 60 and 70 °C. Upon completion, the temperature was reduced to 30 °C at 40 K/minute. The differential scanning calorimeter was then programmed for 3 successive heating regimes from 30 to 150 °C at 10 K/minute to enable the glass transition temperature to be determined.

### **3.3.2 Fourier Transform Infrared Spectroscopy**

A spectrometer (Matrix-F FT-NIR, Bruker, UK) was used to characterise the cross-linking characteristics of the resin system as a function of temperature and processing time. The spectrometer was operated between 4000 and 12000  $\text{cm}^{-1}$ , at a resolution of 4  $\text{cm}^{-1}$  with 64 scans. The spectrometer had an in-built tungsten light source and an InGaAs detector. The spectrometer was equipped with six pairs of SMA connectors for light to be coupled to and from it through optical fibre probes (product code QP1000-2-VIS/NIR, Ocean Optics, USA). The light from the spectrometer was transmitted to a temperature-controlled transmission cell (CUV-QPOD, Ocean Optics, USA), as illustrated in Figure 3.1. A temperature-control unit (TC125, Quantum Northwest, USA) was used to set the temperature of the cell, whilst a water circulation system was used to cool it and maintain the required temperature. The transmission cell offered a temperature accuracy of  $\pm 0.02$  °C. The transmission cell housed a demountable glass cuvette (product code 1-G-1, Starna Scientific, UK) with a 1 mm path length, as shown in Figure 3.2. The two faces of the

demountable cuvette were bonded together using silicone rubber (product code 692-542, RS Components, UK).

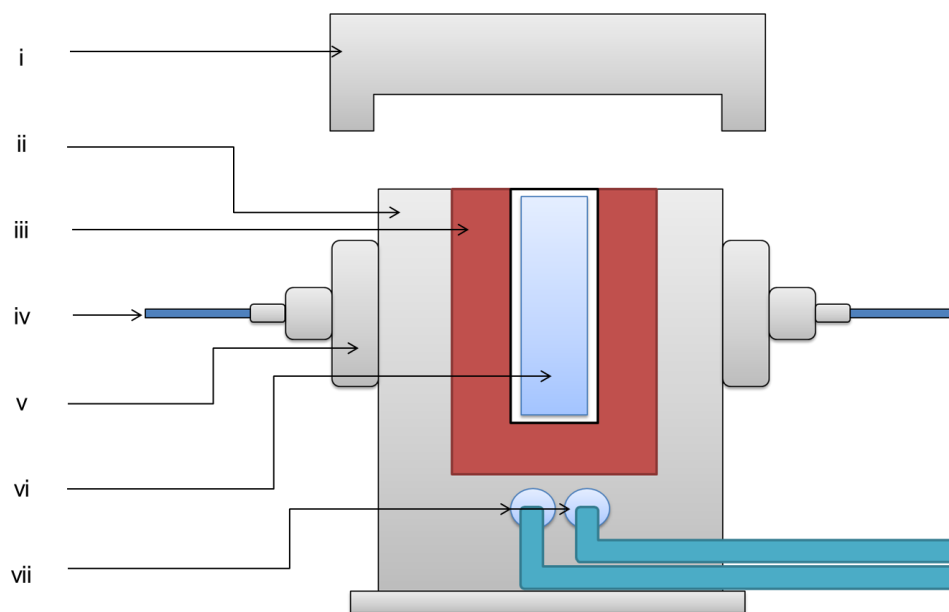


Figure 3.1 Schematic illustration of the temperature-controlled cuvette used for transmission FTIRS: (i) cover, (ii) thermal insulation, (iii) heating element, (iv) fibre-optic cable connection to the spectrometer, (v) collimating lens, (vi) demountable cuvette-containing the resin system, (vii) connections for water circulation.

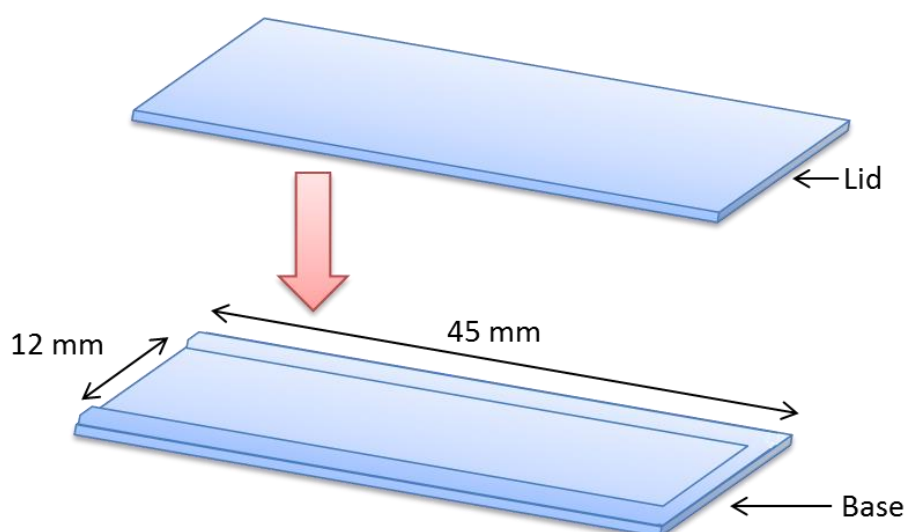


Figure 3.2 Schematic illustration of the demountable cuvette with a 1 mm path length used during transmission FTIRS.

### 3.3.2.1 Temperature Distribution within the Cuvette

The temperature distribution within the cuvette, whilst within the holder and filled with silicone oil, was investigated using six thermocouples. These thermocouples were attached to one face of the demountable cuvette using UV adhesive (product code NOA68, Norland Optical Adhesive, USA) and inserted into the cuvette holder. The relative positions of the thermocouples are shown in Figure 3.3. The temperature was increased from 20 to 70 °C at 5 °C intervals with a 5 minute dwell time at each temperature. The temperature was recorded using a thermocouple logger (product code TC-08, Picolog, UK).

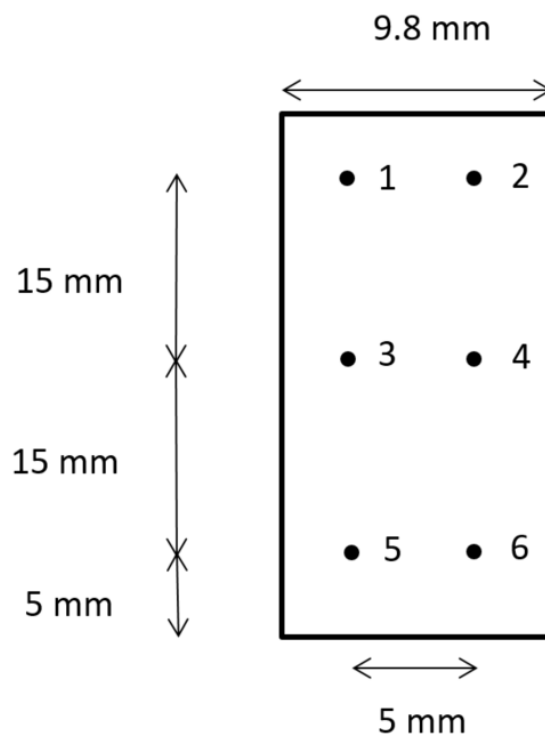


Figure 3.3 Schematic illustration showing the relative positions of the thermocouples on one face of the demountable cuvette to determine the temperature gradient.

### **3.3.2.2 Fourier Transform Infrared Spectroscopy from within the Cuvette Holder**

The Bruker Matrix-F FT-NIR spectrometer mentioned in Section 3.3.2 was used to acquire transmission NIR spectra from the cuvette. A release agent (Frekote NC-700, Aerovac, UK) was applied to the inner surfaces of the demountable cuvette, but it was ensured that the bond line for bonding the two surfaces was masked. The release agent was necessary to ensure easy removal of the cross-linked resin. A background spectrum was recorded at the desired isothermal temperature with the demountable cuvette inserted into the transmission cell. The resin system was prepared as described in Section 3.2.1, and the mixed resin/hardener sample was inserted into the cuvette using a syringe and needle (product code PMC3006, Terumo, Japan). A freshly mixed resin system was dispensed into the cuvette using a micropipette (product code 725020, Biohit, UK). Spectra were recorded every 5 min at a resolution of  $4\text{ cm}^{-1}$  with 64 scans. The cuvette holder was pre-heated to the desired isothermal temperature before the cuvette with the resin was inserted. The LY3505/XB3403 resin system was cross-linked at 50, 60 and 70 °C.

Deconvolution of the FTIR spectra was achieved before integration of the relevant absorbance bands to resolve the contribution from an unidentified band at  $4564\text{ cm}^{-1}$ . This was achieved using a Fourier self-deconvolution routine available within the software (OPUS 6.5, Bruker, UK). A Lorentzian line, using a resolution enhancement of 1.5 with a bandwidth of  $5\text{ cm}^{-1}$  was used. The deconvolution routine used a mathematical formula to enhance the resolution of the absorbance band (Tooke, 1988; Mahendran, 2010). Integration of the spectra was undertaken using the OPUS

software supplied with the Bruker spectrometer. The integration limits were selected manually over the duration of cross-linking.

### **3.3.3 Parallel-plate Rheometry**

An Ares rheometer (ARES, Rheometric Scientific, USA) with 35 mm parallel plates was used to study the viscosity/time characteristics of the resins at specified temperatures. A 1.5 mm gap was chosen for the experiments because increasing the gap caused the resin to flow out of the fixture. A frequency of 1 Hz and a strain of 4% were used for each experiment. In order to annul the effects of thermal expansion on the gap size, the distance between the plates was reduced to zero at the desired isothermal temperature. The parallel plates were maintained at 30 °C for 2 minutes, and the resin system was introduced using a pipette. Approximately 2 mm<sup>3</sup> of the resin system was dispensed into the centre of the bottom plate. The fixture was heated to the desired isothermal value at 40 K/minute. The transducer required a minimum torque of 0.02 N-cm to obtain meaningful data. The experiment was terminated soon after gelation to prevent overloading the transducer. Rheological characterisation was carried out isothermally at 50, 60 and 70 °C.

## **3.4 Fresnel Reflection Sensor**

### **3.4.1 Experimental Setup for the Fresnel Reflection Sensor**

A schematic representation of the experimental setup for the Fresnel reflection sensing system is shown in Figure 3.4. The light source consisted of a pigtailed semiconductor diode operating at 1550 nm, housed within a laser driver and

temperature controller (part number CLD1015, Thorlabs, USA), exhibiting stability of 0.005 °C. Light reflected from the cleaved optical fibre (product code SMF-28e, Corning, USA) was directed to an InGaAs photodiode amplifier (part number APD110C, Thorlabs, USA) using a single-mode circulator (part number 6015-3, Thorlabs, USA) operating at 1550 nm. The circulator directed light from the laser (1) toward the sensing region (2) and re-directed reflected light toward the detector (3). A data acquisition system (USB9162, National Instruments, USA) and a custom-written LabVIEW programme enabled the magnitude of the Fresnel reflection signal to be recorded. The optical fibres had a core refractive index of 1.44961 nm at 1550 nm and a numerical aperture of 0.14. The core and cladding diameters of the SMF-28e fibre were 8.2 and 125  $\mu\text{m}$  respectively. The response on the sensor in air was recorded after the fibre was cleaved. This data was used subsequently to normalise the Fresnel reflection signals acquired during the cross-linking reactions.

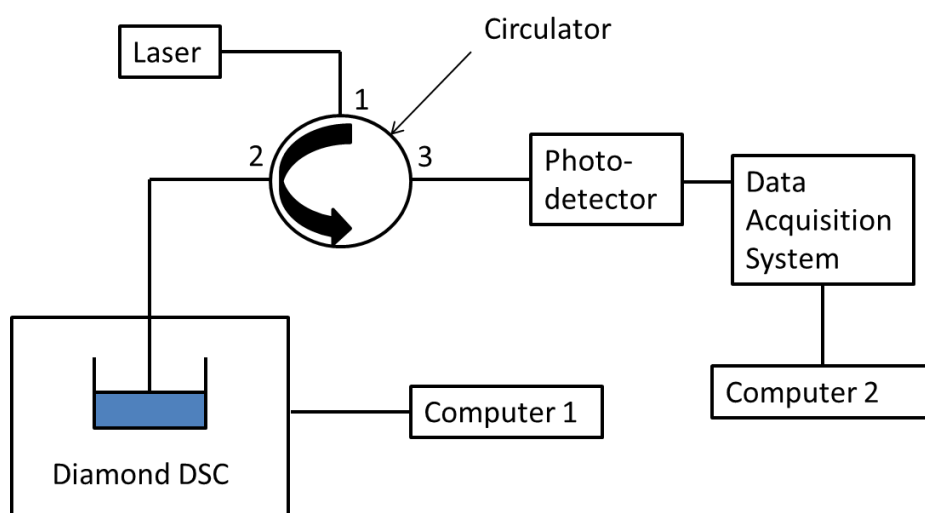


Figure 3.4 Schematic illustration of the experimental set-up for the simultaneous DSC and Fresnel experiments.

The sensing region was prepared by removing the acrylate protective buffer or coating from the optical fibre using a pair of mechanical strippers (product code

AFS900, Thorlabs, USA). The stripped fibre was cleaned using isopropanol (product code W292907, Sigma-Aldrich, USA) soaked in lint-free tissue (product code FB13067, Fisherbrand, USA) to remove any residual acrylate material. The stripped optical fibre was placed in a high-precision fibre cleaver (part number CT-30A, Fujikura, Japan) and cleaved. The device was capable of cleaving the optical fibre at  $(90\pm 0.5)^\circ$  with reference to the length of the optical fibre. After cleaving, the ends of the optical fibres were inspected using an optical microscope (product name Axioskop, Zeiss, Germany). Cleaved sections without the required end-face quality were rejected and the fibre was re-cleaved.

### **3.4.2 Calibration of the Fresnel Reflection Sensor**

The response of the FRS was investigated by using standard refractive-index oils (product code 18005, Cargille, USA) within an Abbe refractometer (product name Abbe 60, Bellingham and Stanley, UK). A FRS and K-type thermocouple were positioned on the edge of the measuring prism of the Abbe refractometer. The small dimensions of the sensor and thermocouple did not impede measurements from the Abbe refractometer. Oils with refractive indices of 1.4, 1.45, 1.5, 1.6 and 1.7 were used; the temperature within the prisms of the refractometer was set at 25, 30, 35 and 40 °C. The temperature was controlled using a water circulation system (product code TE-10D, Techne, UK). The refractometer was permitted to equilibrate for 5 minutes at each temperature prior to acquiring data from the refractometer manually, and from the FRS through the computerised data acquisition system. Five individual readings were taken from the Abbe refractometer at one-minute intervals at each temperature. Each refractive-index oil was measured three times and a fresh FRS was prepared for each oil.



### **3.5 Integrating the Fresnel Reflection Sensor within a Differential Scanning Calorimeter**

A Diamond differential scanning calorimeter (product code N5360021, Perkin Elmer, USA) was used to develop the methodology for integrating the FRS into the calorimeter. The original top lid was replaced with a custom-built cover to accommodate the FRS. A schematic illustration and photograph of the assembly are shown in Figure 3.5; the coded components of the assembly were as follows: Item (i) is a translation stage (part number PT1, Thorlabs, USA), which was attached to the the top cover. The translation stage enabled the fibre (item (ii)) to be translated vertically. The fibre was secured within a fibre chuck (item (iii); part number HFC005, Thorlabs, USA), which allowed for alignment and protection of the fibre. Item (iv) was a grub screw that allowed for the fibre chucks to be secured to the translation stages. The translation stage was used to lower the fibre chucks through orifices above the sample (item (v)) and reference compartments (vi). The fibre protruding from the fibre chuck could be lowered to make contact with the resin contained in the sample pan. Item (vii) was the fixture that secured the translation stages to the custom-built top cover of the differential scanning calorimeter (item (viii)). The underside of the top cover was insulated using an appropriately shaped sheet of calcium–magnesium silicate (part number 724-8909, RS Components, UK). Conventional alumina DSC sample pans (part number 140828, Perkin Elmer, USA) were used in the sample and reference compartments of the calorimeter. A 1 mm orifice was drilled into the platinum lids (product code 0419-0299, Perkin Elmer, USA), which were positioned above the sample and reference chambers to enable the FRS to be lowered towards, and make contact with, the sample. The differential scanning calorimeter was calibrated using pure indium (product code 6.223.5,

Netsch, Germany) and tin (product code 6.223.5, Netzsch, Germany) reference standards. The samples were heated from 30 °C to beyond their melting temperatures at a rate of 10 K/minute and then cooled to 30 °C.

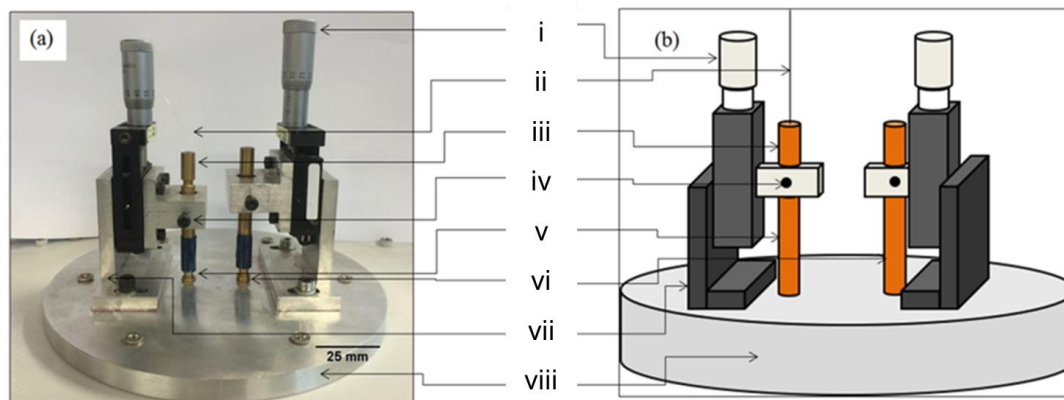


Figure 3.5 (a) Photograph and (b) schematic illustration to show the key components of the custom-modified Perkin Elmer Diamond differential scanning calorimeter top cover: (i) micrometer for vertical translation, (ii) optical fibre, (iii) optical fibre chuck, (iv) grub screw to secure the fibre chuck, (v) orifice in the top lid to accommodate the fibre chuck over the sample compartment, (vi) orifice to accommodate the fibre chuck over the reference compartment, (vii) vertical translation stage attachment to the top lid, (viii) custom-made Diamond differential scanning calorimeter top lid.

### 3.5.1 Investigation into the Reflectivity of Differential Scanning Calorimetry Pans

Reflections from a reflective surface can interfere with the recorded Fresnel reflection signals emanating from a cleaved fibre-end. Common types of DSC pans available commercially include aluminium, copper, gold, platinum and alumina (Perkin-Elmer, 2014). In the current case, it was necessary to select a DSC pan with which reflectivity from the base of the pan was minimal. Assessment of the reflectivity of the DSC pans was carried out using the following procedure. A

translation stage was used to lower a fibre chuck with an FRS towards the base of the pan. The magnitude of the reflected Fresnel signal was recorded as a function of the distance between the cleaved optical fibre end-face and the base of the pan. These experiments were carried out at room temperature. The DSC pan types evaluated were conventional aluminium; an aluminium pan that was sputter-coated with carbon for 5 minutes using a sputter-coater (product code SC500, Emscope, UK); an aluminium pan, the base of which was abraded using P800 silicon carbide grinding paper (product code 139913, Metprep, UK); and an alumina pan. In each case, the cleaved end-face of the optical fibre was lowered from 14 mm above the base of the pan.

Subsequent to these trials, conventional DSC alumina pans (product code 02191072, Perkin Elmer, USA) with a diameter of 5.2 mm and height of 2.5 mm were chosen for use in the sample and reference compartments. The conventional DSC platinum lids were drilled to create an orifice with a diameter of 1 mm in the centre to allow the optical fibre to be inserted and brought into contact with the liquid sample.

#### **3.5.1.1 Cross-Linking of the LY3505/XB3403 Resin System with and without Graphene Nano-particles**

The resin system was prepared as described in Section 3.2.1. Blending of the GNPs into the LY3505 resin was discussed in Section 3.2.2. Approximately 20 mg of the degassed resin system was dispensed into an alumina pan. The pan was placed into the sample compartment of the differential scanning calorimeter at 30 °C with an empty pan in the reference compartment. The FRS was prepared as described in Section 3.4.1 and the reflectivity in air was recorded for 1 minute. The FRS was

lowered towards the sample using the translation stage. When the FRS came into contact with the resin system, a large drop in the magnitude of the FRS signal was observed; the sensor was lowered a further 250  $\mu\text{m}$ . This was necessary to prevent withdrawal of the FRS from the cross-linking resin due to shrinkage. The differential scanning calorimeter was used to heat the sample from 30  $^{\circ}\text{C}$  to the desired isothermal value at 40 K/minute. The sample was held isothermally for 10 hours and then cooled to 30  $^{\circ}\text{C}$  at 40 K/minute. Following this isothermal dwell, the sample was subjected to three successive heating regimes from 30 to 150  $^{\circ}\text{C}$  at 10 K/minute to enable the glass transition temperature ( $T_g$ ) to be determined.

### **3.5.1.2 Cross-Linking of Cytec/Solvay Resins**

The blended resin samples from Cytec/Solvay were stored at -17  $^{\circ}\text{C}$  in air-tight containers. Prior to use, the samples were transferred to a desiccator and equilibrated to room temperature for 30 minutes. Approximately 30 mg of the resin system was dispensed into an alumina pan using a micropipette and placed in the sample compartment of the DSC. The FRS was inserted to bring it into contact with the resin systems, as described in Section 3.5.1.1. The sample was heated from 30 to 180  $^{\circ}\text{C}$  at 40 K/minute and held for 3 hours and cooled to 80  $^{\circ}\text{C}$  at 1 K/minute. This cure schedule was recommended by the supplier of the resin system. After cross-linking, the sample was heated from 30 to 180  $^{\circ}\text{C}$  at 10 K/minute; this was performed three times to determine  $T_g$ .

### 3.6 Integration of the Fresnel Reflection Sensor within the Rheometer

The FRS was incorporated between the parallel plates of a rheometer (ARES, Rheometric Scientific, USA) by drilling a 0.5 mm orifice in the centre of the 35 mm diameter top-plate. A cleaved optical fibre was threaded through the top arm of the parallel-plate holder and into the orifice on the parallel plate. A schematic and photographic illustration of the fixture with the optical fibre is shown in Figure 3.6 in order to bring the FRS into intimate contact with the top parallel plate, the gap between the two plates was reduced incrementally until contact was made. Silicone rubber (product code 555-588, Thorlabs, UK) was used to secure the sensor in position. The resin samples were prepared as described in Section 3.2.1, and the resin system was introduced as described for conventional rheology (Section 3.3.3). Synchronisation between the two data sets (rheometry and FRS) was achieved by switching off the light source momentarily to produce a spike in the FRS signal. The experiment was terminated soon after the manifestation of gelation, as observed by the crossover of the storage modulus ( $G'$ ) and the loss modulus ( $G''$ ).

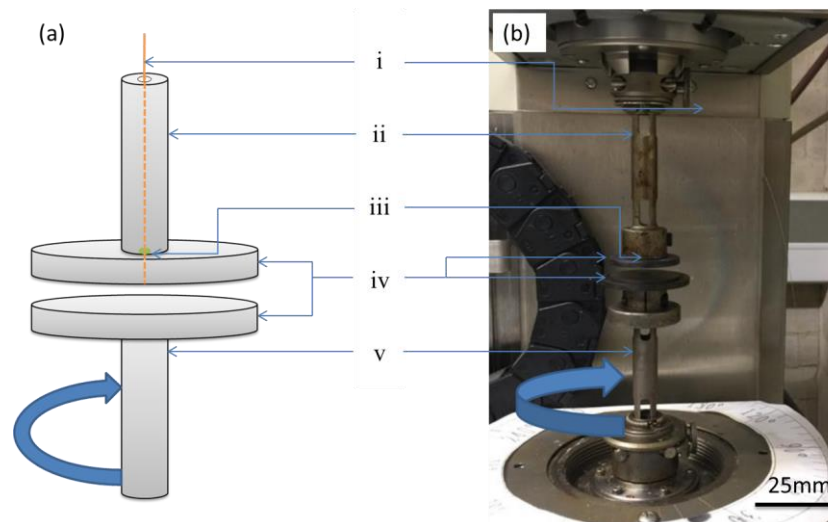


Figure 3.6 (a) Schematic and (b) photographic illustration of the hyphenated FRS/rheometer: (i) optical fibre, (ii) fixture connected to the transducer, (iii) silicone rubber, (iv) 35 mm diameter parallel plates, (v) fixture connected to the motor.

### **3.7 Hyphenated Differential Scanning Calorimetry /Fourier transform Infrared Spectroscopy /Fresnel reflection Sensor**

The top-cover of the calorimeter, which was designed for the simultaneous DSC/FRS experiments, was modified to permit the integration of an FRS/FTIRS probe. The construction of the probe and modification of DSC pans are discussed in Section 3.7.1.

#### **3.7.1 Construction of the Fibre-Optic Probe**

A schematic illustration of the FRS/FTIRS probe is shown in Figure 3.7. One hundred and twenty low-OH optical fibres (product code FG105LCA, Thorlabs, USA) were cut into 1 m lengths. Of these, 60 randomly arranged fibres were housed within a stainless-steel SMA connector (part number 10510A, Thorlabs, USA) to connect the probe, item (i), to the FTIRS light source. The LY3505/XB3403 resin system was used to pot the fibre bundles to the SMA connector. The remaining 60 fibres were potted into a second SMA connector, item (ii), to enable it to be connected to the detector port of the FTIR spectrometer. The potted SMA connectors with the optical fibre ends were polished using an optical polishing wheel (APC 8000, Senko, Japan) with 15, 3, and 1  $\mu\text{m}$  films for 120 seconds each. The opposite ends of the fibres connected to the light source and detector were distributed evenly between a sample probe, item (iii), and reference probe, item (iv). This amounted to an equal number of illumination and detection fibres at each probe. The probes accommodated a channel for a single-mode optical fibre.

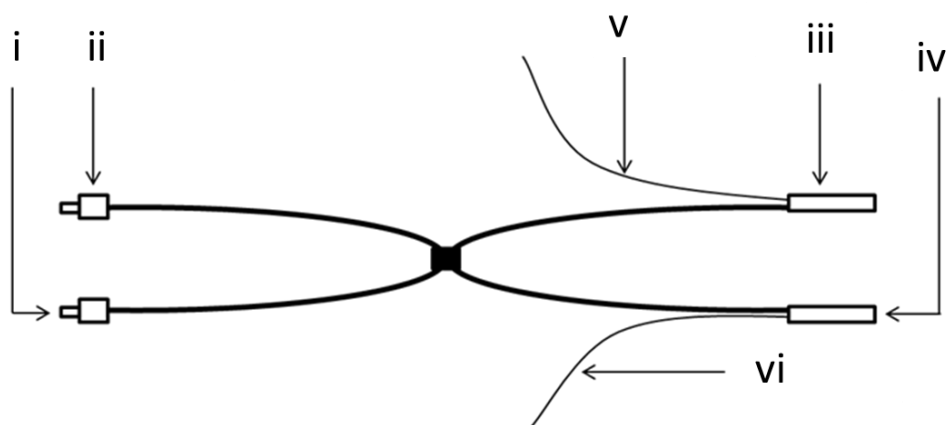


Figure 3.7 Schematic illustration of the FRS/FTIRS probe: (i) SMA connector to the FTIRS light source, (ii) SMA connector to the FTIRS detector, (iii) sample probe, (iv) reference probe, (v) cleaved optical fibre (FRS) housed in the sample probe, (vi) cleaved fibre optical fibre (FRS) housed in the reference probe.

A photograph of the FRS/FTIRS probe and the polished end face of the probe assembly are shown in Figure 3.8 (a) and (b), respectively. The fibre ends which were not potted into SMA connectors were housed in glass capillaries, item (i) (TUG-100-300, Breckland Scientific, UK), which had outer and inner diameters of 5.6 and 4 mm, respectively. Item (ii) shows randomly distributed low-OH fibres, which were potted inside half of the capillary using an epoxy adhesive, item (iii) (product code DP810, 3M, USA). On the opposing side, two capillaries, item (iv), were bonded together using LY3505/XB3403 and attached to the interior of item (i) using item (iii). The larger capillary (product code CV1518-B100, CM Scientific, UK) of item (iv) had inner and outer diameters of 1.5 and 1.8 mm, respectively. The capillary (product code CV7087-100, CM Scientific, UK) located within had inner and outer diameters of 0.7 and 0.87 mm, respectively. The probe faces were polished using conventional optical procedures. A 6 mm orifice was drilled into the platinum lid of the differential scanning calorimeter, item (v) (part number 0419-0299, Perkin

Elmer, USA), and attached to the end of the probes using silicone rubber, item (vi) (product code 692-542, RS Components, UK).

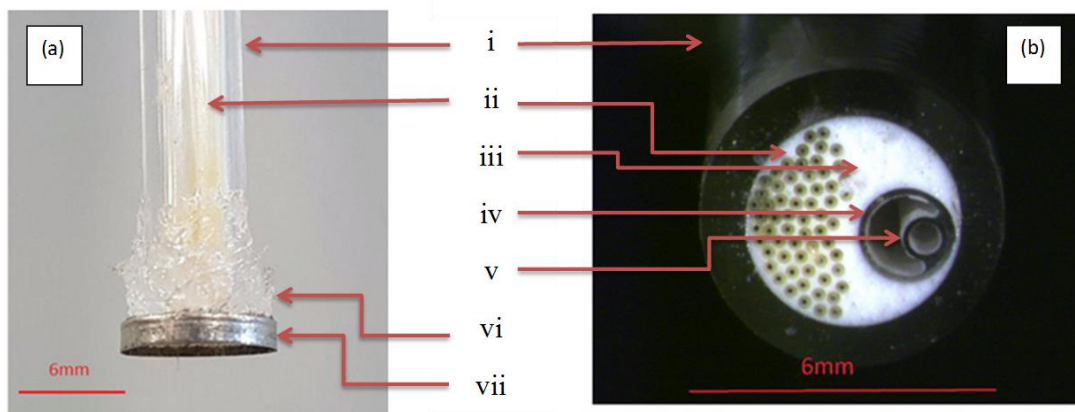


Figure 3.8 (a) Photograph and (b) schematic illustration of the FRS/FTIR probe: (i) glass capillary, (ii) bundle of 60 low-OH optical fibres, (iii) epoxy adhesive, (iv) capillaries for FRS deployment, (v) silicone rubber, (vi) platinum lid containing a 6 mm orifice.

### 3.7.2 Modification of the Differential Scanning Calorimeter Pans to Enable Simultaneous Fourier Transform Infrared Spectroscopy/Fresnel Reflection Sensor

The DSC pan was 'modified' to produce reflective and non-reflective surfaces. This was necessary because the FTIRS probe and the FRS required the base of the pan to be reflective and non-reflective, respectively. This was achieved by cutting a conventional differential scanning calorimeter lid (part number 02190041, Perkin Elmer, USA), and placing it upon a conventional aluminium DSC pan to cover approximately half of the pan. Graphite spray (product code 87-0695, Kontakt-Chemie, Germany) was used to deposit a thin, non-reflective coating on half of the top-face of the DSC pan. The increased mass due to the thin graphite layer could



not be detected by using a five-decimal place analytical balance (Ohaus, Analytical Plus, USA). The graphite layer prevented reflection from the base of the DSC pan. The uncoated section retained the original reflective surface; this was suitable for FTIRS transmission/reflection spectroscopy. Figure 3.9 shows the appearance of an aluminium DSC pan with reflective and non-reflective sections.

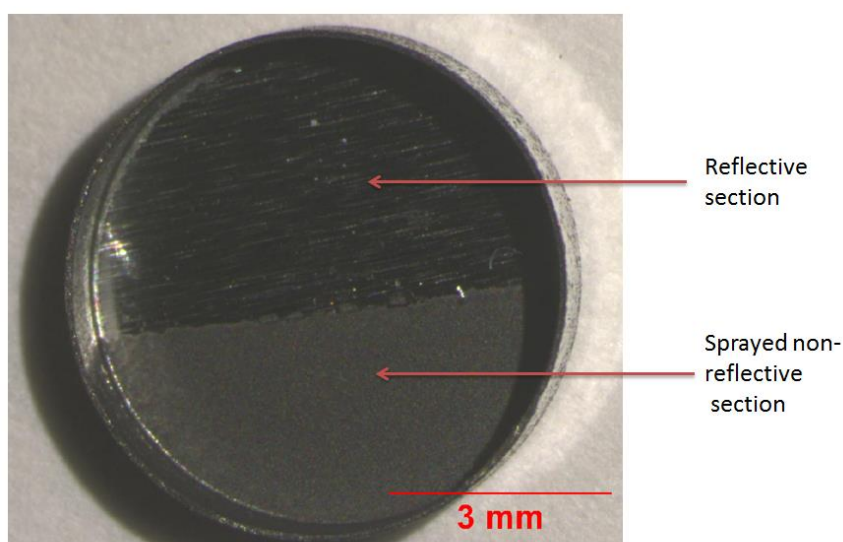


Figure 3.9 Image of a modified aluminium DSC pan showing the reflective and non-reflective sections.

### **3.7.3 Simultaneous Fourier Transform Infrared Spectroscopy and Fresnel Reflection Sensor-based Monitoring of the Cross-Linking of LY3505/XB3403**

The capability of the FTIR/FRS probe to track cross-linking when using a modified DSC pan was investigated. A thermal insulation brick was sectioned to the dimensions illustrated in Figure 3.10. A channel was drilled into each segment to produce an 8 mm orifice, when the two sections were butted together. A micrometer translation stage, item (ii), was attached to the top of the brick. A grub screw, item (iii),

was used to secure the probe to the stage. The probe was lowered towards the insulation brick, item (iv), and through the orifice, item (v). The probe was aligned with the FTIRS and FRS sections of the probe, approximately 3.5 mm above the reflective and non-reflective sections of the pan, respectively. The assembly was placed on a hot-plate (part number CB162, Stuart, UK) with a type-K thermocouple, item (vi), and positioned under the brick in close proximity to the orifice. Approximately 20 mg of LY3505/XB3403 resin system was prepared as described in Section 3.2.1 and dispensed into a modified DSC pan. The hot-plate was preheated to the desired isothermal cross-linking temperature and the resin system in the DSC pan was inserted into the orifice. The resin system was processed at 50, 60 and 70 °C.

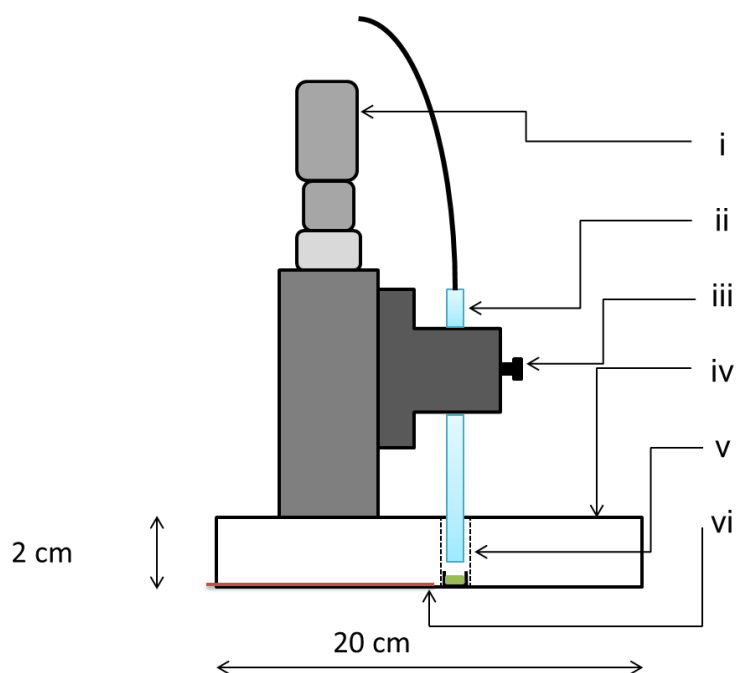


Figure 3.10 Schematic illustration of the translation stage used to lower the FRS/FTIRS probe into the orifice of an insulation brick and towards a partly reflective pan containing the LY3505/XB3403 resin system. The assembly was placed onto a hot-plate: (i) Micrometer for vertical translation, (ii) FRS/FTIRS probe, (iii) grub screw, (iv) insulation brick, (v) orifice in the insulation brick, and (vi) thermocouple.

### **3.7.4 Simultaneous Differential Scanning Calorimetry /Fourier Transform Infrared Spectroscopy and Fresnel Reflection-based Monitoring of the Cross-linking of the LY3505/XB3403 Resin System**

The FTIRS/FRS probe illustrated in Figure 3.8 was introduced into the differential scanning calorimeter (Diamond DSC, Perkin Elmer, USA) using the custom-built top-cover. The custom-built cover, described in Section 3.5 was modified by widening the orifice from 3.6 to 8.5 mm to accommodate the FTIRS/FRS probe; a schematic illustration and a photograph of the assembly is shown in Figure 3.11. The coded components are as follows: Item (i) is a micrometer translation stage (part number PT1, Thorlabs, USA), which was attached to the top-cover to secure the probes in place using grub screws. Items (ii) and (iii) denoted fibre bundles for the sample and reference probe-ends, respectively. The ends of the bundles were housed in glass capillaries, item (iv), and lowered through 8.5 mm orifices above the sample and reference chambers via the translation stages. The platinum lids, attached to the ends of the probes, were inserted into the sample and reference chambers of the differential scanning calorimeter. The probes were aligned to the FTIRS sensor and FRS to be above the reflective and non-reflective surfaces, respectively. A 2.9 mm gap between the glass capillaries and the top-cover was potted using an epoxy adhesive and stainless-steel ferrules to improve insulation. Item (vi) is the fixture that secured the translation stage to the top-cover of the differential scanning calorimeter. The underside of the top-cover was insulated using an appropriately shaped sheet of calcium–magnesium silicate (product code 724-8909, RS Components, UK). The differential scanning calorimeter was calibrated with the FTIRS and FRS engaged using a pure indium reference standard (product code 6.223.5, Netzsch, Germany).

The sample was heated from 30 °C to beyond its melting temperature at 10 K/minute and then cooled to 30 °C.

Approximately 20 mg of the LY3505/XB3403 resin system was dispensed into the centre of a modified DSC pan. The pan was positioned in the centre of the DSC chamber at 30 °C. The orientation, with respect to the reflective and non-reflective sections, was kept constant in each experiment. The sample was permitted to equilibrate for 1 minute prior to heating to the desired isothermal cross-linking temperature at 40 K/minute. The differential scanning calorimeter was heated to the isothermal cross-linking temperatures and maintained for 10 hours. The resin system was processed isothermally at 50, 60 and 70 °C. Upon completion, the temperature was reduced to 30 °C at 40 K/min. The calorimeter was programmed for three successive heating ramps from 30 to 100 °C at 10 K/min to enable the  $T_g$  to be determined.

A FTIR background scan was performed at the isothermal cross-linking temperature, with the probes positioned appropriately over the modified DSC pans. Spectra were recorded every 5 minutes at a resolution of 4  $\text{cm}^{-1}$  with 64 scans. The first spectra were recorded upon initiation of the cross-linking schedule of the differential scanning calorimeter.

A fresh FRS was prepared for each experiment, as described in Section 3.4.1. The cleaved optical fibre protruded approximately 5 mm from the probe-end and was secured using silicone rubber. A 'dummy' sensor was also placed in the reference probe. The FRS data was synchronised with the DSC and FTIRS data by momentarily disengaging the light source upon initiation of the cross-linking

schedule by the calorimeter. This created a spike in the FRS signal enabling it to be synchronised to the other two instruments.

Approximately 20 mg of the LY3505/XB3403 resin system was prepared as described in Section 3.2.1 and this was transferred to the modified DSC pans. The resin system was processed in the calorimeter at 50, 60 and 70 °C for over ten hours.

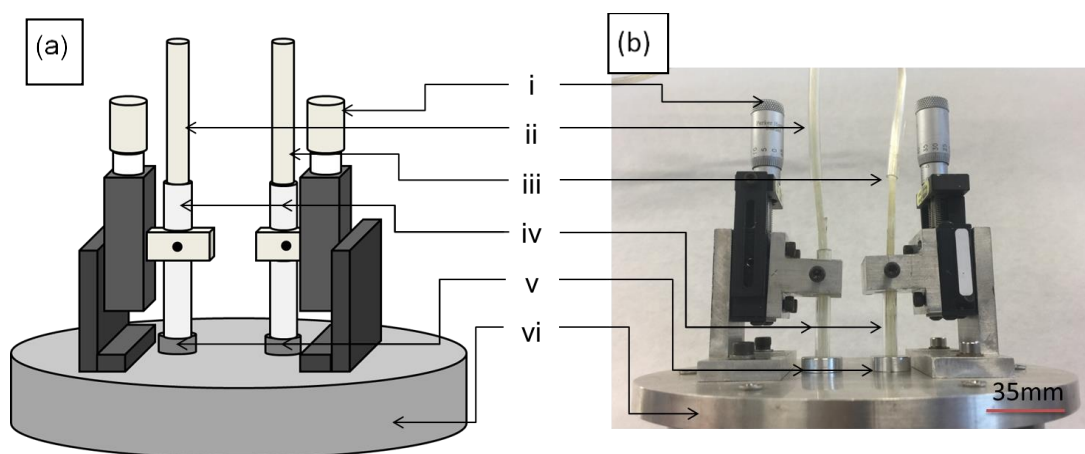


Figure 3.11 (a) Schematic illustration and (b) photograph of the key components of the custom-modified Perkin-Elmer Diamond differential scanning calorimeter top cover: (i) micrometer translation stage, (ii) sample fibre bundle, (iii) reference fibre bundle, (iv) glass capillaries, (v) steel ferrules, (vi) custom-made Diamond differential scanning calorimeter top-lid.

## **4. RESULTS, ANALYSIS AND DISCUSSION: MONITORING CROSS-LINKING USING CONVENTIONAL ANALYTICAL TECHNIQUES**

This chapter reports on the results obtained on the cross-linking of an epoxy/amine resin system (LY3505/XB3403) using conventional analytical techniques. Section 4.1 presents analyses of the results obtained from differential scanning calorimetry (DSC), whereby the calibration of the equipment is first demonstrated, followed by the acquisition of cross-linking data obtained during isothermal and non-isothermal cross-linking. The degree of cross-linking was calculated at various temperatures and the glass transition temperature, following the isothermal cross-linking, was also determined. The cross-linking kinetics were calculated using the isothermal cross-linking data.

Section 4.2 presents the data obtained from transmission Fourier transform infrared spectroscopy (FTIRS). The temperature profile within the cuvette used to contain the resin system was mapped and the absorbance peaks associated with the resin system were identified. The degree of cure or cross-linking was calculated, and an autocatalytic model was applied to investigate the experimentally derived data.

Section 4.3 presents an analysis of the comparison between the DSC and FTIRS data.

Section 4.4 presents rheological data for the resin system. Here, the samples were cross-linked at specified temperatures to determine the temperature/gelation time relationship. The dependence of the gelation time was then investigated and correlated with the DSC and FTIRS results.

## 4.1 Differential Scanning Calorimetry

### 4.1.1 Calibration of the Differential Scanning Calorimeter

The DSC experiments were conducted using a conventional PerkinElmer Diamond DSC. Calibration of the equipment was undertaken using approximately 5 mg of high-purity indium and tin samples in open aluminium. Figure 4.1 shows a typical differential calorimeter trace or thermogram for an indium sample where it was heated at 10 K/minute. The data for the enthalpy of fusion and onset of melt that was measured using the Pyris™ software supplied with the equipment were within the recommended range (Gmelin, 1995). The DSC pan type (aluminium) and heating rate (10 K/minute) were used for the majority of the cross-linking experiments undertaken in the current study. The y-axis on the DSC thermograms were set to indicate the endothermic and exothermic events as pointing “up” and “down”, respectively.

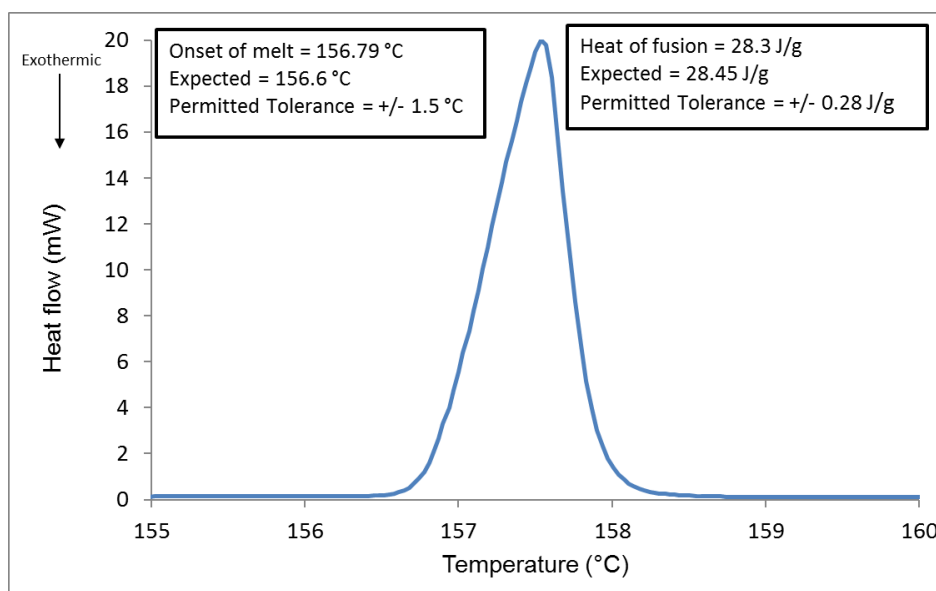


Figure 4.1 DSC calibration trace for indium where the sample was heated at 10 K/minute in air using and open-top aluminium pan. The expected data was obtained from the reference Groenewoud (2001). The tolerance represents the acceptable spread of the data obtained from the paper by Gmelin (1995).

#### 4.1.2 Non-isothermal Cross-linking in the Differential Scanning Calorimetry

The effect of the heating rate on the enthalpy of cross-linking ( $\Delta H_{\text{Total}}$ ) was carried out by programming the DSC to perform ramped or dynamic heating at 1, 10, 20 and 40 K/minute. Calibration was performed using indium at 10 K/minute as shown in Figure 4.1. The thermograms in Figure 4.2 (a) and values in Table 4.1 demonstrate a large exothermic reaction and enthalpy respectively that varied in magnitude with heating rate. At each heating rate, the reaction progressed to an apparent termination which was observed as a horizontal section of the trace. There is no consensus in the literature on the method for constructing the baseline to calculate  $\Delta H_{\text{Total}}$ . The various methods proposed in the literature were discussed in Section 2.3.1.2. With reference to the epoxy/amine resin system used in the current study (LY3505/XB3403) the linear baseline was used between the apparent start and end points of the reaction. A schematic illustration of the baseline construction method is shown in Figure 4.2 (b) for the sample that was heated at 10 K/minute.

Increasing the heating rate led to an increase in the magnitude of the enthalpy of cross-linking and the onset time. This is in agreement with the findings of Richardson and Savill (1975), Richardson (1992), Roşu *et al.* (2002), Kim *et al.* (2012) and Hardis *et al.* (2013) for epoxy systems. Wunderlich (1981) explained that such temperature shifts are due to an increase in the thermal lag between the instrument and the response of the sample. This may have been exacerbated in this case by the use of open-top sample pans and the relatively low thermal conductivity of the resin. During TGA experiments, Dumitrescu (2003a) reported mass losses of up to 2.2% for LY3505/XB3403 during ramped experiments from 30 to 250 °C. Therefore, possible



volatilisation of the epoxy and amine may have contributed to the reduced enthalpy measured at 40 K/min in Table 4.1.

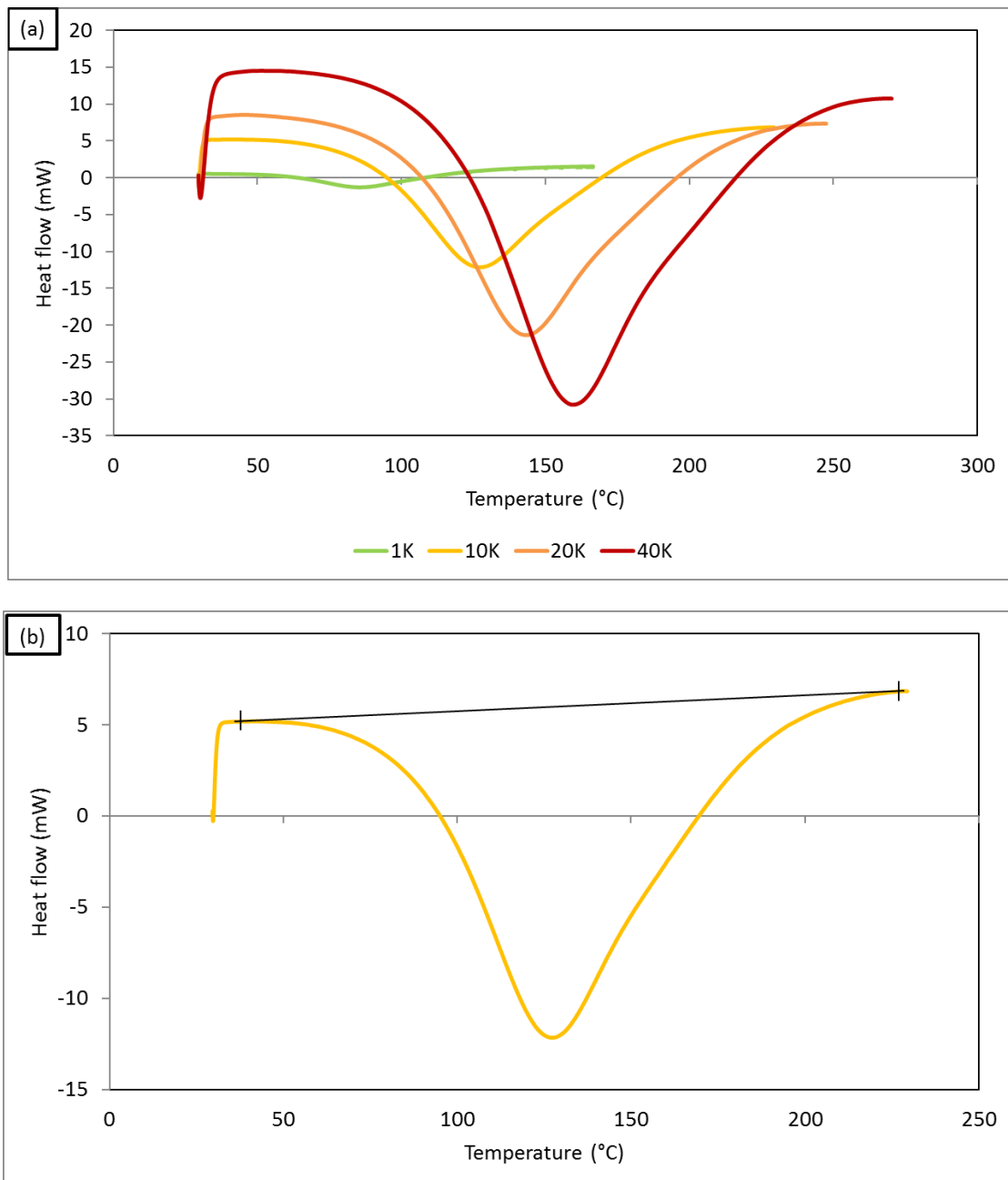


Figure 4.2 (a) Thermograms for the LY3505/XB3403 resin system at specified heating rates; and (b) Baseline construction method for integration.

Table 4.1 Summary of the heating rates and the corresponding enthalpy of cross-linking and peak exothermic temperatures for the LY3505/XB3403 resin system.

Heating Rate (K/minute)	$\Delta H$ (J g <sup>-1</sup> )	Peak Exothermic Temperature
1	320 ±6	86 °C
10	413 ±4	123 °C
20	432 ±6	144 °C
40	417 ±5	162 °C
<b>Average</b>	<b>395.5</b>	NA

Bilyeu *et al.* (2000), Erdoğan *et al.* (2008) and Hardis *et al.* (2013), reported  $\Delta H_{\text{Total}}$  values using a single heating rate, although this can introduce misinterpretation of the data as  $\Delta H$  changes with heating rate. In the current study, it was decided to use the average value over multiple heating rates, as recommended by, Höhne *et al.* (1996) and Menczel and Prime (2009) but also previously demonstrated by Yilgör *et al.* (1981) and Karkanis *et al.* (1996).

#### 4.1.3 Isothermal Cross-linking in the Differential Scanning Calorimetry

The mixed and degassed resin samples were introduced into the DSC chamber at room temperature and heated to the desired isothermal temperature at 40 K/minute; this was chosen in preference to dropping a sample into a preheated chamber, so as to increase experimental reproducibility (Turi, 1997; Cheng, 2002). Figure 4.3 depicts this 'heating up' period and a subsequent period of instability whilst thermal

equilibrium was being established. With reference to Figure 4.3 the following effects are observed:

- (i) Initiation of ramped heating.
- (ii) Heat up period to the desired isothermal cross-linking temperature. A positive gradient indicates power is required to heat the sample mass in the sample compartment.
- (iii) A change in the heating regime from ramped to isothermal.

It has been found previously that the period of thermal instability dominated the data in the first minute of the cross-linking schedule (Fava, 1968; Barton, 1983). In their work, a horizontal baseline was drawn from the end of the cross-linking process in order to eliminate the initial heat-up and non-isothermal portion of the data. A linear baseline construction was also used in this study. Data acquired before the intersection with the baseline was deleted. Previously, Barton (1983) had suggested the subtraction of a 'true' baseline taken upon the fully cured sample, although the use of a linear baseline has since been adopted as the standard procedure (ASTM-D3418, 2015).

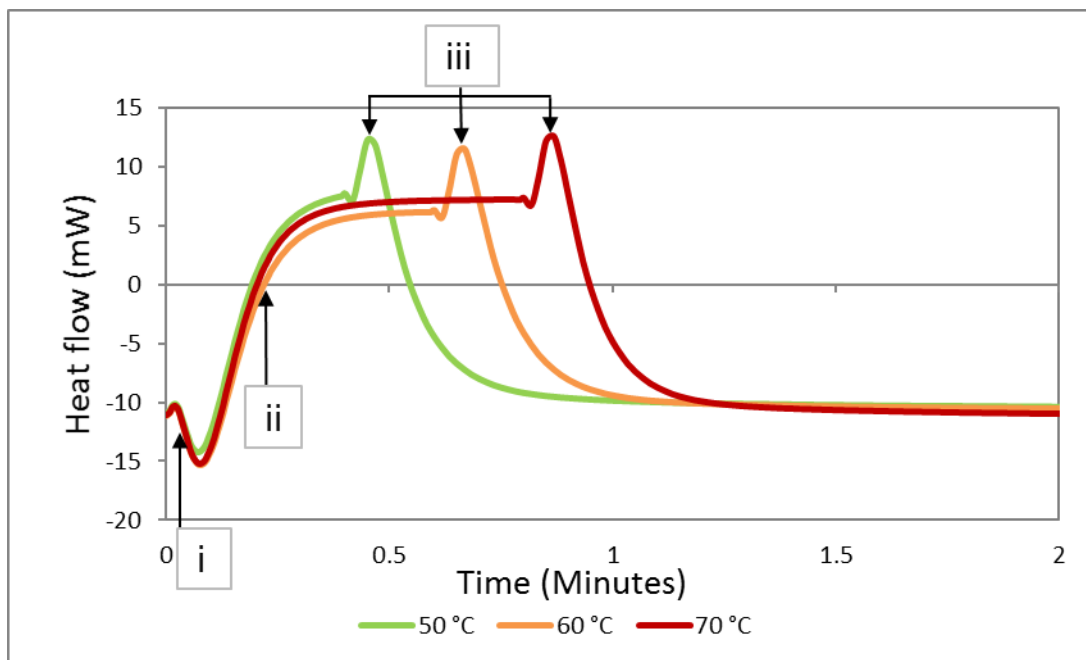


Figure 4.3 Heating up and stabilisation periods from 30 °C to the desired isothermal cross-linking temperature when the samples were heated at 40 K/minute.

The thermograms from the isothermal cross-linking of the LY3505/XB3403 resin system at 50, 60 and 70 °C for 600 minutes are shown in Figure 4.4(a) and a set of repeat experiments are presented in Figure 4.4(b). With reference to Figure 4.4(a), the horizontal baseline construction method is indicated, as well as the segmentation of exotherm to calculate the magnitude of the exotherm for the 70 °C dataset. A summary of the relevant data from Figure 4.4 is shown in Table 4.2. The exothermic reactions occur at each temperature and reach a peak approximately mid-way. Towards the end of the cross-linking process, the magnitude of the exotherm diminished. This is generally attributed to the reaction kinetics changing from 'chemical controlled' to 'diffusion controlled'. Upon increasing the isothermal cross-linking temperature, the magnitude of the exotherm was higher and it peaked earlier. These observations agree with that reported by Pandita *et al.* (2012) for the same resin system.

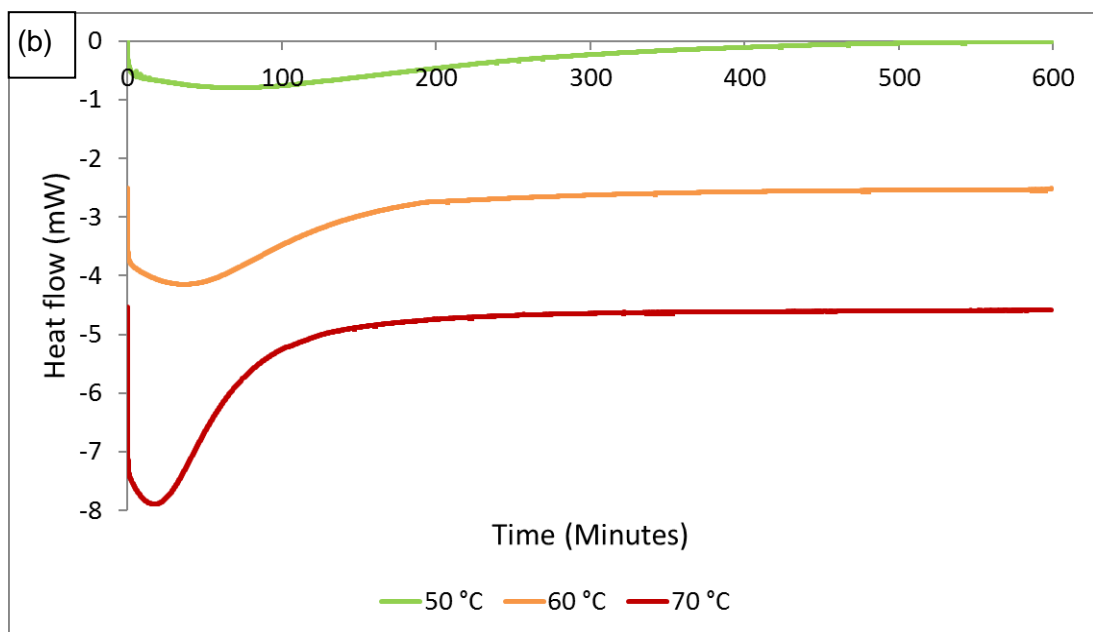
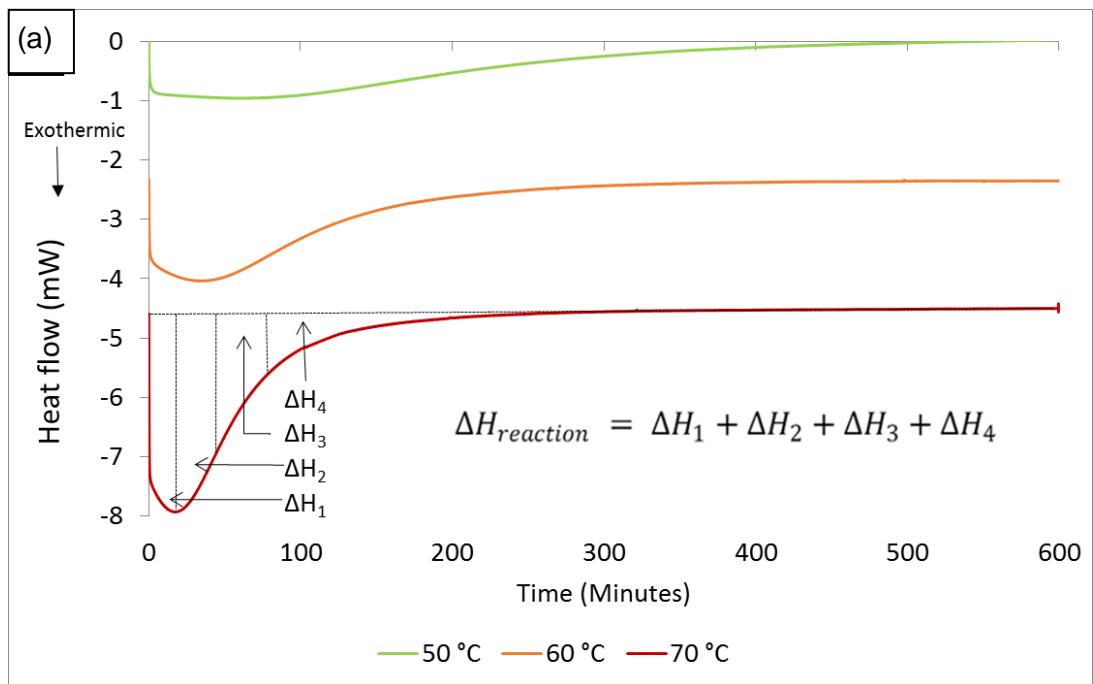


Figure 4.4 Isothermal cross-linking data for the LY3505/XB3403 resin system for isothermal experiments at 50, 60 and 70 °C. The method for constructing the baseline and calculating the enthalpy of cross-linking is also presented:

(a) Experiment 1; and (b) Experiment 2.

Table 4.2 Values obtained from DSC experiments during isothermal and non-isothermal scans.

Isothermal Cross-linking Temperature	$\Delta H$ ( $Jg^{-1}$ )	Peak Exotherm	Degree of Conversion at 600 minutes	Glass Transition Temperatures ( $^{\circ}C$ at 10 K/minute heating rate)		
				$T_{g1}$	$T_{g2}$	$T_{g3}$
50 $^{\circ}C$ - Experiment 1	335	58 mins	84%	56.3	68.2	72.2
50 $^{\circ}C$ - Experiment 2	317	74 mins	80%	55.2	67.9	72.7
60 $^{\circ}C$ - Experiment 1	337	28 mins	85%	67.4	72.5	73.9
60 $^{\circ}C$ - Experiment 2	358	33 mins	90%	67.6	71.7	74.5
70 $^{\circ}C$ - Experiment 1	379	16 mins	95%	73.6	75.3	75.2
70 $^{\circ}C$ - Experiment 2	371	15 mins	94%	74	75.2	75.7

The cumulative heat flow was determined by integrating the area in the thermogram as illustrated in Figure 4.4(a). Despite the reaction appearing to reach completion in Figure 4.4, the enthalpy values obtained indicate “incomplete” cross-linking, based on the data presented in Table 4.2. One or more of the following explanations may be applicable.

- (i) It is believed that the reduction in segmental flexibility, associated with the vitrification process, changes the reaction kinetics from chemical to diffusion-controlled; this is known to severely reduce the reaction rate and hence the heat evolved (Gillham, 1986; Van Assche *et al.*, 1997, Turi, 1997). In the current research, the magnitude of the heat liberated appears to fall below the 0.2  $\mu W$  sensitivity of the Diamond DSC (Perkin-Elmer, 2003), making it appear as though the reaction had completed.

- (ii) Vitrification occurred at lower degrees of conversion at reduced isothermal temperatures, which explained the lower enthalpy values.
- (iii) Statistical scatter of the data of up to 5% is observed for the  $\Delta H$  data in Table 4.2. This could be explained by several factors:
  - (a) Removal of approximately 0.25% of enthalpy contribution during the 'heat up' period displayed in Figure 4.3.
  - (b) Despite degassing and visual inspection of the resin, some air bubbles or dissolved gases may have remained entrapped in the resin.
  - (c) Intrinsic scatter in the resin system whose formulations have a tolerance in their concentration.

The enthalpy values were used to determine the degree of cure using the previously mentioned Equation 2.1, as shown below.  $\Delta H_{\text{Total}}$  was taken as the mean average of the non-isothermal scans listed in Table 4.2.

$$\alpha = \frac{\Delta H_t}{\Delta H_{\text{total}}} \dots \dots \dots \text{Equation 2.1}$$

where

$\alpha$  = extent of reaction,

$\Delta H_t$  = enthalpy at time,  $t$ ,

$\Delta H_{\text{total}}$  = total enthalpy of reaction = 395 Jg<sup>-1</sup>.

An increased degree of cure can be observed for samples cross-linked at increased temperatures in Figure 4.5. The effects of vitrification, where the reaction mechanism changes from chemical controlled to diffusion controlled can be seen at each temperature designated by the 'levelling-off' of the conversion.

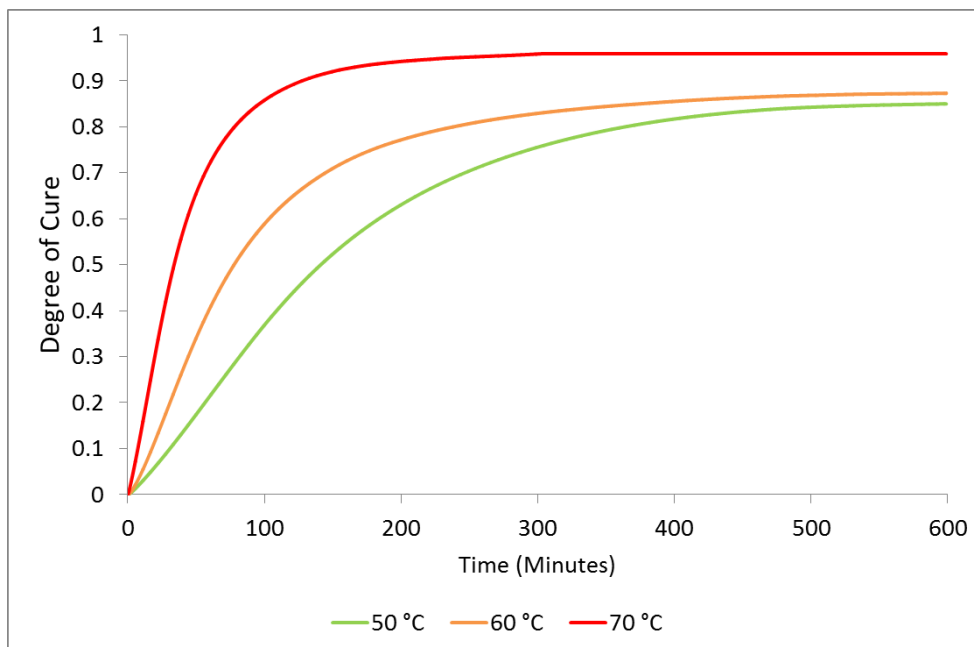


Figure 4.5 Degree of cross-linking under isothermal conditions at 50, 60 and 70 °C for the LY3505/XB3403 resin system.

The  $\Delta H$  values shown in Table 4.3 are comparable to those reported by (Dumitrescu, 2003b) for the same resin system. Discrepancies in the data may be attributed to variations in experimental methods:

- (i) Dumitrescu (2003b) used 80 K/minute to reach the desired isothermal temperature as opposed to the 40 K/minute used in this study.
- (ii) Their isothermal cure lasted for 400 minutes whereas in this work it was 600 minutes.
- (iii) Dumitrescu (2003b) applied a smoothening function to the data due to a large degree of noise. This may have introduced a bias in the analysis.
- (iv) In the previous work, 5 mg sample masses were used and in this study 20 mg were used.



Table 4.3 Summary of relevant cure data for the LY3505/XB3403 resin system (Dumitrescu, 2003b and current work).

<b>Author</b>	<b>Isothermal Cure</b>	<b>Degree of Conversion</b>	<b><math>\Delta H</math> (Jg<sup>-1</sup>)</b>
Dumitrescu, 2003b	10 Hours at 60 °C	78%	344 (+/- 15)
Dumitrescu, 2003b	10 Hours at 70 °C	89%	397 (+/- 22)
Current work	10 Hours at 60 °C	88%	348 (+/- 11)
Current work	10 Hours at 70 °C	95%	375 (+/- 4)

Figure 4.6 shows the rate of cure as a function of the degree of cure. In each case, the peak of the reaction was observed at approximately 20% conversion and confirmed the apparent autocatalytic nature of the reaction. As illustrated in Figure 2.2, the production of the hydroxyl group during the formation of the secondary amine appeared to cause the reaction rate to increase. Pandita *et al.* (2012) also reported the peak reaction after approximately 20% conversion for the resin system using DSC and FTIRS analyses.

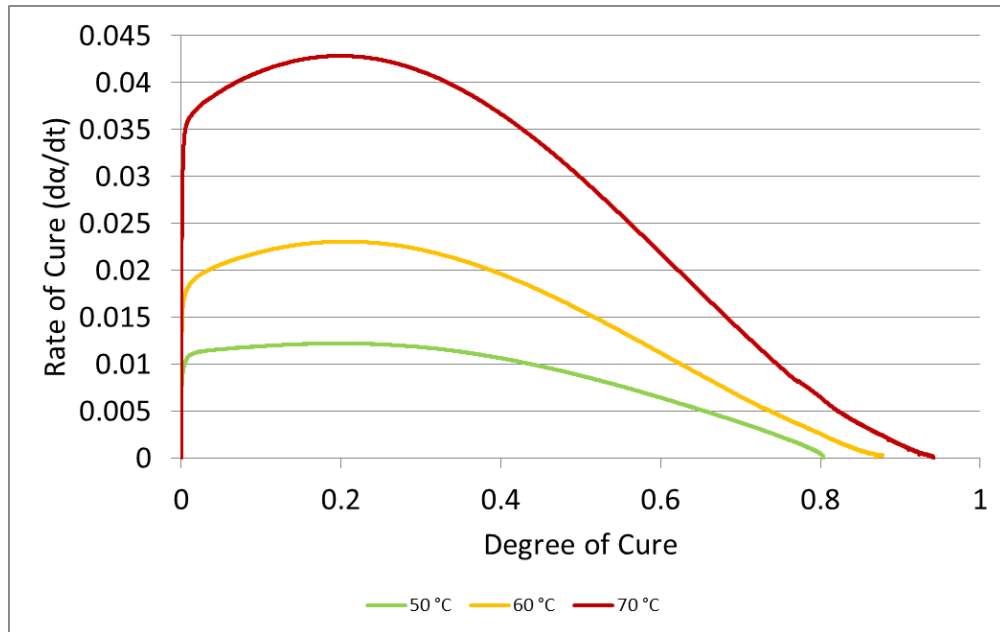


Figure 4.6 Rate of reaction of LY3505/XB3403 as a function of the rate of cure for isothermal processing at 50, 60 and 70 °C.

#### 4.1.4 Ramped Heating In the Differential Scanning Calorimeter

Following isothermal cross-linking, ramped heating from 30 to 150 °C at 10 K/minute were undertaken to determine the glass transition temperature. These experiments were conducted in accordance with ASTM-E1356, 2014, as described in Section 2.3.1.3, Chapter 2. The temperature range used in this work was chosen as heating the sample beyond 150 °C caused discolouration. Gillham (1986), Turi (1997) and Höhne *et al.* (2013) report that the glass transition increases with cross-linking temperature and this correlates with the results presented in Table 4.2 and Figures 4.7 (a) and (b). The presence of post-processing was apparent due to the increasing glass transition temperature after each ramped heating (subsequent to an isothermal cross-linking).

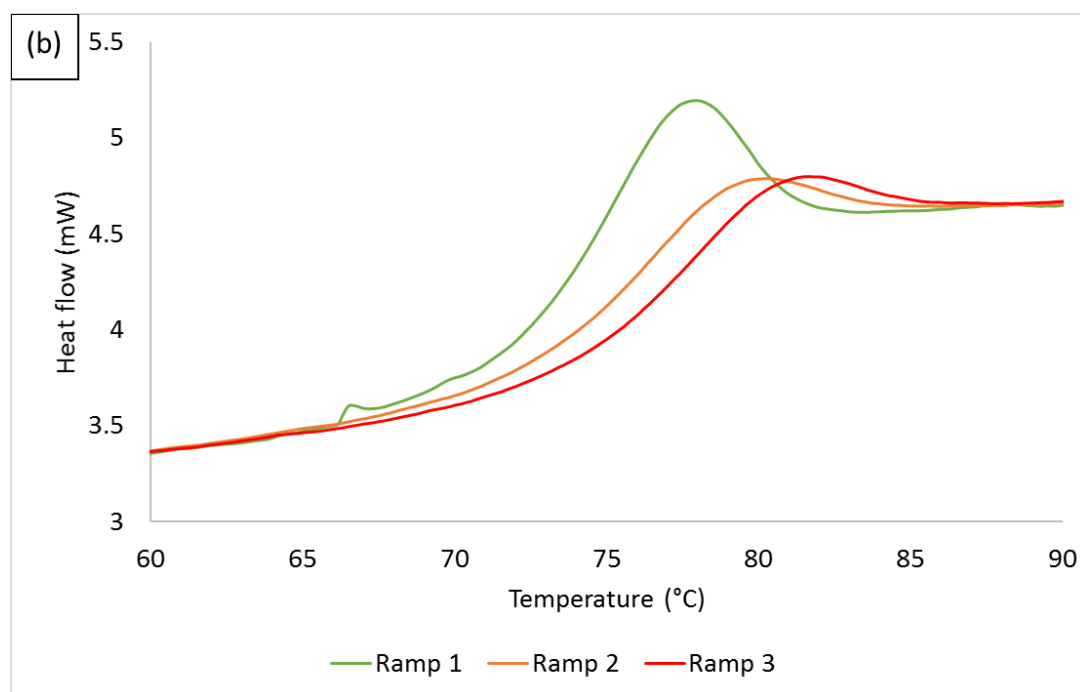
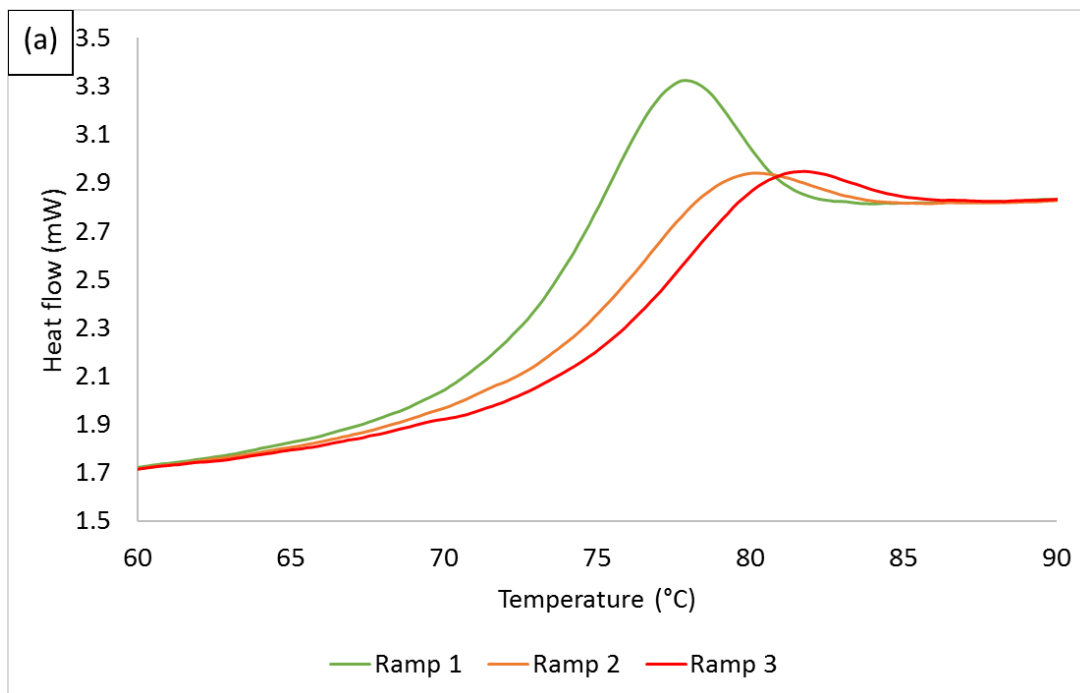


Figure 4.7 Expanded view of the glass transition region for the LY3505/XB3403 resin system that was initially cross-linked isothermally at 70 °C for 600 minutes followed by three consecutive ramped heating at 10 K/minute:  
 (a) Experiment 1; and (b) Experiment 2.

The first heating ramp revealed a glass transition temperature larger than the isothermal cross-linking temperatures, further indicating that vitrification had previously occurred (Gillham, 1986). It has been suggested that upon exceeding the glass transition temperature, de-vitrification can occur allowing the cure mechanism to revert back to a chemically controlled process and enable a significantly higher rate of reaction (Prime, 1981; Van Assche *et al.*, 1997). The extent of the post-cross-linking during the ramped heating in the DSC was revealed by the increase in the glass transition during subsequent scans, as shown in Figures 4.7.

The impact of undercooling, below an amorphous systems  $T_g$  affects enthalpic relaxation and this outcome was discussed in Section 2.3.1.3, Chapter 2. The magnitude of enthalpic relaxation increases with undercooling time and can be observed as an endothermic event superimposed on the  $T_g$  during a subsequent heating ramp. This has been previously reported for both thermoplastic (Kemish and Hay, 1985) and thermoset (Montserrat, 2000) materials. In the current study, the long cure times of ten hours appeared to have facilitated enthalpic relaxation, as evidenced by the endothermic event in the first ramp of Figure 4.7. The standard extrapolated baseline method, ASTM-E1356 (2014), was used to calculate the glass transition temperature.

Table 4.2 and Figure 4.7 show that the glass transition temperature increased during the second heating ramp for each experiment, due to the residual cross-linking during the first heating ramp. De-vitrification is likely to have occurred during the first ramp, upon exceeding the glass transition temperature; thus, changing the reaction from diffusion controlled to chemical controlled and allowing for a significantly increased rate of cross-linking. The increased glass transition temperatures during the second ramp were a result of the residual cross-linking.

Figure 4.4 indicates that the cross-linking reaction had reached completion at 70 °C due to the horizontal baseline at the end of cross-linking. However, the increasing glass transition temperatures shown in Figure 4.7 revealed that cross-linking had not completed. The effect of vitrification on reducing the heat evolved appeared to have exceeded the sensitivity of the DSC. Difficulties in detecting this minor heat evolution was also observed by Dumitrescu (2003a) and Stark (2013), which was discussed as a limitation of DSC-based cure monitoring in Section 4.1.3.

The third DSC heating cycle showed a convergence of the glass transition temperatures to approximately 74.5 ±1 °C for the samples cross-linked at 60 and 70 °C, indicating that residual cross-linking had been completed during the previous heat ramps. The glass transition temperatures were comparable with those reported on the same resin system, which are presented in Table 4.3.

#### 4.1.5 Modelling the Cross-linking Kinetics of the LY3505/XB3403 Resin System

The phenomenological model described by Equation 2.2, Chapter 2, was used in the current study to investigate the cross-linking kinetics of the LY3505/XB3403 resin system using data generated via the DSC. The integral of Equation 2.12 when  $m + n = 2$  gives:

$$t = \frac{1}{k} \frac{1}{n-1} \left( \frac{\alpha}{1-\alpha} \right)^{n-1} \dots\dots\dots \text{Equation 4.1}$$

where

$t$  = time (seconds),

$\alpha$  = degree of cure,

$k$  = rate constant,

$m + n$  = reaction orders.

A variety of values for  $m$  and  $n$  have been reported in the literature as summarised in Table 2.5 in Chapter 2. Using the same resin system that was used in the current study, Pandita *et al.* (2012) and Wang *et al.* (2016) reported values of  $m$  and  $n$  as 0.35 and 1.65 respectively and these have been used in the current study. The rate constant was modified in increments of 0.0001 in order to correlate the model with the DSC degree of cross-linking data. Figure 4.8 shows the comparison between the theoretical prediction using Equation 4.1 and experimental data at specified isothermal cross-linking temperatures. The average rate constant was used with the autocatalytic model shown in Figures 4.8 (a) – (c). In accordance with previous research using LY3505/XB3403 by Pandita *et al.* (2012), error bars of 5% were added, to identify whether there was a significant difference between the experimental data and the autocatalytic model.

With reference to Figures 4.8 (a) – (c), up to approximately 80% of cross-linking, a close correlation was observed between the model and the experimental data. Beyond 80% of cross-linking, a discrepancy was present between the data sets, although values remained within the 5% error bars. The results correlated with that previously reported by Montserrat and Cima (1999), Teil *et al.* (2004) and Garschke *et al.* (2013) for an epoxy system where close agreement in the degree of conversion was observed until the later stages of cross-linking. Pandita *et al.* (2012) and Wang *et al.* (2016) reported that close correlation was seen up to 80% conversion for the same resin system used in this study. It was accepted by each of the authors that the effects of vitrification, changing the reaction from 'chemical controlled' to 'diffusion controlled', contributed significantly to the discrepancy.

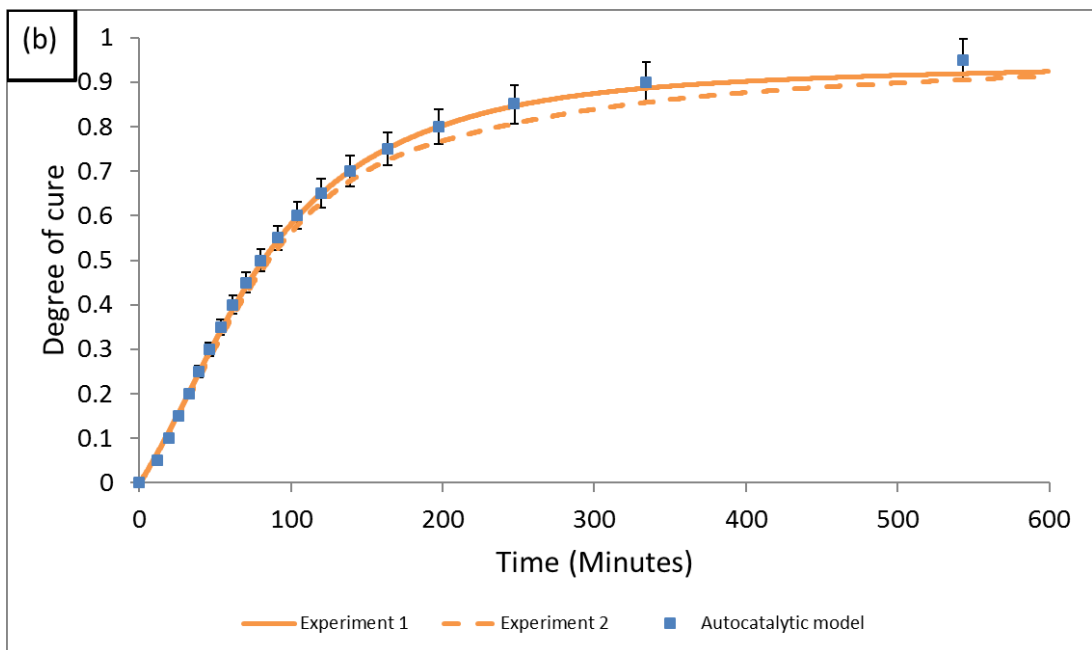
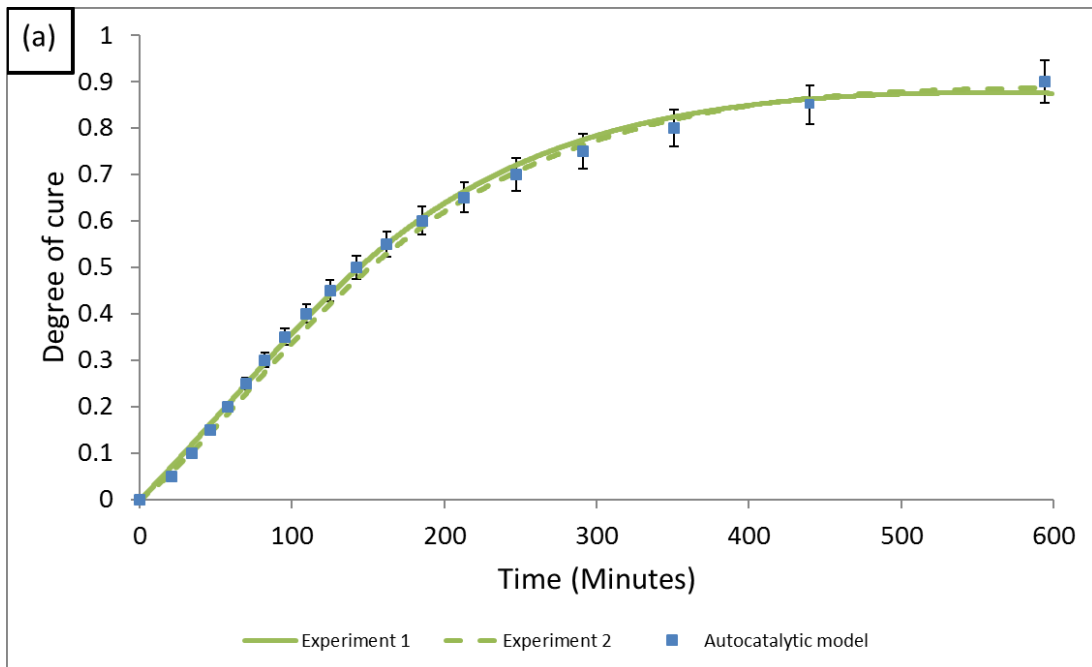


Figure 4.8 Comparison between DSC experimental data and autocatalytic model at:  
 (a) 50 °C; and (b) 60 °C.

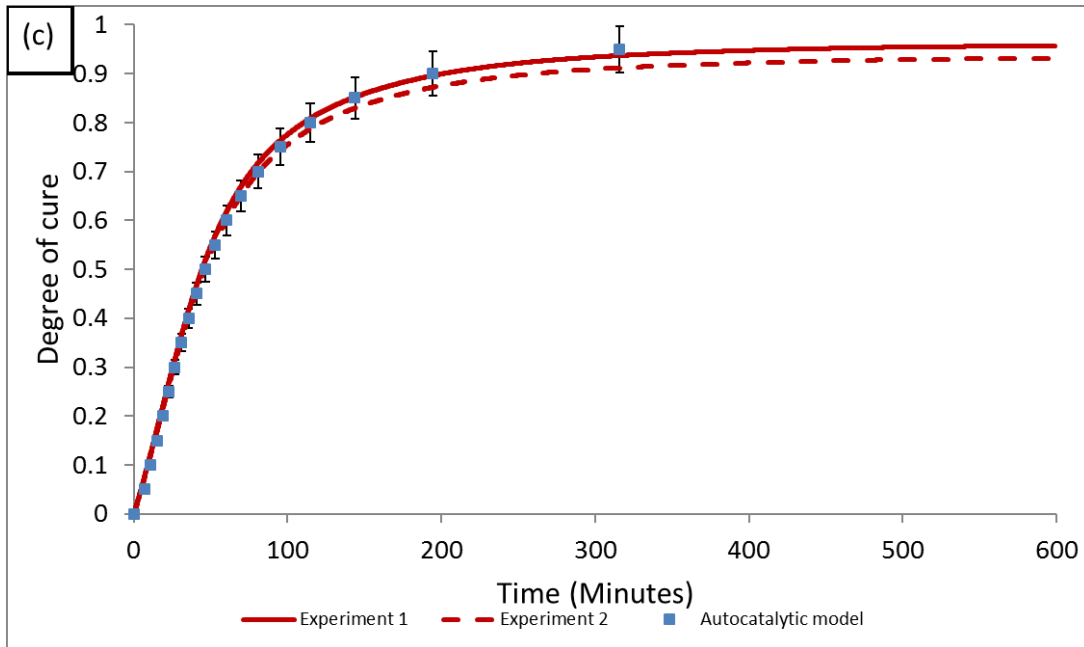


Figure 4.8 (continued) Comparison between DSC experimental data and autocatalytic model at: (c) 70 °C.

The activation energy of the LY3505/XB3403 resin system was determined using Equation 4.2 and plotting the rate constants against the reciprocal of the cross-linking temperature, is shown in Figure 4.10 and presented in Table 4.4. The Arrhenius equation is:

$$k = A \cdot \exp\left(\frac{-E_a}{RT}\right) \dots \dots \dots \text{Equation 4.2 (Pandita et al., 2012)}$$

where

$A$  = pre-exponential constant,

$E_a$  = activation energy,

$R$  = universal gas constant (8.314 J K<sup>-1</sup> mol<sup>-1</sup>),

$T$  = temperature (Kelvin),

$k$  = rate constant (s<sup>-1</sup>).



Equation 4.2 can be re-written as:

$$\ln k = -\frac{E_a}{R} \times \frac{1}{T} + \ln A \dots \dots \dots \text{Equation 4.3}$$

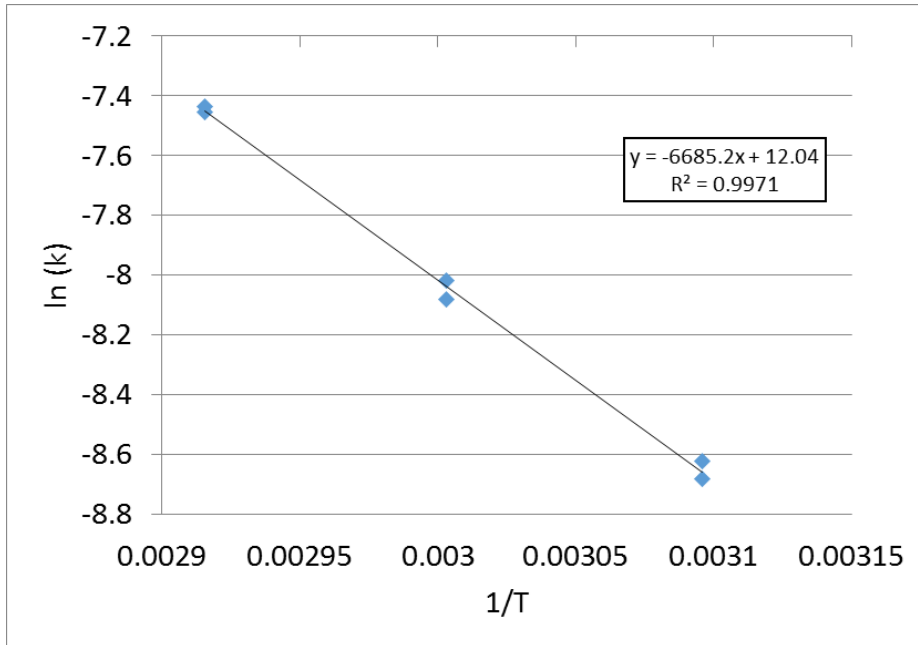


Figure 4.9 Arrhenius plot for the cross-linking of the LY3505/XB3403 resin system.

Table 4.4 Rate constants and activation energy for the LY3505/XB3403 resin system using Equation 4.1 and isothermal data generated using the DSC.

<b>Isothermal Cross-linking</b>	<b>k</b>	<b>ln k</b>	<b>1/T</b>
<b>50 °C - Experiment 1</b>	0.00018	-8.6	0.0031
<b>50 °C - Experiment 2</b>	0.00017	-8.6	0.0031
<b>60 °C - Experiment 1</b>	0.00029	-8.1	0.0030
<b>60 °C - Experiment 2</b>	0.00032	-8.0	0.0030
<b>70 °C - Experiment 1</b>	0.00059	-7.1	0.0029
<b>70 °C - Experiment 2</b>	0.00058	-7.1	0.0029
<b>Activation Energy (kJ mole<sup>-1</sup>)</b>		<b>55.58</b>	

The activation energy of  $55.58 \text{ kJ mole}^{-1}$  obtained from Figure 4.9 is comparable with the reported values of 62.29, 60.82 and  $56.8 \text{ kJ mole}^{-1}$  by Mahendran *et al.* (2009), Pandita *et al.* (2012) and Wang *et al.* (2016).

## **4.2 Fourier Transform Infrared Spectroscopy**

### **4.2.1 Temperature Distribution within the Cuvette**

The cuvette holder used in the current research project contained an 'in-built' Peltier heater which was controlled by an external temperature controller and circulating water. The cuvette holder offered a temperature stability of  $0.01 \text{ }^{\circ}\text{C}$ . The temperature gradient inside a silicone oil filled quartz cuvette was evaluated using an array of thermocouples as shown in Figure 3.3, Chapter 3. Figure 4.10 displays the temperature distribution during step-wise heating from  $20$  to  $70 \text{ }^{\circ}\text{C}$  with a dwell for five minutes at each temperature as a function of (a) time and (b) temperature. Thermocouples 1 and 2 were positioned  $2 \text{ mm}$  from the top of the cuvette and they were separated by  $5 \text{ mm}$ . Thermocouples 3 and 4 were placed in the anticipated trajectory of the transmitted infrared beam during the FTIRS experiments. The temperature measured by thermocouples 3 and 4 were within  $\pm 0.3 \text{ }^{\circ}\text{C}$  of the desired set temperature. Thermocouples 5 and 6 showed a slightly higher temperature than the set value by up to  $1 \text{ }^{\circ}\text{C}$ . The discrepancies of thermocouples 1 and 2 can be explained by:

- (i) The position of the heating elements, as displayed in Figure 3.1, Chapter 3, whereby the elements do not cover the top of the sample.
- (ii) A hole in the insulation material placed inside the lid to allow for thermocouple insertion.

- (iii) The possibility that the thermocouples were not fully immersed in the silicone oil, due to their proximity to the top of the cuvette.

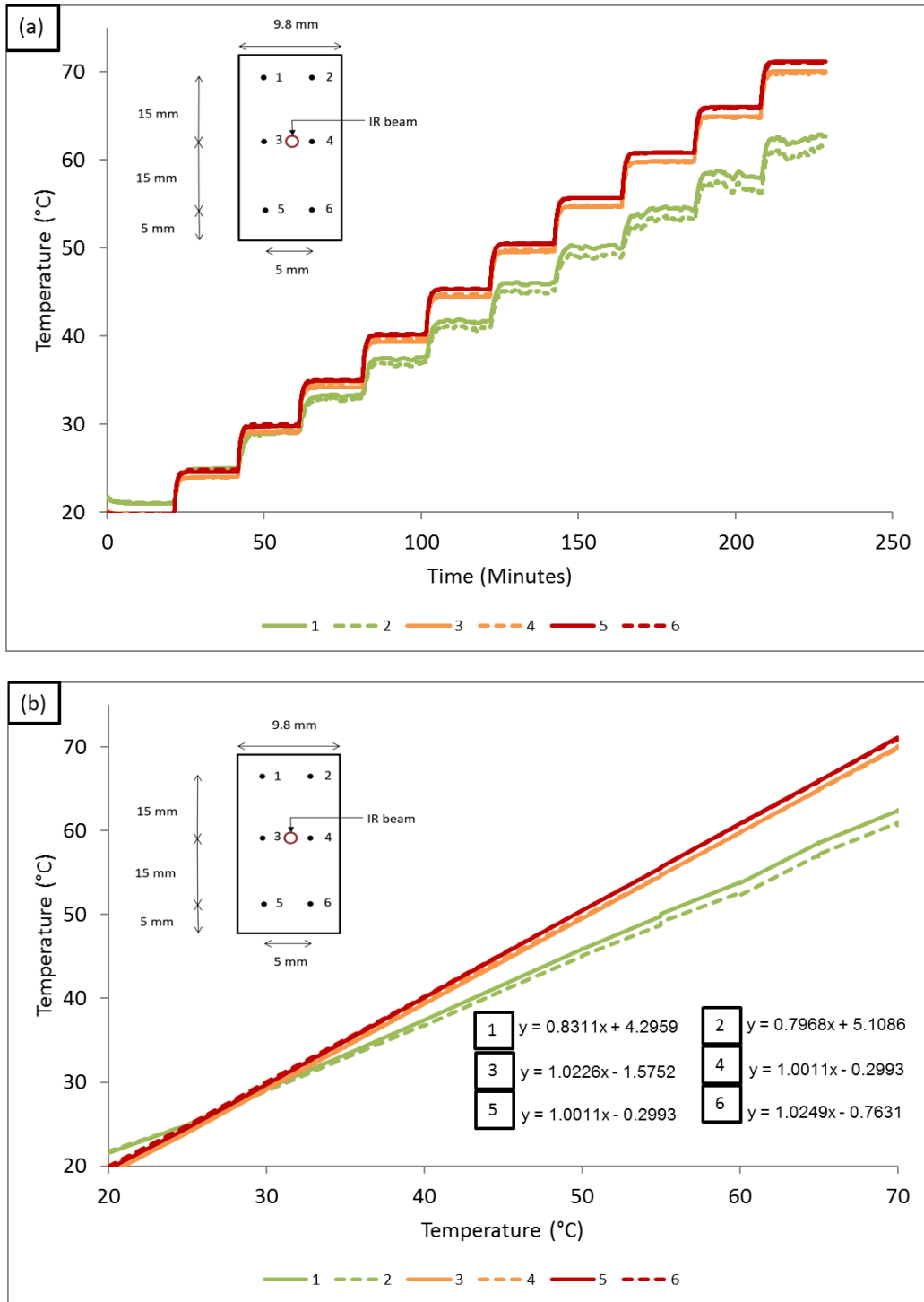


Figure 4.10 Temperature measurements at specified locations within the demountable quartz cuvette filled with silicone oil between 20-70 °C as a function of: (a) Time; and (b) Temperature.

## 4.2.2 Identification of Absorbance Peaks for the LY3505/XB3403 Resin System

Figure 4.11 displays the spectra of the LY3505/XB3403 mixture at the start (prior to increasing the temperature from ambient) and after 600 minutes of cross-linking at 70 °C. The spectra shown in Figure 4.11 and the absorbance peaks presented in Table 4.5 correlate with previous research on the same resin system by Pandita *et al.* (2012), Nair *et al.* (2015) and Wang *et al.* (2016), in addition to investigations into epoxy/amine systems by Mijovic and Andjelic, (1995) and Nikolic *et al.* (2010).

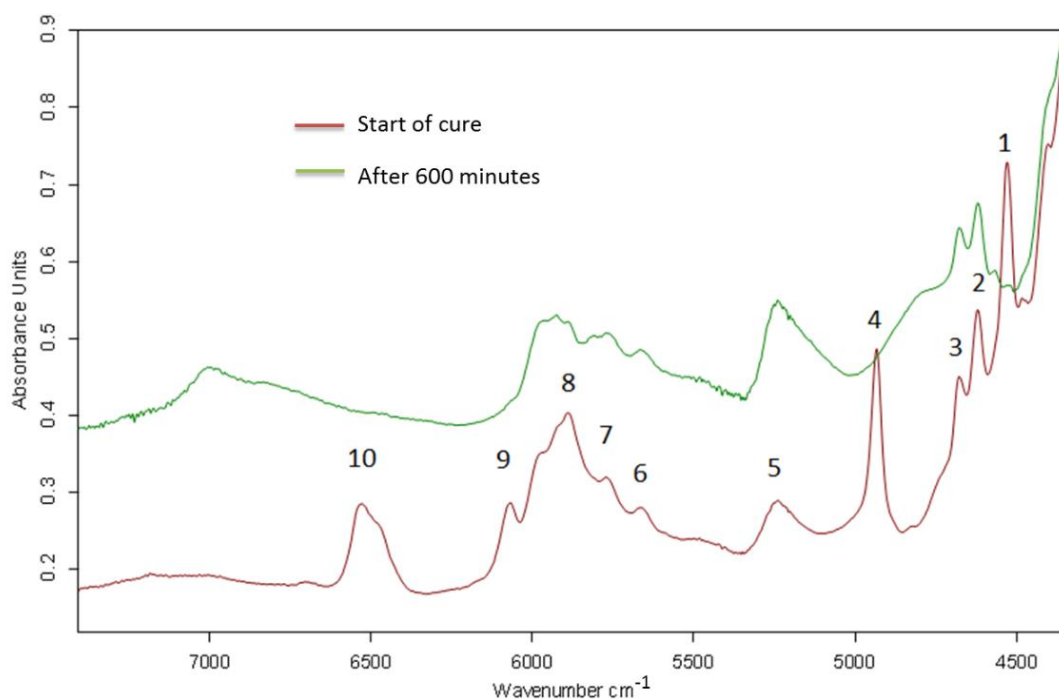


Figure 4.11 Spectra of LY3505/XB3403 resin system at the beginning of cross-linking and after 600 minutes at 70 °C.

Table 4.5 Near-infrared peak assignments identified for the LY3505/XB3403 resin system Pandita *et al.* (2012), Nair *et al.* (2015) and Wang *et al.* (2016).

Wave Number (cm <sup>-1</sup> )	Assigned Peak	Label
4530	Epoxy band	1
4620, 4677	Aromatic CH band	2,3
4935	Primary amine	4
5249	OH due to moisture	5
5668	Terminal, aliphatic R-CH <sub>3</sub>	6
5767	Methyl 1st overtone (C-H Stretching)	7
5889	Combination of epoxy and primary amine	8
6067	Terminal epoxy	9
6635	Primary and secondary amine combination	10

As mentioned in Section 2.3.2, Chapter 2, the C–H stretching band at 4620 cm<sup>-1</sup> has been used widely for normalising peaks associated with functional groups that participate in the cross-linking reactions. The C-H group does not take part in the cross-linking reactions. Despite other inert peaks being present at 4677, 5668 and 5889 cm<sup>-1</sup>; the 4620 cm<sup>-1</sup> peak is not overlapped with other absorbance bands and hence it was chosen as the reference peak in this work.

The strong peak at 4530 cm<sup>-1</sup> indicates the presence of the epoxy group which is consumed as cross-linking proceeds. The epoxy group is involved in each step of the cross-linking reaction and can be used for quantitative analysis of the degree of cross-linking. This peak is also isolated from other reactive functional groups and has been used by previous researchers for quantitative analysis of the cross-linking of thermosets (Poisson *et al.*, 1996; González *et al.*, 2012; Pandita *et al.*, 2012;

Nair *et al.*, 2015; Wang *et al.*, 2016). Therefore, in the current work, the epoxy peak at  $4530\text{ cm}^{-1}$  was used for quantitative analysis.

Towards the end of curing, a small peak around  $4560\text{ cm}^{-1}$  becomes apparent as the epoxy is depleted. This has been reported previously by Dumitrescu (2003b) and Pandita *et al.* (2012), although the origin of the peak is unknown. These authors removed the contribution from this peak to the epoxy absorbance band via Fourier self-deconvolution.

An epoxy peak area at  $6067\text{ cm}^{-1}$  observed a decrease in strength during cross-linking. Billaud *et al.* (2002) noted that this peak's suitability for following the degree of cross-linking is limited by its strength and proximity to nearby peaks, notably the epoxy and primary amine band at  $5889\text{ cm}^{-1}$ . A decrease in the combined primary and secondary amine absorption and the amine primary absorptions at  $6635\text{ cm}^{-1}$  and  $4935\text{ cm}^{-1}$ , respectively during cross-linking, was noted.

#### **4.2.3 Baseline Construction of the Absorption Peak Areas during the Cross-linking of LY3505/XB3403.**

The peak area of the absorbance bands was calculated using the Opus software supplied with the FTIR spectrometer. Figure 4.12 displays the construction of the baseline after specified times. The limits for the integration area were set manually as a function of the processing time. This was undertaken to account for the changes in the relative position and shape of the absorbance band as the cross-linking proceeded. Upon achieving the desired isothermal cross-linking temperature,

an upward shift in the baseline of the spectra indicated an increase in the refractive index as a function of the extent of cross-linking (Powell *et al.*, 1998).

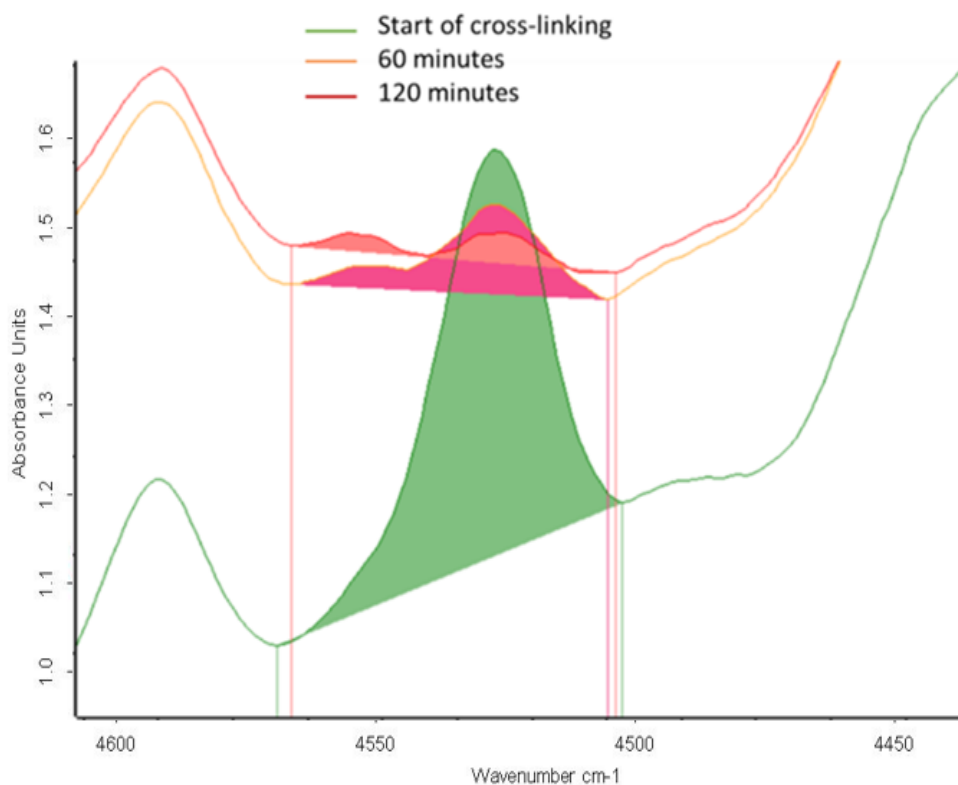


Figure 4.12 Integration of the absorbance spectra peak area during cross-linking of LY3505/XB3403 at 70 °C for specified times.

The epoxy peak area is comprised of a single well-isolated peak at the beginning of cross-linking, as previously reported (Gillham, 1986; Poisson *et al.*, 1996; Nikolic *et al.*, 2010; Wang *et al.*, 2016; Mosiewicki *et al.*, 2011 and Pritchard, 2012). The presence of a peak at 4560  $\text{cm}^{-1}$  becomes apparent part-way through cross-linking and has been reported to be a source of error when investigating cross-linking of epoxy/amine resin systems (Strehmel and Scherzer, 1994; Mijovic and Andjelic, 1995 and Mijovic *et al.*, 1996). Mahendran (2010) reported that this peak could be due to a combination of vibrations from 'C-H stretching' of the aromatic ring and 'aromatic conjugated stretching'. As cross-linking proceeds, the magnitude of the un-assigned peak area becomes greater relative to the epoxy peak area.

Figure 4.13 shows the integration of the  $4530\text{ cm}^{-1}$  peak area after 600 minutes of cross-linking at  $70\text{ }^{\circ}\text{C}$ . The prominence of the un-assigned peak area at  $4560\text{ cm}^{-1}$  distorts the integration of the  $4530\text{ cm}^{-1}$  peak area. Integration of the  $4560\text{ cm}^{-1}$  peak area after 600 minutes reveals it contributes to approximately 4% of the initial epoxy peak area. This correlates with the 5% value reported by Pandita *et al.* (2012).

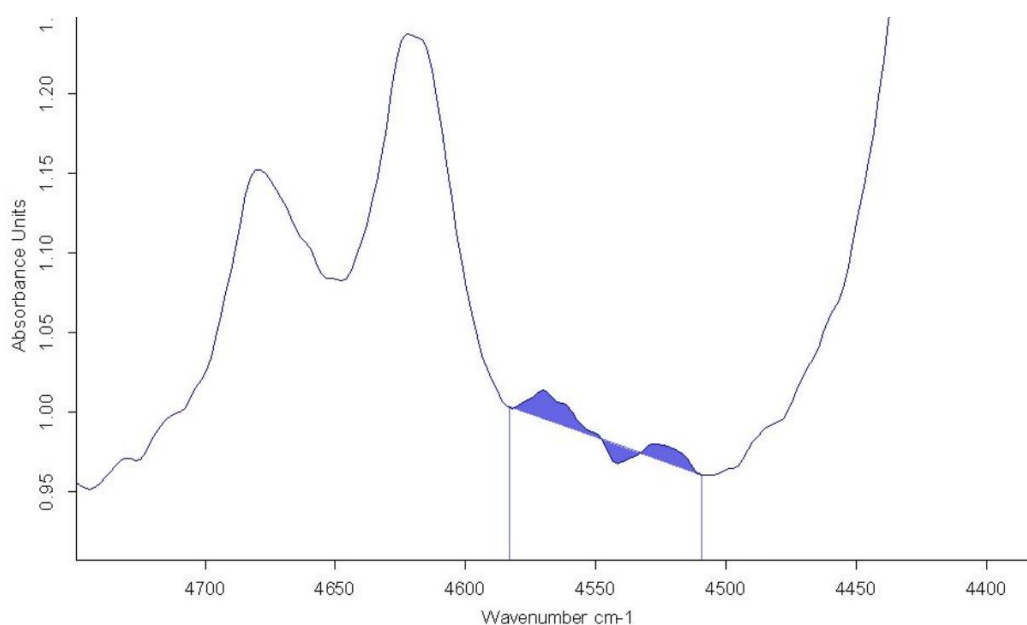


Figure 4.13 Integration of the absorbance spectra of the LY3505/XB3403 resin system cross-linked at  $70\text{ }^{\circ}\text{C}$  after 600 minutes.

Mahendran (2010) reported upon three integration methods for quantitative analysis of the LY3505/XB3403 resin system during FTIRS. The methods were:

Method 1: Integration of the epoxy peak and the peak at  $4560\text{ cm}^{-1}$ . This produced a higher amount of residual epoxy content towards the end of the reaction.

Method 2: Remove the contribution of the hidden peak gradually as it becomes visible. This produced low reproducibility due to difficulty in defining the baseline of the integration.



Method 3: Deconvolution. Good reproducibility of the peak area was present with clear boundaries. The area of the peak at  $4560\text{ cm}^{-1}$  remained constant throughout cure and therefore method 3 was selected for quantitative analysis.

Previous investigations into the cross-linking of LY3505/XB3403 by Mahendran (2010) and Pandita *et al.* (2012) employed a Fourier self-deconvolution routine to resolve the contribution of the un-assigned peak to the epoxy peak at  $4530\text{ cm}^{-1}$ . Similar to their work, a Lorentzian line shape was employed in the current study, with a bandwidth of  $5\text{ cm}^{-1}$  and a resolution enhancement of 1.5 to investigate if the contribution of the unknown peak at  $4560\text{ cm}^{-1}$  could be resolved.

Fourier self-deconvolution enhances the spectral bandwidth to resolve overlapping peak areas. The routine mathematically enhances the separation of overlapping peaks by multiplication of the interferogram with a smoothing function and a Lorentzian or Gaussian band shape (Tookey, 1988; Mahendran 2010). This method does not increase the resolution of the instrument. The routine alters the peak size and shapes using Fourier self-deconvolution. In this work, the routine provided information upon the evolution of the hidden peak area at  $4560\text{ cm}^{-1}$ .

Figure 4.14 displays spectra from Figure 4.13 following the deconvolution routine. Throughout cross-linking, the un-assigned peak was isolated from the epoxy peak at  $4530\text{ cm}^{-1}$ . Similar to work undertaken by Pandita *et al.* (2012), the peak was approximately constant throughout cross-linking. This enabled clear boundaries to be identified for the integration of the epoxy peak throughout cross-linking.

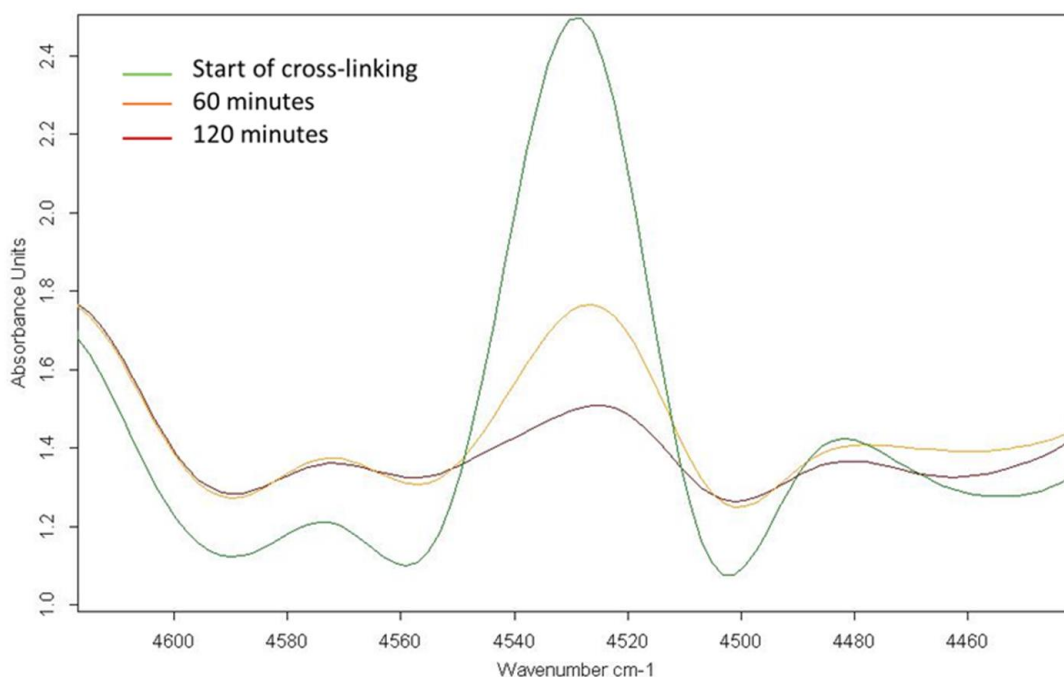


Figure 4.14 Deconvoluted spectra of Figure 4.12 using the Fourier self-deconvolution routine in the OPUS software at: the start of cross-linking, after 60 minutes and 120 minutes.

#### 4.2.4 Impact of Deconvolution on the Degree of Cross-linking

The impact of the deconvolution routine upon the degree of cross-linking was investigated using spectra obtained at 70 °C. The degree of cure,  $\alpha$ , was determined using Equation 2.4. The deconvolution routine was not applied to the C-H reference peak at 4620cm<sup>-1</sup>.

$$\alpha = \left[ \frac{(A_{Epoxy(4530)}/A_{CH(4620)})_t}{(A_{Epoxy(4530)}/A_{CH(4620)})_{t=0}} \right] \dots\dots\dots \text{Equation 2.4}$$

The degree of cross-linking using the raw spectra and the de-convoluted spectra is shown in Figure 4.15 (a) and (b).

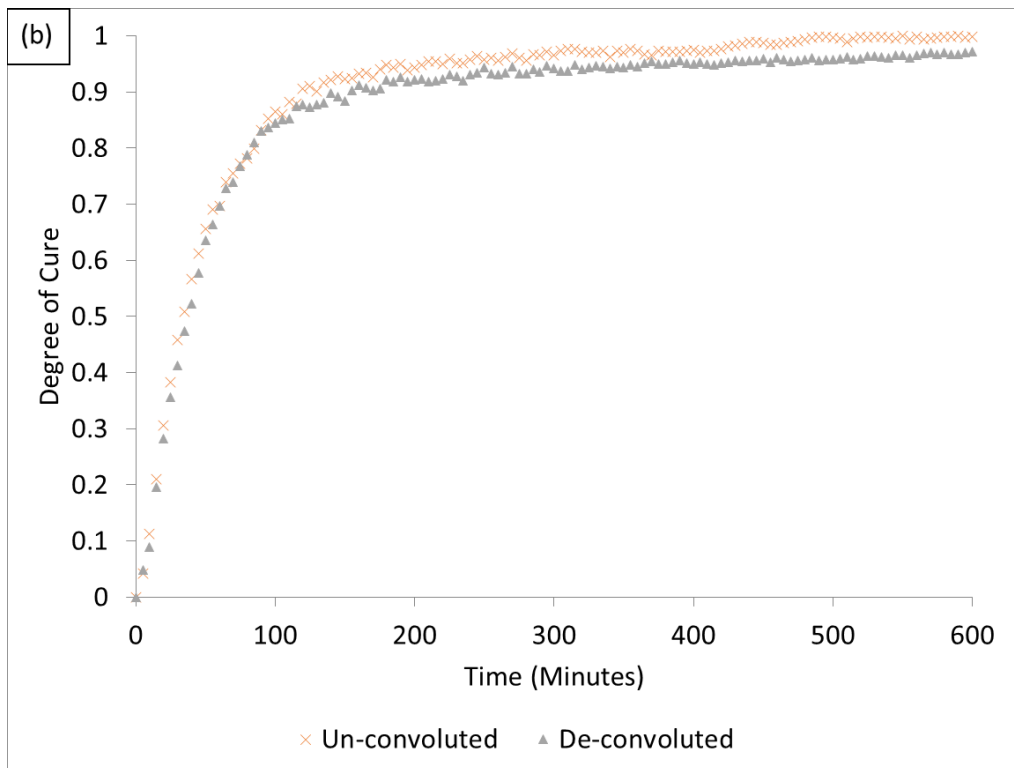
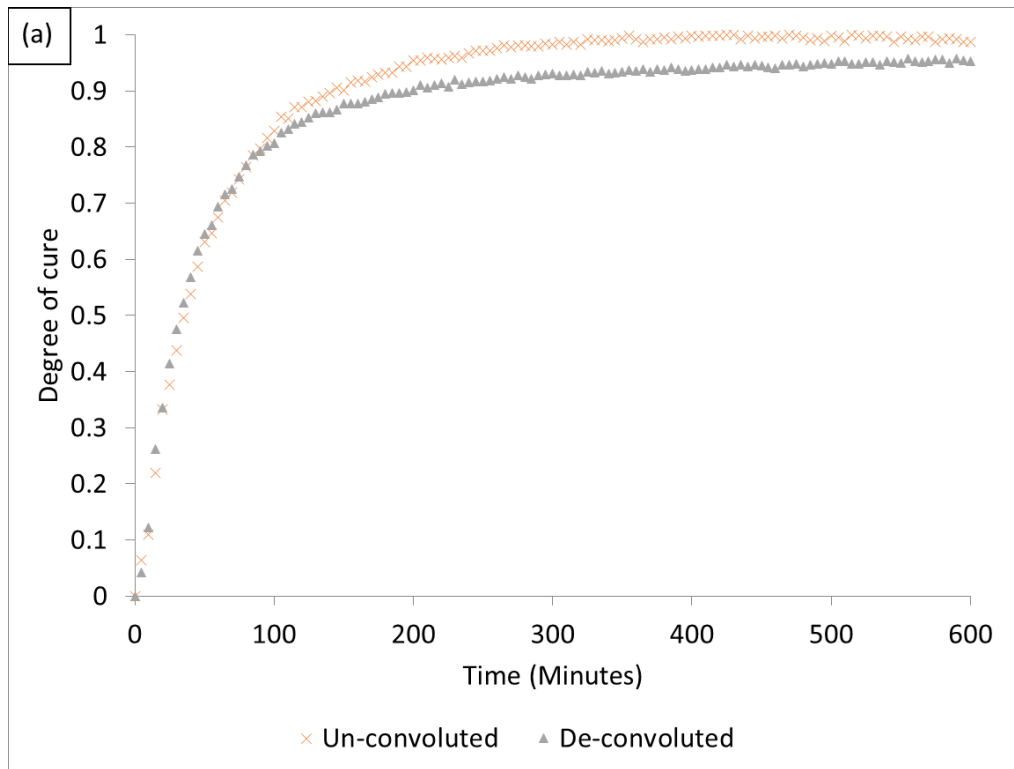


Figure 4.15 Degree of cross-linking calculated using Equation 2.4 for LY3505/XB3403 at 70 °C using raw spectra and de-convoluted spectra:  
 (a) Experiment 1; and (b) Experiment 2.

A similar relationship between the datasets is observed until approximately 80% of conversion. After 80% conversion, the prominence of the un-assigned peak at 4560 cm<sup>-1</sup> affects the baseline construction of the spectral peak area, as shown in Figure 4.13. This produced a conversion above 99% which does not correlate with Table 4.6. The de-convoluted spectra produced lower conversions whilst the epoxy area remained isolated over the entire cross-linking period. This produced a lower conversion of 94% which correlates with previous research into the LY3505/XB3403 resin system during cross-linking at 70 °C as shown in Table 4.6.

Table 4.6 Reported conversions during the cross-linking of LY3505/XB3403 at 70 °C using FTIRS.

<b>Isothermal Cross-linking</b>	<b>Degree of Cure</b>	<b>Reference</b>	<b>Deconvolution</b>
<b>400 minutes at 70 °C</b>	96%	Mahendran (2010)	Yes
<b>600 minutes at 70 °C</b>	95%	Pandita <i>et al.</i> (2012)	Yes
<b>400 Minutes at 70 °C</b>	94%	Wang <i>et al.</i> (2016)	Not stated
<b>600 minutes at 70 °C</b>	98%	Harris (2011)	Not stated

It was decided that using the de-convoluted spectra was the most suitable technique for determining the epoxy peak area for the following reasons:

- (i) The retardation of the baseline construction method by the un-assigned peak at 4560 cm<sup>-1</sup> caused un-expectedly high conversion values to be obtained.
- (ii) The de-convoluted spectra produced a well isolated epoxy peak throughout cross-linking where the baseline could be clearly defined.

Figure 4.16 depicts the degree of cross-linking at specified isothermal curing temperatures. The increase in the degree of cross-linking and cross-linking rate with increasing temperature correlates with data previously reported using the same resin system (Dumitrescu, 2003b; Pandita *et al.*, 2012; Wang *et al.*, 2016). Similar to the DSC data, an initial rapid reaction was experienced during the initial 50% of the reaction which 'levelled off' after approximately 80% of cross-linking.

Figures 4.17 (a) – (c) show a comparison between the experimental cross-linking data at specified isothermal cross-linking temperatures and the theoretical prediction using Equation 4.1. Error bars of 5% were added to the predictive model values, showing that there was no significant difference between the experimental data and the autocatalytic model. As mentioned in Section 4.1.5, a 'mismatch' between the data sets can be observed during the later stages of cross-linking, due to the possible impact of vitrification upon the reaction control mechanism. However, the experimental values remain within the 5% error.

The activation energy was determined to be 55.08 kJ mol<sup>-1</sup> and the rate constants are shown in Table 4.7. The data are comparable with previously reported values obtained using transmission FTIR spectroscopy for the LY3505/XB3403 resin system. Pandita *et al.* (2012) and Wang *et al.* (2016) reported values of 60.9 kJ mol<sup>-1</sup> and 56.8 kJ mol<sup>-1</sup> respectively.

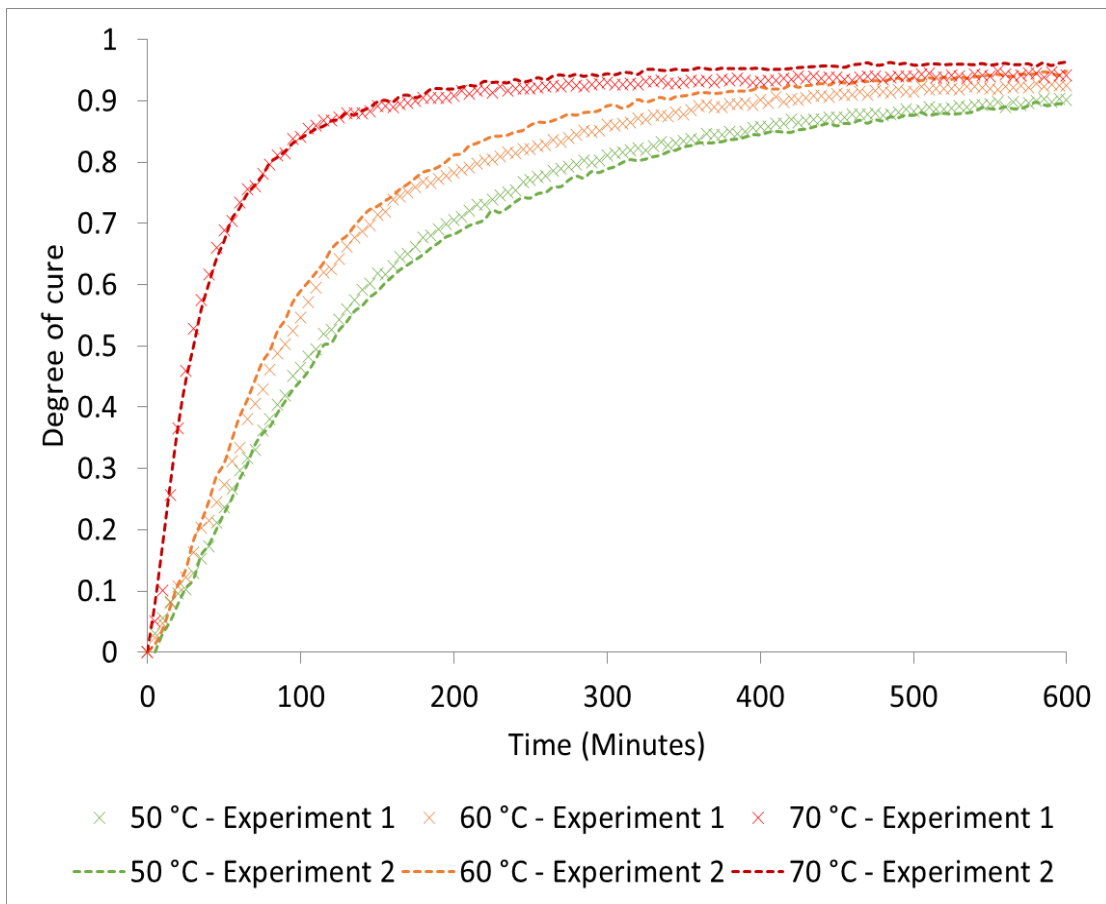


Figure 4.16 Degree of cure for the LY3505/XB3403 resin system at 50, 60 and 70 °C. The data was generated using conventional FTIR spectroscopy.

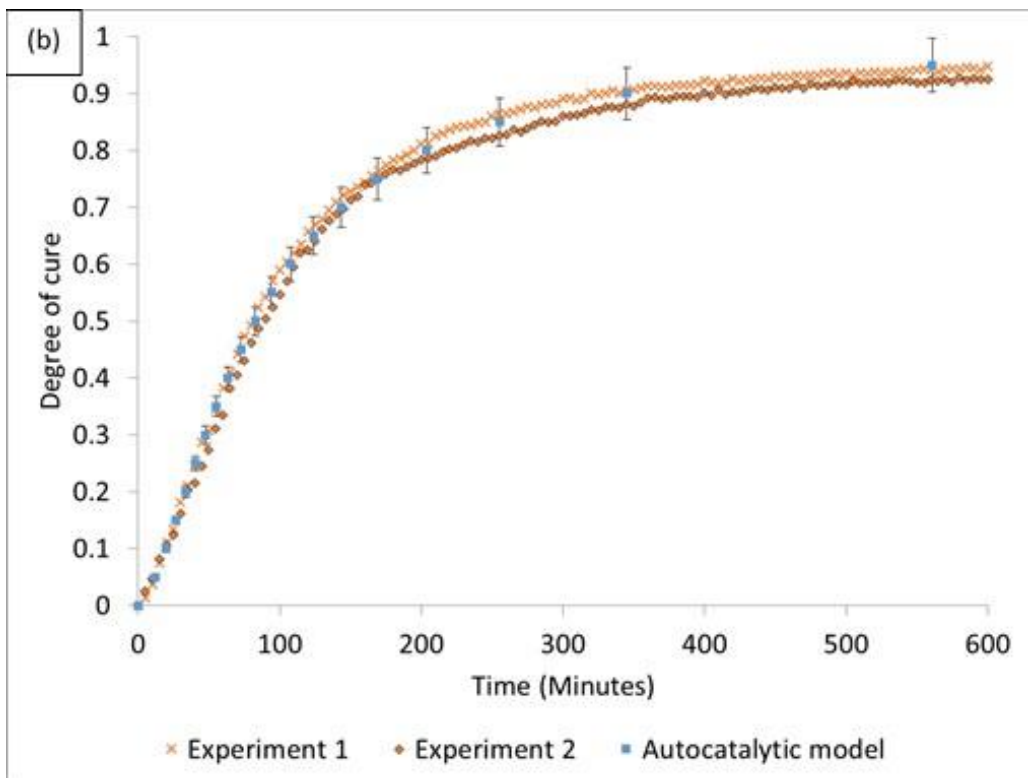
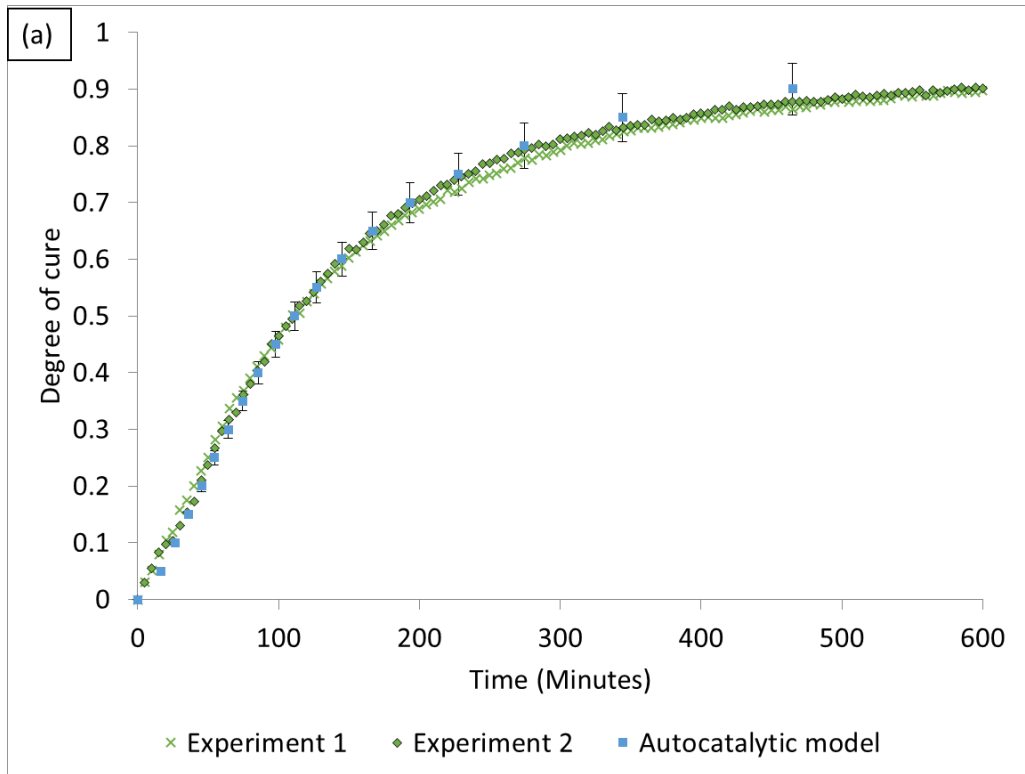


Figure 4.17 Comparison between transmission FTIR experimental data that were generated isothermally at: (a) 50 °C; and (b) 60 °C; and simulated data using Equation 4.1 with the average rate constant for each specified temperature.

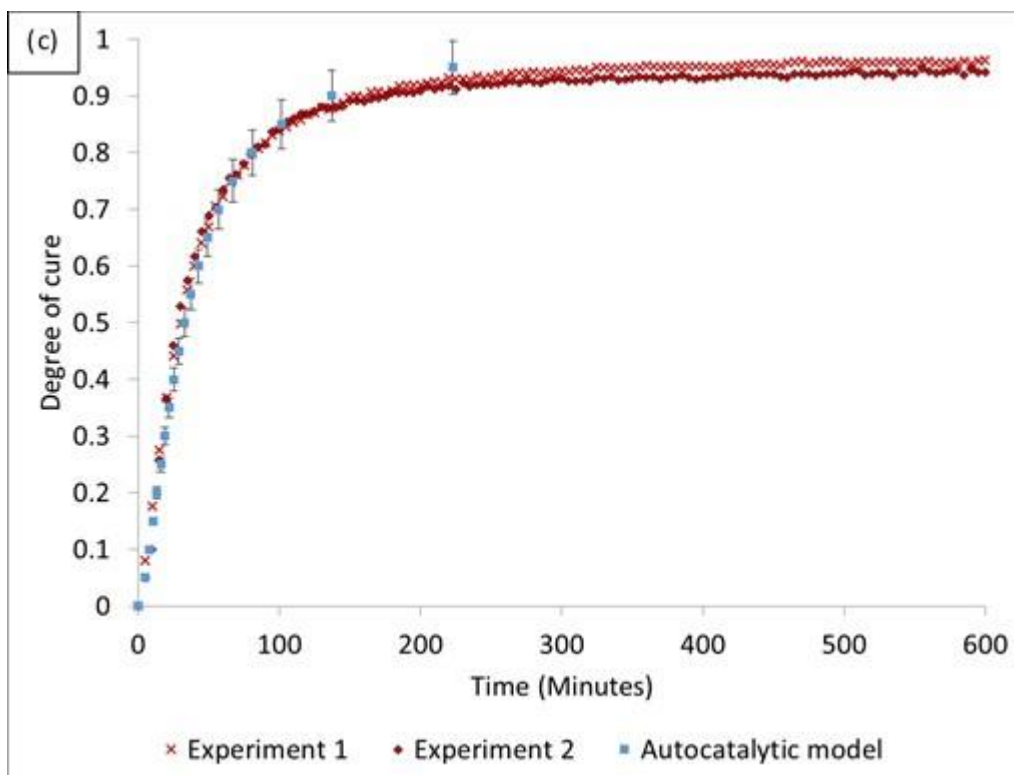


Figure 4.17 (continued) Comparison between transmission FTIR experimental data that were generated isothermally at: (c) 70 °C; and simulated data using Equation 4.1 with the average rate constant for each specified temperature.

Table 4.7 Rate constants and activation energy for the LY3505/XB3403 resin system using FTIRS data and Equation 4.1.

<b>Isothermal Cross-linking</b>	<b>k (s<sup>-1</sup>)</b>	<b>ln k</b>	<b>1/T</b>
<b>50 °C - Experiment 1</b>	0.00020	-8.62	0.0031
<b>50 °C - Experiment 2</b>	0.00021	-8.68	0.0031
<b>60 °C - Experiment 1</b>	0.00033	-8.15	0.0030
<b>60 °C - Experiment 2</b>	0.00032	-8.02	0.0030
<b>70 °C - Experiment 1</b>	0.00068	-7.14	0.0029
<b>70 °C - Experiment 2</b>	0.00068	-7.16	0.0029
<b>Activation Energy (kJ mole<sup>-1</sup>)</b>		<b>55.08</b>	



### **4.3 Comparison between Independent Cross-linking Data obtained using Differential Scanning Calorimetry and Fourier Transform Infrared Spectroscopy**

Figures 4.18 (a) and (b) show the degree of cross-linking obtained from DSC and FTIRS. The gradient during the initial 30% of cross-linking was calculated to compare the initial reaction rate. The gradient lines are shown in Figure 4.18 (a) and (b) and the results for both experiments are summarised in Table 4.8. Generally, a quicker initial rate of cross-linking was observed for the FTIRS experiments. The magnitude of the discrepancy between the measurement techniques was largest with the cross-linking at 70 °C. In the case of FTIRS experiments, the cuvette containing the resin sample was inserted into a pre-heated cuvette holder at the desired isothermal cross-linking temperature. In comparison, the DSC resin samples were inserted at 30 °C and ramped at 40 K/minute to the desired isothermal cross-linking temperature. It can be inferred that the resin was heated at a quicker rate for FTIRS experiments contributing to the increased rate of reaction.

Furthermore, the contribution of the exothermic cross-linking to the sample temperature for FTIRS experiments may have contributed to the initial rate of reaction. Machavaram *et al.* (2014) observed a 15 to 25 °C sample temperature increase for 2.4 g of LY3505/XB3403 when cross-linked at 70 °C. Therefore, deviations from the desired isothermal temperature are possible.

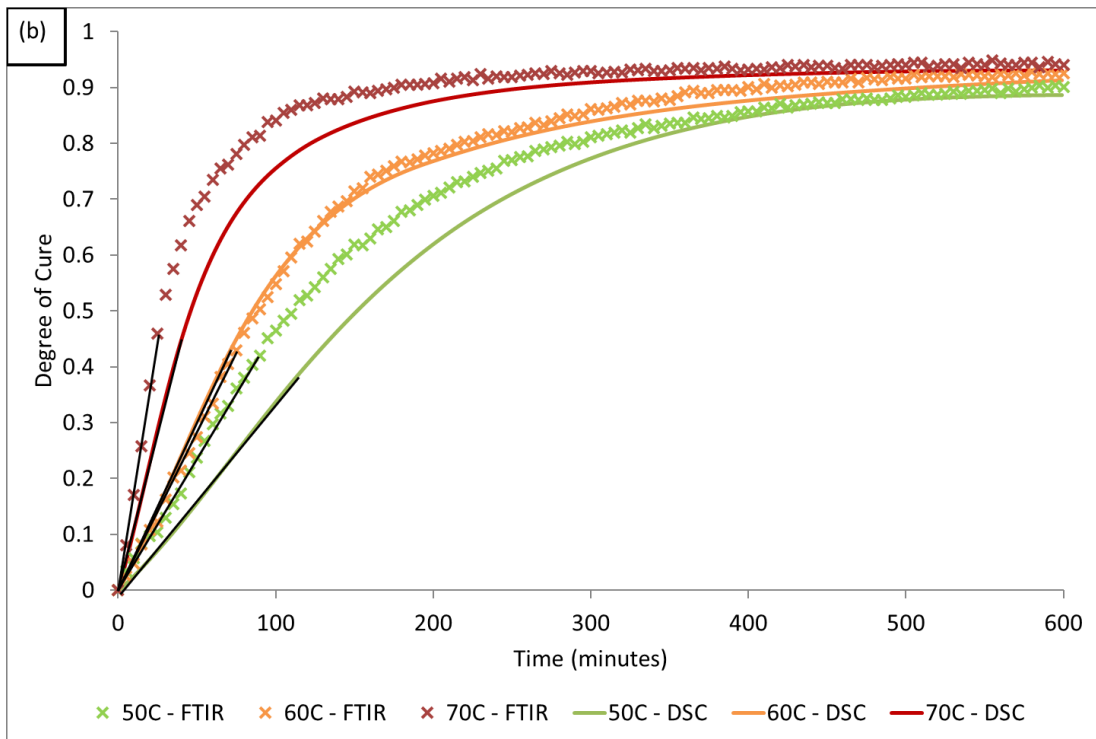
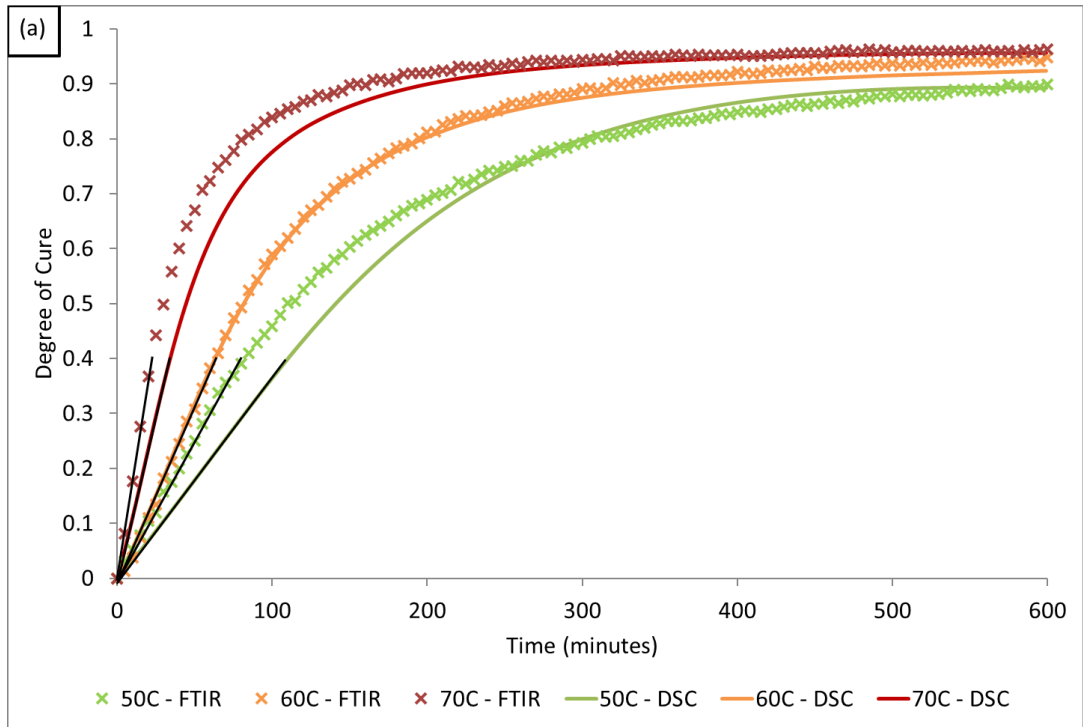


Figure 4.18 Comparison of the Degree of Cross-linking for the LY3505/XB3403 resin system from isothermal FTIRS and DSC: (a) Experiment 1; and (b) Experiment 2.

Table 4.8 Initial rate of reaction during the cross-linking of LY3505/XB3403 at specified isothermal temperatures using DSC and FTIRS experiments.

<b>Isothermal Cross-linking</b>	<b>Initial Cross-linking Rate (0-50 minutes, da/dt)</b>	
	<b>DSC</b>	<b>FTIRS</b>
<b>50 °C - Experiment 1</b>	0.0037	0.0050
<b>50 °C - Experiment 2</b>	0.0035	0.0045
<b>60 °C - Experiment 1</b>	0.0065	0.0066
<b>60 °C - Experiment 2</b>	0.0062	0.0060
<b>70 °C - Experiment 1</b>	0.0119	0.0181
<b>70 °C - Experiment 2</b>	0.0116	0.0192

The data in Figures 4.18 (a) and (b) also show that experiments conducted at higher isothermal cross-linking temperatures 'levelled-off' earlier than temperatures conducted at lower temperatures. At the end of the cross-linking period, the extent of the reaction was greater for the FTIRS data. This may be explained by several factors:

- (i) The previously discussed differing methods of heating the samples to the desired isothermal cross-linking temperature.
- (ii) Samples tested using FTIRS were heated using a temperature controller maintaining a target temperature of 70 °C, which appears accurate to 0.2 °C from Figure 4.10. The contribution of the heat generated by the exothermic reaction to the environmental temperature may have impacted the sample temperature. Therefore, deviations from the desired temperature are possible.

- (iii) Unlike the FTIRS technique, the DSC method was able to compensate for exothermic contributions from the sample. The heat sensors in intimate contact with the sample holder are accurate to 0.1 °C (PerkinElmer, 2001).
- (iv) In the later stages of cross-linking, vitrification causes a rapid reduction in the rate of cross-linking (Gillham, 1986). The relatively low reaction rate may yield magnitudes of heat below the 0.2 μW sensitivity of the calorimeter and hence are undetected.
- (v) Different thermal environments for each experimental technique contribute to the mean cross-linking temperature and hence cross-linking characteristics.

Pandita *et al.* (2012) observed an increased degree of cross-linking of LY3505/XB3403 resin system using transmission FTIRS when compared to DSC and the data from the authors' research is shown in Figure 4.19. The previously discussed factors were identified as possible sources for the observed discrepancy. The correlation between the measurement techniques was significantly improved when the authors developed a simultaneous DSC/FTIRS technique by positioning transmission/reflectance probes over the reflective DSC pans. The data strengthens the argument for developing hyphenated analytical techniques and highlights issues when cross-correlating data between thermal analysis techniques.

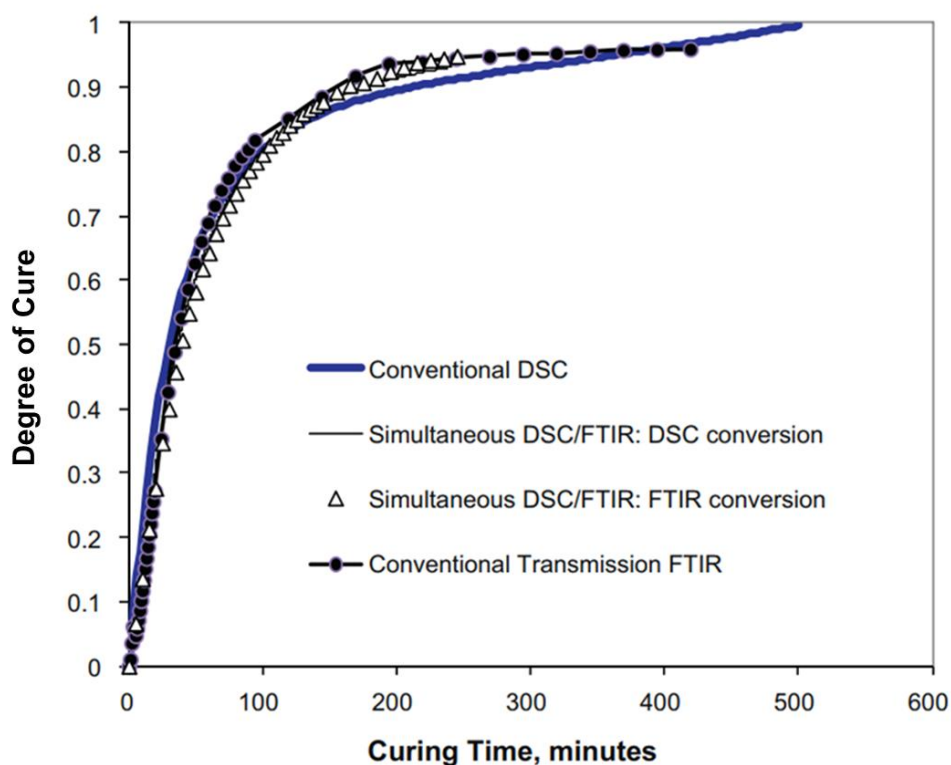


Figure 4.19 Degree of cross-linking of the LY3505/XB3403 resin system studied by conventional DSC, conventional FTIR and using a hyphenated simultaneous DSC/FTIR technique at 70 °C (Pandita *et al.*, 2012).

#### 4.4 Rheology

Figures 4.20 (a) – (c) show the increase in the storage modulus ( $G'$ ) and loss modulus ( $G''$ ) during isothermal crosslinking of LY3505/XB3403 at 70 °C in three repeat experiments. The transducer required a minimum torque of 2 g.cm for meaningful data acquisition. The resin was loaded into the rheometer at room temperature and ramped at 40 K/minute to the specified isothermal cross-linking temperature. A frequency of 1 Hz and a strain of 4% were selected to prevent overloading of the transducer at the gelation region, although during the early stages of cross-linking the torque applied upon the sample was not sufficient to acquire meaningful data. Therefore, in each of the experiments, an initial period of noisy

data were obtained due to the low viscosity of the freshly mixed resin and the inability of the transducer to detect liquids with low viscosities. The parallel plate fixture generates shear on the sample and therefore measures the shear modulus. Upon cross-linking, the viscosity increased several orders of magnitude and subsequently the 2 g.cm minimum torque value of the instrument was surpassed to allow for meaningful data acquisition. Experiments were terminated soon after the  $G'/G''$  crossover to prevent overloading the load-cell of the instrument.

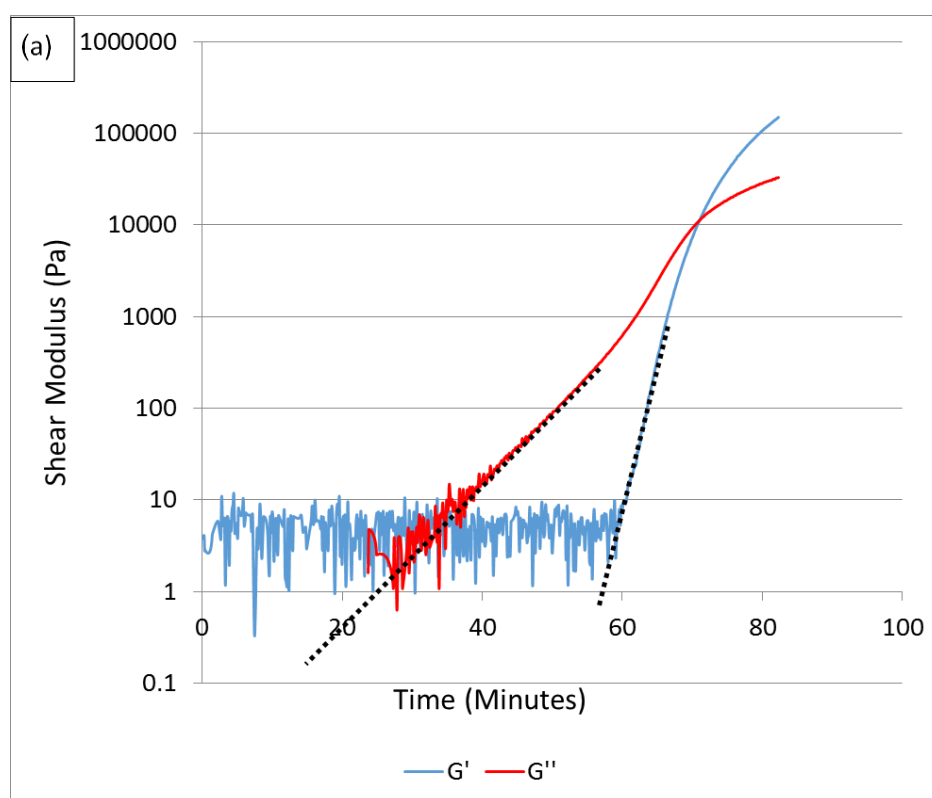


Figure 4.20 Evolution of  $G'$  and  $G''$  during isothermal cross-linking of the resin system LY3505/XB3403 at 70 °C: (a) Experiment 1.

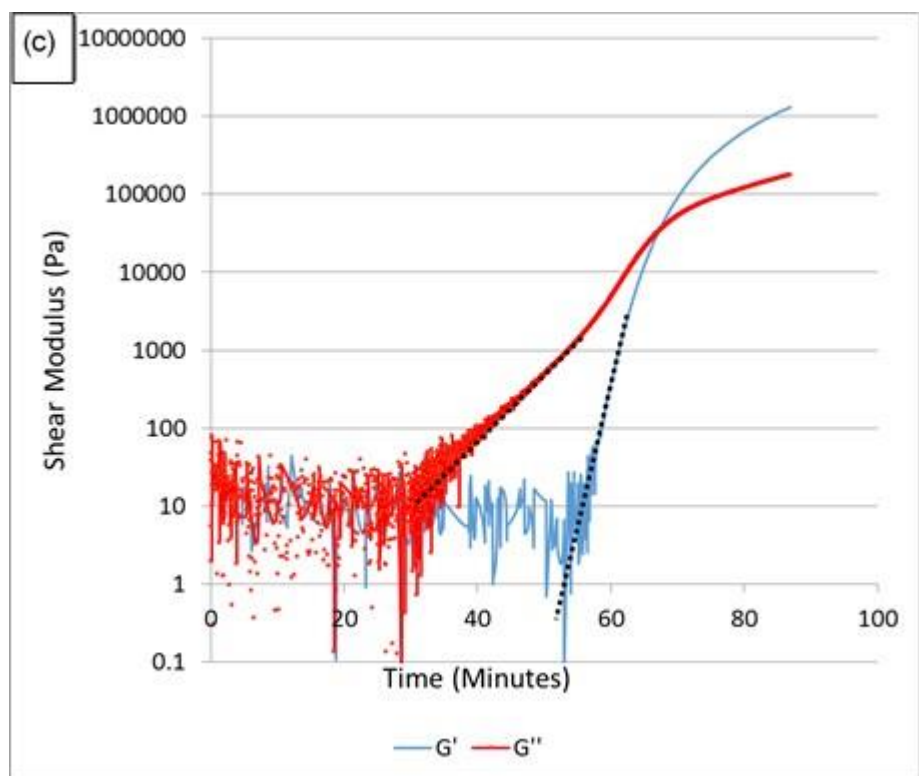
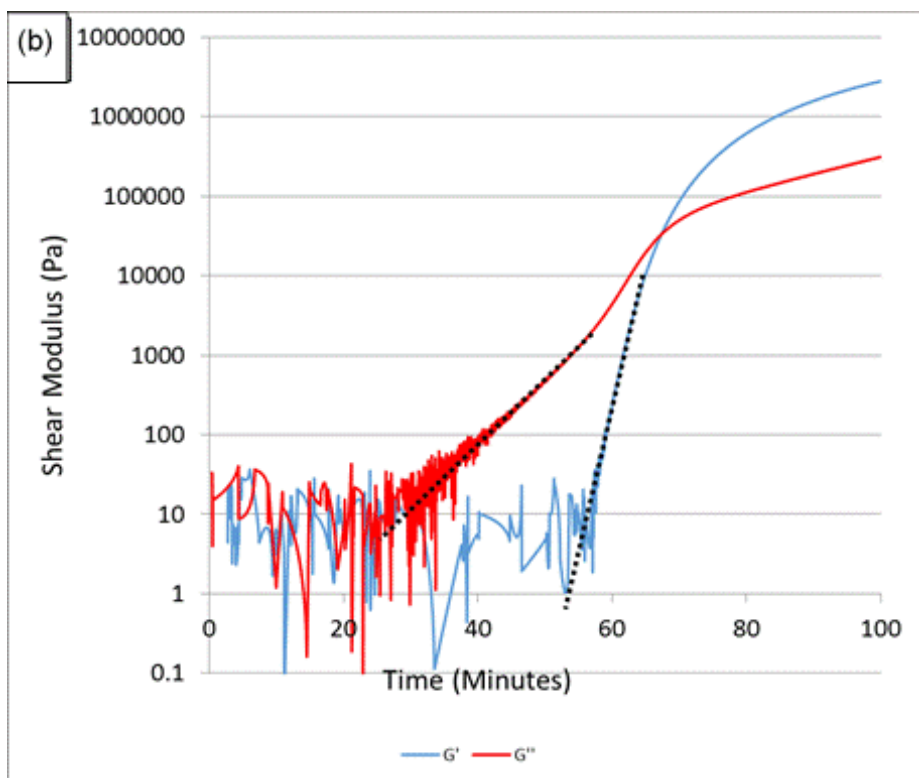


Figure 4.20 (continued) Evolution of  $G'$  and  $G''$  during isothermal cross-linking of the resin system LY3505/XB3403 at 70 °C: (b) Experiment 2; and (c) Experiment 3.

Due to the significant noise generated during the early stages of cross-linking, a tangent was drawn to the initial logarithmic increase of  $G'$  and  $G''$  and data that occurred before the intersection of this line was removed. The tangent construction is shown in Figures 4.20 (a) – (c).

Figures 4.21 (a) – (c) display the graphs following the removal of the data. This did not alter the  $G'/G''$  crossover and removed data acquired below the minimum torque value of the rheometer. The method was used for all the remaining rheological experiments.

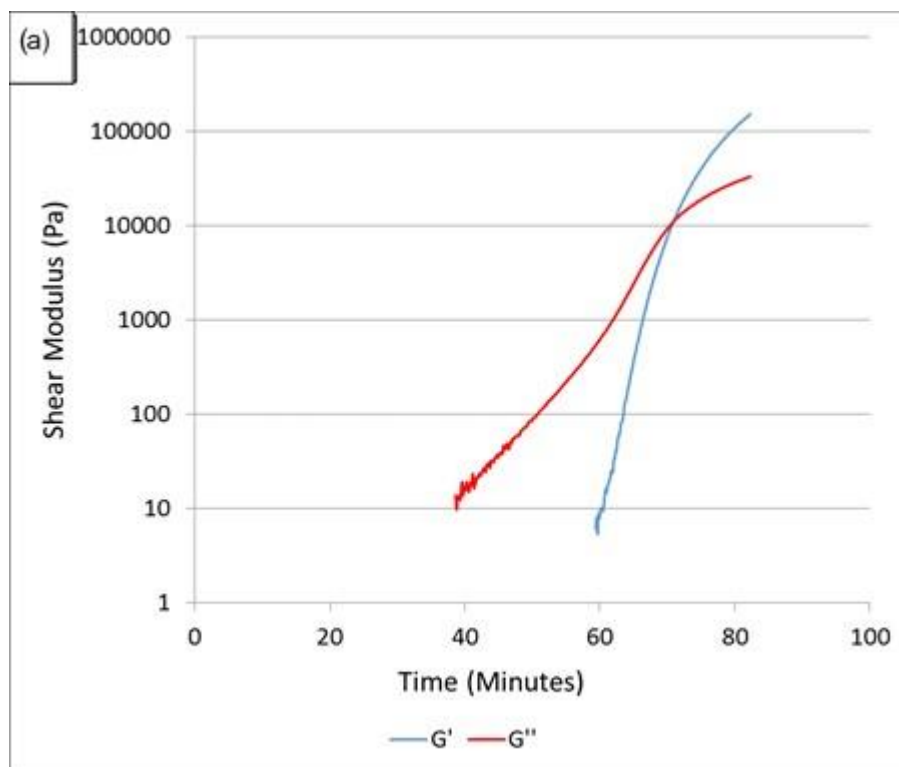


Figure 4.21 Evolution of  $G'$  and  $G''$  during isothermal cross-linking of the resin system LY3505/XB3403 at 70 °C following the removal of data: (a) Experiment 1.



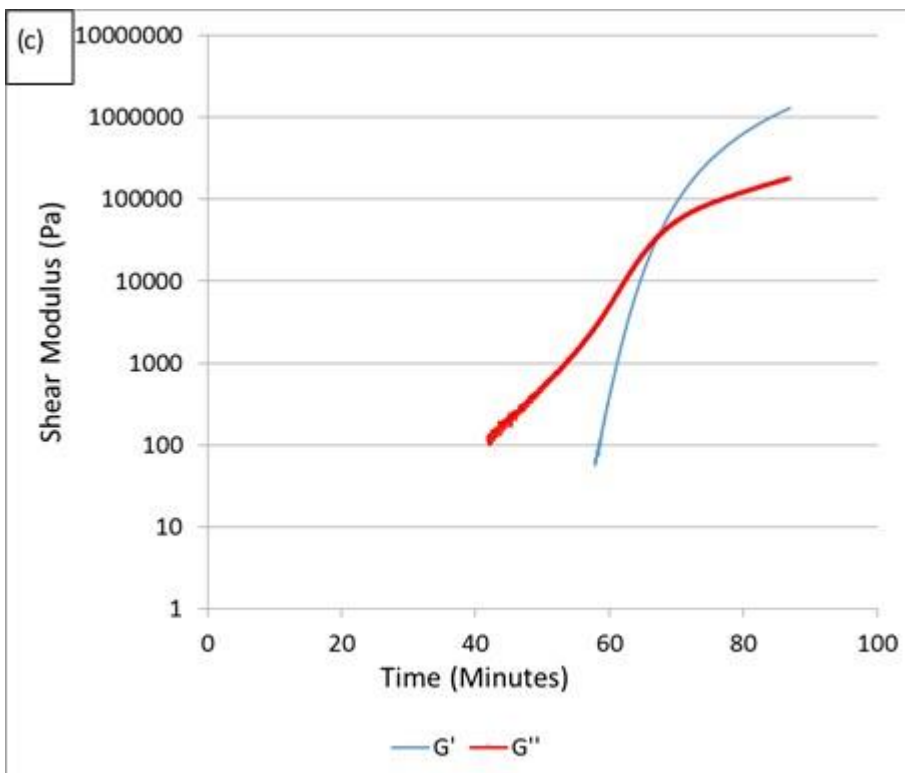
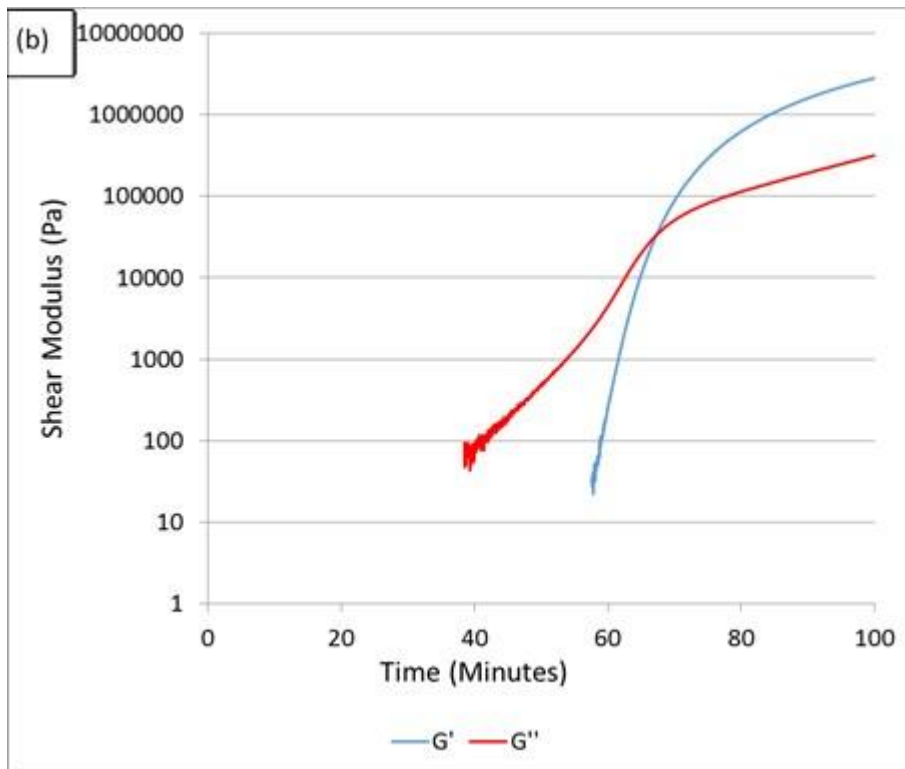


Figure 4.21 (continued) Evolution of  $G'$  and  $G''$  during isothermal cross-linking of the resin system LY3505/XB3403 at 70 °C following the removal of data: (b) Experiment 2; and (c) Experiment 3.

Three distinct stages observed during the rheological cross-linking of an epoxy resin, were reported (Barton and Wright, 1985; Matějka, 1991; Cheng *et al.*, 1994) in Section 2.3.2.4, Chapter 2, and the relevance of each stage to Figures 4.21 (a) – (c) is discussed:

- (i) The  $G''$  value was dominant during the initial stages of cross-linking. The parameters used in the current study did not impart sufficient deformation to obtain meaningful data during most of this period. After 40 minutes the extent of cross-linking was sufficient to obtain a relatively steady loss modulus. At this stage, the  $G''$  magnitude was larger than the  $G'$  value and relatively stable after approximately 55 minutes. In this state, the majority of the imparted energy was lost, and the material behaved as a liquid.
- (ii) After approximately 60 to 70 minutes in each experiment,  $G'$  and  $G''$  dramatically increased due to the formation of a highly cross-linked material as a gel was formed.  $G'$  and  $G''$  crossover and this stage is indicative of gelation (Tung and Dynes, 1982; Lange *et al.*, 2000). The material transitions from behaving like a liquid to a semi-solid plastic (Teil *et al.*, 2004).
- (iii) After approximately 70 minutes in each experiment, there was a period where  $G''$  was dominant and the rate of increase of  $G'$  and  $G''$  levelled off. To prevent overloading of the transducer, the experiments were terminated soon after gelation and prevented data acquisition for the entirety of this stage.

Table 2.9 in Section 2.3.2.5 presents the various criteria which have been used for rheological gelation determination. The frequency independence of  $G'$  and  $G''$  has been considered to be the most precise method of gelation determination (Lange *et*

*al.*, 1999b; Teil *et al.*, 2004; Stark, 2013) although the criteria can require multiple experiments and has been reported to be unsuitable for epoxy systems below 80 °C (Lange *et al.*, 2000). The G'/G'' criteria has been widely adopted as a method for gelation determination of epoxy resins; it has shown to correlate with other criteria such as steady state viscosity extrapolations (Tung and Dynes, 1982), TMA experiments (Yu *et al.*, 2005), the G' frequency independence during rheology and strain measurements (Harsch *et al.*, 2008). The G'/G'' crossover has been shown to be obtainable at the cross-linking temperatures of 50 - 70 °C and these were used in the current study (Cheng *et al.*, 1994).

The repeatability of the G'/G'' crossover method for defining gelation was investigated by undertaking five repeat experiments at 70 °C. A mean G'/G'' crossover time of 68 minutes was recorded with a standard deviation of 2.3 minutes as summarised in Table 4.9. Hence, the capability to obtain repeatable gelation approximations was demonstrated and lies within the variation range reported by Yu *et al.* (2005) of 10% for an epoxy system.

Table 4.9 Repeatability of gelation times during the cross-linking of LY3505/XB3403 at 70 °C.

<b>Experiment</b>	<b>G'/G'' (Minutes)</b>
<b>1</b>	61.0
<b>2</b>	57.3
<b>3</b>	57.2
<b>4</b>	60.1
<b>5</b>	54.7
<b>Mean</b>	58.0
<b>S.D.</b>	2.3

The change in magnitude of  $G'$  and  $G''$  during isothermal cross-linking at 50, 60 and 70 °C is presented in Figures 4.22 (a) and (b) and the gelation times are presented in Table 4.10.

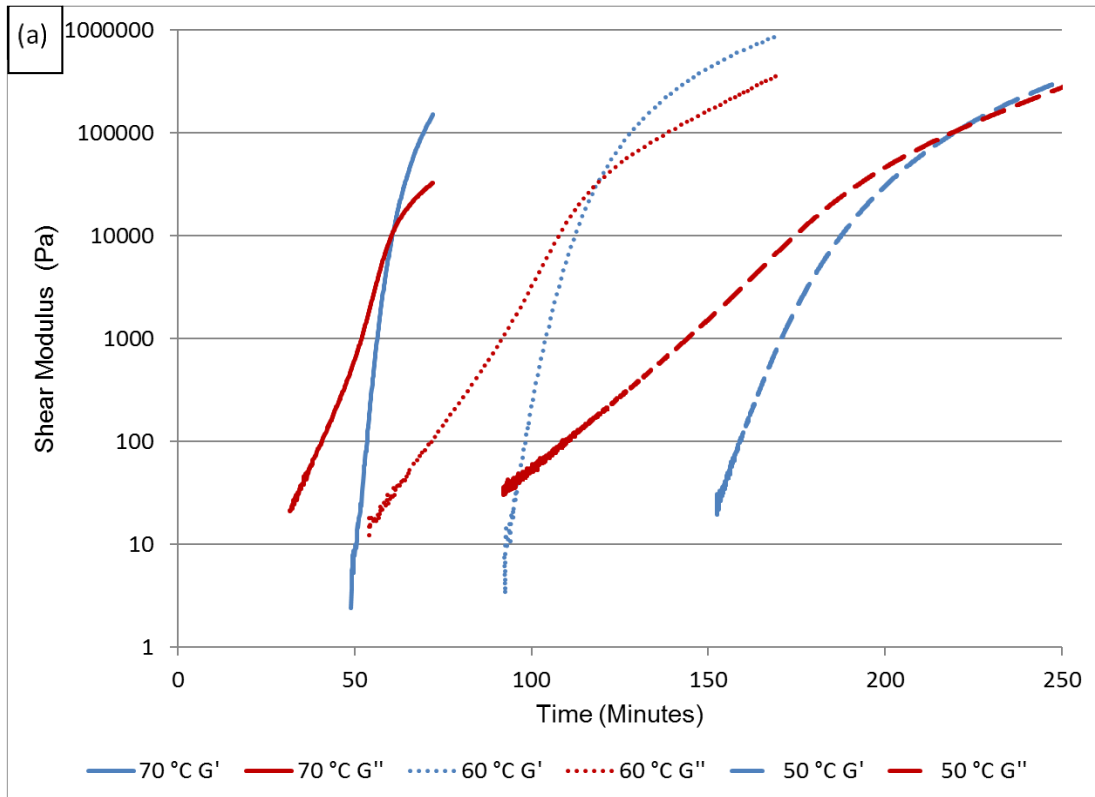


Figure 4.22 Evolution of  $G'$  and  $G''$  during the cross-linking of LY3505/XB3403 at specified isothermal temperatures: (a) Experiment 1.

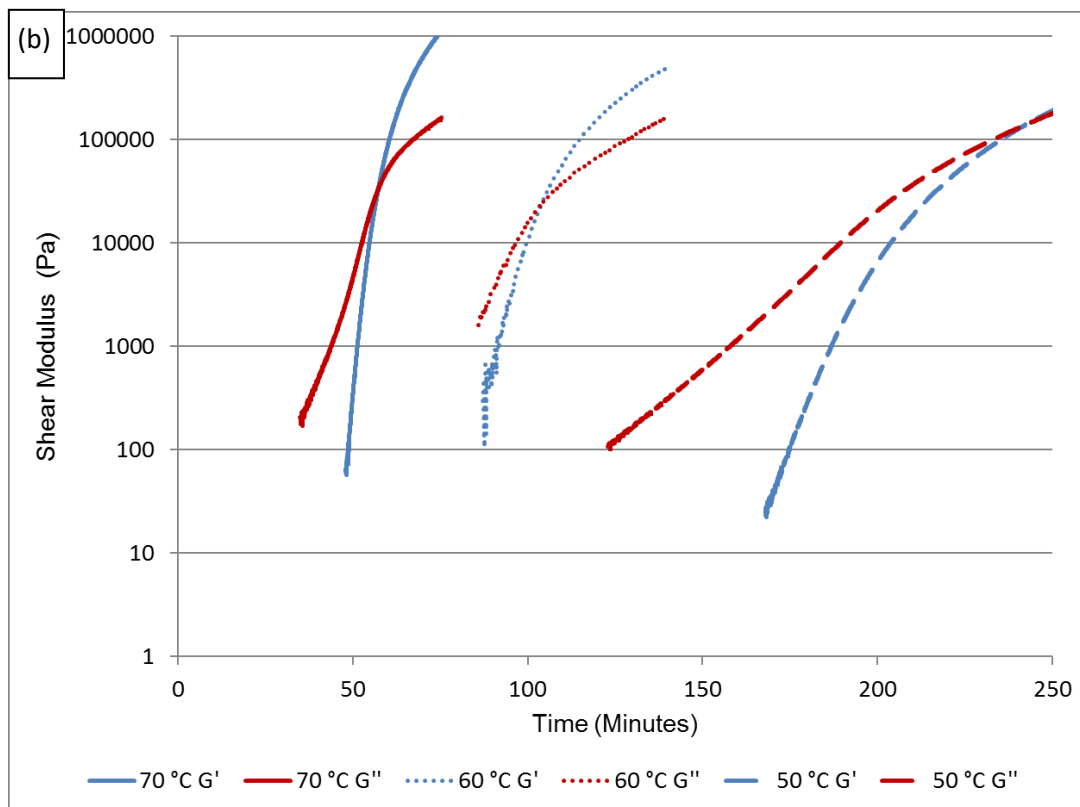


Figure 4.22 (continued) Evolution of  $G'$  and  $G''$  during the cross-linking of LY3505/XB3403 at specified isothermal temperatures: (b) Experiment 2.

Table 4.10 Gelation times at various isothermal temperatures and the corresponding degree of cure (DoC) when cross-correlating with the FTIRS and DSC data.

<b>Isothermal Cross-linking Temperature (°C)</b>	<b>Average <math>G'</math>, <math>G''</math> Crossover (minutes)</b>	<b>Average DoC via FTIRS at Time of <math>G'/G''</math></b>	<b>Average DoC via DSC at Time of <math>G'/G''</math></b>
<b>50 °C</b>	223	72	67
<b>60 °C</b>	112	65	64
<b>70 °C</b>	61	72	64

As expected, the evolution of the mechanical properties and appearance of gelation were delayed at lower temperatures. The gelation time of 105-125 minutes at 60 °C

agrees with the manufacturer's data sheet (Huntsmann, 2017). It has been reported that gelation of a thermosetting resin system is independent of the cross-linking temperature and it occurs at a constant degree of cross-linking (Chambon, 1987; Lange *et al.*, 2000; Yu *et al.*, 2005). Upon inspection of the DSC and FTIRS data presented in Table 4.10, gelation appeared to occur at a degree of cross-linking between 64-74% and this is seen to correlate with the theoretical gelation point calculated using Equation 2.15. The discrepancy in the cross-correlated conversion at gelation between the rheological and DSC/FTIRS data sets may be explained by:

- (i) Inaccuracies when cross-correlation between differing thermal analytical techniques are present. These could be due to the differing sample sizes, thermal environment and thermal management methods of rheology, DSC and FTIRS (Degamber and Fernando, 2004; Pandita *et al.*, 2012).
- (ii) Discrepancies in the FTIRS and DSC degree of cure data, as shown in Figure 4.18.

Overloading of the transducer due to a logarithmic increase in the resin viscosity during cross-linking can be observed in Figure 4.23. Similar to Figure 4.22, an initial period of noise was present during the initial stages of cross-linking due to the inability of the transducer to detect low viscosity liquids. The viscosity then increases logarithmically until termination of the experiment.

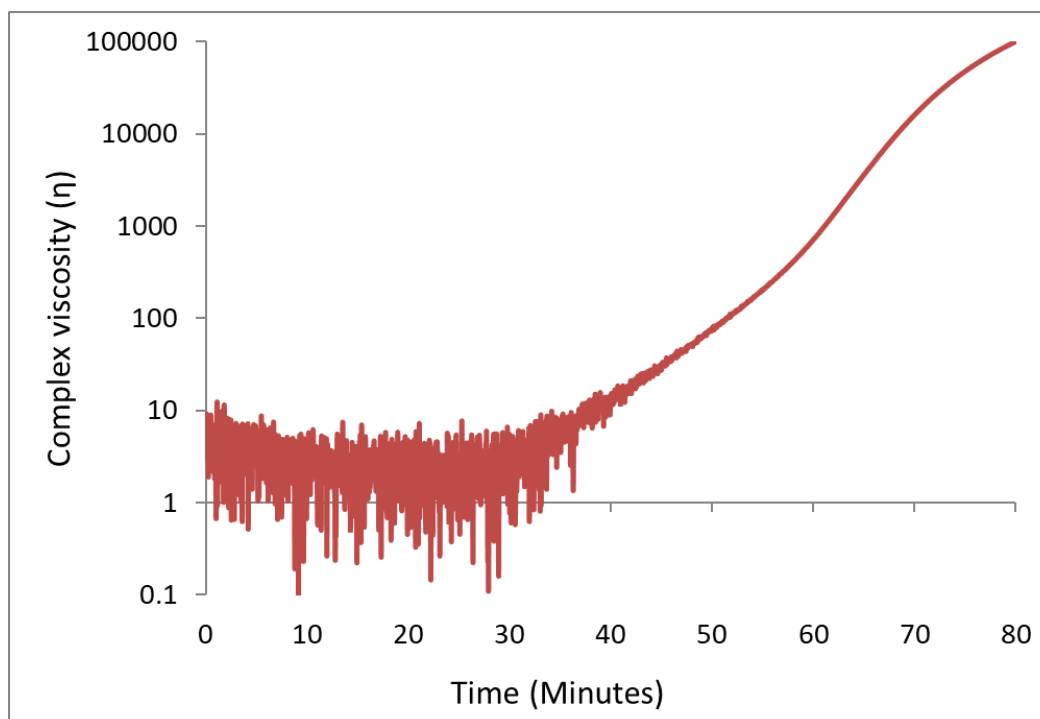


Figure 4.23 Typical plot of the evolution of the complex viscosity during the cross-linking of LY3505/XB3403 at 70 °C.

#### 4.5 Summary of Conventional Methods for Characterising Cross-linking Reactions

The isothermal cross-linking of the LY3505/XB3403 resin system was analysed using DSC, FTIR spectroscopy and rheology. The degree of cure data from FTIR spectroscopy showed a higher final conversion in comparison to the DSC data. This was attributed to the differing thermal control, thermal environment and sample size. The baseline construction of DSC data, the instruments sensitivity and sample distribution may also have influenced the results.

The auto-catalytic model used showed a good correlation with each data set, although discrepancies were observed during the later stages of cross-linking. The activation energies were comparable to previously reported values. The kinetic

results obtained in this Chapter will be used in later sections for comparing the conventional methods with hyphenated cure monitoring techniques, which is the main theme of this thesis.

The gelation times for LY3505/XB3403 were determined by the  $G'/G''$  crossover when conducting isothermal parallel plate rheological experiments. A clear  $G'/G''$  crossover was obtained, which correlated with values quoted by the supplier.



## **5. CURE MONITORING USING SIMULTANEOUS DIFFERENTIAL SCANNING CALORIMETRY AND THE FRESNEL REFLECTION SENSOR**

### **5.1 Development of the Hyphenated Technique for the Differential Scanning Calorimetry**

This chapter reports on the development of a hyphenated thermal and optical analytical technique by incorporating a Fresnel reflection sensor (FRS) into a differential scanning calorimeter (DSC). The technique was used to track the cross-linking kinetics of the epoxy/amine resin system LY3505/XB3403 and an aerospace resin provided by Cytec/Solvay.

#### **5.1.1 Calibration of the Fresnel Reflection Sensor using Standard Refractive Index Oils**

The response of the FRS to a range of standard refractive index oils, when placed between the two prisms of an Abbe refractometer was investigated. A thermocouple was also placed between the prisms, in contact with the liquid, to obtain independent temperature data of the liquid that was contained between the prisms; this was in addition to that obtained from the instrument display panel. After a five-minute temperature stabilisation period, the maximum temperature variation recorded from the thermocouple was  $\pm 0.3$  °C.

The response of five repeat measurements from the Abbe refractometer and the FRS, using reference oils with refractive indices of 1.4000, 1.4500, 1.5000, 1.6000 and 1.7000, between 25 to 40 °C are shown in Figures 5.1 (a) and (b). Table 5.1 presents the values recorded manually from the Abbe refractometer at 25 °C; they are in excellent agreement with those supplied by the manufacturer.

Upon increasing the temperature, a linear decrease in the refractive index is observed for each oil. The thermo-optic coefficient of the oils was determined by the gradient of the Abbe refractometer data ( $dn/dT$ ) in Figures 5.1 (a) and (b); these values are listed alongside the data specified by the manufacturer in Table 5.1. A good correlation is observed between the three datasets. The coefficient of determination ( $R^2$ ) values shown in Figure 5.1 all lie above 0.94 indicating that the regression equations account for at least 94% correlation in the data. Error bars were not displayed as the scatter was negligible.

On heating the oil exhibiting a refractive index of 1.4, Figure 5.1(a) shows that an increase in the normalised Fresnel reflection is observed as the contrast with the fibre core refractive index ( $n_f=1.45$ ) is increased. Similarly, upon heating the oil with a refractive index of 1.45, an increase in the normalised Fresnel reflection is observed, although the magnitude of the reflection is relatively small due to the similarity in refractive index of the oil and the fibre core ( $n_s=1.45$ ).

Ide and Yuskel (2016) calibrated an FRS system using defined concentrations of glycerol exhibiting refractive index values between 1.33 and 1.44, with the sensor fibre-core with a refractive index of 1.45. The magnitude of the FRS response

decreased as the refractive index of the glycerol was increased and this correlates with the results presented in Figure 5.1(a).

With reference to Figure 5.1(b), the magnitude of the normalised Fresnel reflection decreases upon increasing the temperature, due to the increased refractive index offset with the core. A more negative gradient is observed as the offset between the reference oil with the fibre increases. Chen *et al.* (2011) also used an FRS system with a fibre core of 1.45. The sensor response was tested from 50 – 120 °C with cross-linked epoxy resin samples surrounding the sensor. The refractive indices of the resins ranged from 1.52 to 1.56. A near-linear reduction in the magnitude of the Fresnel reflection was observed with heating. The results correlate with that displayed in Figure 5.1(b).

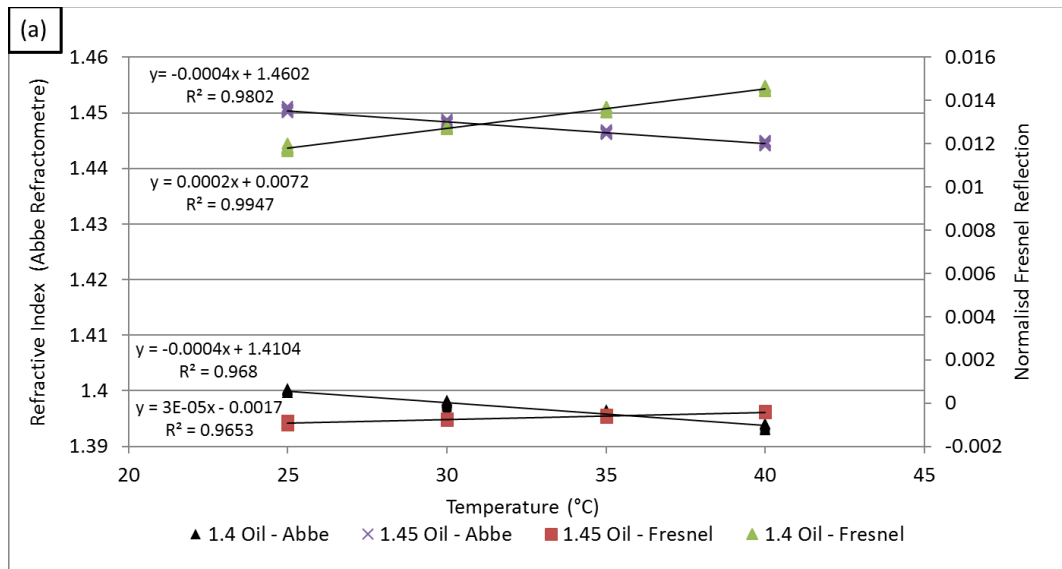


Figure 5.1 Simultaneous data acquisition from the Abbe refractometer and a FRS for standard refractive index oils between 25 to 40 °C. Five repeat readings are shown at each temperature: (a) Oils with a refractive index 1.4 and 1.45.

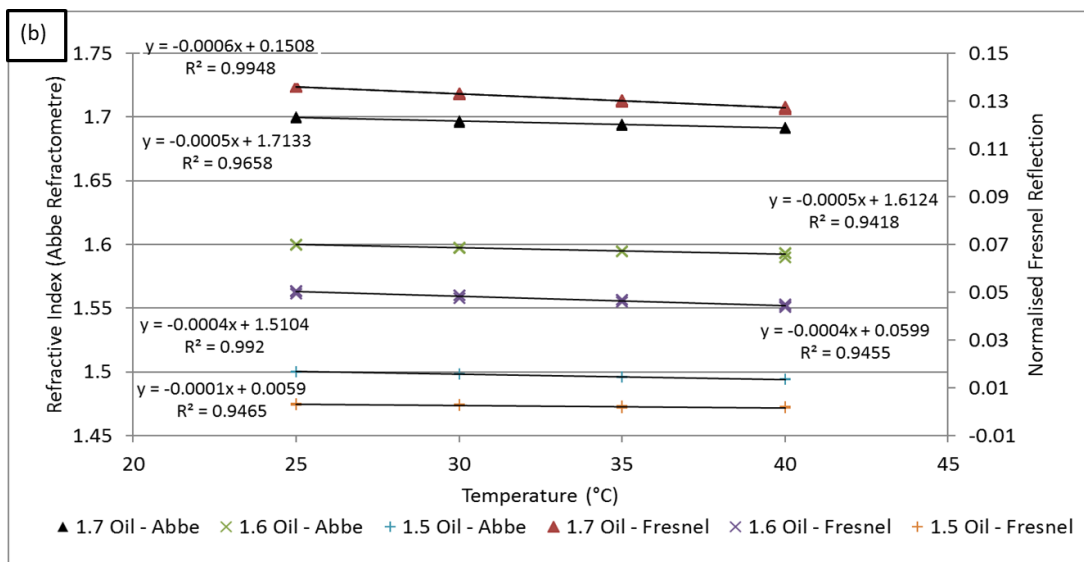


Figure 5.1 (continued) Simultaneous data acquisition from the Abbe refractometer and an FRS for standard refractive index oils between 25 to 40 °C. Five repeat readings are shown at each temperature: (b) Oils with a refractive index of 1.5, 1.6 and 1.7.

Table 5.1 Refractive indices and thermo-optic coefficients quoted by the manufacturer (Cargille, USA) and those obtained experimentally via the Abbe refractometer.

Refractive Index at 25 °C		Thermo-optic Coefficient (°C <sup>-1</sup> )	
Manufacturer's Data	Experimentally Derived	Manufacturer's Data (dn/dT)	Experimentally Derived (dn/dT)
<b>1.4000</b>	1.4008 ±0.0004	-0.0004	-0.0004
<b>1.4500</b>	1.4504 ±0.0003	-0.0004	-0.0004
<b>1.5000</b>	1.5003 ±0.0002	-0.0004	-0.0004
<b>1.6000</b>	1.5998 ±0.0002	-0.0004	-0.0005
<b>1.7000</b>	1.6997 ±0.0004	-0.0005	-0.0006

The FRS data were normalised to its response in air, prior to its immersion in the refractive index oil. As discussed in Section 2.4.6, Chapter 2, the normalised data, for

each oil, were plotted alongside the predicted Fresnel reflection at normal incidence using Equation 2.10:

$$R = \left( \frac{n_1 - n_2}{n_1 + n_2} \right)^2 \dots\dots\dots \text{Equation 2.10}$$

where

$n_1$  = refractive index of fibre core,

$n_2$  = refractive index of the liquid surrounding the cleaved end,

$R$  = Fresnel reflection coefficient at normal incidence.

(Crosby *et al.*, 1996; Sampath *et al.*, 2015; Singh, 2015; Goldstein, 2016).

The experimental data compares favourably with the theoretical prediction; whereby a parabolic relationship is observed. The oils with a lower refractive index than the fibre core show an increase in Fresnel reflection as the temperature is raised (Figure 5.1(a)), whilst those above the fibre core index experience a decrease (Figure 5.1(b)). In accordance with Equation 2.10, an increased mismatch between  $n_1$  (index of the fibre core) and  $n_2$  (index of the oil) will result in larger Fresnel reflections. The data presented in Figure 5.2 reflects observations made during similar studies by Crosby *et al.* (1996) and Hewa-Gamage and Chu (2002). Small differences between the two data sets can be attributed to measurement inaccuracies as the refractive indices of the sample approach that of the optical fibre core.

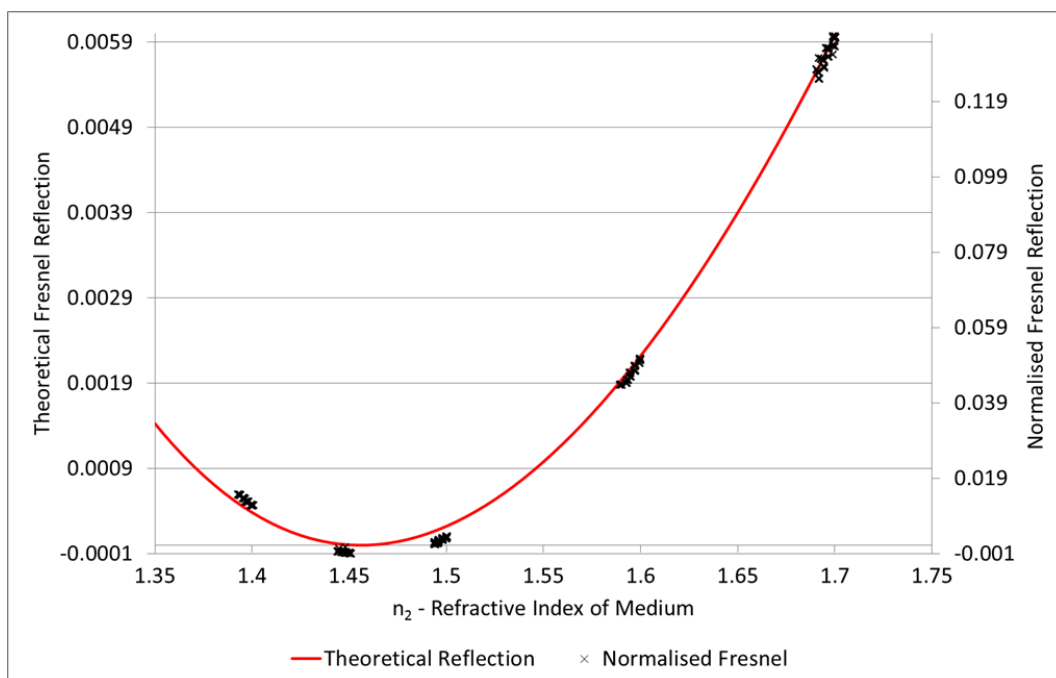


Figure 5.2 Comparison of theoretical Fresnel reflection alongside the experimentally-derived FRS data using standard refractive index oils between 25 and 40 °C.

### 5.1.2 Stability of the Light Source and Detector

The intended use of the FRS was to monitor isothermal cross-linking reactions over 10 hours. Hence, the long-term stability of the light source and detector were investigated. Figure 5.3 shows the response of the FRS at room temperature for 15 hours within the DSC chamber. With reference to previous fibre-optic Fresnel reflection sensing systems demonstrated by Chang-Bong and Chin (2004), Buggy *et al.* (2007) and Xu *et al.* (2013), they utilised a 2x2 coupler to split the power equally between a Fresnel sensor and a power meter, where the power meter allowed normalisation of the data to the light source. The laser driver used in the current study exhibited temperature and current-control of  $\pm 0.005$  °C and  $\pm 0.1\%$  respectively. The long-term stability of the instrumentation is shown in Figure 5.3. The small fluctuations can be attributed to fluctuations in temperature, humidity and power,

although the magnitude was deemed insignificant. The stability of the light source and detector allowed for a simpler system to be used without requiring a power meter.

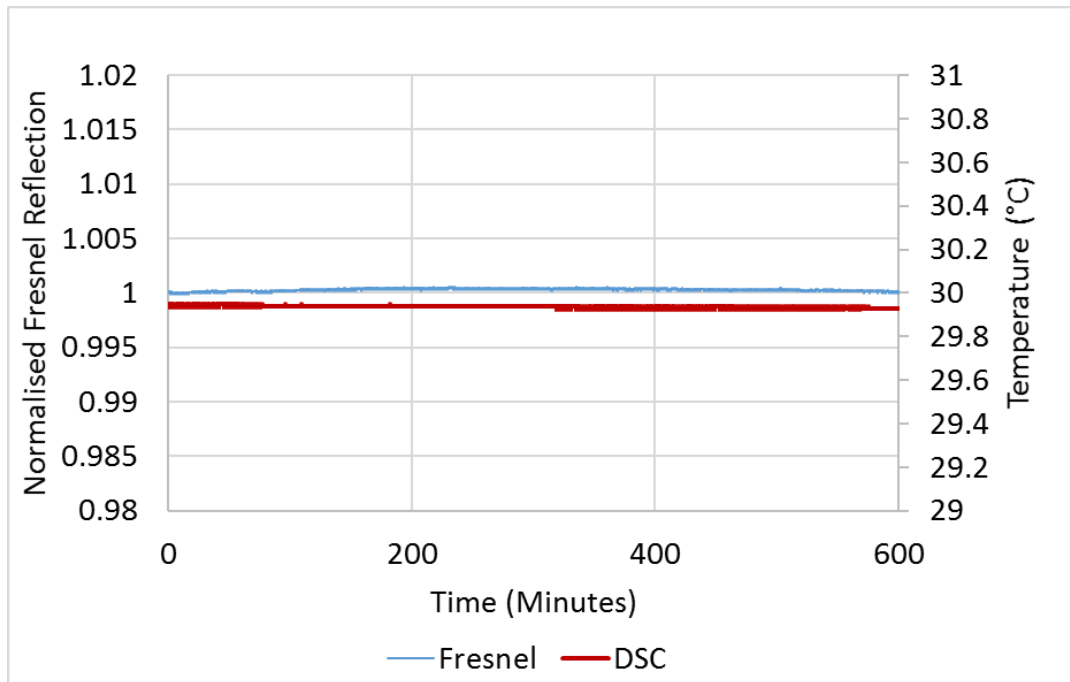


Figure 5.3 Fresnel reflection data obtained in air at 30 °C using hyphenated DSC/Fresnel.

### 5.1.3 Interaction between the Fresnel Reflection Sensor and the Differential Scanning Calorimeter Sample Pan

The integration of the FRS sensor into the DSC meant that it was in close proximity to the base of a DSC pan. An investigation was carried out to establish the conditions required to minimise the magnitude of the reflected light from the base of the pan from being coupled back into the FRS. Figure 5.4 illustrates the magnitude of the Fresnel reflections for specified substrates within the DSC as a function of distance between the end-face of the cleaved optical fibre and the pan. It is seen that when the end-face of the cleaved optical fibre (FRS) is above 1.2 mm, the reflection from the substrates is

negligible. The heights of conventional aluminium and alumina DSC pans are 15 and 25 mm respectively. It was required to minimise the reflection from the substrate coupling back into the cleave-end of the optical fibre; this was necessary to ensure that the acquired data represented that corresponding to Fresnel reflections exclusively. A few techniques were attempted to reduce the reflectivity of the conventional aluminium DSC pans, including abrasion with P800 silicon carbide abrasive paper and sputter coating with carbon, as seen in Figure 5.4. However, these were not successful, and the decision was to use alumina pans as they displayed a significantly lower reflectivity at the measured heights. Hence alumina pans were chosen for the hyphenated DSC/FRS experiments. This decision was a compromise, as alumina has a relatively low thermal conductivity compared to aluminium. A substrate or pan with a high thermal conductivity is desired to enable efficient heat transfer between the furnace compartment of the calorimeter and the sample.

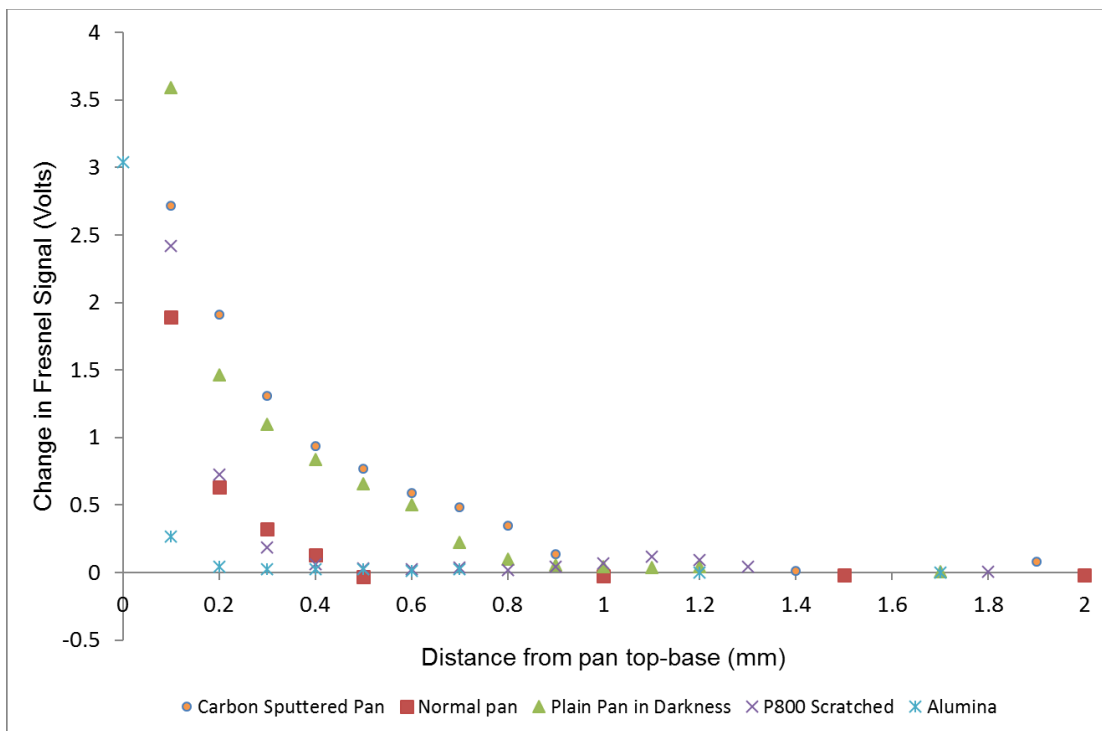


Figure 5.4 Response of FRS as a function of height from the base of DSC pan types.



#### 5.1.4 Calibration of the Differential Scanning Calorimeter

The FRS was lowered into the DSC using the micrometer translation stage shown in Figure 3.4, Chapter 3. The sensor was positioned approximately 1 mm from the base of the DSC pan. The DSC was calibrated using indium with alumina pans. Data acquisition of the FRS was synchronised with the DSC by momentarily disengaging the light source which produced a downward 'spike' in the data. Figure 5.5 displays the thermogram for indium where the calibration was conducted with and without illuminating the FRS. The enthalpy of fusion for indium was within the  $\pm 0.6 \text{ Jg}^{-1}$  recommended tolerance (Gmelin, 1995). The average enthalpy of fusion with and without the light source was 28.73 and 28.45 J/g respectively. The small standard deviation indicates adequate repeatability. The limits of the enthalpy integration were between 155.5 and 162 minutes and the FRS induced a 0.23 J/g average increase in the measurement. Therefore, the FRS introduced a 0.00065 J/s enthalpy increase.

The melt onsets for six repeat experiments were within the recommended  $\pm 0.3 \text{ }^\circ\text{C}$  tolerance (Gmelin, 1995). An increase of 0.31  $^\circ\text{C}$  in the melt onset was observed when the light source was activated. The small standard deviations for the various parameters are summarised in Figure 5.5 and they represent six individual experiments.

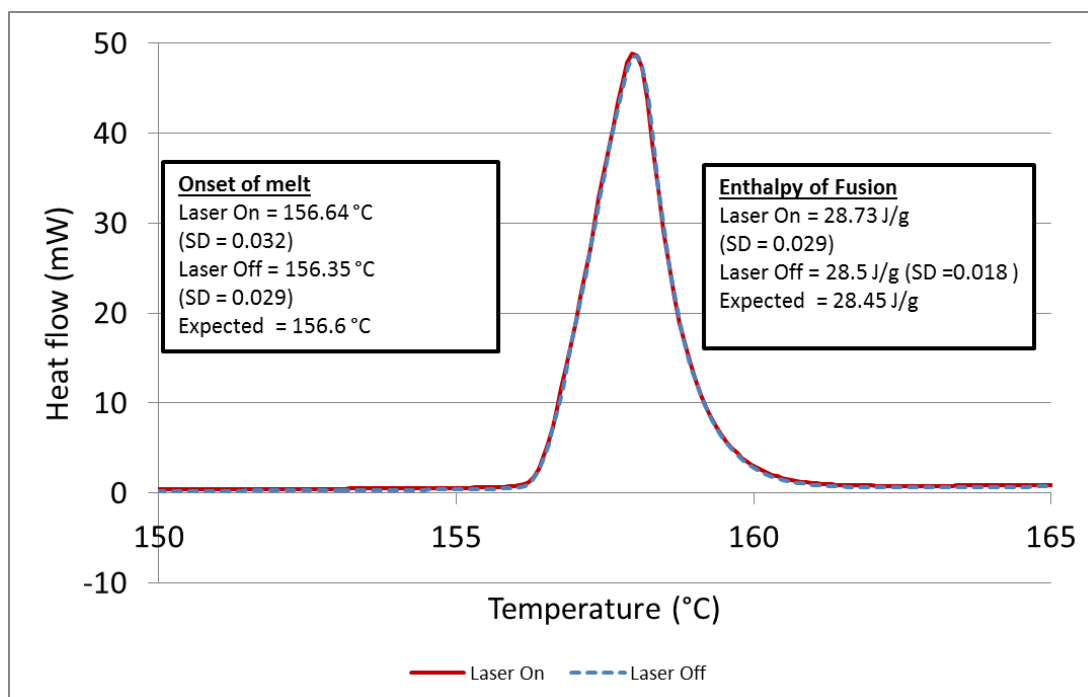


Figure 5.5 Summary of the enthalpy and melt onset for indium using the DSC/Fresnel system. The effect of the light source is also included. The data are derived from six independent experiments.

### 5.1.5 Impact of Light Source on the Differential Scanning Calorimeter

The impact of the light source on the stability of the DSC was investigated when the probe was in contact with the alumina pan. The temperature within the DSC was maintained at 30 °C for 30 minutes. The light source was switched on for five minutes and then switched off for a further five minutes; this sequence was repeated a few times. The effect of this light on/off sequence is shown in Figure 5.6(a). Upon illumination of the sample compartment, an abrupt “exothermic” event is detected by the DSC when the laser was switched on and an equally rapid return to the baseline is observed when the light source was switched off. The magnitude of this apparent exotherm caused by the laser is  $0.54 \pm 0.0018$  mW. From Figure 5.7(a) variability is

observed for each on/off cycle. This may be attributed to the upward slope in the baseline of the DSC signal.

A similar experiment was undertaken where the alumina pan was filled with LY3505 resin and the FRS was positioned 100  $\mu\text{m}$  below the surface of the resin and approximately 1 mm from the base of the pan. The output from this experiment is shown in Figure 5.6(b). The resin had a focusing effect upon the heat generated by the light source and caused a 0.57 mW exothermic shift in the baseline. This may be due to the resin absorbing the heat generated by the laser source whereas previously the heat dissipated in air. With reference to 5.7(b), similar magnitudes of the FRS upon the DSC were recorded upon engaging the laser power on and off.

A positive gradient in the DSC trace in Figure 5.6(a) indicates the calorimeter had not established thermal equilibrium. In Figure 5.6(b), the introduction of the LY3505 resin to the pan and sensor position of approximately 1 mm from the base of the pan enabled thermal equilibrium to be achieved as evidenced by the relatively flat baseline. This provided appropriate conditions for isothermal cross-linking experiments as a horizontal baseline facilitates calculation of the enthalpy of reaction.

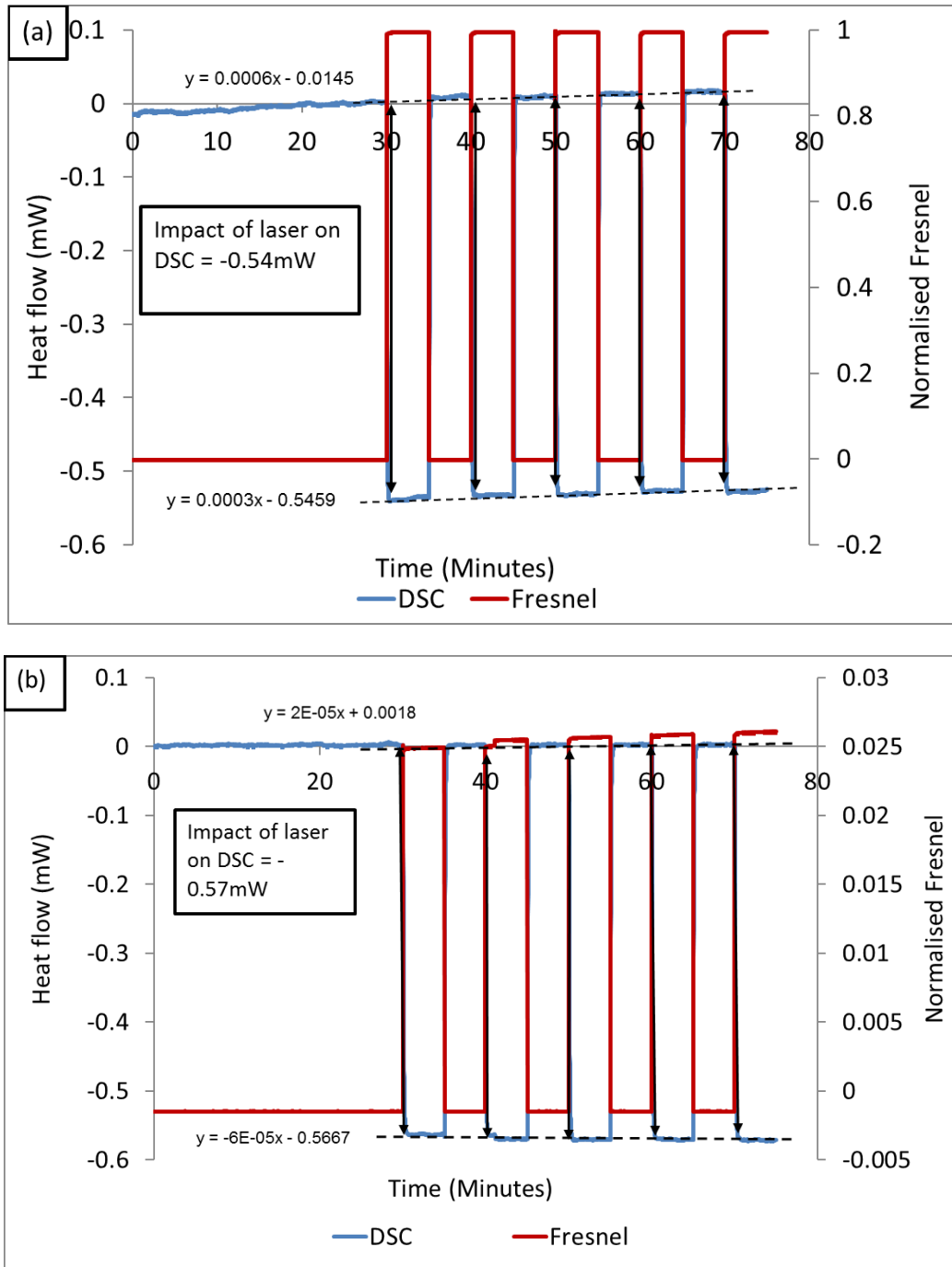


Figure 5.6 Impact of the Fresnel light source on DSC when the cleave-end of the optical fibre was (a) in contact with base of empty alumina pan and (b) 1 mm from the base of a pan containing LY3505 resin.

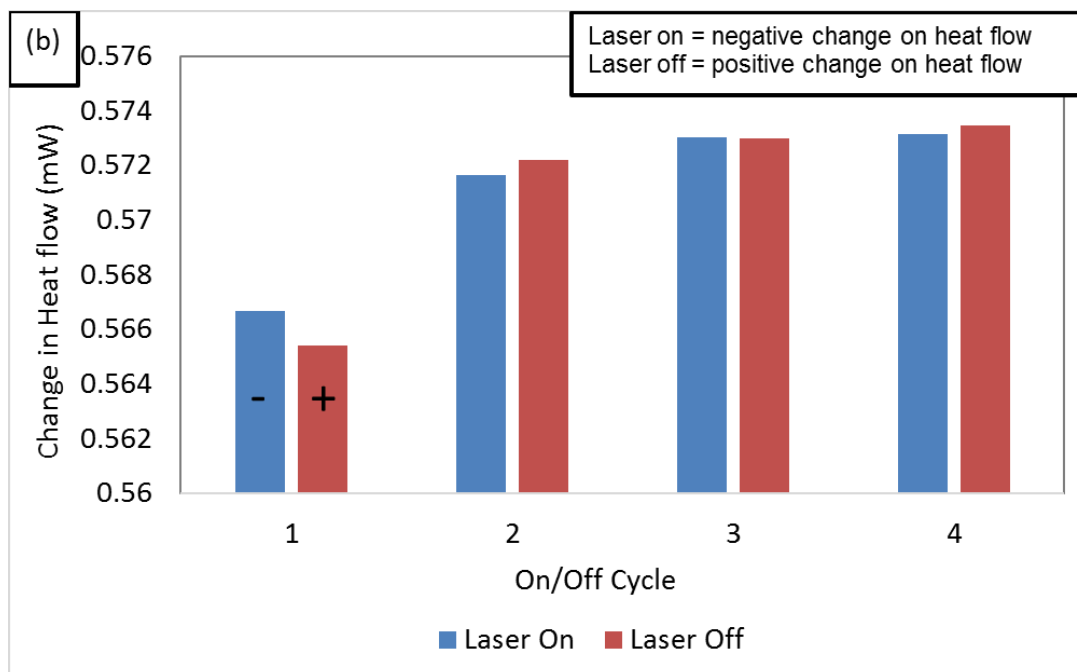
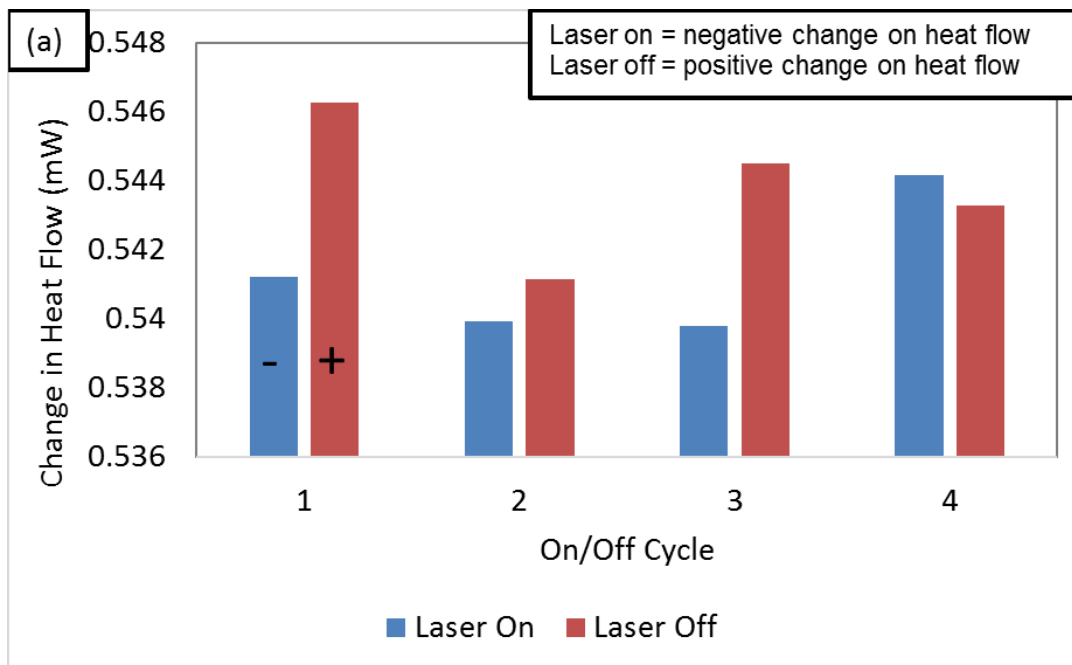


Figure 5.7 Magnitude of the FRS upon the DSC for each on/off cycle for (a) the sensor in contact with an empty alumina pan and (b) the sensor 1 mm from the base of an alumina pan containing LY3505 resin.

## **5.2 Hyphenated Differential Scanning Calorimetry/Fresnel using the LY3505/XB3403 Resin System**

### **5.2.1 Isothermal Cross-linking**

The response of the DSC during isothermal cross-linking at 50, 60 and 70 °C is shown in Figures 5.8 (a) and (b) for data obtained during conventional DSC and DSC/FRS, respectively. The same sample loading method and heating regime were used as with the conventional DSC experiments. Alumina pans were used for FRS/DSC experiments due to their low reflectivity.

The cross-linking experiments completed at 50 °C using the FRS/DSC showed a peak reaction after 56 and 66 minutes; this correlated with the conventional DSC data. The enthalpy of the cross-linking showed smaller values when compared with the conventional DSC data, where the values remained within 4%.

As expected, an increased enthalpy and peak of reaction were observed upon increasing the cross-linking temperature to 60 and 70 °C. The results compared favourably with the conventional DSC experiments and previously reported DSC and FTIR data presented in Tables 4.3 and 4.6. From Table 5.2, similar values were obtained during DSC/FRS when compared with conventional DSC.

Discrepancies in the data during experiments undertaken at 70 °C, as presented in Table 5.2, may be attributed to inhomogeneous mixing. A five-minute mixing period and subsequent visual inspection of the resin may have been insufficient to ensure a homogenous mixing.

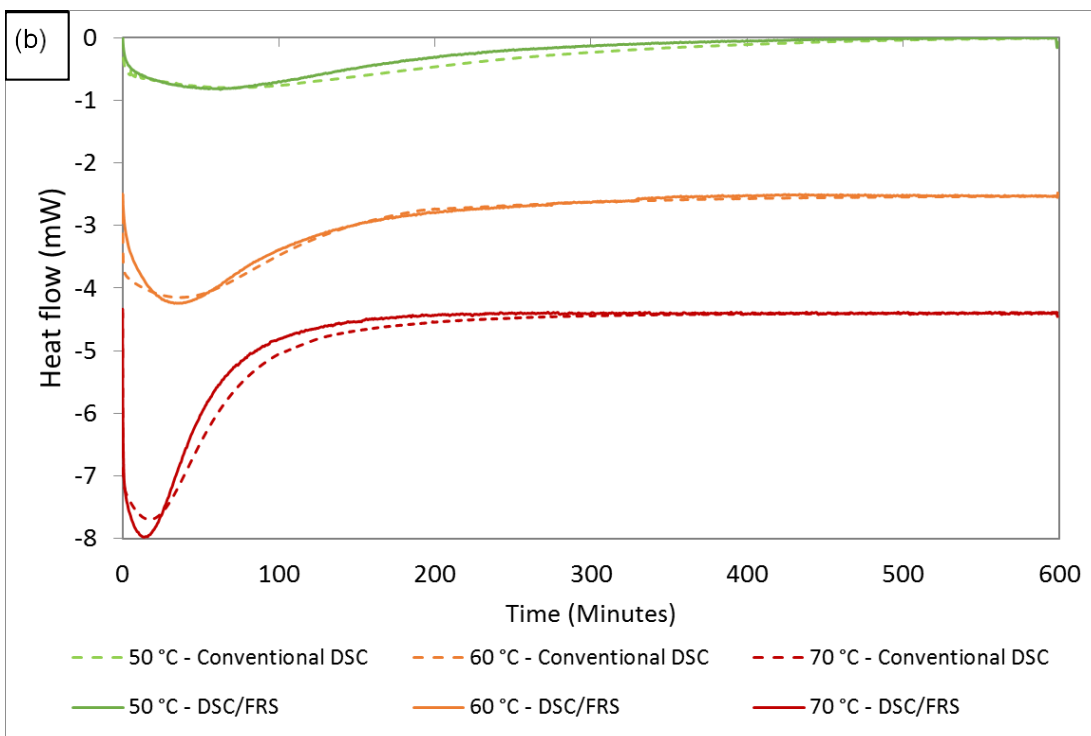
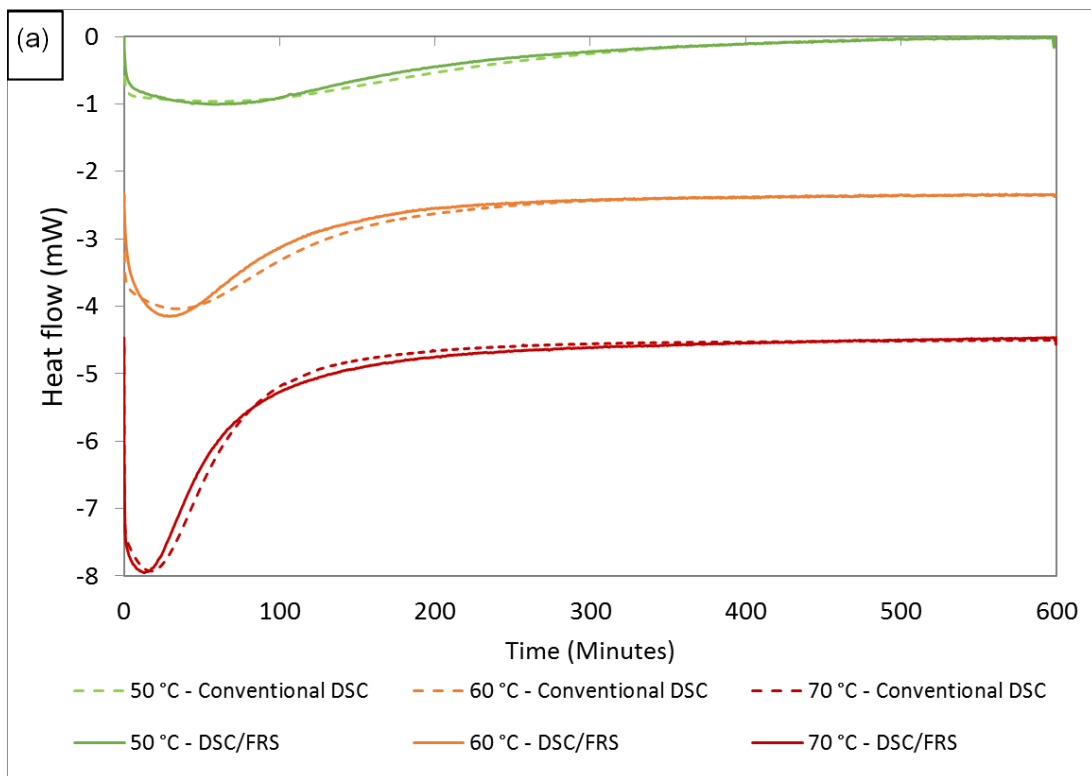


Figure 5.8 DSC traces for cross-linking of LY3505/XB3403 obtained using the hyphenated DSC/Fresnel and conventional techniques at specified isothermal cross-linking temperatures: (a) Experiment 1 (b) Experiment 2.

Table 5.2 Summary of the enthalpy of crosslinking and other relevant parameters from the conventional and hyphenated DSC/FRS experiments during isothermal experiments. DoC = Degree of cure

Isothermal Cross-linking Temperature	FRS/DSC: DSC		
	$\Delta H$ (J/g)	Time to Peak Exotherm (minutes)	DoC after 600 minutes
50 °C - Experiment 1	314:335	59:58	80%:84%
50 °C - Experiment 2	305:317	66:74	78%:80%
60 °C - Experiment 1	348:337	36:28	86%:85%
60 °C - Experiment 2	324:358	41:33	85%:90%
70 °C - Experiment 1	375:379	8:16	94%:95%
70 °C - Experiment 2	360:371	16:15	91%:94%

The FRS data were normalised by its output when measured in air. Similar normalised Fresnel reflection values were observed for each sensor when immersed in the LY3505/XB3403 at 30 °C as shown in Table 5.3. Upon heating to the desired isothermal cross-linking temperature, a decrease in the signal occurred as the refractive index of the resin system was reduced. The magnitude of the decrease was greatest for experiments completed at 70 °C. The FRS data were plotted to show the increase during isothermal cross-linking in Figures 5.8 (a) and (b), together with the degree of cross-linking determined via the DSC using the data in Figures 5.7 (a) and (b).



Table 5.3 Normalised Fresnel reflection readings during cross-linking experiments.

Experiment	Normalised Fresnel Reflection Data			
	Start of experiment at 30 °C.	At desired isothermal cross-linking temperature.	After 600 minutes at isothermal cross-linking.	Increase during isothermal cross-linking.
50°C - Experiment 1	0.0203	0.0175	0.0349	0.0174
50°C - Experiment 2	0.0201	0.0179	0.0357	0.0178
60°C - Experiment 1	0.0199	0.0162	0.0350	0.0188
60°C - Experiment 2	0.0217	0.0169	0.0348	0.0179
70°C - Experiment 1	0.0205	0.0155	0.0345	0.0190
70°C - Experiment 2	0.0197	0.0151	0.0338	0.0187

Upon reaching the isothermal value, an increase in the signal is attributed to cross-linking. As the reaction proceeds, the average density and molecular weight increase giving a corresponding increase in the refractive index. The FRS response increases during cross-linking as the difference between the refractive indices of the fibre core and the cross-linking resin increases. This has previously been reported during the cross-linking of epoxy resin systems by Crosby *et al.* (1996), Liu *et al.* (1997) and Mahendran *et al.* (2010).

To compare the FRS and DSC datasets, three positions were determined: the point where the plot deviates from the initial linear evolution (Point A); the crossover of the extrapolation of the initial and final linear regions (Point B) and; the point where the lot deviates from the final linear evolution (Point C). The points are shown in Figures 5.9 (a) and (b) and compared in Figure 5.10. Each of the points occurs earlier at higher

temperatures due to the increased rate of cross-linking. The points occur at similar times for both measurements during each experiment. Figure 5.10 indicates a similar evolution of the thermal and optical signals during cross-linking at each temperature.

The initial rate of reaction for each experiment is indicated by the gradient of the FRS data upon reaching the desired isothermal cross-linking temperature and is shown in Figure 5.9 (a). The rate of reaction is higher at increased temperatures and correlates well with the conventional DSC data as presented in Table 5.4 and shown in Figure 5.11.

A lower rate of reaction toward the end of the experiments is likely to be due to the glass transition temperature of the cross-linking resin exceeding that of the isothermal cross-linking temperature causing vitrification. The rate of the reaction is quantified in Table 5.5 and shown in Figure 5.11. The greatly reduced reaction rate occurs after approximately 420, 330 and 275 minutes for the data obtained at 50, 60 and 70 °C, respectively. The increase in the FRS was greatest for the experiments performed at higher temperatures as presented in Table 5.5 and shown in Figures 5.9 (a) and (b).

The FRS shows a close agreement to the degree of cure obtained from the DSC. The graphs compare favourably as evidenced by the similar trend in the initial rate of reaction with temperature and the similarity for points A, B and C. This relationship between the refractive index and degree of cure obtained from the DSC has previously been demonstrated by Vacher *et al.* (2004) and Crosby *et al.* (1996), although their research was undertaken as independent or separate experiments. The current work has demonstrated the first hyphenated DSC/Fresnel reflection sensor-based technique.

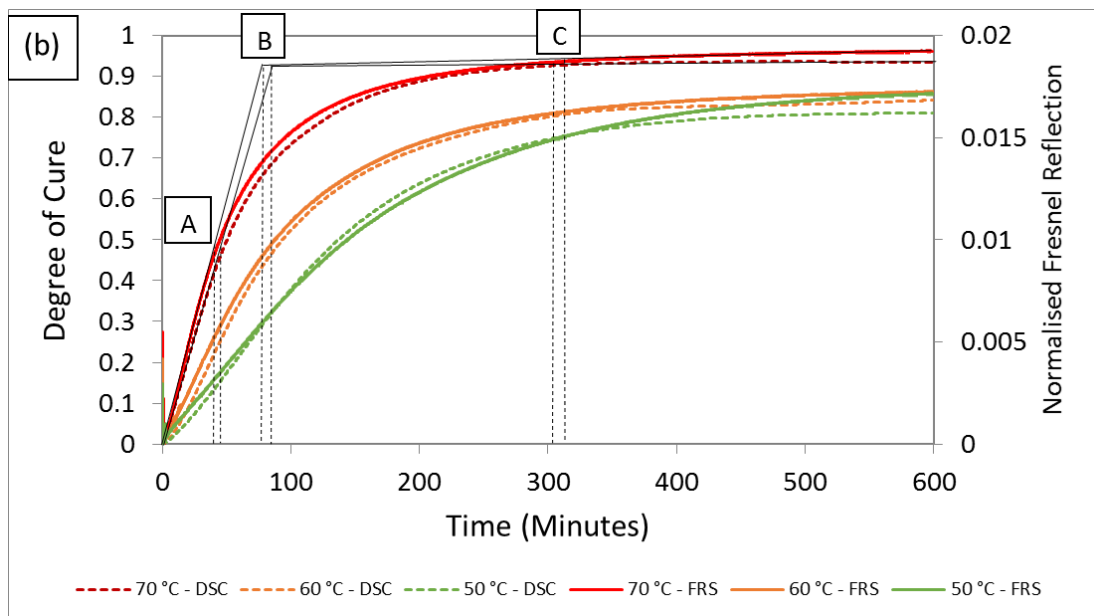
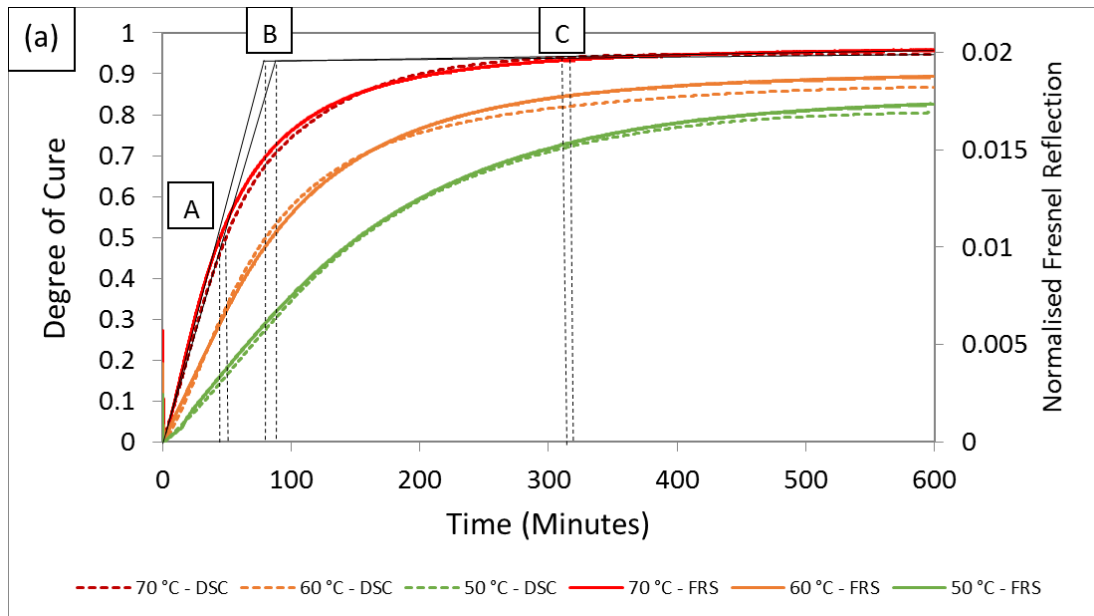


Figure 5.9 Simultaneous FRS/DSC data acquisition showing the degree of cross-linking using DSC and the normalised Fresnel reflection at isothermal cross-linking temperatures of 50, 60 and 70 °C: (a) Experiment 1; and (b) Experiment 2.

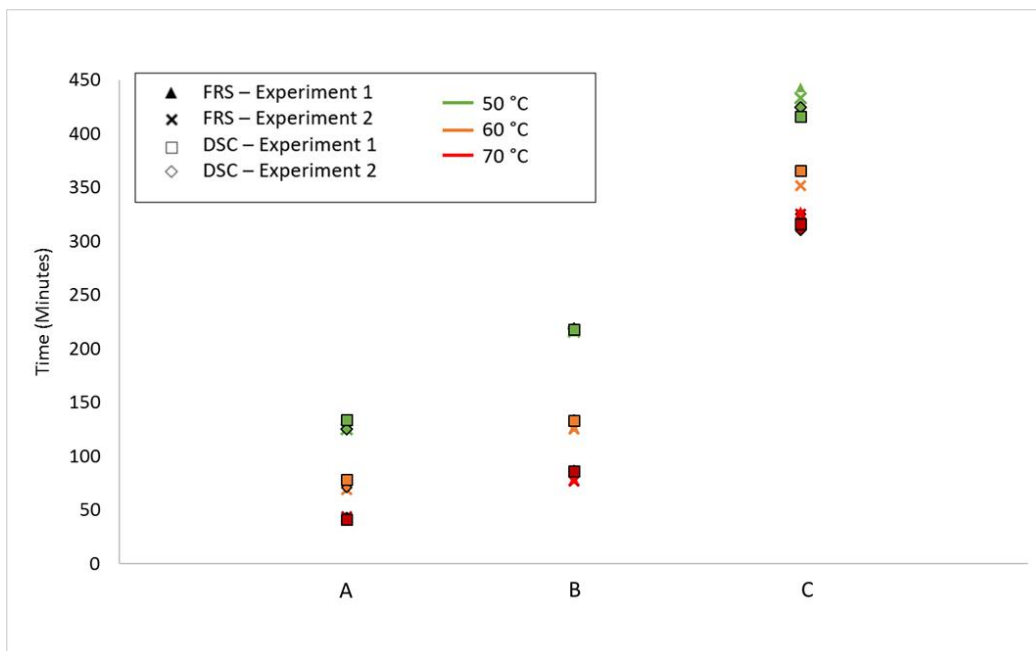


Figure 5.10 Time to reach points A, B and C during the cross-linking of LY3505/XB3403 at 50, 60 and 70 °C during DSC/FRS. A = Deviation from initial linear region; B = Intersection of extrapolation of initial and final linear regions; and C = Deviation of from final linear region. See Figures 5.9 (a) and (b)

Table 5.4 Initial rate of cross-linking during the cross-linking of LY3505/XB3403 as detected by the FRS and DSC.

Isothermal Cross-linking	Initial Rate of Cross-linking (0-50 Minutes)		
	da/dt		Normalised Fresnel Reflection/minute
	DSC/FRS: DSC Data	Conventional DSC	DSC/FRS: FRS Data
50 °C - Experiment 1	0.0033	0.0037	0.0005
50 °C - Experiment 2	0.0031	0.0035	0.0006
60 °C - Experiment 1	0.0071	0.0065	0.001
60 °C - Experiment 2	0.0062	0.0062	0.0009
70 °C - Experiment 1	0.0107	0.0119	0.0018
70 °C - Experiment 2	0.0105	0.0116	0.0018

Table 5.5 Rate of cross-linking of LY3505/XB3403 toward the end of the isothermal heating as detected by the FRS and DSC.

	Rate of Cross-linking towards the End of Cross-linking (550-600 Minutes)		
	da/dt		Normalised Fresnel Reflection/minute
Isothermal Cross-linking	DSC/FRS: DSC Data	Conventional DSC	DSC/FRS: FRS Data
50 °C - Experiment 1	2.E-04	1.E-05	2.E-07
50 °C - Experiment 2	1.E-04	1.E-05	3.E-06
60 °C - Experiment 1	1.E-04	8.E-05	3.E-07
60 °C - Experiment 2	3.E-05	1.E-04	2.E-06
70 °C - Experiment 1	1.E-06	2.E-05	6.E-07
70 °C *- Experiment 2	5.E-06	7.E-05	9.E-07

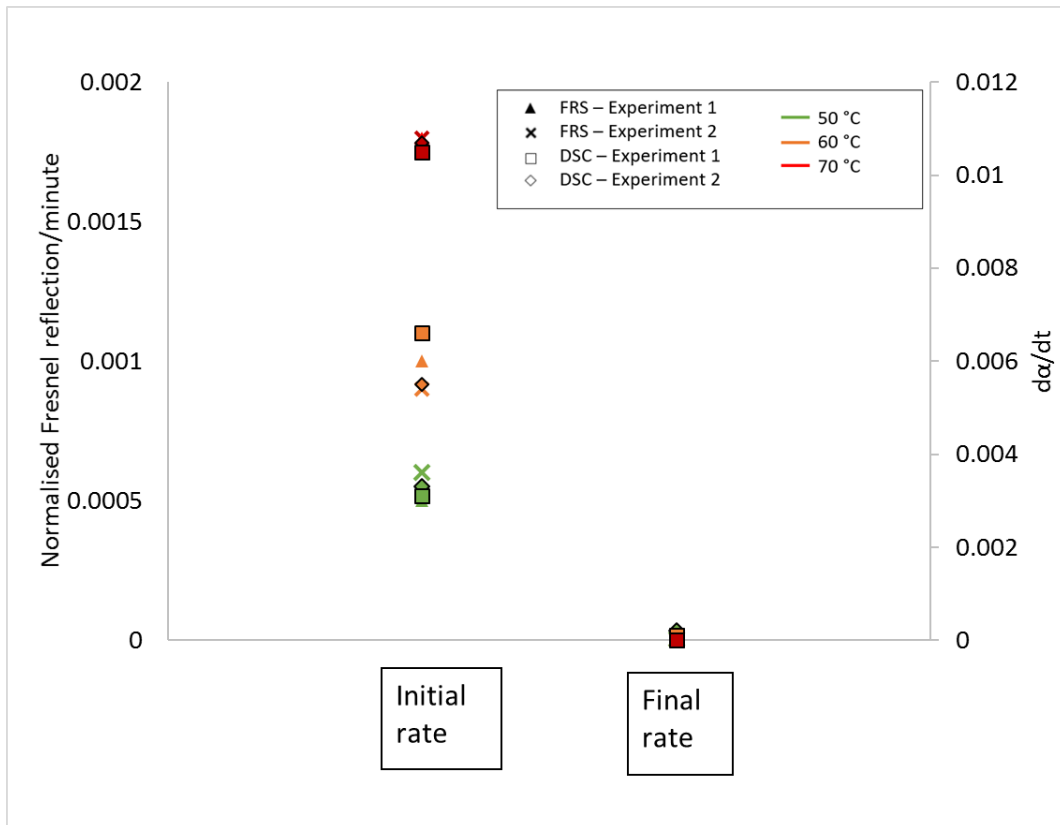


Figure 5.11 Magnitude of gradient of the FRS and DSC signal at the beginning and end of the cross-linking experiments. See Figure 5.9.

## 5.2.2 Isothermal Cross-linking Kinetics

The autocatalytic model (Equation 4.1) was plotted alongside the isothermal kinetic data obtained using the hyphenated DSC/Fresnel at 50, 60 and 70 °C, as shown in Figures 5.12, 5.13 and 5.14 respectively. With reference to Figures 5.12 (a) and (b), the DSC, FRS and autocatalytic model showed a close correlation during cross-linking at 50 °C until approximately 75% conversion. After approximately 400 minutes, the autocatalytic model showed an increased conversion compared to the DSC and FRS data; this may be due to the reaction rate changing from being chemical controlled to diffusion controlled. Vyazovkin and Sbirrazzuoli (1996b), Ruiz *et al.* (2006) and Rabearison *et al.* (2011) have all reported this discrepancy upon comparing the autocatalytic model with isothermal cross-linking of epoxy resin systems.

Interestingly, the FRS increases at an increased rate when compared to the DSC from 400 to 600 minutes; this may be explained by the following reasons:

- (i) The FRS may be detecting minor changes in the cross-linking which fall below the 0.2 mW sensitivity detection of the DSC.
- (ii) Heating below the glass transition temperature of a cross-linking system can lead to enthalpic relaxation, also known as physical ageing (Hay, 1995). The FRS may be detecting physical ageing of the resin. Previously, Tanio *et al.* (2006) reported that the refractive index of a glass increases with undercooling.

The data from the experiments completed at 60 °C are shown in Figures 5.13 (a) and (b). On comparing this with the 50 °C experiments, an increased initial drop in

the FRS signal is observed. This is due to the reduction in the refractive index of the resin when heating from 30 to 60 °C. Similar to the 50 °C experiments, close correlation between the model, DSC and FRS was observed until approximately 75% conversion.

At 70 °C a close correlation was observed with the DSC, FRS and the autocatalytic model throughout cross-linking. After 75% conversion, a closer correlation is observed in Figures 5.14 (a) and (b) when compared to those shown in Figures 5.12 and 5.13. On investigating the cross-linking of epoxy systems using conventional isothermal DSC, Montserrat and Cima (1999), Janković (2010) and Román *et al.* (2013) also observed an improved correlation of the autocatalytic model with data generated at higher temperatures. The authors noted the time to vitrification would affect correlation between the data but attributed small differences to experimental scatter.

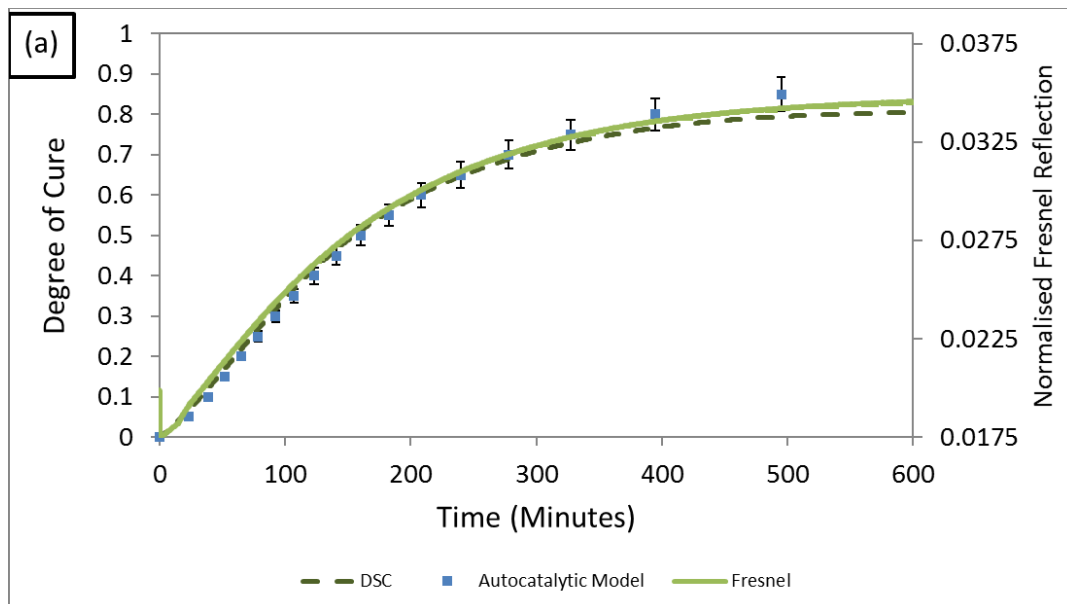


Figure 5.12 FRS and DSC data from isothermal cross-linking experiments during simultaneous DSC/Fresnel at 50 °C: (a) Experiment 1.

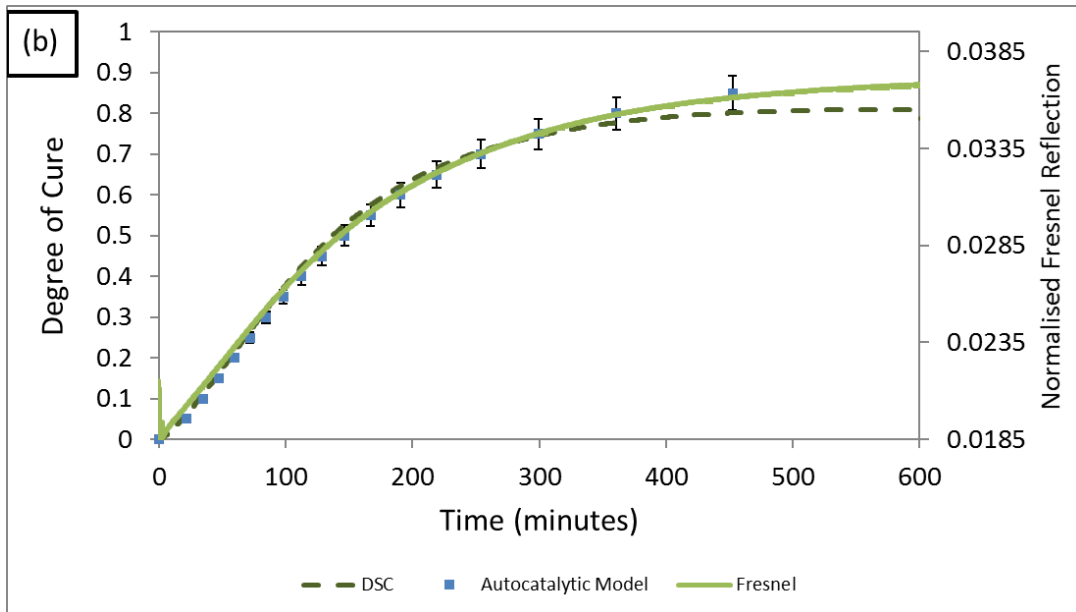


Figure 5.12 (continued) FRS and DSC data from isothermal cross-linking experiments during simultaneous DSC/Fresnel at 50 °C: (b) Experiment 2.

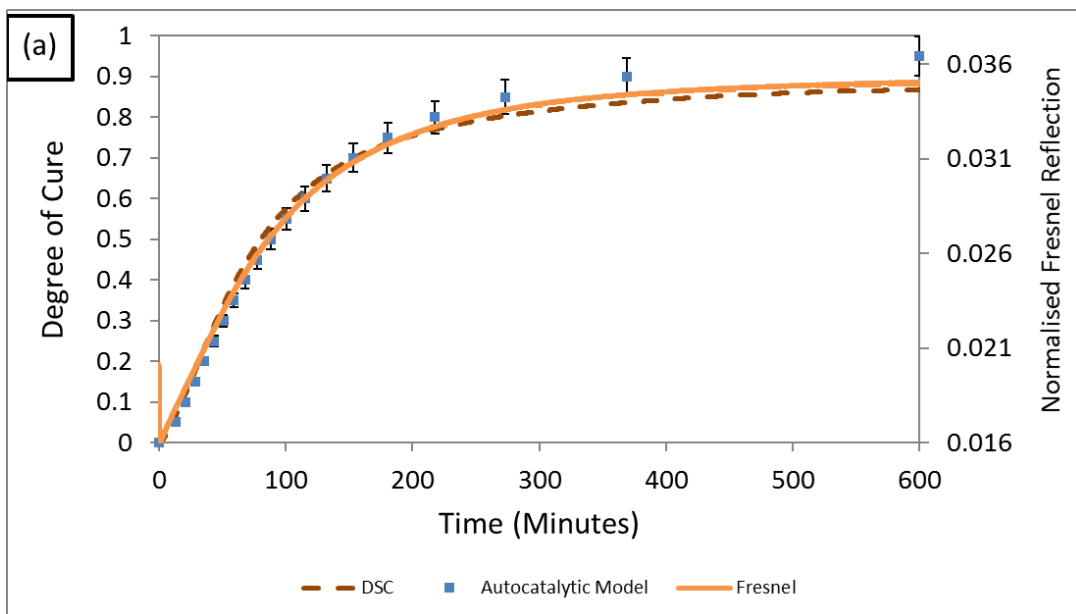


Figure 5.13 FRS and DSC data from isothermal cross-linking experiments during simultaneous DSC/Fresnel at 60 °C: (a) Experiment 1.



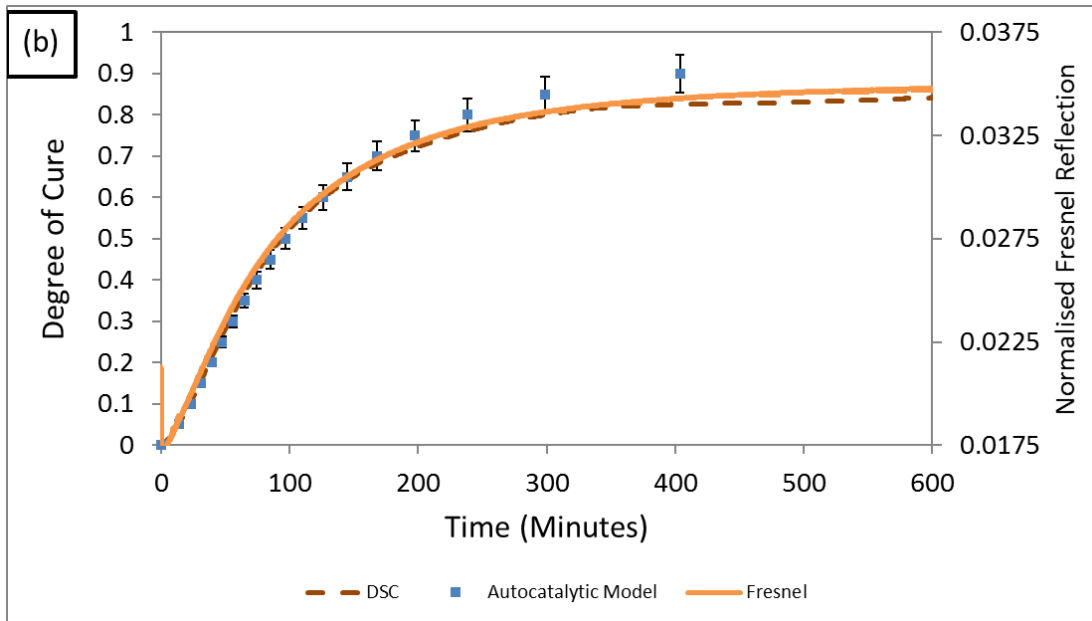


Figure 5.13 (continued) FRS and DSC data from isothermal cross-linking experiments during simultaneous DSC/Fresnel at 60 °C: (b) Experiment 2.

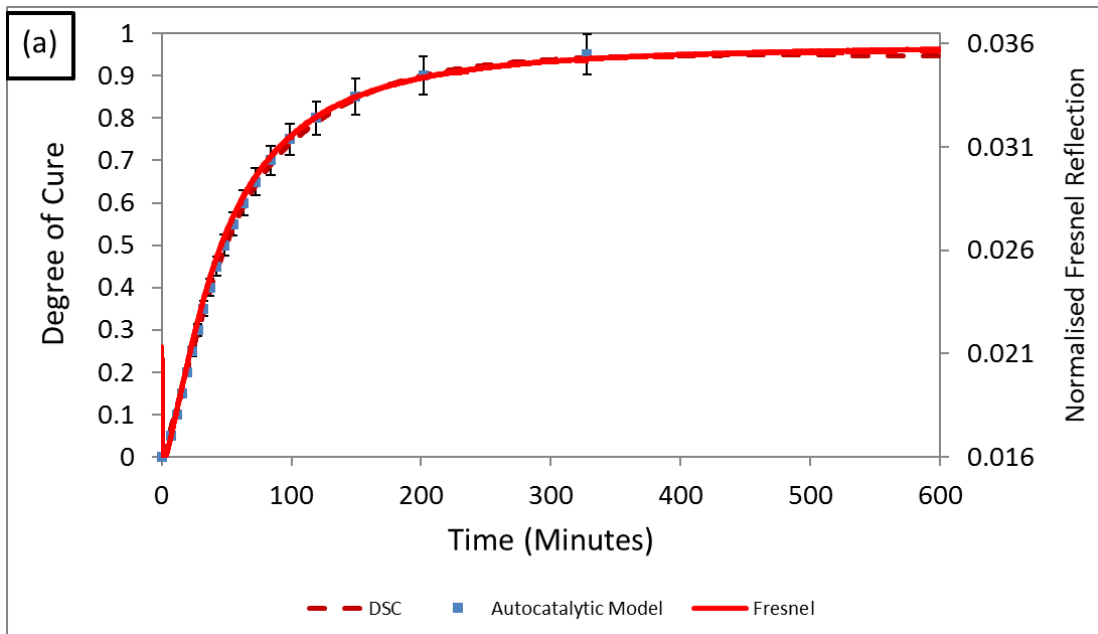


Figure 5.14 FRS and DSC data from isothermal cross-linking experiments during simultaneous DSC/Fresnel at 70 °C: (a) Experiment 1.

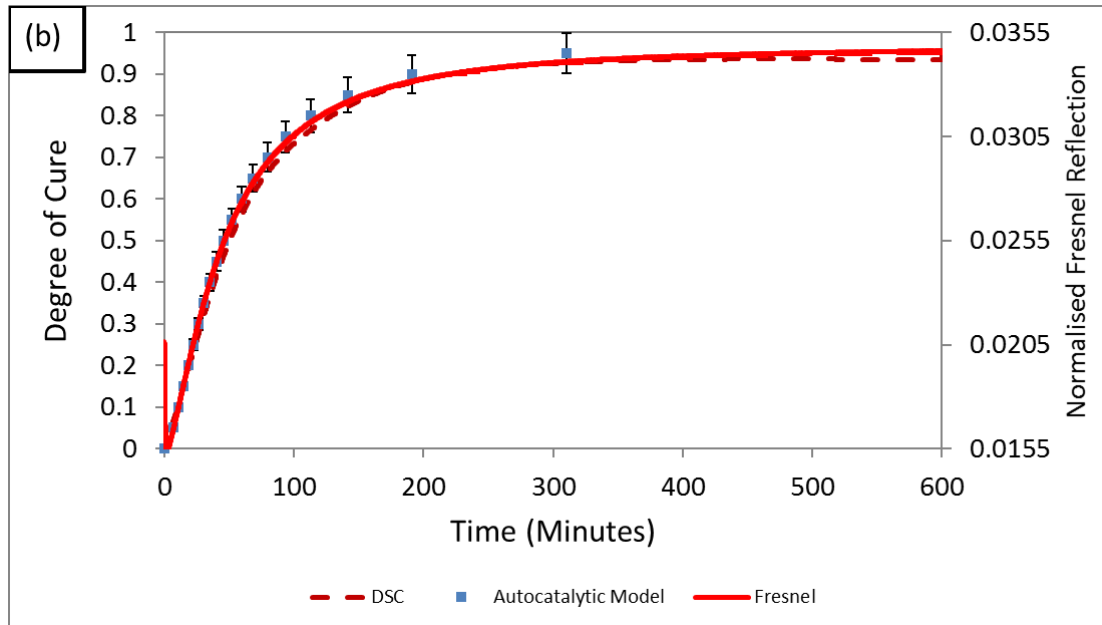


Figure 5.14 (continued) FRS and DSC data from isothermal cross-linking experiments during simultaneous DSC/Fresnel at 70 °C: (b) Experiment 2.

The Arrhenius relationship (Equation 5.1) calculates the temperature dependency of the rate constant for the autocatalytic model (Equation 2.12)

$$k = A \cdot \exp\left(\frac{-E}{RT}\right) \dots \dots \dots \text{Equation 5.1}$$

where

A = pre-exponential factor,

K = Rate constant,

E<sub>a</sub> = activation energy,

R = Universal gas constant (8.314 J mol<sup>-1</sup>),

T = Temperature (Kelvin).

Figure 5.15 shows the rate constants for the cross-linking reactions of the LY3505/XB3403 resin system. The corresponding rate constants and activation energies, presented in Table 5.6, are in general agreement with the conventional DSC data and those reported by Mahendran (2010) and Pandita *et al.* (2012), as

presented in Table 5.7. Upon comparing the rate constants for the conventional and DSC/FRS data, similar values were obtained. Minor discrepancies may be due to one or more of the following reasons:

- (i) Despite insulation of the system, the introduction of a custom-made lid and introduction of the FRS alters the thermal environment of the calorimeter. Calibration of the instrument was completed with indium to compensate for the change in environment.
- (ii) Intrinsic variability of the LY3505/XB3403 resin system.

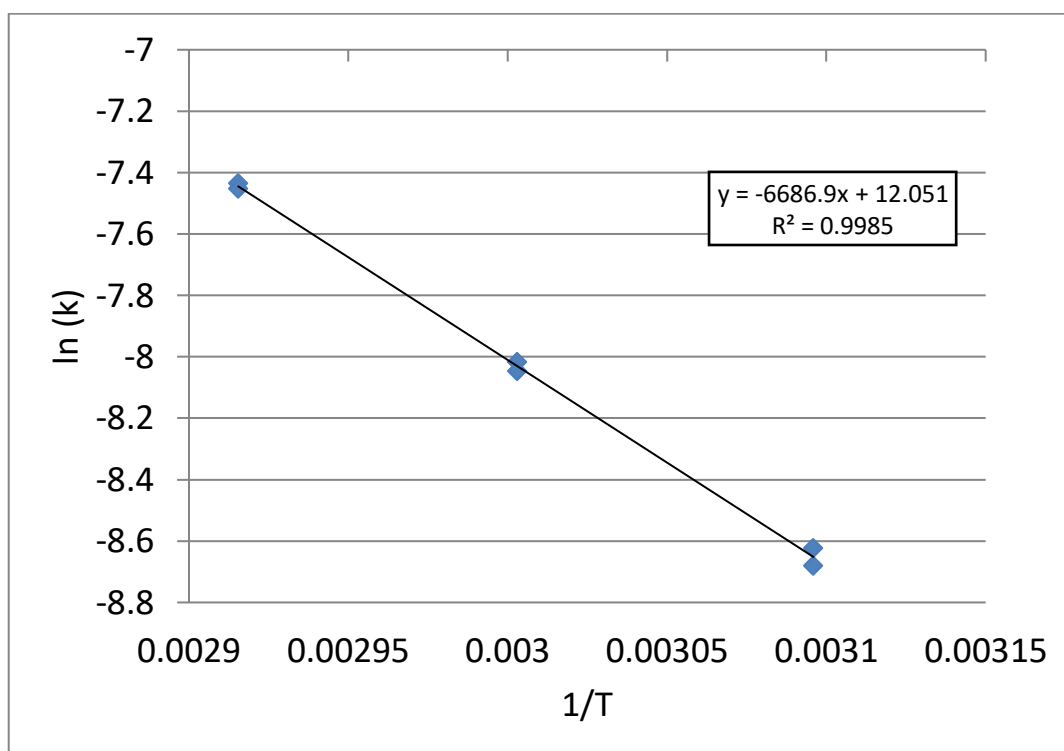


Figure 5.15 Arrhenius plot for the cross-linking LY3505/XB3403 during FRS/DSC.

Table 5.6 Rate constants and activation energy for the LY3505/XB3403 resin system obtained using hyphenated DSC and conventional DSC.

	Rate Constant, $k$ ( $s^{-1}$ )			
	Conventional DSC Experiment 1	Conventional DSC Experiment 2	DSC/FRS Experiment 1	DSC/FRS Experiment 2
<b>Isothermal Cross-Linking Temperature (<math>^{\circ}C</math>)</b>	$K$ ( $s^{-1}$ )	$K$ ( $s^{-1}$ )	$K$ ( $s^{-1}$ )	$K$ ( $s^{-1}$ )
<b>50</b>	0.00018	0.00017	0.00016	0.00017
<b>60</b>	0.00033	0.00032	0.00029	0.00027
<b>70</b>	0.00059	0.00058	0.00053	0.00056
<b>Activation Energy (<math>kJ\ mol^{-1}</math>)</b>	58.68		55.58	

Table 5.7 Previously reported activation energies for LY3505/XB3403.

Reference	Pandita <i>et al.</i> (2012)	Pandita <i>et al.</i> (2012)	Mahendran <i>et al.</i> (2010)	Wang <i>et al.</i> (2016)
<b>Method</b>	DSC/FTIRS	Conventional DSC	Conventional DSC	Transmission FTIRS
<b>Activation Energy (<math>kJ\ mol^{-1}</math>)</b>	60.22	60.82	60.82	56.8

The close correlation of the optical and thermal data during the cross-linking of LY3505/XB3403 demonstrates the performance of the FRS as a cure monitoring technique. The simultaneous data acquisition by the DSC and the FRS upon the same sample ensured identical cross-linking conditions and, for the first time, permits direct comparison between measurement techniques.

The rate constants and activation energy for experiments completed using DSC/FRS correlate with data from a conventional DSC and with previously reported

data in the literature. Therefore, the modifications to the instrument appear to have not significantly altered the performance of the DSC to track cross-linking kinetics.

### **5.2.3 Detecting the Glass Transition Temperature Subsequent to Isothermal Cross-linking**

Following isothermal cross-linking in the DSC/FRS equipment, three successive ramps from 30 to 150 °C at 10 K/minute were performed to detect the glass transition temperature,  $T_g$ . The  $T_g$  was calculated using the method described in ASTM-D3418 (2015) and discussed in Section 2.3.1.3. Figures 5.16 (a) to (c) show typical thermograms upon heating through the glass transition region after cross-linking at 70 °C. Heating above the  $T_g$  of a cross-linked polymer has shown to facilitate changes in the specific volume (Machavaram *et al.* (2014) and Yu *et al.* (2005). As reported by Giordano *et al.* (2004), Machavaram *et al.* (2014) and Robert and Dusserre (2014), a change in the thermo-optic coefficient was also observed from the FRS signal upon approaching and passing the  $T_g$ . The point of the transition was determined by the intersection of extrapolated lines before and after the transition as demonstrated by Giordano *et al.* (2004) and Robert and Dusserre (2014).

With reference to Table 5.8 and Figure 5.16 (a), the first temperature ramp reveals a  $T_g$  which is larger than the isothermal cross-linking temperature. This indicates vitrification occurred during the isothermal cross-linking and contributed to the low rate of reaction towards the end of crosslinking, shown in Figures 5.12 - 5.14. During the first temperature ramp (Figure 5.16(a)), when the temperature rises above the  $T_g$ , de-vitrification can occur, allowing for a greatly increased rate of

reaction (Assche *et al.*, 1997; Wunderlich, 1981). This post-cross-linking contributes toward an increased  $T_g$  in the second ramp (Figure 5.16(b)). An increased  $T_g$  was observed for each experiment, as shown in Table 5.8. Further post-cross-linking occurs during the second ramp and is observed by an increased glass transition during the third ramp, as shown in Figure 5.16(c).

Table 5.8 presents a summary of the glass transition values measured by the DSC and FRS and in each case the two datasets were within 1 °C. This study has demonstrated conclusively that the observed change in the thermo-optic coefficient is a consequence of approaching and passing the  $T_g$ . Although previous researchers have observed a change in the thermo-optic coefficient upon heating an epoxy resin through the  $T_g$ , this current work represents the first direct correlation between optic and thermal data in an identical environment, as opposed to independent and separate experiments.

The  $T_g$ s obtained following isothermal cross-linking using conventional DSC are presented in Table 5.8. Upon comparison with the  $T_g$ s obtained during DSC/FRS, similar values were obtained and correlate to  $\pm 2$  °C. Variations may be explained by intrinsic scatter in the resin system.

In Section 2.2.1, Equation 2.9 was derived, that relates the refractive index to the molar refractivity and the molar volume. Using the binomial theorem, the equation approximates to a linear function of refractive index as a function of refractivity. The refractive index depends upon the chemical nature of the molecules and the molar volume.

$$n_r = \left\{ \left( 1 + \frac{2R_M}{V_M} \right) / \left( 1 - \frac{R_M}{V_M} \right) \right\}^{\frac{1}{2}} \dots\dots\dots \text{Equation 2.9}$$

From Figures 5.16 (a) – (c), a change in the normalised Fresnel reflection FRS occurs at the  $T_g$ . The chemical bonds and therefore the molar refractivity should remain unchanged during this period. The relationship between the normalised Fresnel reflection with temperature appears to be influenced by a difference in the relationship of the resin density with temperature in the glassy and gel state.

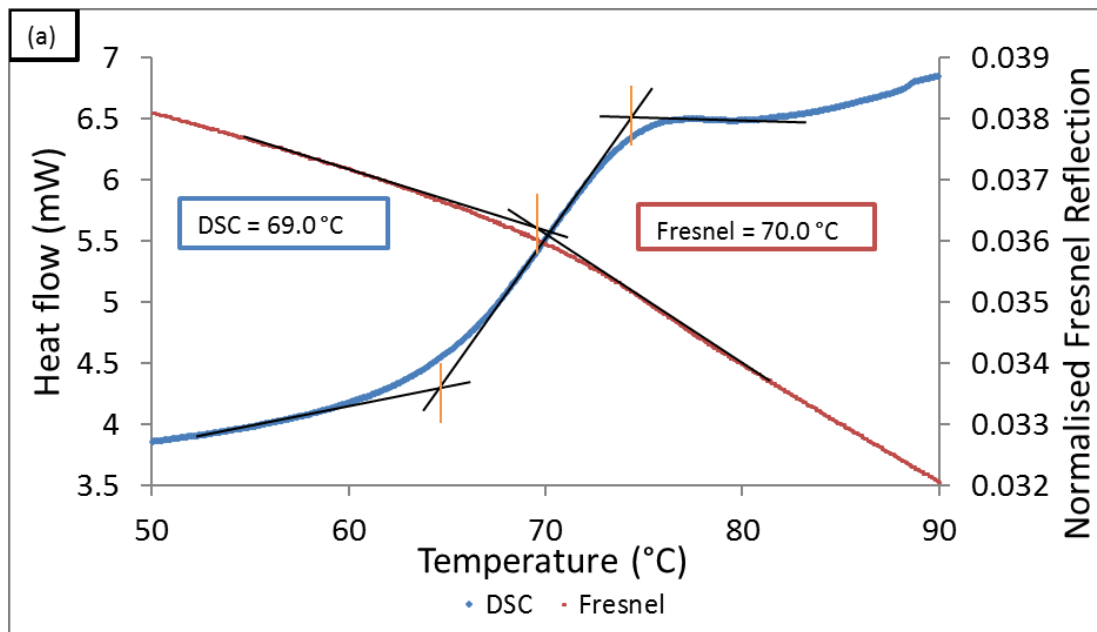


Figure 5.16 Thermogram obtained from DSC during a non-isothermal scan through the  $T_g$  for the LY3505/XB3403 resin system along with data obtained from the Fresnel reflection sensor: (a) First non-isothermal heating ramp

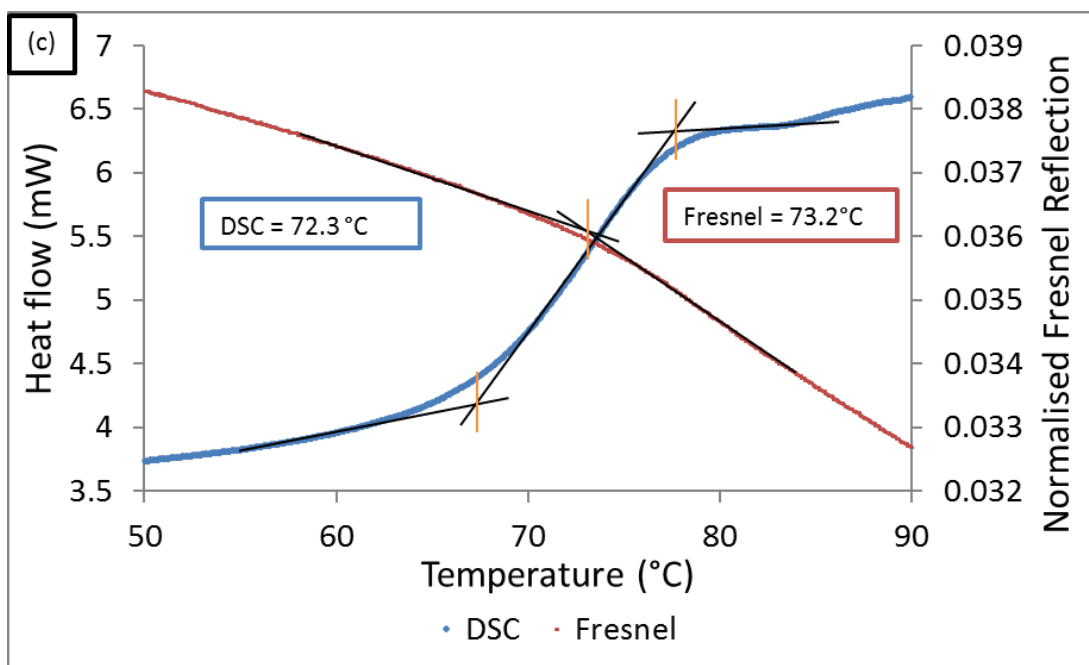
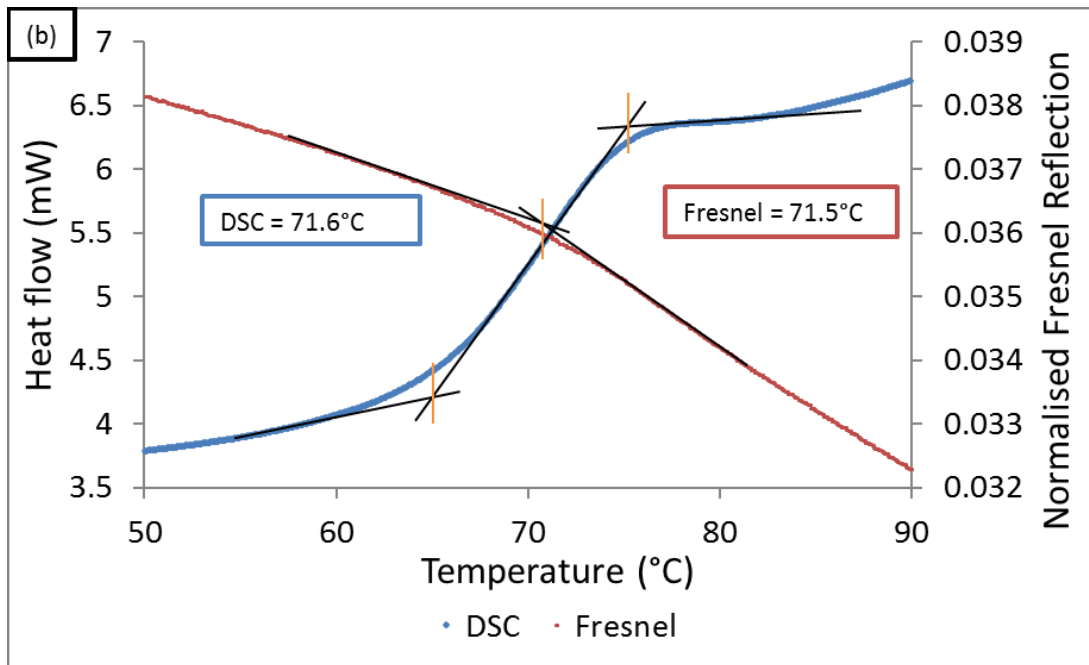


Figure 5.16 (continued) Thermogram obtained from DSC during a non-isothermal scan through the  $T_g$  for the LY3505/XB3403 resin system along with data obtained from the Fresnel reflection sensor: (b) Temperature ramp 2; and (c) Temperature ramp 3.



Table 5.8 Glass transition temperatures of LY3505/XB3403 after cross-linking using the simultaneous DSC/Fresnel technique and using conventional DSC.

Isothermal Cross-linking Temperature	DSC/ Fresnel T <sub>g</sub> 1 (°C)	DSC/ Fresnel T <sub>g</sub> 2 (°C)	DSC/ Fresnel T <sub>g</sub> 3 (°C)	DSC T <sub>g</sub> 1 (°C)	DSC T <sub>g</sub> 2 (°C)	DSC T <sub>g</sub> 3 (°C)
50 °C - Experiment 1	57.6/56.6	69.05/68.1	72.6/70.7	56.3	68.2	72.2
50 °C - Experiment 2	56.9/56.6	68.4/69.1	73.0/71.4	55.2	67.9	72.7
60 °C - Experiment 1	66.7/65.9	69.6/68.3	71.0/71.0	67.4	72.5	73.9
60 °C - Experiment 2	67.5/68.9	69.4/68.5	70.9/70.2	67.6	71.7	74.5
70 °C - Experiment 1	69.0/70.0	71.5/71.6	73.2/72.3	73.6	75.3	75.2
70 °C - Experiment 2	71.9/70.1	73.0/71.5	73.8/72.8	74.0	75.2	75.7

#### 5.2.4 Detecting the Glass Transition Temperature for a Stoichiometrically Un-Balanced Resin System

The previous detection of the T<sub>g</sub> using a FRS was undertaken using stoichiometrically balanced systems (Giordano *et al.*, 2004; Machavaram *et al.*, 2014; Robert and Dusserre, 2014). The capability of using the FRS to study the effect of stoichiometry on the T<sub>g</sub> was investigated by altering the stoichiometric ratio by +/- 3, 6 and 9%. This was performed by altering the quantity of hardener. The samples were cured at 70 °C for 10 hours before three heating ramps were performed from 30 to 150 °C at 10 K/minute. The T<sub>g</sub> was determined using the DSC and FRS with the method shown in Figures 5.16. Table 5.9 presents the T<sub>g</sub> determined at each stoichiometric ratio. The close correlation between the two detection methods shows that the sensor can detect T<sub>g</sub>s of a non-stoichiometric epoxy resin system.

Table 5.9 Glass transition temperatures of LY3505/XB3403 systems with specified stoichiometric ratios following isothermal cross-linking at 70 °C for 600 minutes.

<b>Stoichiometry Change in Hardener (Weight %)</b>	<b>DSC/Fresnel T<sub>g</sub> 1 (°C)</b>	<b>DSC/Fresnel T<sub>g</sub> 2 (°C)</b>	<b>DSC/Fresnel T<sub>g</sub> 3 (°C)</b>
9	54.2/54.3	54.6/55.3	54.9/55.1
6	64.5/64.3	64.8/64.2	65.1/65.3
3	68.7/68.6	70.2/70.1	70.7/70.9
0	71.2/71.2	74.1/74.1	74.5/74.4
-3	71.5/70.9	75.5/75.7	77.3/76.9
-6	64.1/63.8	65.2/64.4	65.0/65.2
-9	54.8/54.5	56.2/55.7	56.3/56.6

Figures 5.17 (a) – (c) show the T<sub>g</sub>s for each temperature ramp following isothermal cross-linking at 50, 60 and 70 °C. The data are summarised in Figure 5.18 showing an increasing glass transition temperature after each sequential ramp due to post cross-linking. The glass transition temperatures of the systems, containing 0 wt% and -3 wt% hardener, were the largest in all three temperature ramps.

Meyer *et al.* (1994) investigated the effect of changing the stoichiometry on the T<sub>g</sub> of a DGEBA/DDS system when altering the hardener content by ±20% and using various cross-linking conditions. The T<sub>g</sub> of the cross-linked system was then determined using dynamic mechanical thermal analysis (DMTA). The T<sub>g</sub> of the epoxy rich system showed an increased T<sub>g</sub> (216 °C) when compared to the stoichiometrically balanced system (206 °C). The authors stated that during post-cross-linking of epoxy rich systems, etherification of the epoxy group can occur. The etherification process can therefore allow for increased consumption of epoxy

groups leading to a higher cross-link density and  $T_g$ . Figures 5.17 (a) – (c) correlate with Meyer *et al.* (1994), by showing a reduction in the  $T_g$  of the epoxy rich systems.

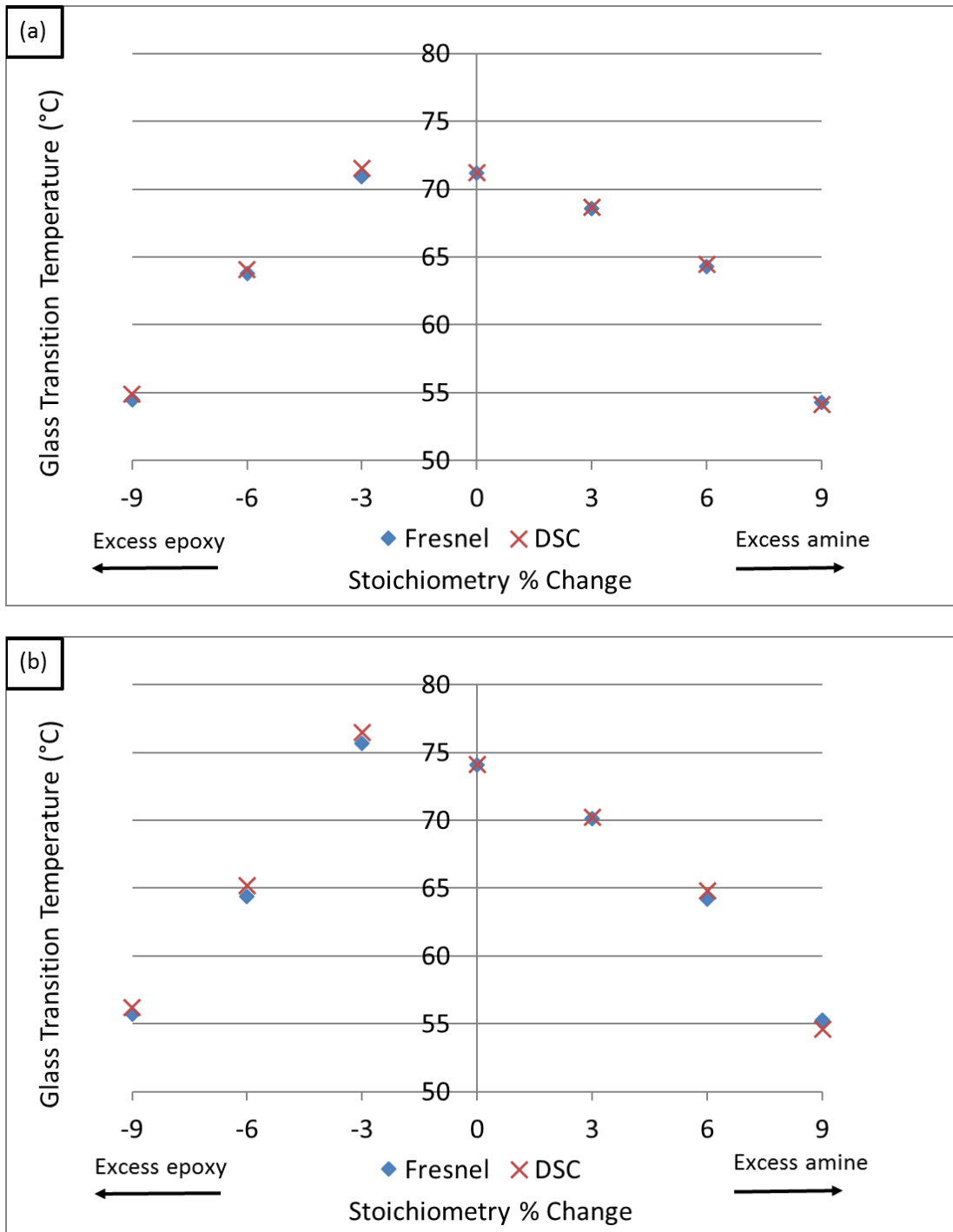


Figure 5.17 Graphic representation of variation in glass transition temperature with stoichiometry change following isothermal cross-linking at 70 °C:

(a) Temperature ramp 1; and (b) Temperature ramp 2.

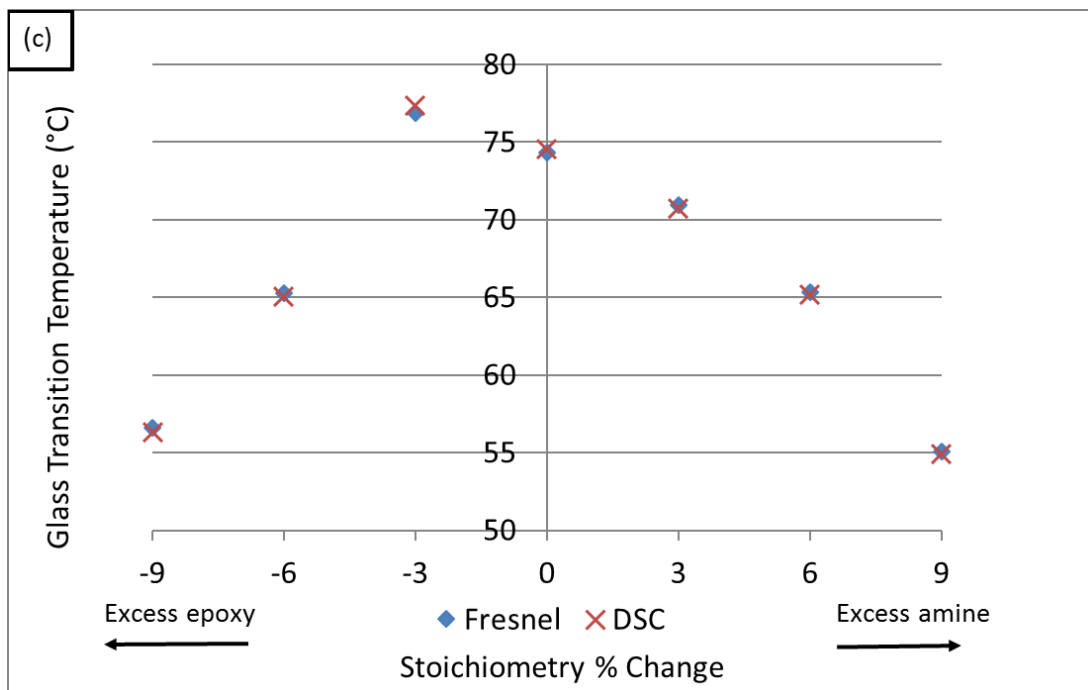


Figure 5.17 (continued) Graphic representation of variation in glass transition temperature with stoichiometry change following isothermal cross-linking at 70 °C:  
(c) Temperature ramp 3.

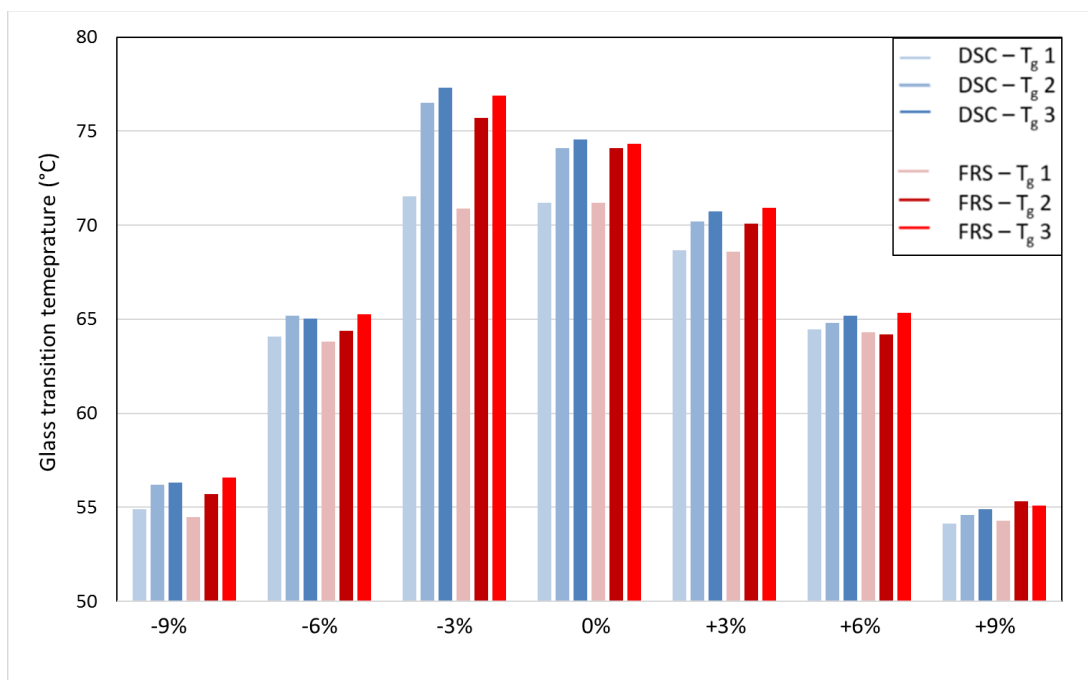


Figure 5.18 Histogram showing variation in the  $T_g$  following isothermal cross-linking at 70 °C.

### 5.3 Isothermal Cross-linking of Cytec/Solvay Phase Separating Resins

A series of epoxy resin formulations were prepared in collaboration with Cytec/Solvay Ltd. The resins were cured using the previously described combination DSC/Fresnel assembly, under isothermal conditions at 180 °C. Figures 5.19 (a) and (b) show the cross-linking data from DSC and the FRS. The sample was permitted to equilibrate in the DSC at 30 °C for 1 minute before heating at 40 K/minute to 180 °C. This caused the observed initial drop in the FRS signal. As cross-linking proceeded, an increase in the Fresnel signal was observed throughout the experiment. The DSC thermogram shows a large exothermic reaction, peaking at approximately 35 minutes. At the end of the isothermal period, the horizontal DSC baseline suggesting a cessation of the cross-linking reactions or the detection limit of the instrument being reached.

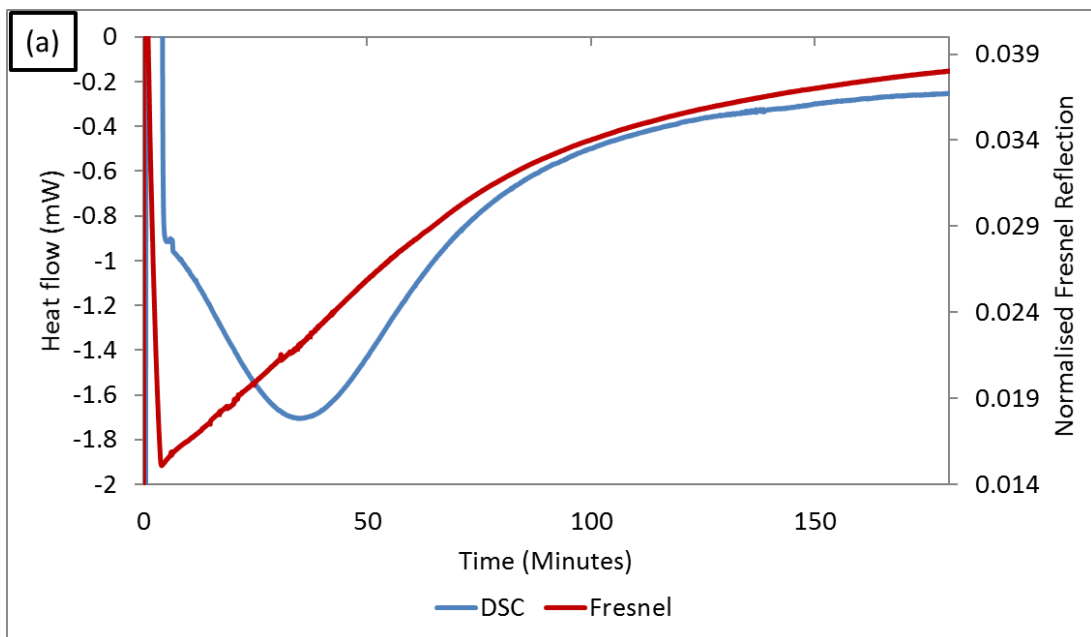


Figure 5.19 Isothermal cross-linking of Cytec/Solvay resin system at 180 °C without a thermoplastic additive: (a) Experiment 1.

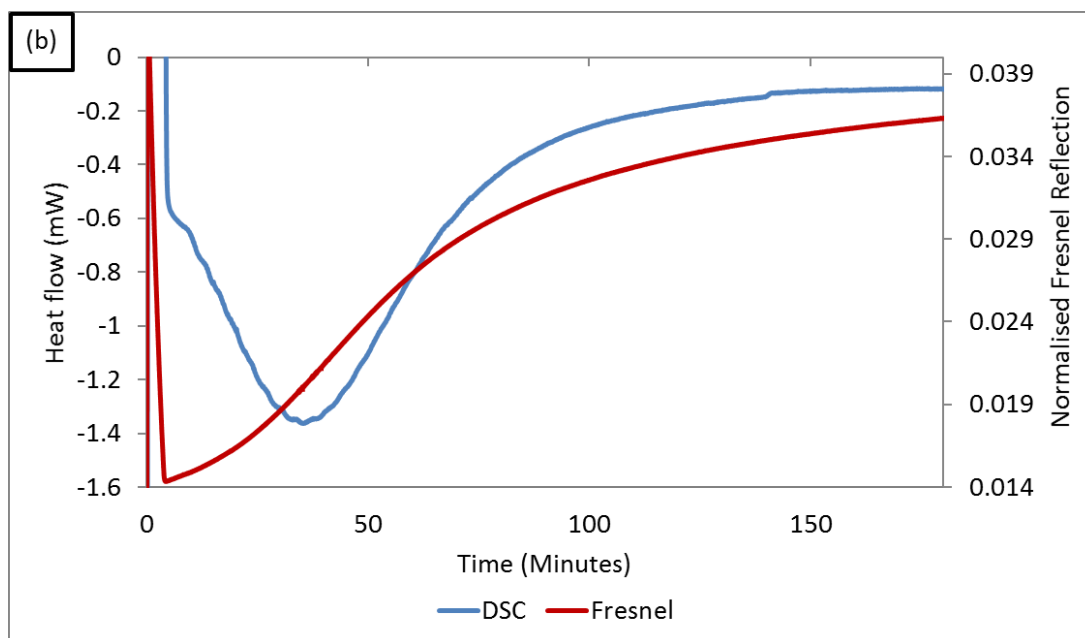


Figure 5.19 (continued) Isothermal cross-linking of Cytec/Solvay resin system at 180 °C without a thermoplastic additive: (b) Experiment 2.

Formulations of the epoxy system containing 10, 20 and 30% by mass of a thermoplastic material were also prepared to induce phase separation. Typical data from the DSC/Fresnel experiments for the 10, 20 and 30 % thermoplastic additive are shown in Figures 5.20 (a) – (c); relevant data from the experiments are presented in Table 5.10.

The enthalpy of the reaction was determined by drawing a horizontal baseline from the end of the isothermal cross-linking period. Similar values for the peak reaction time and enthalpy were obtained for 0 to 20% thermoplastic, the data is presented in Table 5.10. The enthalpy of reaction was reduced by approximately 6% for the sample containing 30% thermoplastic.

With reference to Table 5.11, a reduction in the enthalpy of the reaction has generally been reported in the literature. Mackinnon *et al.* (1993), Su *et al.* (1995),

Swier *et al.* (1999) and Thomas *et al.* (2010) have all reported reductions in the enthalpy of reaction when introducing thermoplastic additives to epoxy resin systems. The authors cite dilution of the system by the thermoplastic as a contributing factor for the reduced enthalpy. As the cross-linking reaction progresses, the epoxy concentration decreases further, causing a reduction in the entropy of mixing leading to phase separation. Similar to the previously reported examples presented in Table 5.11, a decrease in the enthalpy of reaction was observed as the thermoplastic content was increased to 30 wt %.

With reference to Figures 5.20 (a) – (c), an initial decrease in the FRS is observed whilst heating to the isothermal cross-linking temperature. The signal then increased in intensity until approximately 45 minutes. Signal fluctuation begins after approximately 44, 45 and 48 minutes for samples containing 10, 20 and 30 wt% thermoplastic, respectively. The fluctuations persisted for approximately 21 minutes for samples containing 10 wt% thermoplastic and approximately 16 minutes for those containing 20 and 30 wt% thermoplastic. Previously, Dimopoulos *et al.* (2009) reported similar FRS data fluctuation during the cross-linking of an aerospace epoxy resin system known to display phase separation. A UV lamp was used to heat the resin system for 2 hours at 140 °C. Fluctuations in the FRS data were observed from the beginning of the reaction to after approximately 40 minutes. The authors proposed two possible explanations for the fluctuations:

- (i) Despite degassing, tiny air bubbles passing by the sensor head.
- (ii) The formation and movement of thermoplastic-rich regions.

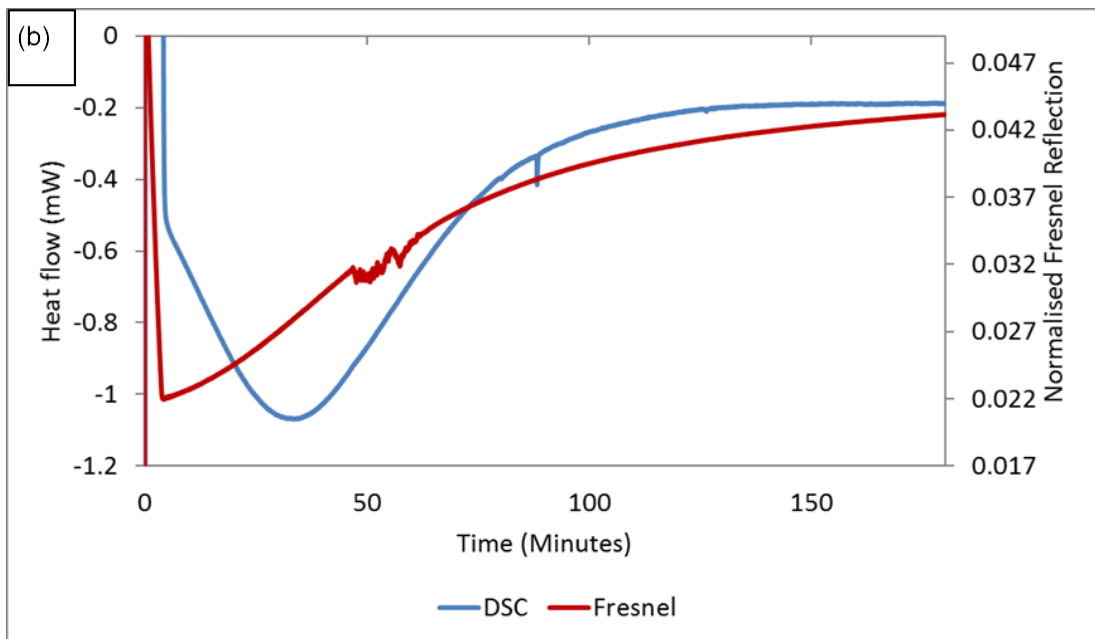
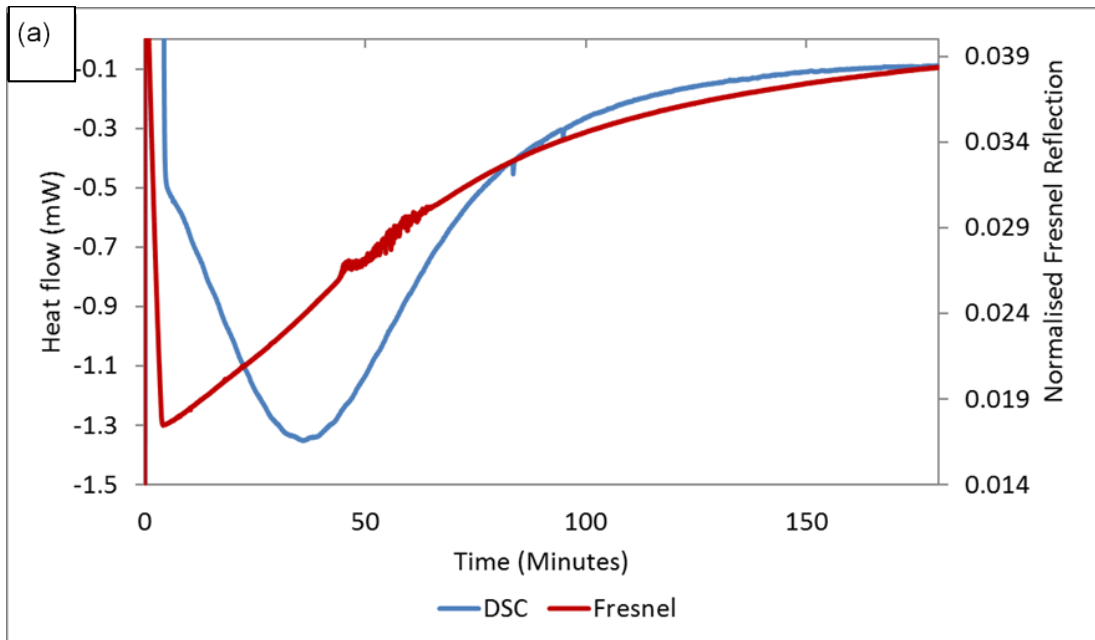


Figure 5.20 Isothermal cross-linking of Cytec/Solvay resin system with specified quantities of thermoplastic additive: (a) 10 wt%; and (b) 20 wt%.



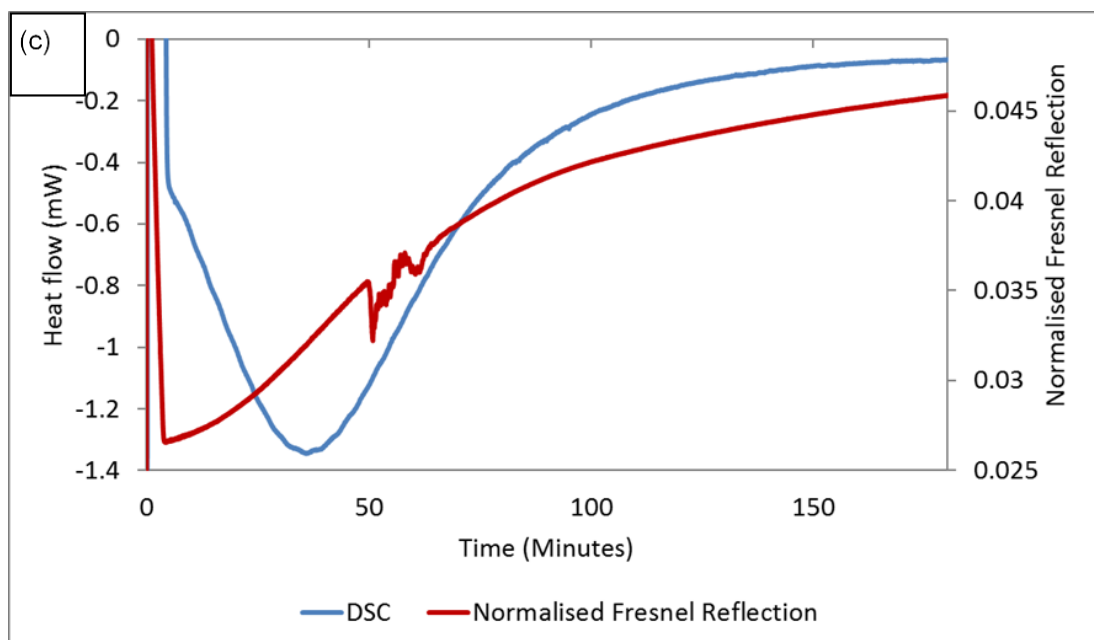


Figure 5.20 (continued) Isothermal cross-linking of Cytec/Solvay resin system with specified quantities of thermoplastic additive: (c) 30 wt%.

Table 5.10 Relevant data from DSC/FRS experiments during the isothermal cross-linking of the Cytec/Solvay resins systems at 180 °C.

wt% Thermoplastic	DSC data		FRS Data		
			Time (minutes)		
	$\Delta H$ (J/g)	Peak Reaction Time (minutes)	Commencement of Fluctuating Signal	Termination of Fluctuating Signal	Duration of Fluctuation Region
0	266	35	NA	NA	NA
0	275	35	NA	NA	NA
10	261	36	44	65	21
10	264	33	45	65	20
20	271	33	45	62	17
20	273	33	46	62	16
30	245	35	49	65	16
30	249	34	48	65	17

Figure 5.21 shows SEM micrographs of samples following the isothermal cross-linking. A featureless morphology is present for the resin without the thermoplastic. Particle-like features of approximately 1  $\mu\text{m}$  diameter were evident with 10% thermoplastic; these features increased in size and quantity as the content was increased to 20%. For the 30% thermoplastic system an interpenetrating morphology was present.

Bonnet *et al.* (1999) reported on the microstructural changes upon adding 10, 20, 30, 45 and 60 wt% polyetherimide to an epoxy-diamine system after cross-linking for 12 hours. Optical microscopy showed particle-like thermoplastic phases for samples containing 10% thermoplastic. The thermoplastic regions grew in size for samples containing 20% thermoplastic. Above 30% a bi-continuous structure was reported. Similar findings have been reported for epoxy systems containing quantities of polyethersulphone (PES) (Yamanaka and Inoue, 1989; Blanco *et al.*, 2004) and polysulphone (PS) (Tercjak *et al.*, 2005). These findings correlate with Figures 5.21 (a) – (d).

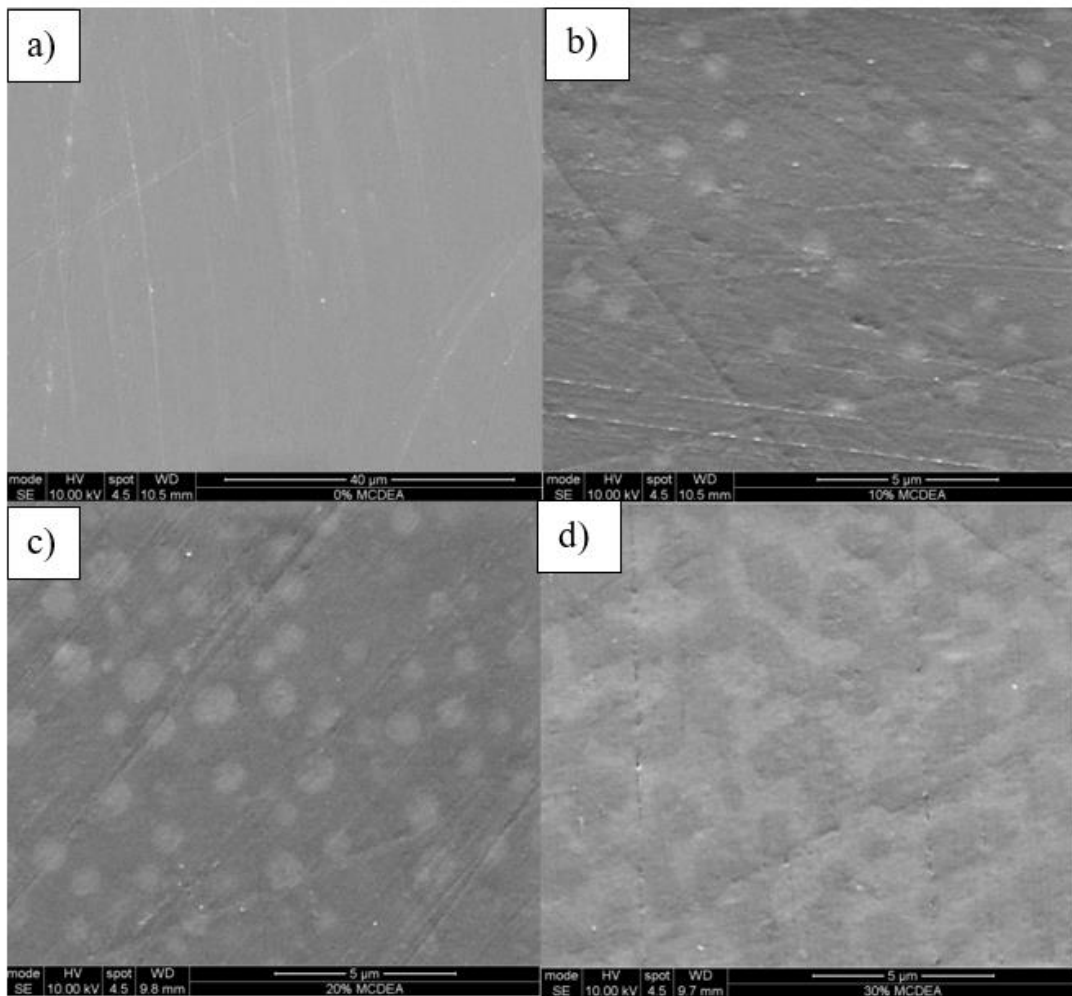


Figure 5.21 SEM micrographs of cryo-fracture surfaces of Cyttec/Solvay resins containing specified concentration of thermoplastic: (a) 0%; (b) 10%; (c) 20%; and (d) 30%. Image provided by Cyttec/Solvay.

With reference to Figure 5.21 (a) the featureless SEM micrograph indicates phase separation has not occurred during the cross-linking of the system containing 0% thermoplastic. The absence of the thermoplastic appears to allow for a steady-increase from the FRS signal throughout cross-linking and correlates with data previously reported upon the cross-linking of epoxy resin systems by Crosby *et al.* (1996), Liu *et al.* (1997) and Mahendran *et al.* (2010).

Upon the addition of 10% thermoplastic, a microstructure containing particle-like features were present and approximately 1  $\mu\text{m}$  in size, comparable with the 8  $\mu\text{m}$  core of the optical fibre. During cross-linking, this produced a period of FRS fluctuations from 44 to 65 minutes. Similar behaviour was reported by Dimopolous *et al.* (2009) and the authors stated that the behaviour is likely due to the movement of 'thermoplastic rich' phases during cross-linking. This proposed explanation is supported by the DSC/FRS and SEM images in the current study. The termination of the fluctuations during the later stages of cross-linking may be explained by formation of a cross-linked network that restricts particle movement.

The system containing 20% thermoplastic showed FRS fluctuations from approximately 46 to 62 minutes; this period commenced at a similar time to the 10% thermoplastic system but decreased in length by 3 to 4 minutes. The particle morphology from SEM micrographs grew in size and quantity when compared to the 10% thermoplastic sample to approximately 1-2  $\mu\text{m}$  in diameter.

An interpenetrating morphology was observed upon increasing the thermoplastic content to 30%. The microstructural changes correlate with previous reports of adding specified thermoplastic quantities to epoxy systems, whereby a particle-like morphology develops into an interpenetrating morphology upon the addition of increased thermoplastic content (Yamanaka and Inoue, 1989; Blanco *et al.*, 2004; Tercjak *et al.*, 2005) The fluctuation period initiates 3 minutes later than the 20% thermoplastic systems and has a similar duration.

Table 5.11 Literature citing the effect of thermoplastics upon the cross-linking of epoxy resin systems.

Resin System	Additive	Effect on Cross-linking	Notes	Reference
DGEBA/44DDS	20 wt% amine terminated PS	Reduced from 666J/g to 506.5 J/g	Particulate phase - TP acts as a diluent	Mackinnon <i>et al.</i> , 1993
DGEBA/44DDS	30 wt% amine terminated PS	Reduced from 666J/g to 431.7 J/g	Co-continuous phase - TP acts as a diluent	Mackinnon <i>et al.</i> , 1993
TGDDM/DDS	20% Poly carbonate	Increased T <sub>g</sub> by 10-15 °C but reduced initial rate by approximately 20%.	Incorporation of the PC into the TGDDM/DDS system.	Su <i>et al.</i> , 1995
DGEBA/Aniline	20% PES	Negligible effect on total enthalpy	Particulate phase - TP acts as a diluent	Swier <i>et al.</i> , 1999
DGEBA/Anhydride hardener	20 wt% CTBN	Reduced enthalpy by approximately 10%.	Reduction in the reactive groups causes fall in enthalpy (dilution effect).	Thomas <i>et al.</i> , 2010
Epoxy/thermo-plastic	30 wt % thermo-plastic	Reduced enthalpy by approximately 10%	Co-continuous phase observed.	Current work

## 5.4 Summary

The focus of this work was to develop a combination DSC and FRS analyt technique to enable direct comparison between thermal and optical data d cross-linking during real-time cross-linking processes. The calibration of th was demonstrated with the top-cover attached and the FRS probe *in situ*. probe was demonstrated to correlate with the predicted performance over

refractive indices and shown to display long-term stability. The impact of the FRS on the DSC was also quantified.

The DSC/FRS combination technique was then used to study the cross-linking of LY3505/XB3403 at 50, 60 and 70 °C. An excellent correlation between the degree of cross-linking and the increase in the normalised Fresnel reflection was demonstrated. The autocatalytic model was used to model the reaction kinetics. The model showed good correlation with the experimental data.

Following isothermal cross-linking of samples, non-isothermal scans were completed to determine the glass transition characteristics of the system. It was observed that a change in the thermo-optic coefficient in the FRS signal correlated within 1 °C to the glass transition properties determined by the DSC method. Thus, it was conclusively shown that the FRS probe can be used to determine the glass transition characteristics of an epoxy resin system. Further experiments wherein the stoichiometric ratio was altered demonstrated the glass transition could be detected in non-stoichiometric systems.

The combination DSC/FRS technique was then used to study the cross-linking of a set of aerospace resin formulations prepared in collaboration with Cytac/Solvay Ltd. The resin systems were designed to display phase-separation during cross-linking at 180 °C. Periods of sensor fluctuation was observed during cross-linking of systems containing thermoplastic. It is believed the fluctuations were caused by phase separation. SEM images of the cross-linked material showed a two-phase morphology indicative of phase separation. The experiments appear to demonstrate that phase separation can be detected during the cross-linking of epoxy resin systems using the FRS.

## **6. EVALUATION OF THE FRESNEL REFLECTION SENSOR WITH LY3505/XB3403 CONTAINING GRAPHENE NANO-PARTICLES**

This chapter reports on the effect of dispersed graphene nano-particles (GNPs) on the cross-linking characteristics of the LY3505/XB3403 resin system. The GNPs were blended with the LY3505 resin using high-shear mixing by the Gwent Group (UK) and supplied to the author. The required mass of the XB3404 hardener was added to the resin, mixed and degassed as described in Section 3.2.2, Chapter 3. The resin system was analysed using the hyphenated DSC/FRS technique as described in Chapter 5. The introduction of the GNPs cause fluctuations in the Fresnel reflection sensor (FRS) signal during the early stages of cross-linking. A series of experiments were designed to identify the cause of the fluctuations.

### **6.1 Simultaneous Differential Scanning Calorimetry /Fresnel Reflection Sensor**

The technique developed in Section 5 was used to examine the impact of introducing various weight percentages (wt%) of GNPs on the chemical and physical characteristics of LY3505/XB3403, during and after cross-linking. Alumina pans were used.

### 6.1.1 Isothermal Cross-linking

Isothermal cross-linking experiments were performed at 70 °C for the resin systems containing 0, 0.01, 0.1, 0.5, 1 and 2 wt% GNP. This temperature was chosen, as previous cross-linking experiments using LY3505/XB3403 appeared to have reached near completion after 600 minutes. Similar to the conventional DSC analysis of LY3505/XB3403, a large exothermic reaction was present, which reduced in intensity before reaching a horizontal baseline, as shown in Figures 6.1 (a) – (f).

With reference to Figure 6.1(a), without the addition of any GNP, the FRS data showed an initial drop as the temperature was heated to the desired isothermal cross-linking temperature. The refractive index of the resin increased with cross-linking time, which produced an increase in the normalised FRS data. The data previously presented in Section 5.2.1 is also plotted in Figure 6.1(a) for comparison purposes, and similar thermal and optical responses are observed.

Upon the addition of 0.01 wt% GNP, small fluctuations were observed during the early stages of cross-linking as shown in Figure 6.1(b). The fluctuations reduced in frequency and amplitude before reaching a relatively stable signal after approximately 30 minutes.

An increase in the amplitude and frequency of the fluctuations was observed upon increasing to 0.1 wt% GNP, as shown in Figure 6.1(c). The fluctuations diminish and a relatively stable signal was achieved after 33 minutes. Similarly, the fluctuations



were increased upon the addition of 0.5 wt% GNP, as shown in Figure 6.2(d), where the signal stabilises after approximately 37 minutes.

Further increases to the fluctuation amplitude were observed for 1 wt% GNP and 2 wt% GNP as shown in Figure 6.1(e) and Figure 6.1(f). The stabilisation of the signal was delayed from previous experiments to 48 and 51 minutes for 1 and 2 wt% GNP, respectively.

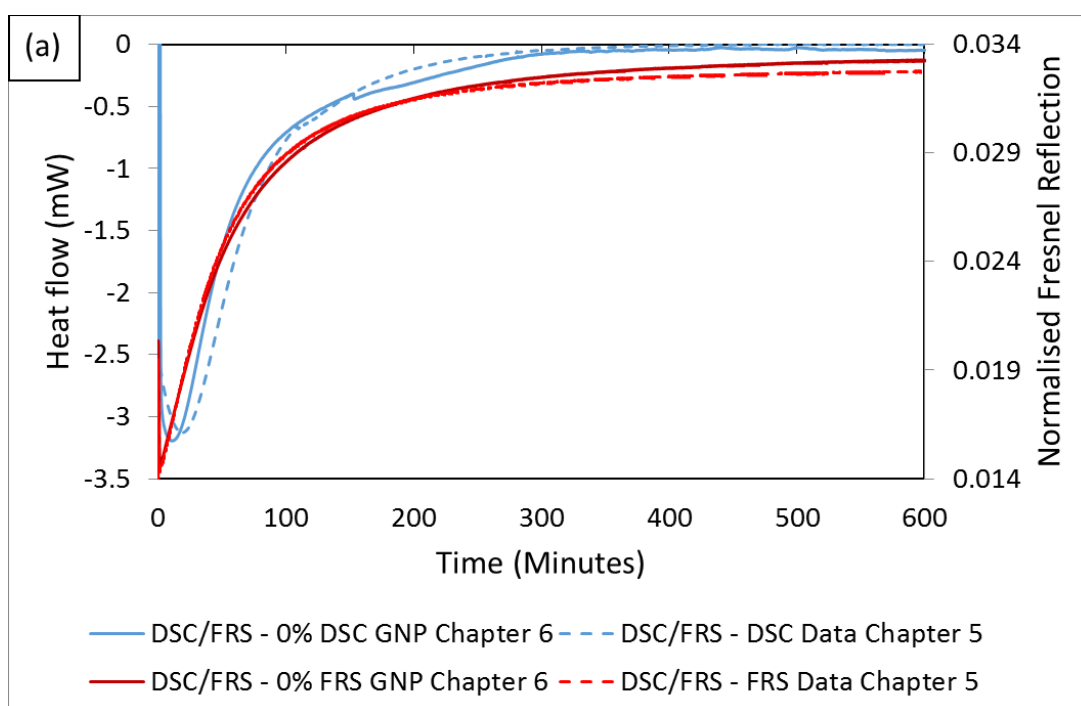


Figure 6.1 Isothermal cross-linking of LY3505/XB3403 at 70 °C with: (a) 0% GNP.

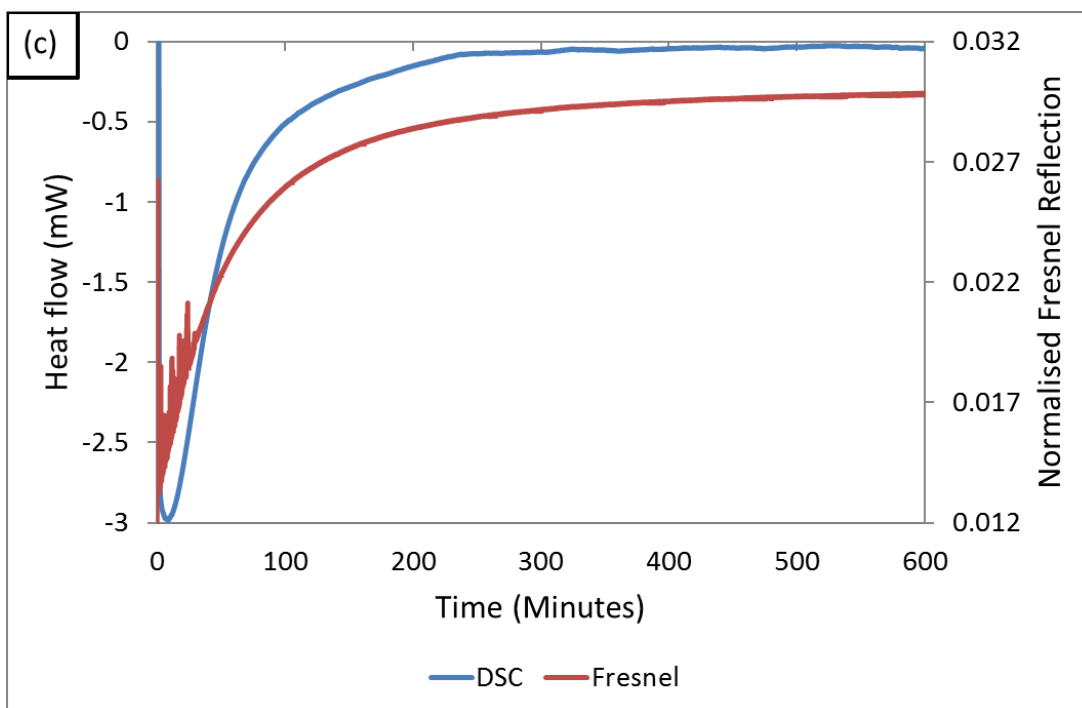
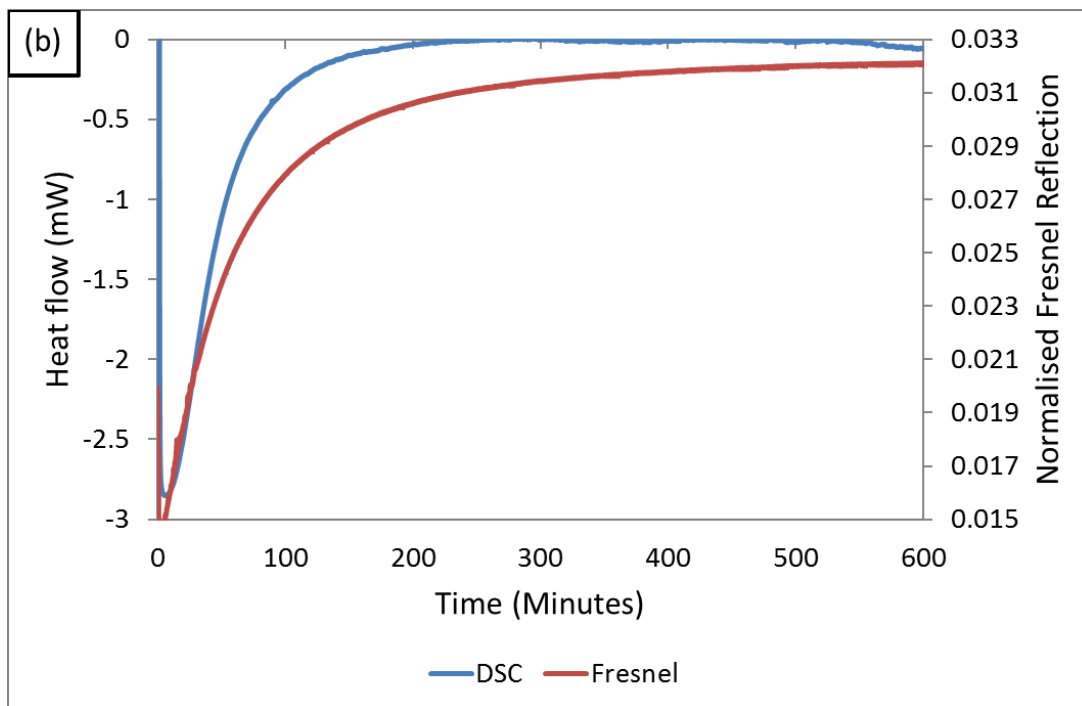


Figure 6.1 (continued) Isothermal cross-linking of LY3505/XB3403 at 70 °C with:  
 (b) 0.01 wt%; and (c) 0.1 wt% GNP.

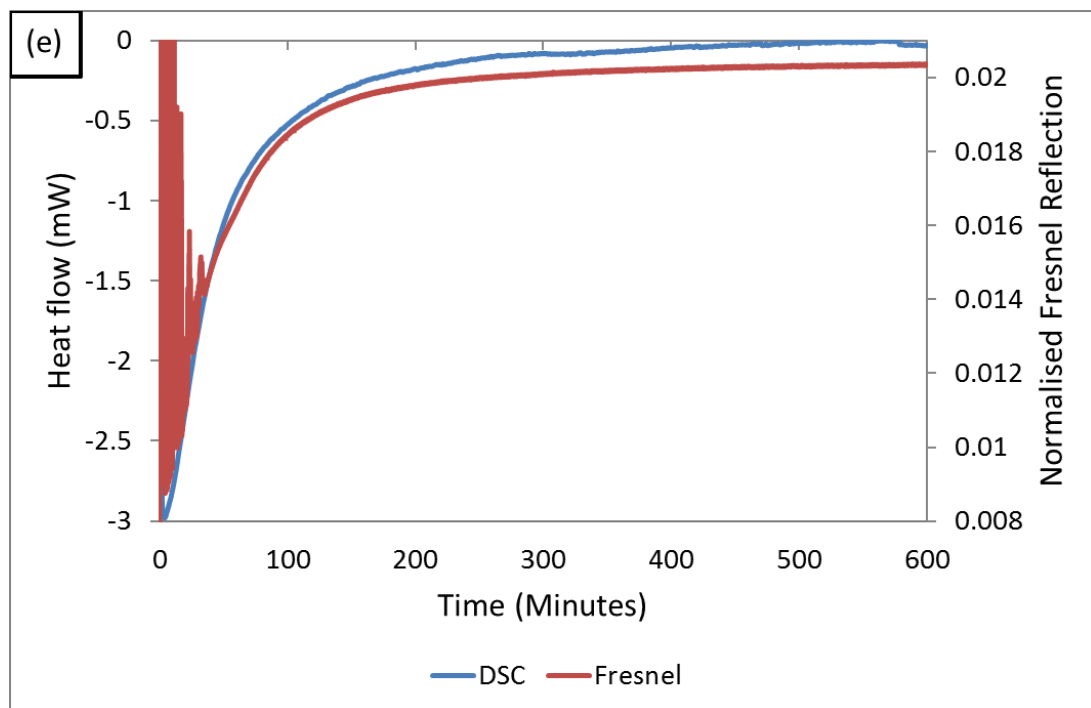
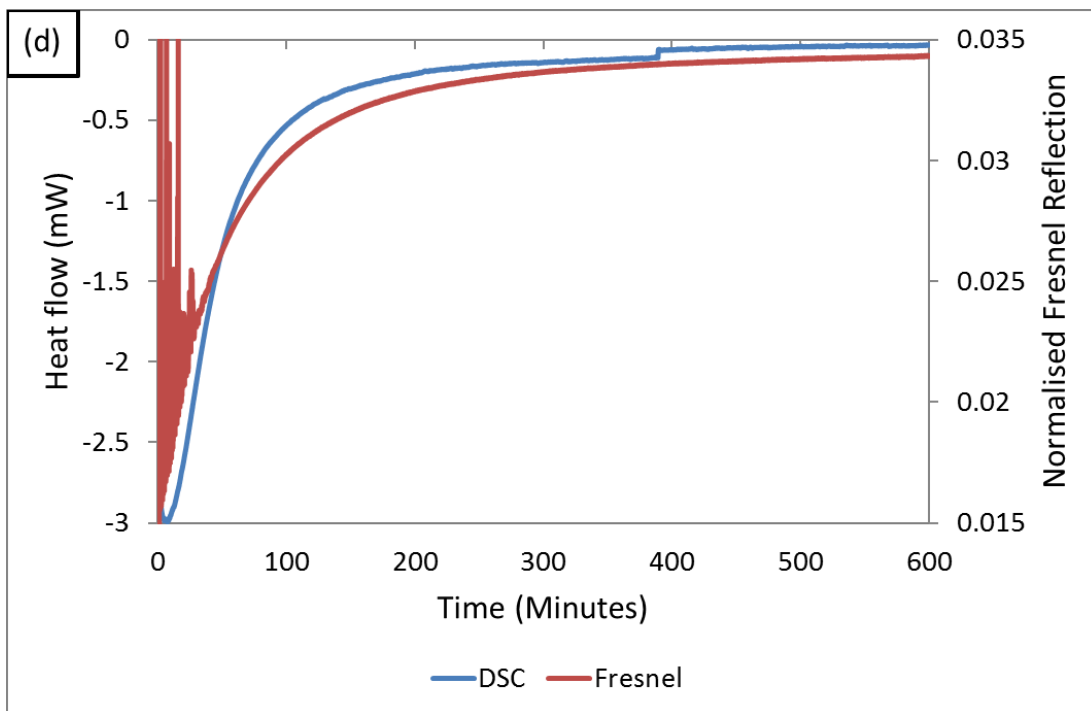


Figure 6.1 (continued) Isothermal cross-linking of LY3505/XB3403 at 70 °C with:  
 (d) 0.5 wt%; and (e) 1 wt% GNP.

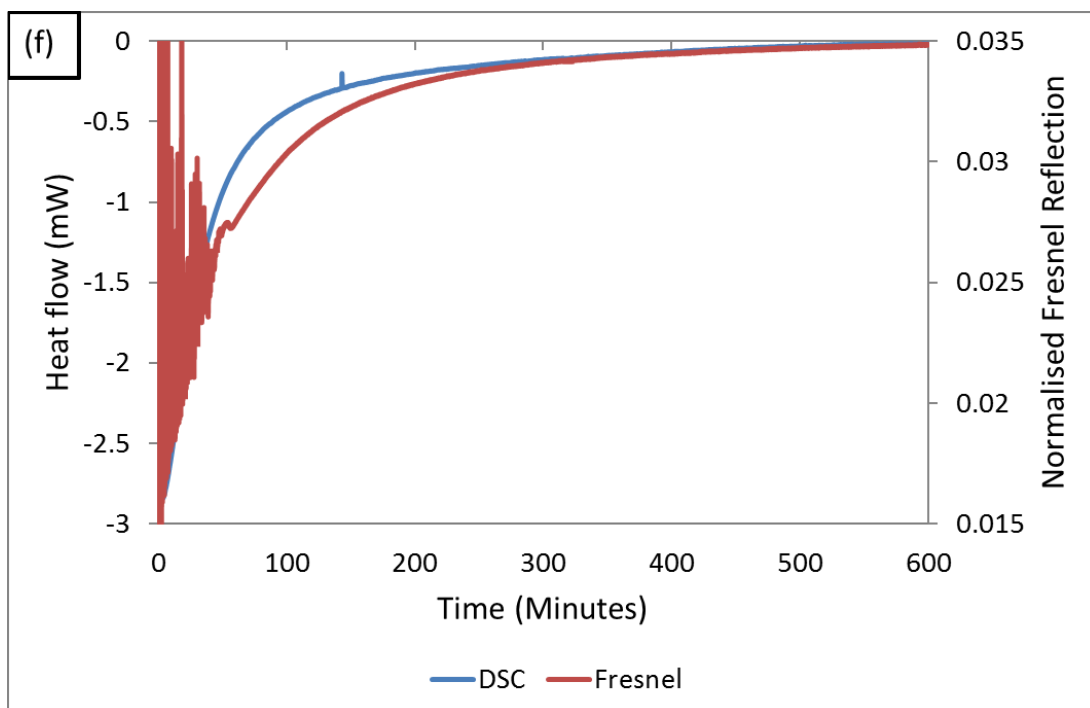


Figure 6.1 (continued) Isothermal cross-linking of LY3505/XB3403 at 70 °C with:  
(f) 2 wt% GNP.

In Section 2.3.3, Chapter 2, the impact of graphene particulates on the cross-linking kinetics of epoxy resins was discussed and Table 2.14 summarised the literature results. However, it was noted that consensus was not achieved in the literature with regards to the effect of introducing low quantities of GNPs into epoxy resin systems (Teng *et al.*, 2011; Ryu *et al.*, 2014; Galpaya *et al.*, 2015; Li *et al.*, 2015; Prolongo *et al.*, 2016). Complex interactions between the resin, hardener and particulates influence the cross-linking behaviour (Galpaya *et al.*, 2015). In the current study, similar magnitudes of the enthalpy of cross-linking were observed for each wt% GNP as shown in Figure 6.2.

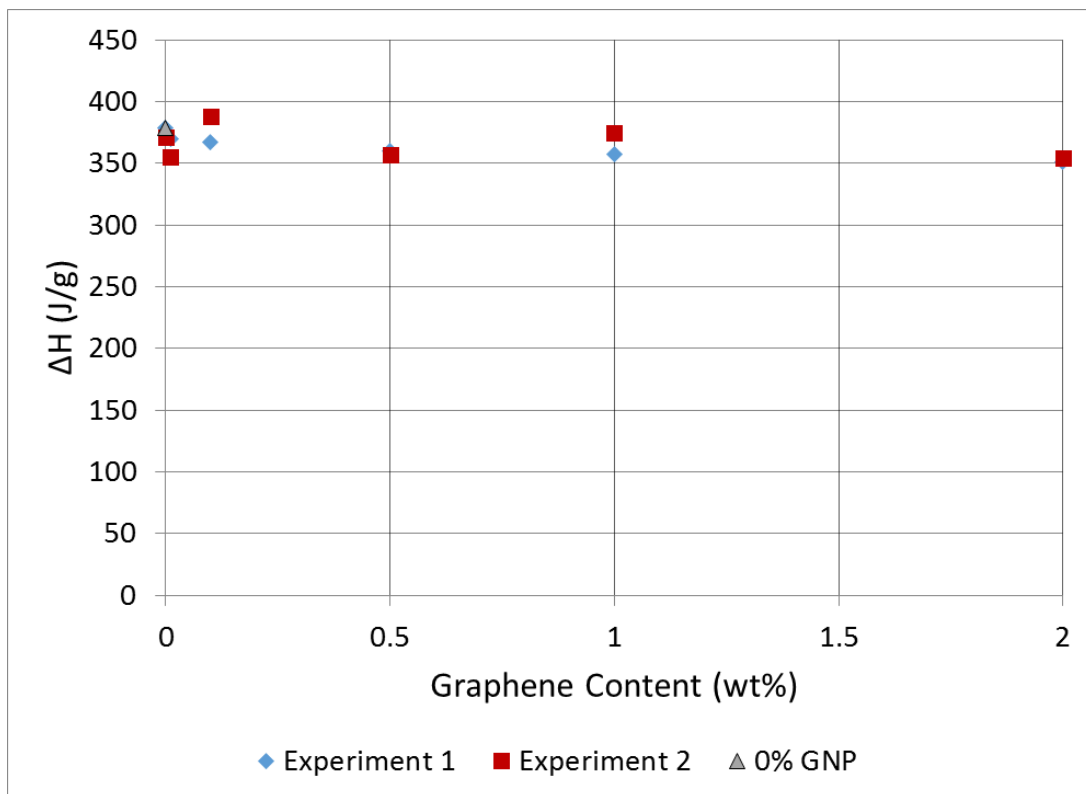


Figure 6.2 Magnitude of enthalpy during cross-linking at 70 °C of LY3505/XB3403 containing specified wt% of GNP.

The normalised Fresnel reflection data for each concentration of GNPs are shown in Figure 6.3(a) with an expanded view of the first 40 minutes of crosslinking shown in Figure 6.3(b). The increase in fluctuation amplitude and frequency is evident as the wt% of GNP is increased.

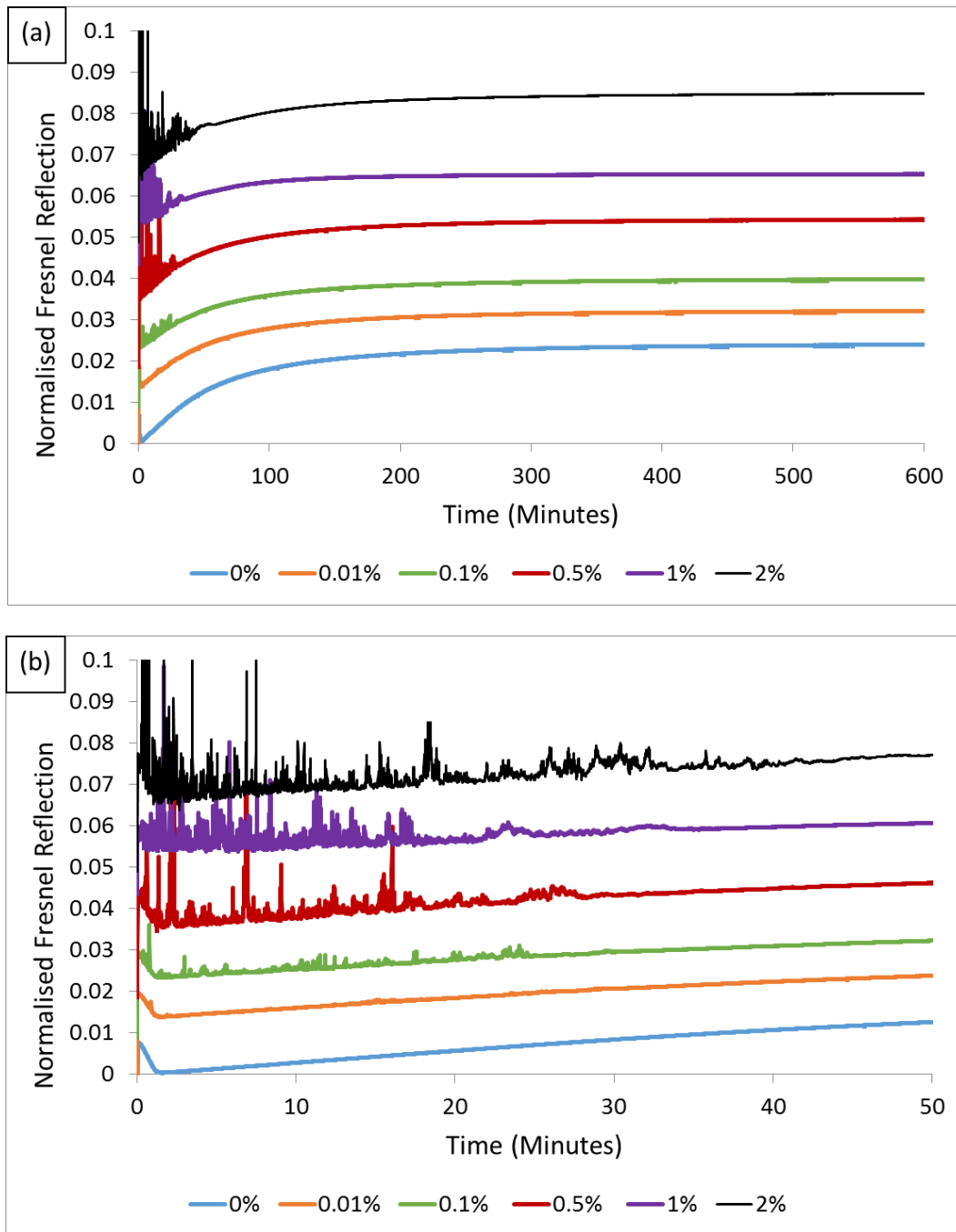


Figure 6.3 Response of the FRS during isothermal cross-linking of LY3505/XB3403 at 70 °C containing specified wt% of GNP: (a) Over 600 minutes; and (b) Expanded view from 0-40 minutes. The graphs have been moved in the y-axis to allow visibility.

Table 6.1 lists the times when the noise becomes negligible, the normalised Fresnel reflection at the start of isothermal cross-linking, after 600 minutes and the increase

over this period. The 'normalised Fresnel reflection upon increasing 70 °C' data point was taken as the lowest value at 70-71 °C. A general trend of a decreasing initial normalised Fresnel reflection value with increasing GNP content was observed. The introduction of the GNPs produced a blackening effect on the resin, preventing measurement of the refractive index using the Abbe refractometer. Upon reaching 70 °C, reduced normalised Fresnel values were observed with increasing GNP content. This could be explained by the absorption of light by the GNP preventing Fresnel reflection. There was an increase in the normalised Fresnel reflection over the 600-minute cross-linking period, although the magnitude of the increase was greater for the systems containing up to 1 wt% GNP. Systems containing 2 wt% showed approximately 25% lower increase during cross-linking.

Table 6.1 A summary of the times at which the fluctuations were detected in the FRS signal during the cross-linking of LY3505/XB3403 with specified wt% of GNP.

wt% GNP	Approximate time when noise becomes negligible (minutes)		Normalised Fresnel reflection on reaching 70 °C.		Normalised Fresnel reflection after 600 Minutes of isothermal cross-linking		Magnitude of increase in normalised Fresnel reflection during 600-minute cross-linking period.	
	Experiment		Experiment		Experiment		Experiment	
	1	2	1	2	1	2	1	2
<b>0</b>	N/A	N/A	0.0185	0.0183	0.0375	0.0419	0.0190	0.0236
<b>0.01</b>	32	30	0.0139	0.0143	0.0321	0.0347	0.0182	0.0204
<b>0.1</b>	33	36	0.0133	0.0149	0.0298	0.0346	0.0165	0.0197
<b>0.5</b>	37	36	0.0149	0.014	0.0343	0.0321	0.0194	0.0181
<b>1</b>	38	39	0.0110	0.0151	0.0315	0.0344	0.0205	0.0193
<b>2</b>	51	50	0.0090	0.0135	0.0203	0.0280	0.0113	0.0145

Dimopoulos *et al.* (2009) reported fluctuations in the FRS signal during the early stages of cross-linking of an epoxy/amine system containing carbon nanotubes. They postulated that the fluctuations were caused from either the movement of air bubbles, which were not removed during degassing, or due to the stochastic movement of particulates within the sensing region. In the current work, the degassing routine mentioned in Section 3.2.1 was used for all resin systems, indicating degassing issues were not responsible for the fluctuations.

In order to observe the interaction of the epoxy/GNP with the FRS over a defined period, the sensor was inserted into an alumina pan containing LY3505/0.1 wt% GNP (no amine). The DSC/FRS technique was used to study the effect of the GNP without the amine hardener. The sample was held at 30 °C for 20 minutes before ramping to 70 °C with a dwell for 10 hours. The output from the thermocouple and the FRS are shown in Figure 6.4. At 30 °C, the stochastic behaviour of the FRS signal emanates from a consistent minimum value of 0.0294. This value is equal to that recorded from neat LY3505. As the temperature was increased to 70 °C, the minimum baseline value was reduced from 0.0386 to 0.0299, whilst an increase in the fluctuation intensity was observed.



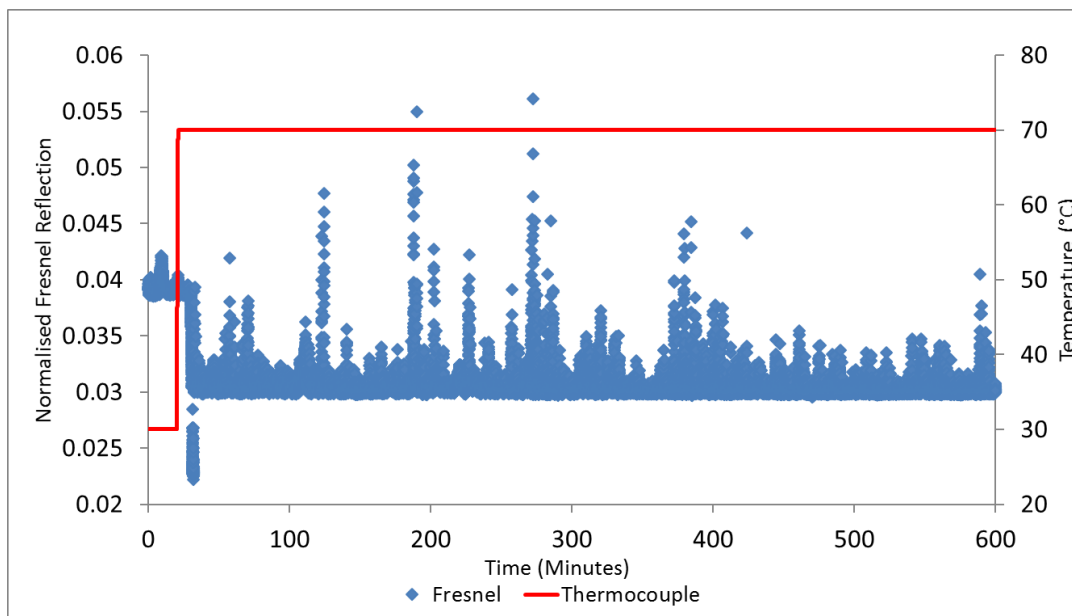


Figure 6.4 FRS signal emanating from the epoxy resin (LY3505) containing 0.1 wt% GNP at 30 and 70 °C using hyphenated DSC/FRS.

To observe the fluctuation in the FRS signals further, the FRS probe was inserted into a LY3505/0.1 wt% GNP sample at room temperature with an increased acquisition rate of 10 Hz, compared to the previously used 2 Hz. Figure 6.5 shows the FRS signals over a one-minute interval. Similar to Figure 6.4, a stochastic signal is seen. The minimum normalised Fresnel reflection value is equal to that when the sensor is immersed in LY3505 resin.

A magnified plot of the FRS data for LY3505 containing 0.1 wt% GNPs is shown in Figure 6.5; the fluctuations increased the FRS signal. One or more of the following reasons may have contributed to the observed fluctuations in the FRS signal during the initial stages of cross-linking:

- (i) Local temperature and refractive index fluctuations due to the presence of the GNP. Thermal gradients in the sample, introduced by the DSC and

the FRS, may have caused convection within the resin and hence contributed towards the fluctuations.

- (ii) Intermittent creation of a Fabry-Perot “cavities” between the tip of the sensor and GNPs. It is speculated that some of the noise may be attributed to the formation of interference fringes. The variation of the fluctuations may have been due to the sensor/GNP distance in addition to their relative orientation.
- (iii) Specular reflections from GNP particles within the sensing region.

It is unclear if the GNPs interfere with the FRS data due to Fabry-Perot-type interference, reflection or by temporary proximity of the GNPs around the sensor. Interestingly, Figure 6.5 appears to show an isolated fluctuation that resembles Fabry-Perot interference fringes. The minimum baseline value appears to be indicative of a moment when there were no particles lying within the sensing region, as this reproducible minimum value was equal to that of the neat resin. The upward fluctuations may represent periods where agglomerations of GNP pass within the interaction region. It is unclear how far the sensing region reaches into the resin. The amplitude of the fluctuations may be influenced by particle size, shape, quantity, orientation and proximity to the sensor. Sections 6.2 and 6.3, later in this chapter, aim to further investigate these hypotheses.

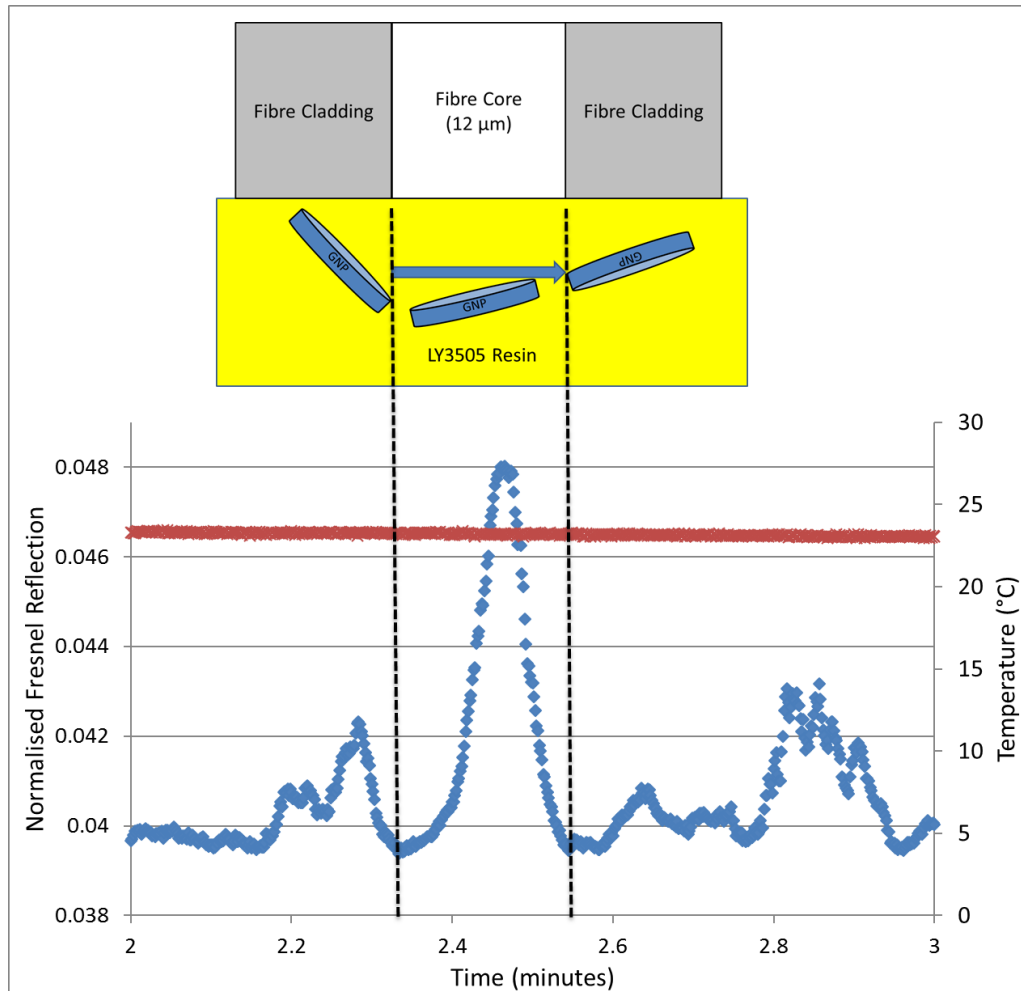


Figure 6.5 FRS signal emanating from the LY3505 resin containing 0.1 wt% GNP at room temperature using an increased acquisition rate of 10 Hz. A schematic representation of the cause of the fluctuations is also shown.

## 6.2 Impact of Ultrasonic Mixing of Resin on the Fresnel Reflection Sensor Signal

As discussed in Section 2.3.3, it has been reported widely that GNPs have a tendency to agglomerate (King *et al.*, 2013; Chandrasekaran *et al.*, 2014; Wan *et al.*, 2014a). It was suspected that the fluctuations of the FRS were a result of the movement of micron sized particles across the sensor. Previously, Zaman *et al.* (2012); King *et al.* (2013) and Prolongo *et al.* (2014) reported that uniform dispersion

of GNPs can be achieved using sonication techniques. Therefore, the impact of sonicating the resin/GNP mixture as a function of time was investigated. The response of the FRS on the resin/GNP as a function of the sonication time, at room temperature is presented in Figure 6.6. The sonication process was undertaken using 50% of the sonication amplitude that was available, as above this level, a rapid increase in the temperature was observed. With reference to Figure 6.6, the sonication of the resin/GNP did not remove the fluctuations but appears to have removed the largest perturbations. This may have been due to de-cohesion of the agglomerated GNPs. Beyond this, no significant reductions were observed.

At the end of the experiment, 100% amplitude was used for 3 minutes despite introducing significant temperature increases. A decrease in the fluctuation intensity was observed. It is possible that the 'higher amplitude' mixing broke-up some GNP agglomerations.

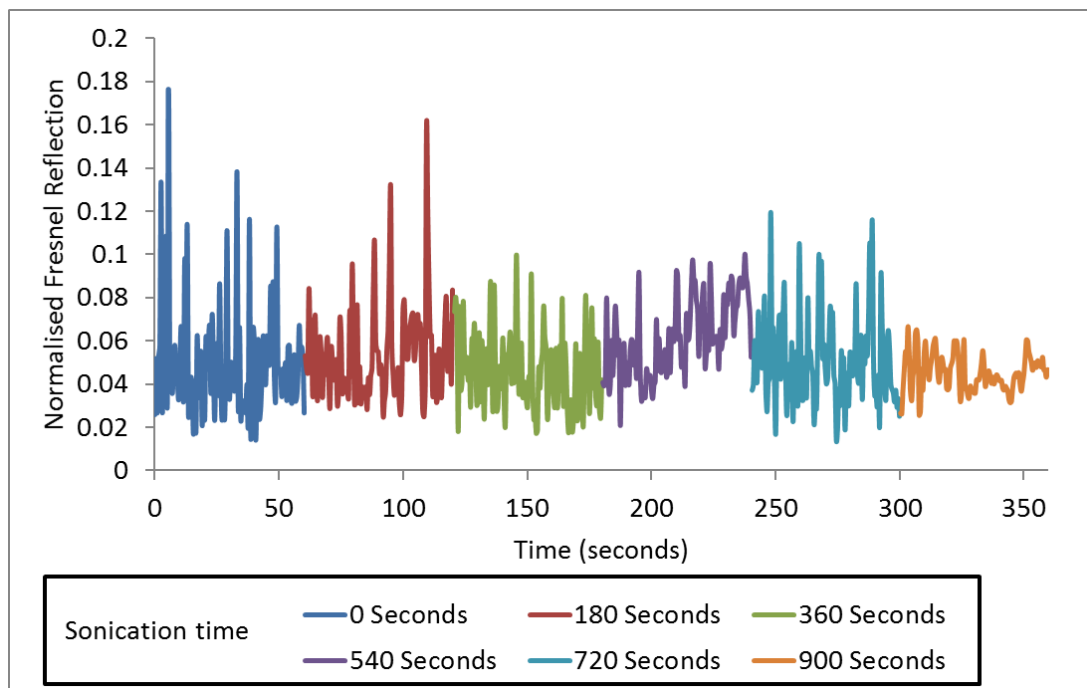


Figure 6.6 Impact of sonication of the resin/GPN on the FRS signal for LY3505 containing 2% GNP (no hardener) after various times, using an amplitude of 12 kHz.

### **6.3 Effect of Freezing the Epoxy Resin on the Output from the Fresnel Reflection Sensor**

LY3505/GNP resins were frozen using liquid nitrogen with the FRS probe inserted, to investigate if restricting particle movement would affect the observed fluctuations in the FRS signal. The sensor and a thermocouple were immersed in epoxy/GNP sample contained in an aluminium dish. The dish was then lowered into a bath of liquid nitrogen. After cooling, the sample was left to return to room temperature.

Figure 6.7 shows the effect of cooling the neat resin on the output from the FRS. The signal remained constant at room temperature for 20 minutes, before liquid nitrogen was introduced. Upon adding the liquid nitrogen, the temperature was reduced to  $-196\text{ }^{\circ}\text{C}$ . This caused a reduction in the refractive index and thus the FRS signal recorded a decrease. As the resin warmed, a period of large Fresnel fluctuations was observed. Following this, the signal gradually returned to its original value at room temperature.

At approximately  $-100\text{ }^{\circ}\text{C}$ , large fluctuations in the FRS signal are observed. Interestingly, the first of these fluctuations causes a normalised Fresnel reflection value of 1 to be recorded momentarily. This value is equivalent to that recorded in air and is shown in the insert of Figure 6.7. The fluctuations continue during warming until approximately  $-0\text{ }^{\circ}\text{C}$  where the signal returns to the original value of 0.039 indicating the sensor is fully submerged in the neat resin.

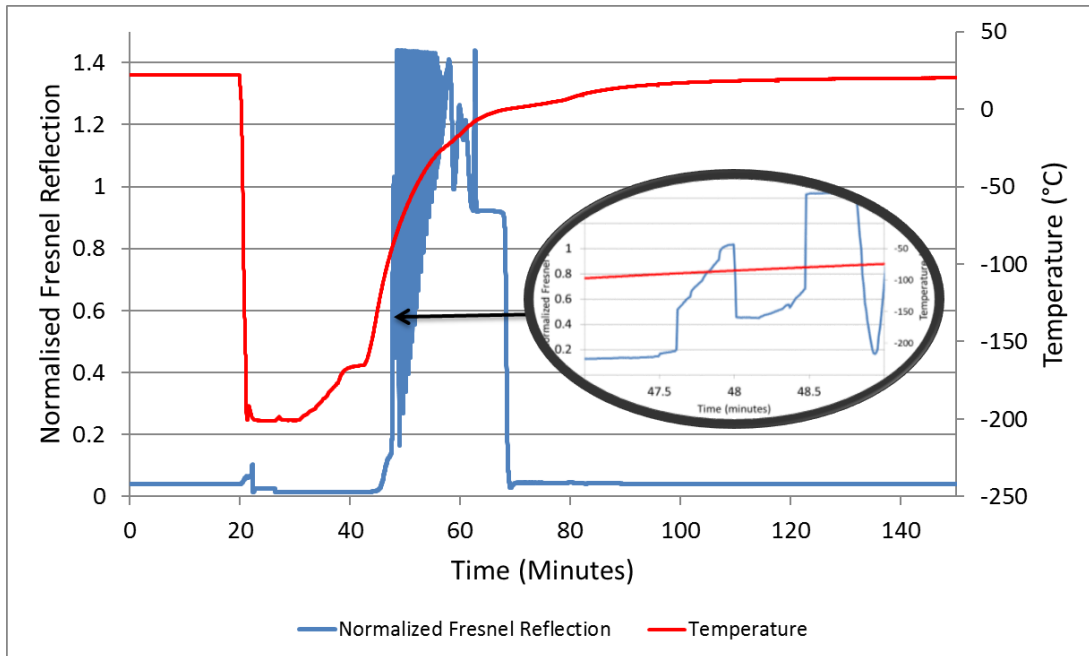


Figure 6.7 The response of a FRS when immersed in LY3505 (without GNP) and cooled using liquid nitrogen. The insert shows a period where the signal momentarily records 1 during warming

Mani *et al.* (2016) investigated the effect of melting ice on the FRS signal. As the ice warmed, a gradual increase in the FRS signal was observed until approximately  $-45$  °C. Between  $-45$  and  $-4$  °C, abrupt changes in the signal were observed, similar to those observed between 45 and 60 minutes in Figure 6.7. The authors gave the following reason for the abrupt changes. As the temperature increased, the differing thermal expansion coefficients of the silica fibre and the ice may have produced a strained region around the sensor. This could be exacerbated by the light absorption of the sample close to the sensing region. Eventually the strain becomes large enough to cause de-bonding of the fibre and the surrounding medium. The abrupt change initially changed to that of the freshly cleaved fibre in air. Following this, further fluctuations were observed. It was postulated by the authors that upon de-bonding, Fabry-Perot interference between the sensor and the

light, reflected by the ice, caused continued fluctuations. After complete melting of the ice, the FRS signal returned to the signal recorded in water.

Similar to the work of Mani *et al.* (2016), Figure 6.7 shows an abrupt change in the Fresnel signal during warming, to a value equivalent to that recorded in air. This indicates possible de-bonding of the sensor and the resin. It is possible that Fabry-Perot interferences were present until melt of the resin after 70 minutes, when the signal returned to that upon first insertion to the resin.

Figure 6.8 displays the FRS signal during a similar experiment where the sensor was immersed in LY3505 containing 2% GNP during four cooling regimes. Similar to the cross-linking experiments shown in Figure 6.3, the addition of GNP caused fluctuations in the FRS signal at room temperature. An increase in the intensity of the fluctuations was observed at higher concentrations. Four cooling/thaw cycles were undertaken for each resin/GNP concentration. With reference to Figure 6.8, a large abrupt increase in the signal occurs during the first cooling regime which saturates the sensor response. As the resin warmed, the fluctuations reduced in amplitude and increased in intensity before returning to the original fluctuating behaviour above -20 °C.

Upon the second cooling regime, a steady normalised Fresnel reading of 0.071 was recorded between 129 and 135 minutes, whilst the temperature was below -180 °C. Between 136 and 145 minutes, the FRS signal decreased linearly as the temperature increased from -180 °C to -56 °C. The relatively steady signal response of the FRS whilst the resin was frozen indicated that the movement of particles within the liquid resin could be the primary source of the observed fluctuations in the output from the FRS.

Between 145 and 153 minutes, the resin warmed from  $-56\text{ }^{\circ}\text{C}$  to  $-18\text{ }^{\circ}\text{C}$  and large fluctuations in the sensor signal occurred which were reduced in magnitude as the temperature increased. After 153 minutes, the signal returned to the fluctuating behaviour observed upon first insertion as the resin warmed from  $-18\text{ }^{\circ}\text{C}$  to room temperature.

The third cooling regime also induced a steady normalised Fresnel signal below  $-180\text{ }^{\circ}\text{C}$  with a value of 0.061. The signal response and refractive index of the system decreased as the resin warmed from  $-178\text{ }^{\circ}\text{C}$  to  $-80\text{ }^{\circ}\text{C}$ . From  $-78\text{ }^{\circ}\text{C}$  to  $-18\text{ }^{\circ}\text{C}$ , large signal fluctuations occurred. The sensor response returned a similar value as it warmed from  $-18\text{ }^{\circ}\text{C}$  to room temperature.

A steady signal response was also observed during the fourth cooling regime. The normalised Fresnel value of 0.094 was recorded at  $-200\text{ }^{\circ}\text{C}$  and the value then decreased as the resin warmed to  $-60\text{ }^{\circ}\text{C}$ . From  $-60\text{ }^{\circ}\text{C}$  to  $-16\text{ }^{\circ}\text{C}$ , large fluctuations occurred which caused saturation of the signal and decreased in amplitude with time. The signal response then returned to the characteristic fluctuating state present upon first insertion.

During the cooling regimes, four distinct zones were observed:

- (i) Initial fluctuation: Fluctuation of the sensor at ambient temperature before cooling. The movement of GNP particles is expected to be in-part responsible for the fluctuations.
- (ii) Steady signal state: Upon cooling, the frozen state of the resin prevents particle movement causing the sensor response to become steady at temperatures below  $-90\text{ }^{\circ}\text{C}$ . A different normalised Fresnel reflection was detected on each cooling cycle at  $-200\text{ }^{\circ}\text{C}$ . This may be due to variations



in the particles size, concentration and proximity to the sensing region on each cooling regime.

- (iii) Large fluctuations: These fluctuations caused saturation of the signal during warming, starting between -90 °C and -60 °C and finishing at -20 °C. The fluctuations reduced in amplitude and increased in intensity as the resin warmed. Similar fluctuations were observed during the cooling of the resin containing no GNP (Figure 6.7). It is postulated that de-bonding of the sensor and the resin may have occurred due to strains induced by the thermal expansion coefficient difference between the resin and the optical fibre; hence contributing toward the signal fluctuations.
- (iv) Re-immersion of the sensor: As the resin warmed above -20 °C, the sensor response returned to the fluctuating state observed upon initial insertion.

The removal of the characteristic FRS fluctuations upon freezing of the resin was observed at each GNP concentration.

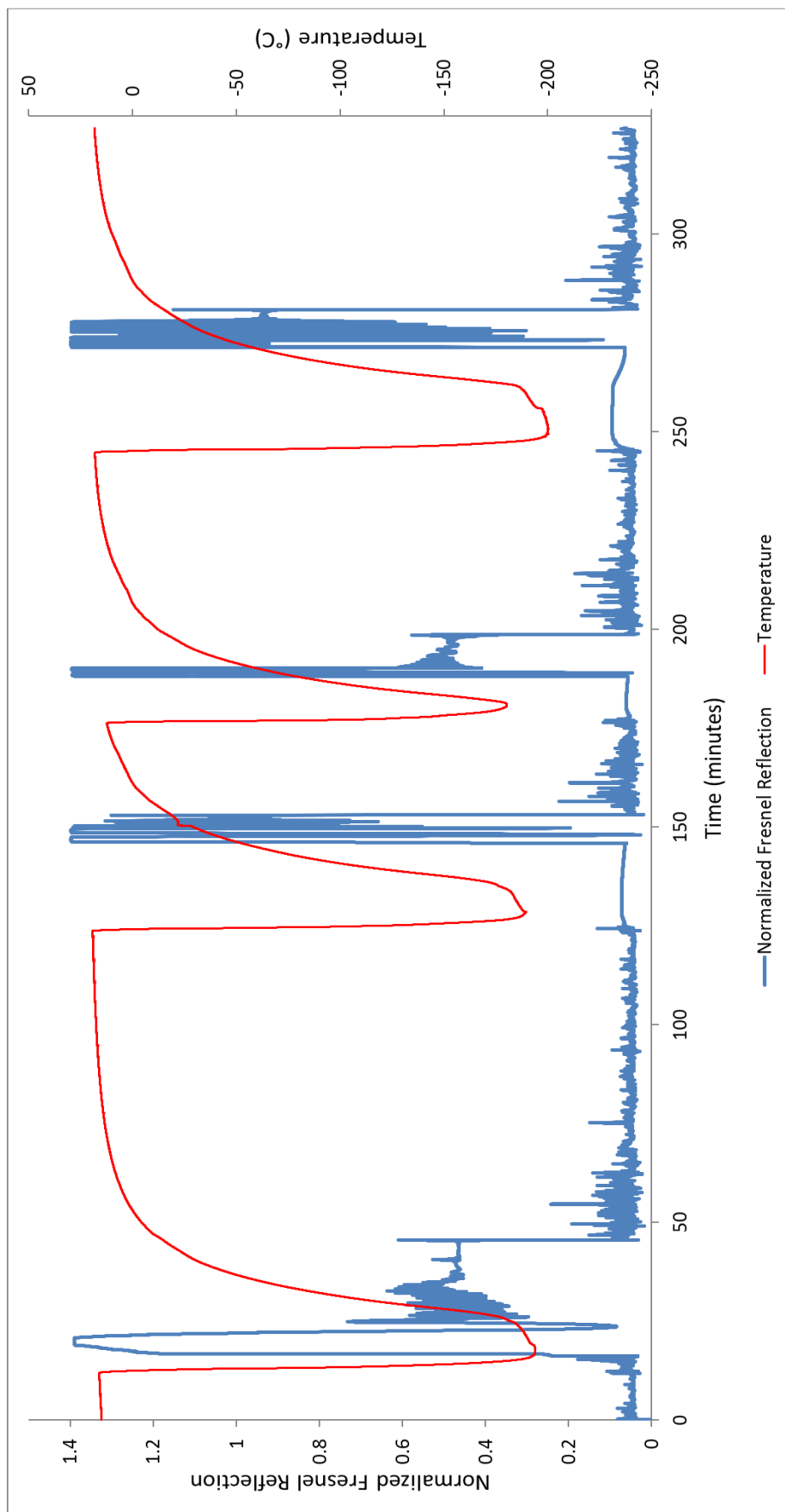


Figure 6.8 Response of a FRS that was immersed in LY3505 resin containing 2 wt% GNP. The blended resin was subjected to four cycles of cooling/recovery to ambient temperature in a bath of liquid nitrogen.

## **6.4 Hyphenated Rheology/Fresnel Reflection Sensor**

In Section 6.1.1, the FRS displayed fluctuations for the LY3505/XB3403/GNP systems that diminished during cross-linking. It was then shown in Section 6.3 that freezing the samples reduced movement of the GNP in the epoxy resin and the fluctuations subsided. It was considered that during cross-linking, gelation may restrict the movement of the GNPs particles. To investigate this hypothesis, a FRS was introduced into a rheometer to enable direct comparison of the optical and rheological characteristics during cross-linking at 70 °C.

### **6.4.1 LY3505/XB3403**

Figure 6.9 shows the rheology/FRS result for the LY3505/XB3403 resin system without GNP at 70 °C. Erratic data were initially generated by the load-cell that was used; it was not meant to be used for resins with low viscosities. As cross-linking proceeded, the 2 g.cm minimum torque sensitivity of the rheometer was surpassed, and meaningful data were recorded. As the cross-linking reaction progressed,  $G'$  and  $G''$  increased. The crossover of these parameters is at approximately 60 minutes and this, as discussed previously, was taken as an indication of the gelation point.

Upon comparison with conventional rheometry, as described in Section 4.4, it was apparent that the introduction of the FRS had not produced any observable difference in the rheological data.

The FRS signal showed an initial decrease as the temperature of the resin system was increased from ambient to the required isothermal cross-linking temperature. Following this period, the increase in the FRS signal was due to the refractive index increasing as a function of cross-linking. Some signal fluctuation was observed in the early stages of cross-linking as seen in Figures 6.9 (a) and (b). This may be attributed to the movement of the shearing action of the parallel plates. After approximately 20 minutes, no fluctuations are observed.

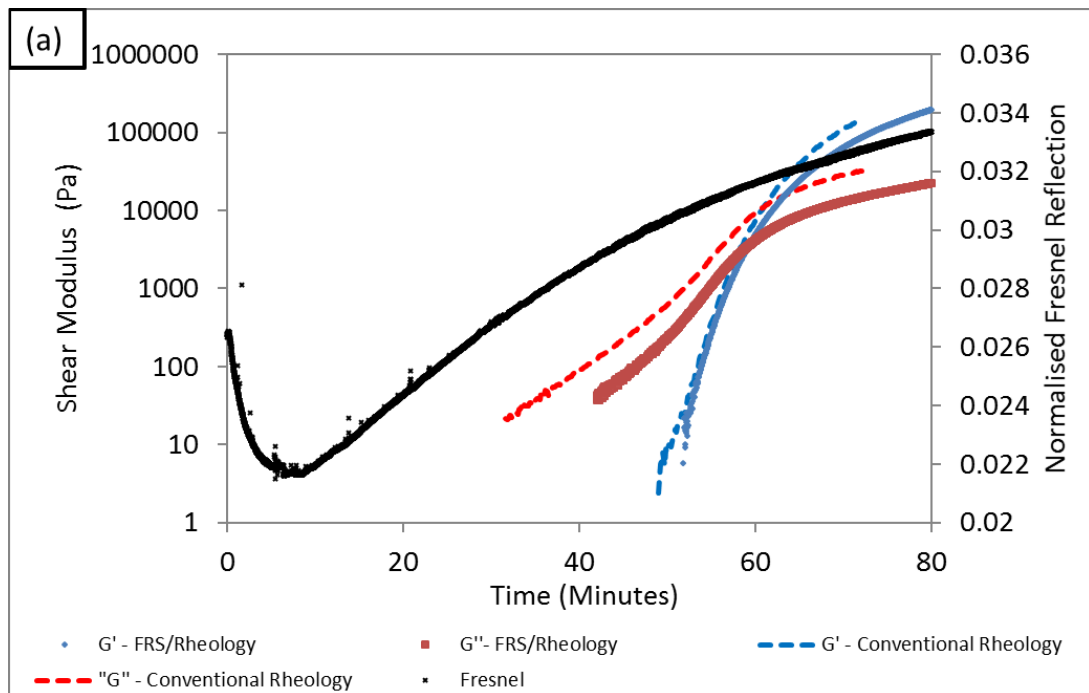


Figure 6.9 Simultaneous rheology/FRS and conventional rheology during cross-linking of LY3505/XB3403 at 70 °C: (a) Experiment 1.

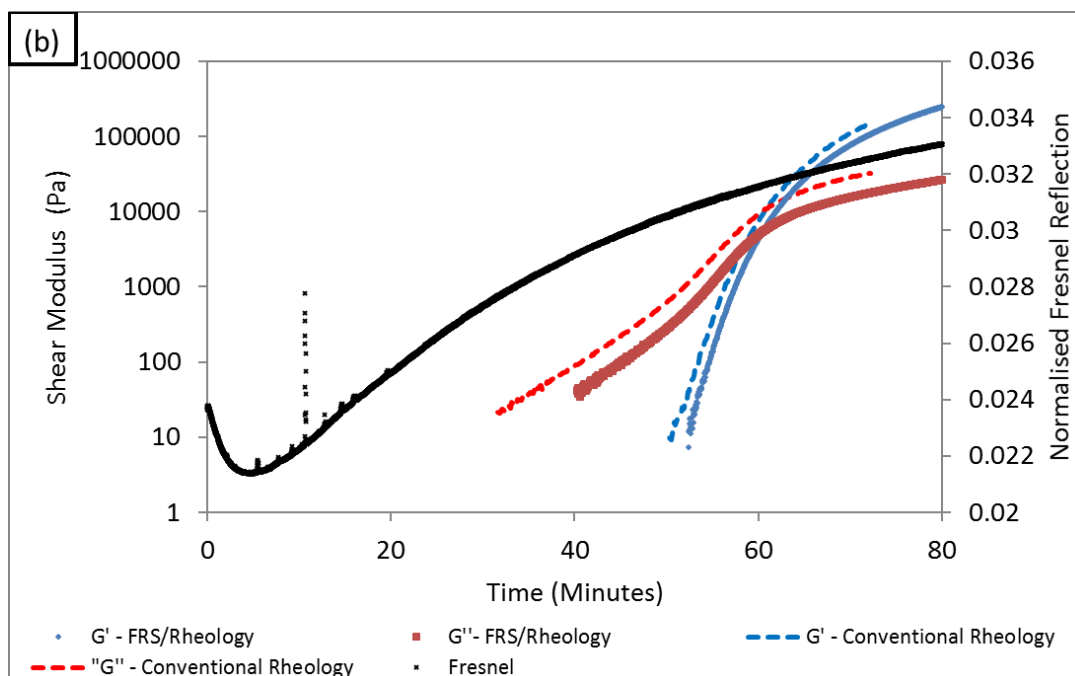


Figure 6.9 (continued) Simultaneous rheology/FRS and conventional rheology during cross-linking of LY3505/XB3403 at 70 °C: (b) Experiment 2.

#### 6.4.2 Rheological Characteristics of the LY3505/XB3403 Resin System with Graphene Nano-particles

The LY3505/XB3403 resin system containing 2 wt % GNPs was selected for isothermal hyphenated rheology/FRS experiments at 50, 60 and 70 °C. Figures 6.10 (a) – (c) show data obtained at each isothermal cross-linking temperature. Similar to previous experiments, a noisy period was observed during the early stages of cross-linking in the rheological data, where the viscosity of the resin was below the sensitivity of the instrument. Meaningful data were then acquired as the viscosity of the resin increased and surpassed the minimum torque value of 2 g.cm of the rheometer. As cross-linking progressed, a logarithmic increase in  $G'$  and  $G''$  was observed. The increase in  $G'$  and  $G''$  was delayed at lower temperatures, as well as the crossover of  $G'/G''$ . The experiments were

terminated after gelation to prevent overloading of the rheometer transducer. The addition of graphene nano-particles introduced fluctuations in the FRS data, as observed previously with the DSC/Fresnel technique.

With reference to Figure 6.10(a) when the experiments were conducted at 50 °C, the FRS data showed large fluctuations up to approximately 140 minutes. The fluctuations appeared to reduce in magnitude and frequency with cross-linking time. It is postulated that the cross-linking network restricts the movement of the GNPs which reduces the frequency of the fluctuations. From approximately 150 minutes onwards, a relatively stable signal was acquired, which increased linearly after approximately 160 minutes. These observations were observed at earlier times for experiments cross-linked at 60 and 70 °C, as shown in Figure 6.10 (b) and (c).

To draw correlation between the FRS data and the rheometer data, a linear line was extrapolated from the relatively linear FRS data toward the end of the experiments, as shown in Figures 6.10 (a) – (c). The time when the data deviated before this extrapolation was then compared with the  $G'/G''$  crossover and was termed the 'onset of linearity'. In comparison to the  $G'/G''$  crossover, the onset of linearity was generally detected at earlier times as shown in Figure 6.11, for each of three repeat experiments. The difference between the two times decreased at higher temperatures. The data show that the FRS can be used to estimate the gelation time of this epoxy/GNP system.

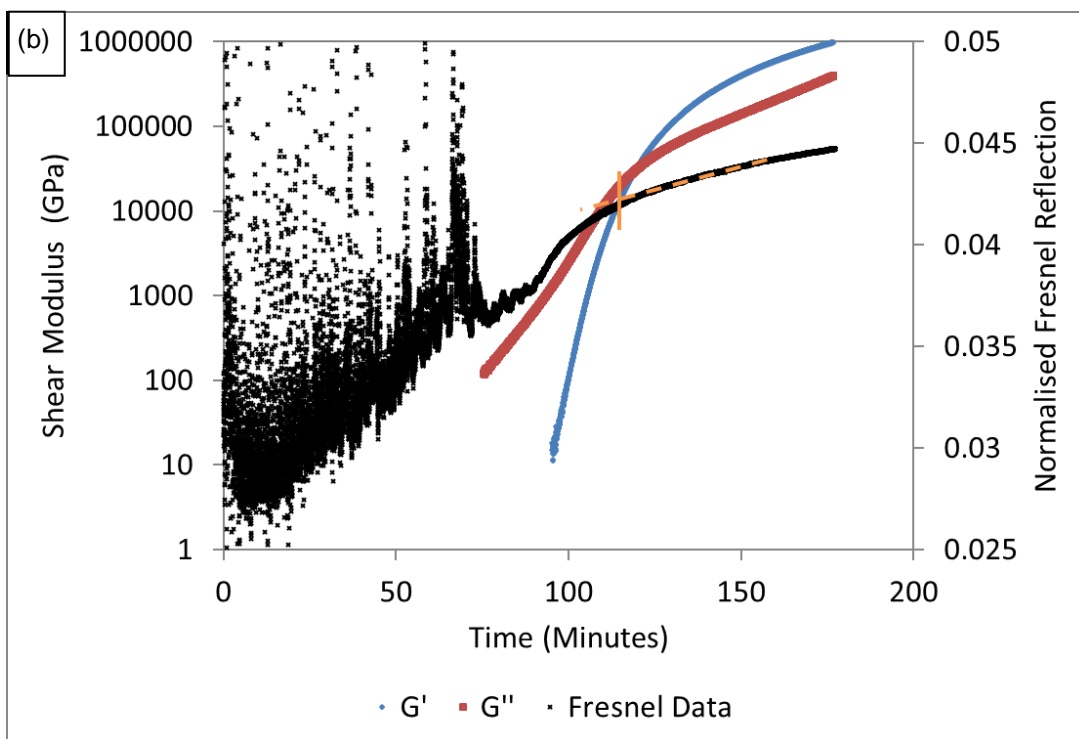
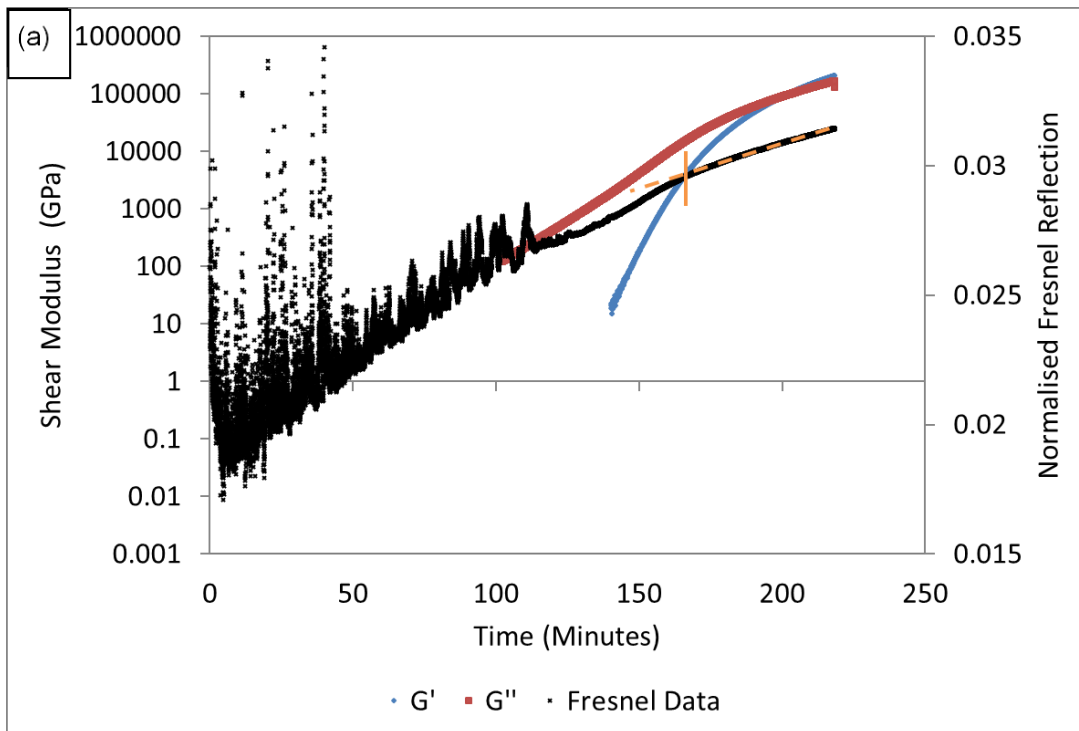


Figure 6.10 Hyphenated rheology/FRS during cross-linking of LY3505/XB3403/2 wt% GNP at: (a) 50 °C; and (b) 60 °C.

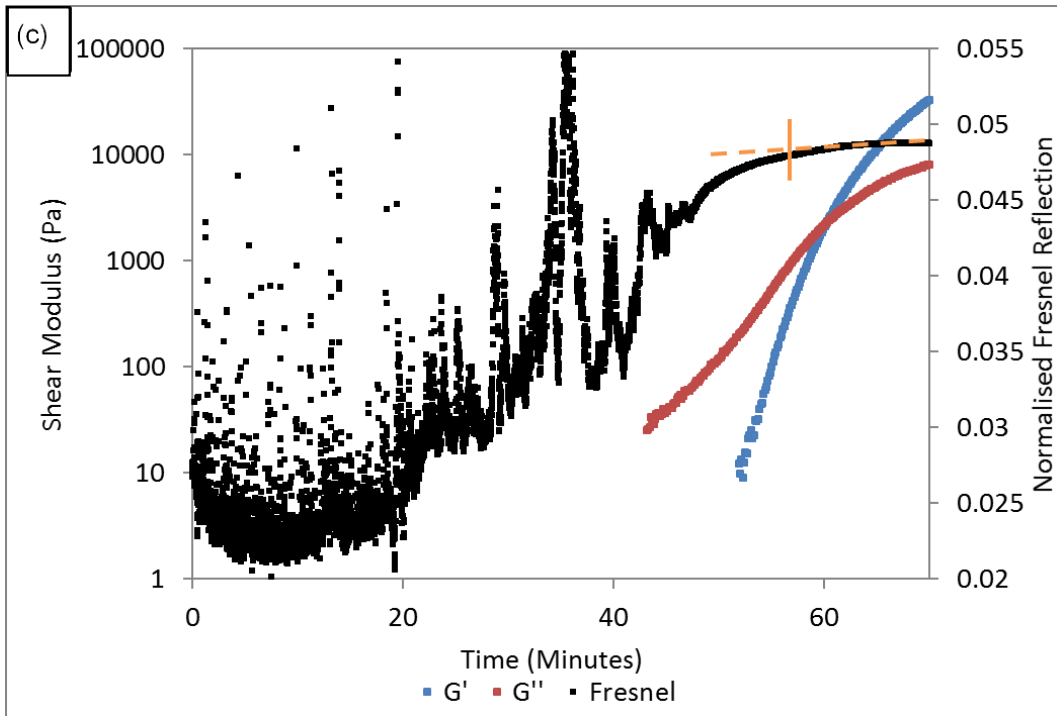


Figure 6.10 (continued) Hyphenated rheology/FRS during cross-linking of LY3505/XB3403/2 wt% GNP at: (c) 70 °C.

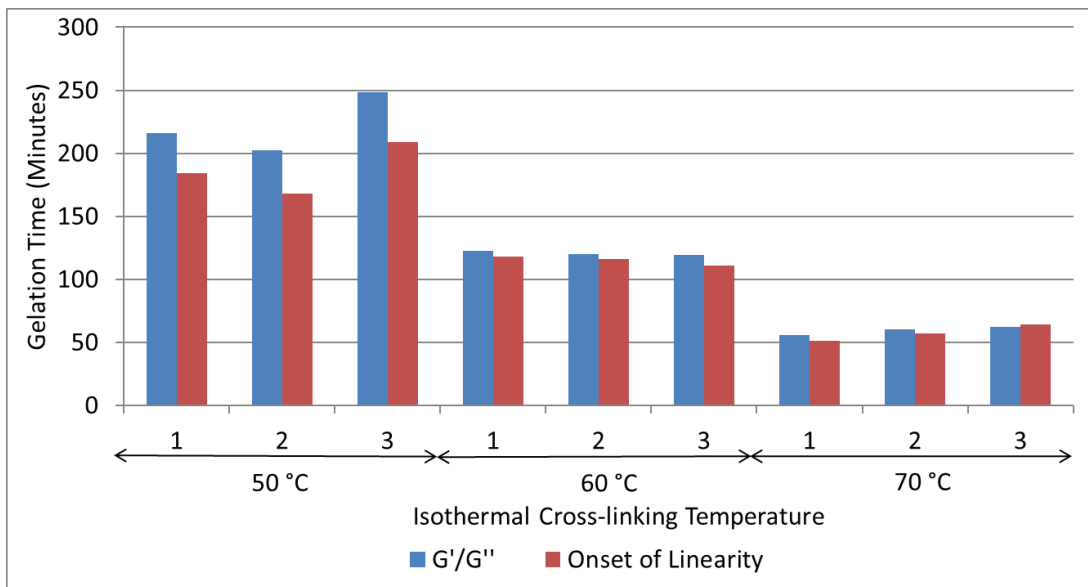


Figure 6.11 Comparison of the  $G'/G''$  crossover and the onset of linearity during hyphenated rheology/FRS of LY3505/XB3403/2 wt% GNP.



## 6.5 Summary

The introduction of GNPs was found to have a negligible effect on the enthalpy of reaction for the LY3505/XB3403 resin system. The FRS output showed a fluctuating signal during cross-linking that increased in intensity and frequency with the GNP concentration. In each experiment, the initial noise fluctuations in Fresnel reflection diminished with cross-linking time.

Previous authors had noted the importance of sonication as an effective way to disperse GNPs. Sonication of the resin containing the GNP appeared to reduce some of the larger fluctuations but failed to remove them completely. High amplitude mixing appeared to reduce the fluctuations even further, although the technique generated rapid temperature increases which could have affected the chemical integrity of the resin.

To test the hypothesis that the GNPs were responsible for the observed fluctuations in the FRS signal during the initial stages of cross-linking, the resin with the FRS was frozen using liquid nitrogen. For each concentration of GNP tested (0.1, 1 and 2 wt%), the fluctuations were reduced upon freezing. The steady signal indicated that local refractive index variations, due to the presence of GNPs, as opposed to Fabry-Perot standing waves, were responsible for the fluctuations. The fluctuations continued as the resin thawed.

The FRS was also introduced in a rheometer to investigate the relationship between the  $G'/G''$  gelation estimation with the dissipation of fluctuation observed during cross-linking. A good correlation was observed at the higher temperature cures, with

the fluctuation dissipation point showing increased reproducibility at times before  $G'/G''$ .

Overall the FRS technique was demonstrated to be capable of tracking the degree of cure. The detected fluctuations in the FRS signals gave an indication of the content of graphene particulates within the system, by their frequency and intensity. It has also been shown that the fluctuations appeared to have been caused by stochastic movement of the particles and that the dissipation can be an indicator of gelation. The fluctuating sensor reading was comparable to the epoxy/thermoset system during phase separation, which was reported in Section 5.3.

## **7. HYPHENATED DIFFERENTIAL SCANNING CALORIMETRY, FRESNEL REFLECTION SENSOR AND FOURIER TRANSFORM INFRARED SPECTROSCOPY**

### **7.1 Development of the Differential Scanning Calorimetry /Fresnel Reflection Sensor /Fourier Transform Infrared Spectroscopy Technique**

The development of the DSC/FRS/FTIRS technique commenced with the design and construction of the FRS/FTIRS probe. The DSC pan had to be modified because the FRS required a non-reflective surface and the FTIRS relied on reflections off the surface of the pan. This was achieved by making part of the surface of the DSC pan non-reflective. The probe was introduced into the custom-modified DSC and it was calibrated in the normal manner using indium. The cross-linking kinetics of the LY3505/XB3403 resin system was carried out at 50, 60 and 70 °C. The data from the DSC/FRS/FTIRS technique were compared with those derived from the conventional DSC instrument. The cross-linking kinetic parameters were derived and compared for the two analytical methods.

#### **7.1.1 Reflectivity of the Differential Scanning Calorimeter Pans**

To render part of the surface of the DSC pan non-reflective (in order to fulfil the requirements for the FRS), half the surface was covered and sprayed with a graphite spray. The effectiveness of the non-reflective coating was assessed by lowering the FRS, with the aid of a micrometer translation stage, to quantify the reflectivity as a function of the distance from the base of the pan. It was found that the graphite

coating prevented reflected light from the base of the DSC pan being coupled back into the FRS. An investigation was also undertaken to establish if the uncoated reflective area of the pan was sufficient to conduct transmission/reflection FTIRS. Approximately 20 mgs of LY3505/XB3403 was dispensed into a pan and the Fresnel/FTIRS probe was lowered towards the pan; due care was taken to ensure that the optical fibres that enabled FTIRS were positioned over the reflective portion of the DSC pan. The probe was lowered to the height of the sidewall of the DSC pan, 1.5 mm. Figure 7.1 shows the intensity of the epoxy and amine absorbance bands at  $4530\text{ cm}^{-1}$  and  $4935\text{ cm}^{-1}$  as a function of distance from the reflective portion of the base of the pan. A linear relationship was observed between the peak areas and the distance from the top-base of the DSC pan. During DSC/FTIRS/FRS, the probe was held 3.3 mm from the top-base of the DSC pan. It was concluded that the signal strength was adequate at this distance.

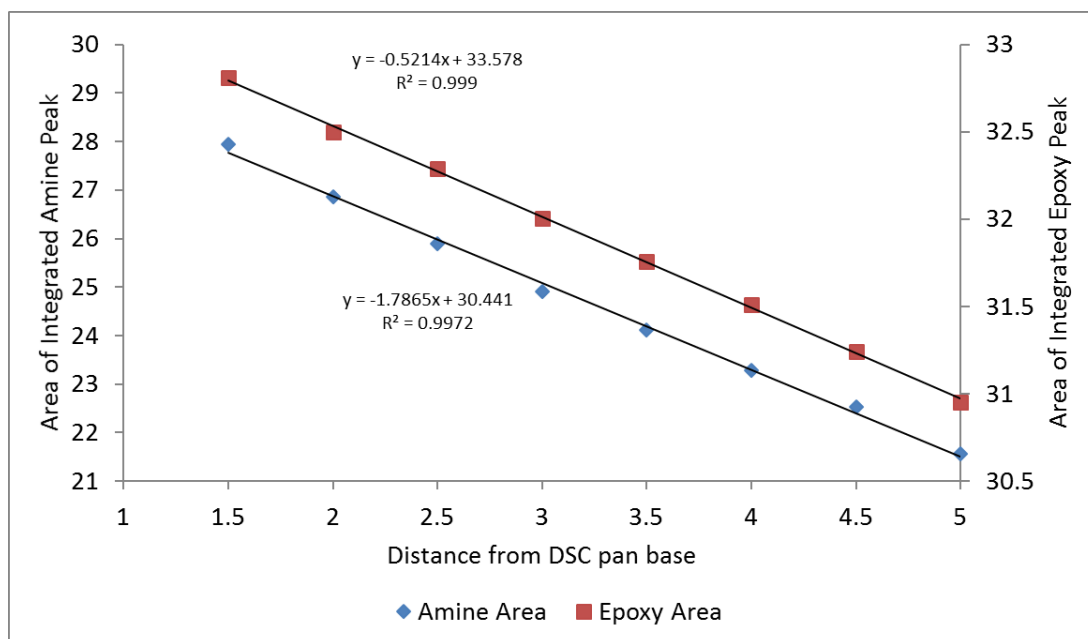


Figure 7.1 Epoxy and amine peak areas as a function of the height of the FTIRS probe from the top-base of the DSC pan.

Figure 7.2 shows the spectra of freshly mixed LY3505/XB3403, obtained from conventional transmission spectroscopy, alongside that from the FTIRS/Fresnel probe using the part-reflective DSC pans. The probe was held at 3.3 mm from base of a sprayed pan using a micrometer translation stage to replicate the distance in later FTIRS experiments that were carried out within the DSC. A similar response was evident from the two techniques. The absorbance bands for the epoxy ( $4530\text{ cm}^{-1}$ ) and CH reference peak ( $4620\text{ cm}^{-1}$ ) were adequate for tracking the cross-linking reactions. With reference to Figure 7.2, each of the assigned peaks in Table 4.5, in Chapter 4, were observed. At wavenumbers below approximately  $4400\text{ cm}^{-1}$ , a 'noisy' region was present for the spectra acquired by the FRS/FTIRS probe. This was due to the wavelength range ( $4200\text{-}25000\text{ cm}^{-1}$ ) of the fibres as detailed by the manufacturer (Thorlabs, 2017). Figure 7.2 demonstrates the capability of the FRS/FTIRS probe to acquire transmission/reflection infrared spectra.

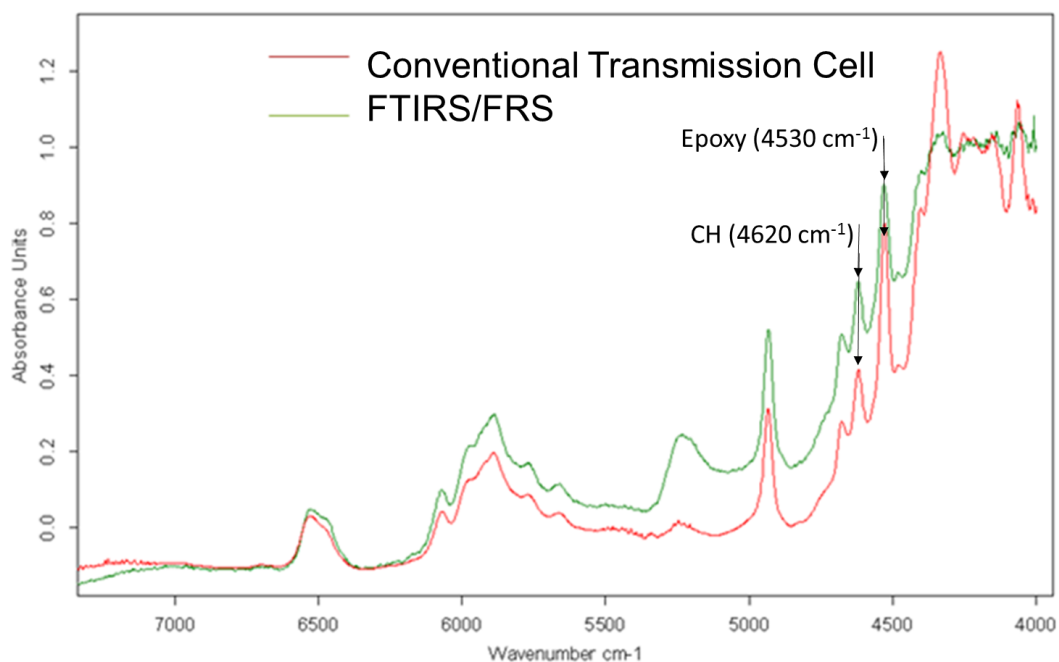


Figure 7.2 Spectra of freshly mixed LY3505/XB3403 at  $70\text{ }^{\circ}\text{C}$  from a conventional transmission cell and the FRS/FTIRS probe. The arrows represent the absorbance peaks that were used to calculate the peak areas for the kinetic analysis.

### 7.1.2 Cure Monitoring outside the Differential Scanning Calorimeter

Prior to integrating the FRS/FTIRS probe in the DSC, it was evaluated outside the instrument to track the cure of LY3505/XB3403. A mixed resin sample was dispensed onto a modified pan and placed onto a hot-plate. A thermally insulated brick (see Figure 3.10) was sculptured to accommodate the DSC pan and to permit the insertion of the FRS/FTIRS probe using a micrometer translation stage. The hot-plate was turned on after the probe was positioned as required, and the cross-linking of the resin system was monitored for 10 hours. A thermocouple was placed in close proximity to the DSC pan and the output is shown in Figure 7.3. The observed fluctuations in the data from the thermocouple may be attributed to the mode of operation of the hot-plate, whereby the heating is activated and switched off intermittently when temperature falls above or below a set range. Since the thermocouple was measuring the air temperature below the insulation brick, as shown in Figure 3.10, local air turbulence could also have contributed to the observed fluctuations.

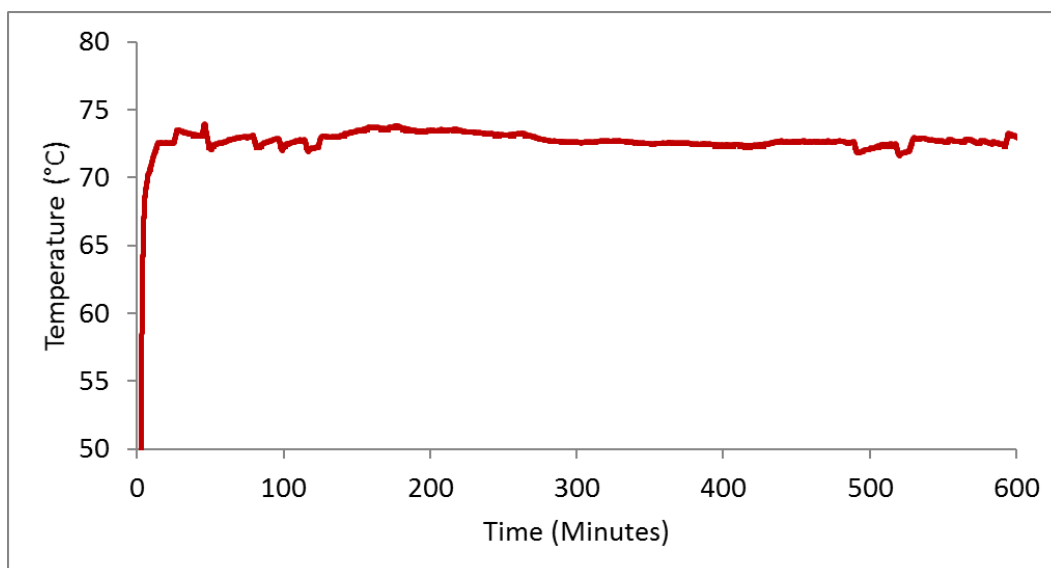


Figure 7.3 Thermocouple reading in air during the cross-linking of the LY3505/XB3403 resin system at 70 °C. The thermocouple is denoted as item (vi) in Figure 3.10.

Figure 7.4 illustrates the evolution of the degree of cure obtained via the FRS/FTIRS probe for the LY3505/XB3403 resin system at 50, 60 and 70 °C. A sampling frequency of 2 Hz was used in accordance with previous experiments. The evolution of the FRS and FTIRS data correlated closely with previously reported data in Chapters 4 and 5. However, the discrepancy between the FRS and FTIRS data sets was apparent at 50 °C. This may be associated with the difficulty in maintaining isothermal conditions within the test fixture. The “blips” in the FRS output was probably due to the on/off mode of operation of the hot-plate. This does suggest that the FRS may be used to detect non-isothermal conditions. These experiments demonstrated the feasibility of using a half reflective/non-reflective DSC pan for conducting simultaneous FRS and FTIRS measurements. These experiments also demonstrated that a single probe, containing optical fibres for acquiring FRS and FTIRS, was ‘fit-for-purpose’. It was concluded that introducing the probe to the DSC should be pursued as it would provide a more stable thermal environment for the FRS and FTIRS experiments.

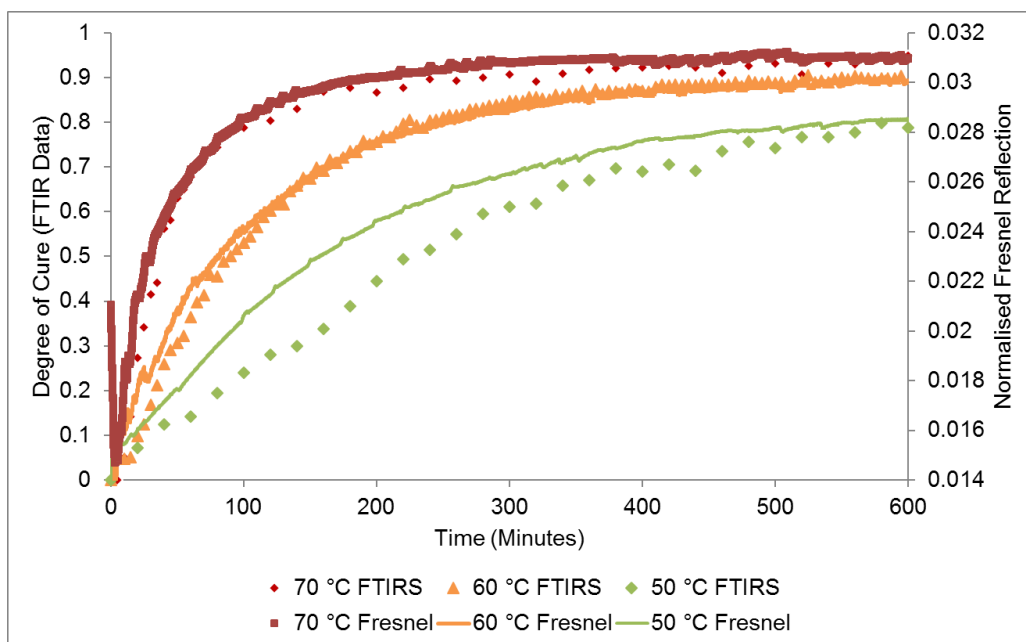


Figure 7.4 Simultaneous FTIRS and Fresnel acquisition during curing of LY3505/XB3403 using a partially reflective DSC pan. These experiments were conducted on a hot-plate using a thermally insulated enclosure.

### 7.1.3 Calibration of the Differential Scanning Calorimeter with the Fresnel Reflection Sensor /Fourier Transform Infrared Spectroscopy Probe

The accommodation of the FRS/FTIRS probe into the DSC required the platinum lids to be drilled to a diameter of 3.7 mm. To ensure minimal perturbation to the thermal environment and ease of location of the probe within the DSC, the platinum lids were attached to the end of the sample and reference probe, using silicone rubber. This allowed for the probes to be placed at a fixed height inside the DSC via the translation stage. The DSC was calibrated with the FTIRS probe illuminating the reference and sample compartments. Fresnel sensors were placed over the sample and reference compartments. The calibration of the DSC was undertaken using indium and the DSC pans were made partially reflective, as described previously. Figure 7.5 shows the characteristic melting of indium following calibration. The onset and the enthalpy of



melting are within the recommended tolerances (Gmelin, 1995). A temperature ramped scan was performed using a partially sprayed and conventional DSC pan. The onset and heat of fusion are presented in the insert in Figure 7.5.

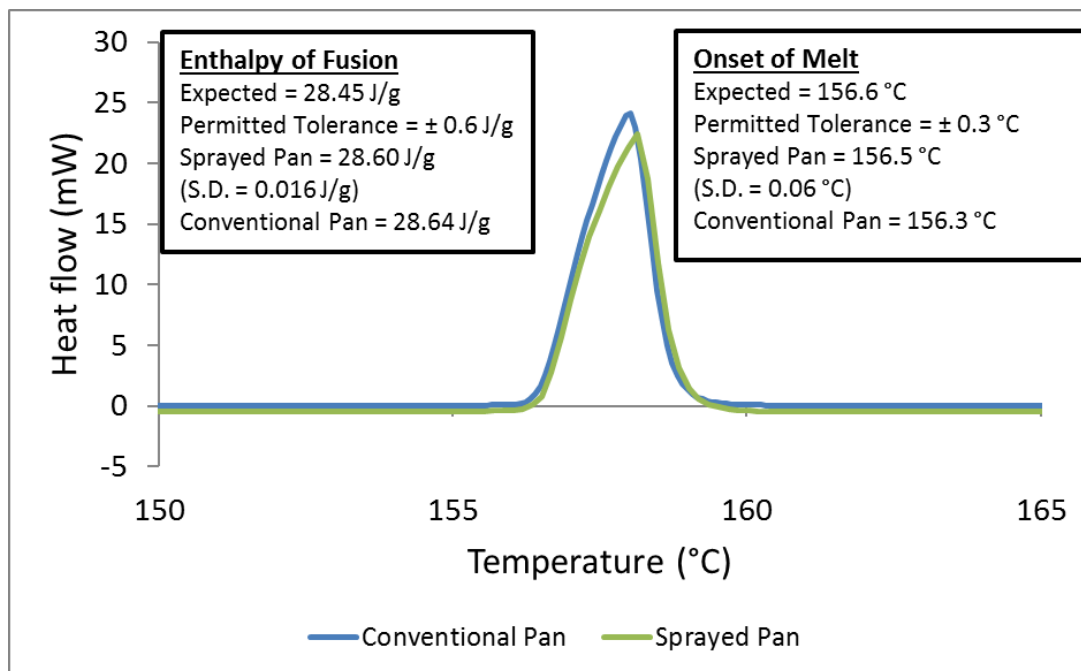


Figure 7.5 Thermograms for indium after calibration with FRS/FTIRS probe inserted in the DSC. Note: S.D. = Standard deviation

## 7.2 Isothermal Cross-linking

### 7.2.1 Differential Scanning Calorimetry Data Obtained via the Fresnel Reflection Sensor /Fourier Transform Infrared Spectroscopy Probe

As with the previous experiments, a large exothermic reaction was observed for the LY3505/XB3403, which peaked in intensity part-way through the reaction. The rate of reaction and  $\Delta H$  increased with temperature as expected (Turi *et al.*, 1997; Hardis *et al.*, 2013). A horizontal baseline from the end of the cross-linking period was used for the integration as undertaken previously by following ASTM E1356 (2014).

Figure 7.6 (a) and (b) shows typical isothermal cross-linking characteristics obtained via the DSC for the LY3505/XB3403 resin system at 50, 60 and 70 °C. The data for the conventional DSC has also been included to aid comparison.

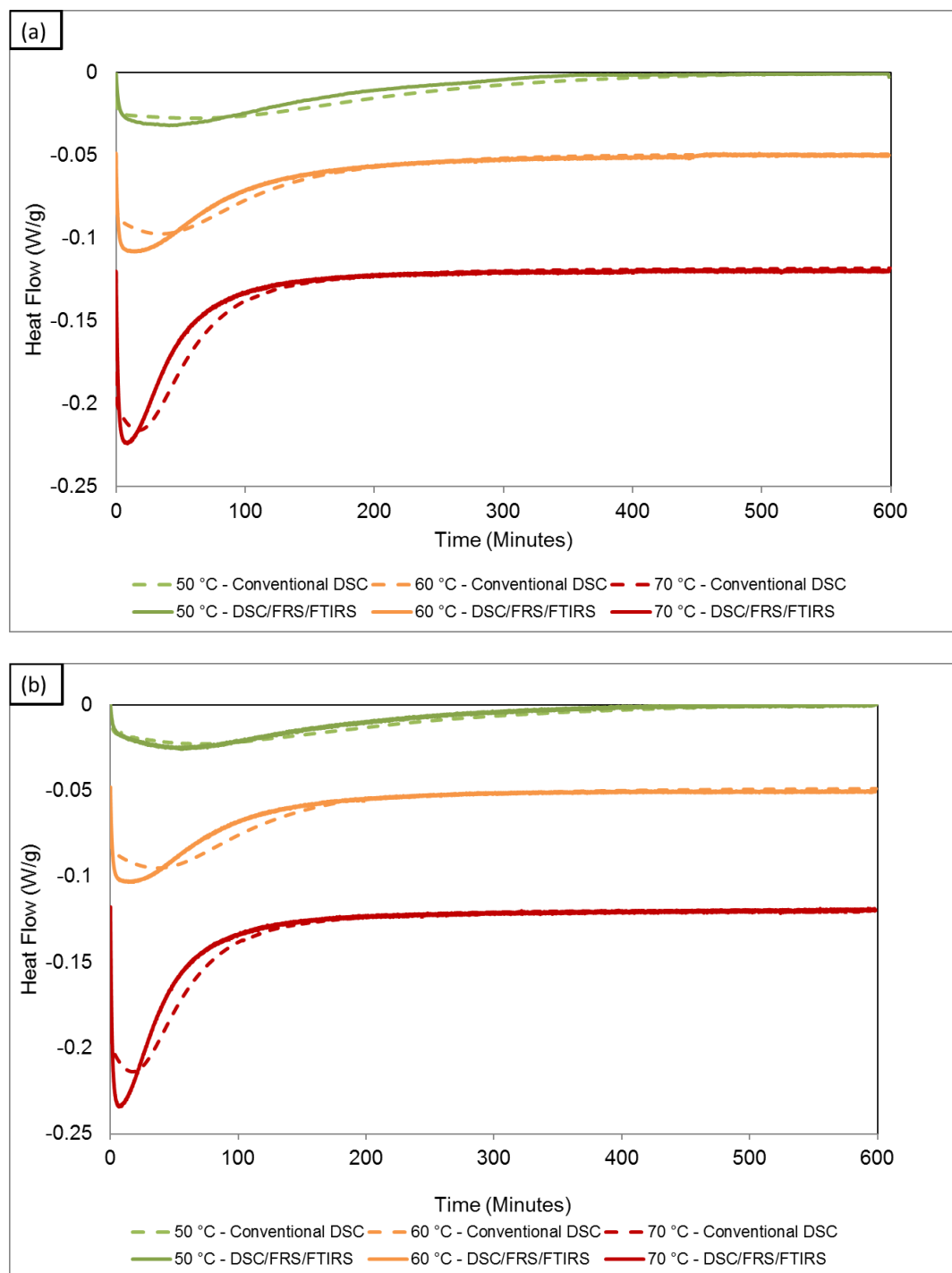


Figure 7.6 Typical DSC data obtained during cross-linking of the LY3505/XB3403 resin system at 70 °C using the simultaneous DSC/Fresnel/FTIRS technique:

(a) Experiment 1; and (b) Experiment 2.

The enthalpy of the reaction is shown in Figure 7.7 for each experiment; the conventional DSC data is also shown for comparison. The initial cross-linking rate and final degree of cross-linking are presented in Table 7.1. As expected, an increase in the  $\Delta H$  and degree of cure was present upon increasing from 50 to 70 °C. Upon comparison with the conventional data, a higher initial rate of cross-linking was obtained during DSC/FRS/FTIRS. After approximately 300 minutes the extent of cross-linking for conventional DSC surpasses that of DSC/FTIRS/FRS and to achieve similar conversion values after 600 minutes.

At 50 °C an average degree of conversion of 84% was obtained after 600 minutes which correlated with the 87.5% obtained during conventional DSC. The initial rate of reaction was lowest at 50 °C. Some discrepancy in the initial rate of reaction may be explained by inhomogeneous mixing of the resin and hardener.

Upon increasing the cross-linking temperature to 60 °C the initial rate of reaction increased by approximately 85%. The extent of cross-linking increased to 89% which compares closely to the 92% obtained during conventional DSC.

The initial rate of reaction increased a further 87% when increasing the cross-linking temperature to 70 °C. At the end of cross-linking, a conversion of 95% correlated with the 94% obtained during conventional experiments.

The discrepancy between conventional DSC and DSC/FRS/FTIRS was largest at the lower temperatures. This observation was previously reported by Pandita *et al.* (2012), when modifying a Diamond DSC to introduce fibre-optic probes into the sample and reference compartments, to conduct simultaneous DSC/FTIRS. In their work, differences between the conventional and DSC/FTIRS were attributed to the

influence of the fibre optic probes upon the thermal environment. In the current work, the impact of the FRS/FTIRS probe upon the thermal environment was minimised by using fused silica to construct the probe, which has relatively low thermal conductivity. The platinum lids attached to the end of the probe were also designed to maintain adequate insulation and emulate the conditions during conventional DSC.

The data presented in Figure 7.6 (a) and (b) is reflected in Figures 7.8 (a) – (c) for each of the temperatures 50, 60 and 70 °C, together with the conventional DSC data plotted to aid comparison. The previously discussed increase in the initial rate of reaction and similar final conversion values can be observed.

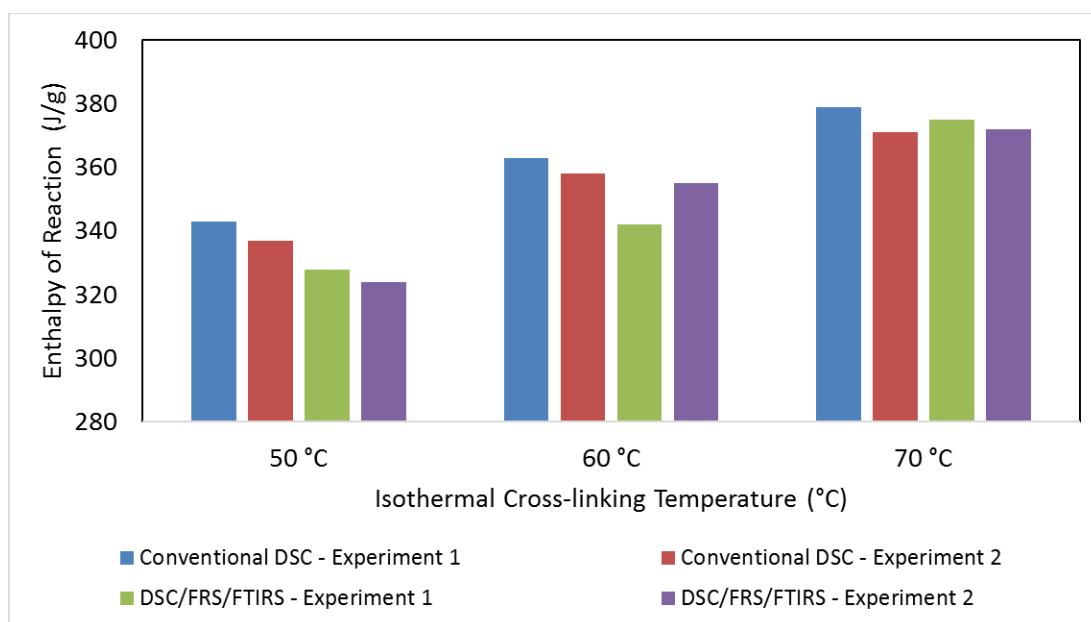


Figure 7.7 Magnitude of the enthalpy of reaction during isothermal cross-linking of LY3505/XB3403 using DSC/FRS/FTIRS and conventional DSC at specified temperatures.

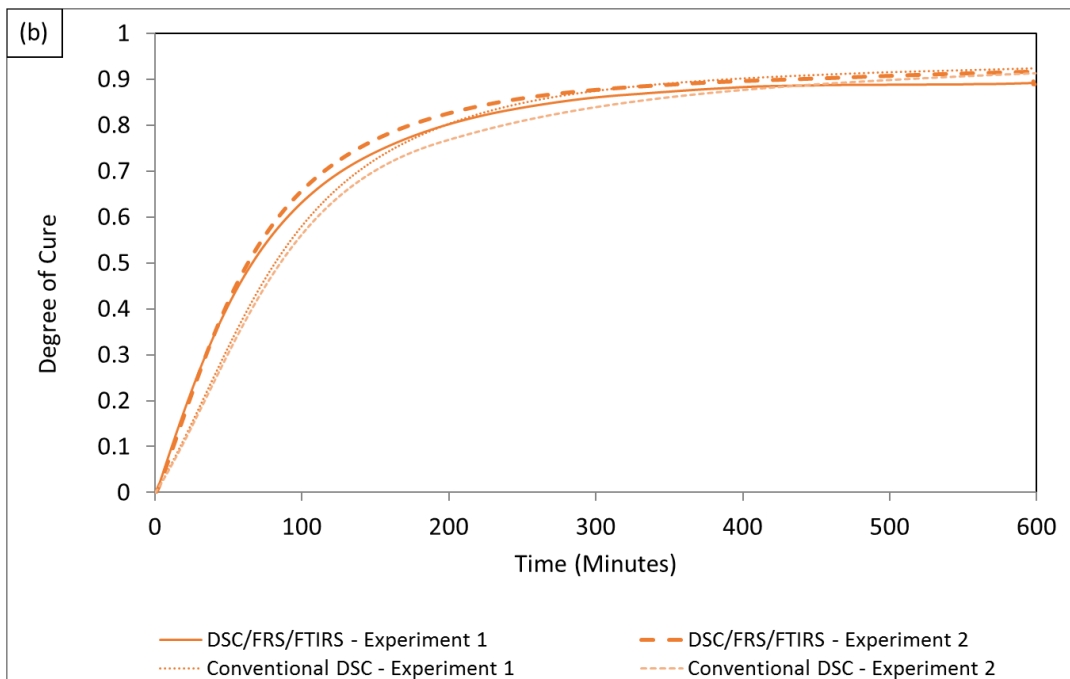
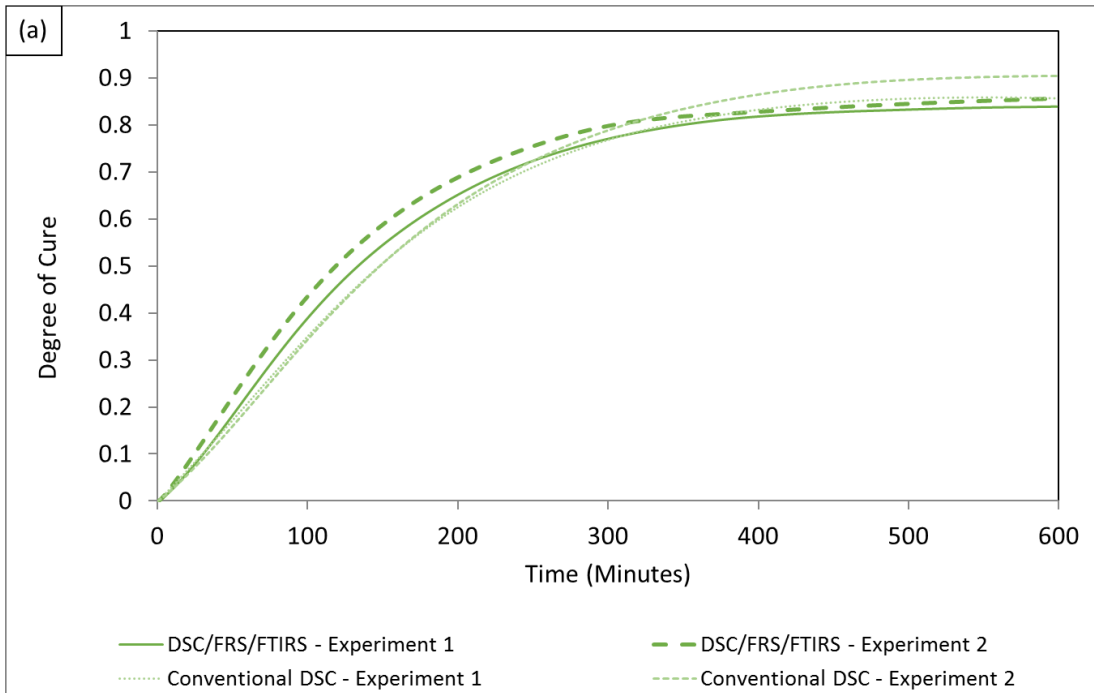


Figure 7.8 Degree of cross-linking obtained from DSC during isothermal DSC and DSC/FRS/FTIRS experiments for the LY3505/XB3403 resin system completed at: (a) 50; and (b) 60 °C.

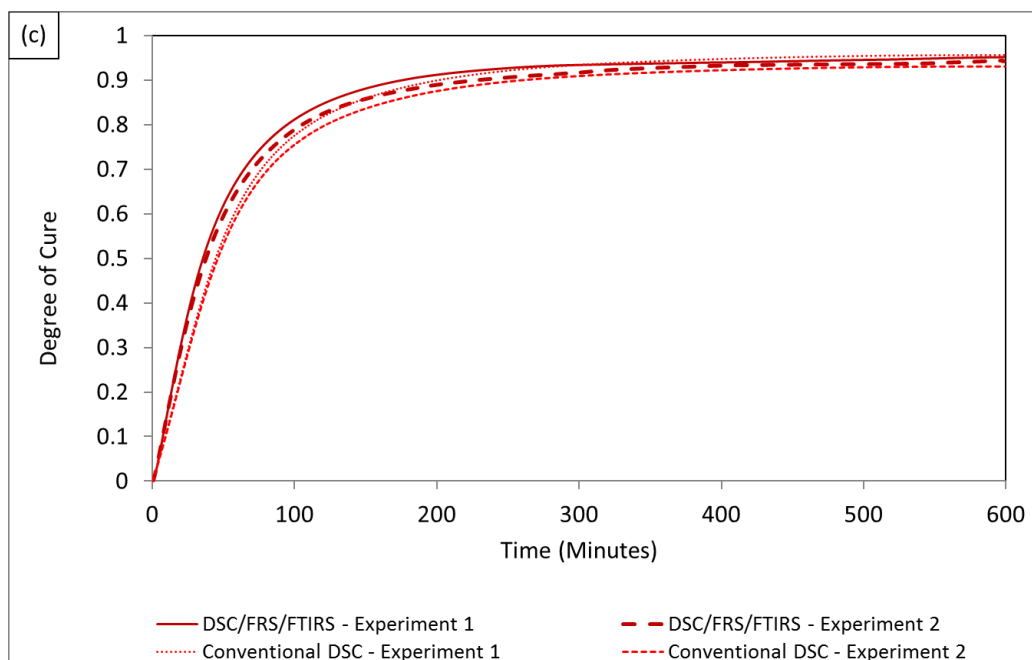


Figure 7.8 (continued) Degree of cross-linking obtained from DSC during isothermal DSC and DSC/FRS/FTIRS experiments for the LY3505/XB3403 resin system completed at: (c) 70 °C.

Table 7.1 Degree of cure and initial rate of reaction of LY3505/XB3403 during isothermal DSC/FRS/FTIRS and conventional DSC experiments.

Isothermal Cross-linking	Initial Rate of Cross-linking (da/dt)		Degree of Cure after 600 Minutes	
	DSC/FRS/FTIRS	Conventional DSC	DSC/FRS/FTIRS	Conventional DSC
50 °C - Experiment 1	0.0046	0.0037	83%	87%
50 °C - Experiment 2	0.0041	0.0035	85%	88%
60 °C - Experiment 1	0.0079	0.0065	89%	92%
60 °C - Experiment 2	0.0080	0.0062	88%	91%
70 °C - Experiment 1	0.0150	0.0119	95%	95%
70 °C - Experiment 2	0.0148	0.0116	94%	93%

## 7.2.2 Fourier Transform Infrared Spectroscopy Data

Figure 7.9 shows the progression of the spectra obtained from LY3505/XB3403 after specified cross-linking times. Similar to the work reported in Section 4.2.3, the depletion of the de-convoluted epoxy peak at  $4530\text{ cm}^{-1}$  was calculated by normalisation to the inert C-H peak at  $4620\text{ cm}^{-1}$ . Concurrent with the conventional transmission FTIRS, an increase in the initial rate of cross-linking and final extent of degree of cure was experienced with increasing temperature and a summary is presented in Table 7.2.

A similar initial rate of reaction was obtained at  $50\text{ }^{\circ}\text{C}$  when comparing the spectra obtained using conventional FTIRS and DSC/FRS/FTIRS. As the temperature increased, the initial rate of the conventional FTIRS was 10% and 25% faster than the DSC/FRS/FTIRS at  $60$  and  $70\text{ }^{\circ}\text{C}$ , respectively. This may be due to the different thermal management systems of the techniques. The sample temperature during DSC/FRS/FTIRS was maintained by the DSC and was accurate to  $0.01\text{ }^{\circ}\text{C}$  (Perkin-Elmer, 2003) whilst the conventional transmission FTIRS was controlled by a cuvette holder with recirculating water. The contribution of the exothermic cross-linking to the sample temperature may have caused the observed discrepancy in the initial rate of reaction. As previously mentioned, Machavaram *et al.* (2014) observed a  $15\text{-}25\text{ }^{\circ}\text{C}$  temperature increase during cross-linking of LY3505/XB3403 at  $70\text{ }^{\circ}\text{C}$ , which may lead to sample temperature deviations during conventional FTIRS. These findings are in accordance with Pandita *et al.* (2012) who also observed an increase in the initial rate of reaction of LY3505/XB3403 during conventional FTIRS when compared to DSC/FTIRS.

The degree of cross-linking increased with temperature and showed a good correlation with the conventional FTIRS data as shown in Table 7.2, Figures 7.10 (a) – (c) and Figure 7.11. A summary of previous investigations into the cross-linking of LY3505/XB3403 at 70 °C using FTIRS was presented in Table 4.6, Chapter 4. The data obtained during DSC/FRS/FTIRS correlates with previous data on the cross-linking of the LY3505/XB3403 resin system using conventional FTIR (Pandita *et al.*, 2012; Mahendran, 2010) and evanescent wave spectroscopy (Harris, 2011; Wang *et al.*, 2016) and a multimode fibres chemical sensor (Nair *et al.*, 2015).

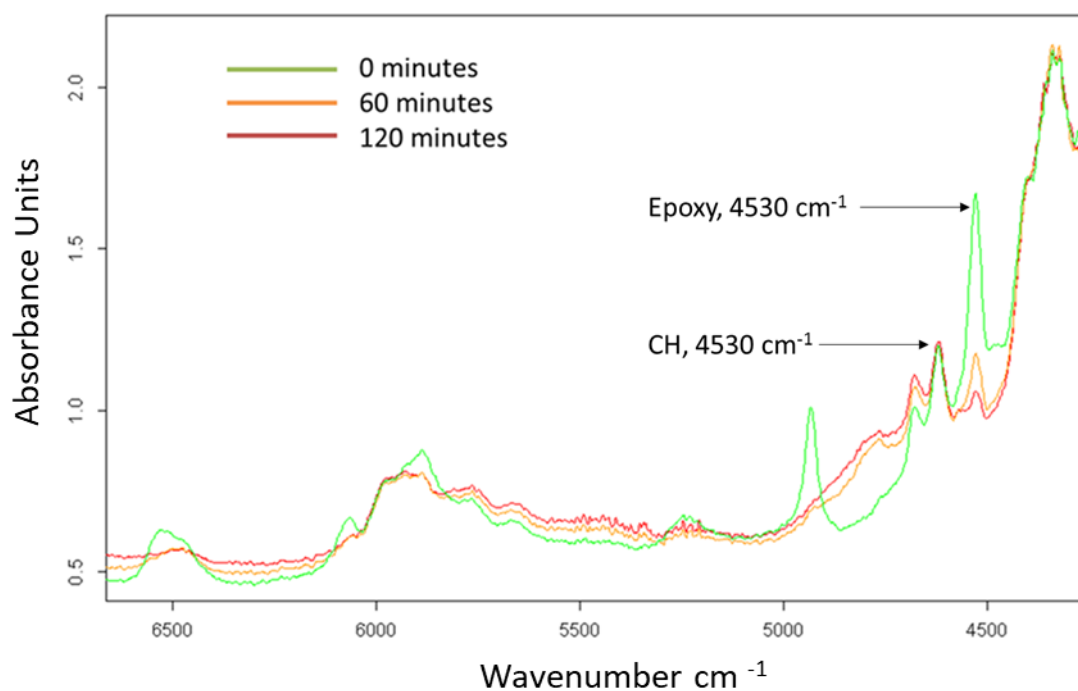


Figure 7.9 Spectra taken at various stages of cure of LY3505/XB3403 at 70 °C using simultaneous DSC/Fresnel/FTIRS technique. The arrows represent the absorbance peaks that were used to calculate the peak areas for the kinetic analysis.



Table 7.2 Degree of cure and initial rate of reaction of LY3505/XB3403 during isothermal DSC/FRS/FTIRS and conventional FTIRS experiments.

Isothermal Cross-linking	Degree of Cure after 600 Minutes		Initial Rate of Cross-linking ( $da/dt$ )	
	DSC/FRS/FTIRS	Conventional FTIRS	DSC/FRS/FTIRS	Conventional FTIRS
50 °C - Experiment 1	88%	89%	0.0044	0.0050
50 °C - Experiment 2	88%	90%	0.0055	0.0045
60 °C - Experiment 1	91%	94%	0.0074	0.0066
60 °C - Experiment 2	94%	92%	0.0066	0.0060
70 °C - Experiment 1	96%	96%	0.0138	0.0181
70 °C - Experiment 2	97%	94%	0.0144	0.0192

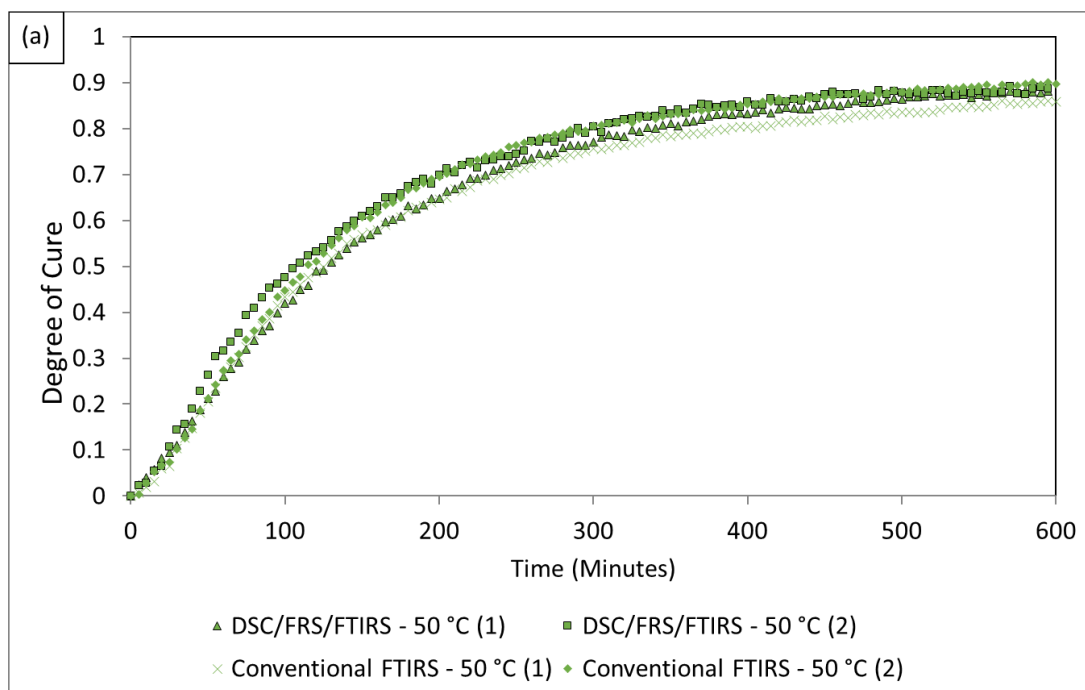


Figure 7.10 Degree of cross-linking of LY3505/XB3403 using spectral data during simultaneous DSC/FRS/FTIRS and conventional transmission FTIRS at: (a) 50 °C.

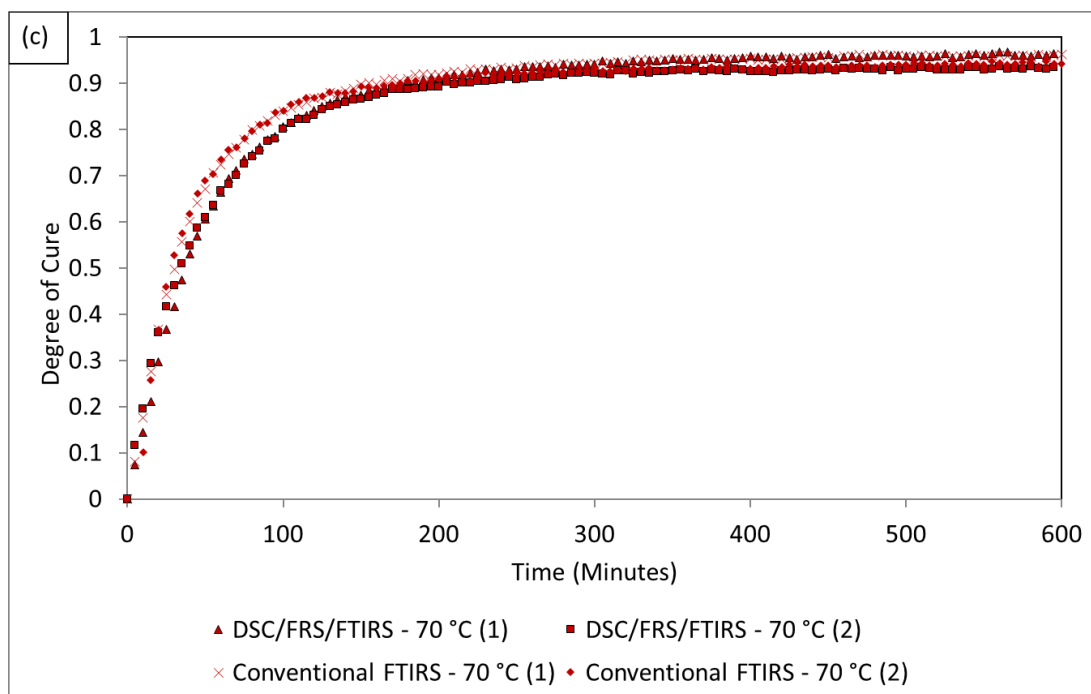
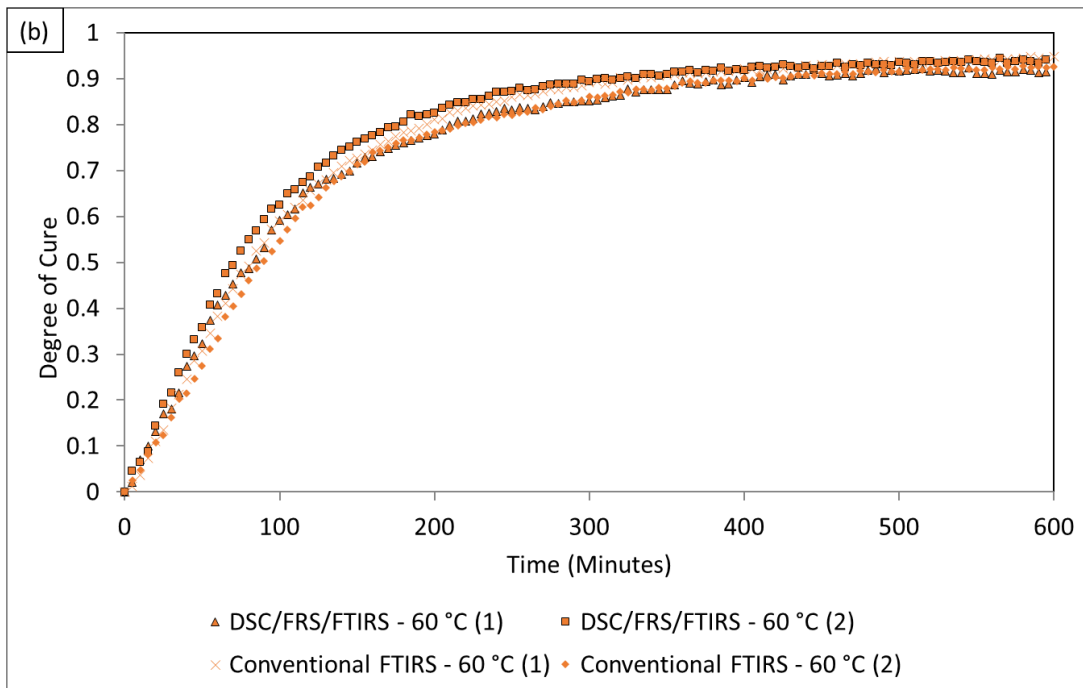


Figure 7.10 (continued) Degree of cross-linking of LY3505/XB3403 using spectral data during simultaneous DSC/FRS/FTIRS and conventional transmission FTIRS at: (b) 60 °C; and (c) 70 °C.

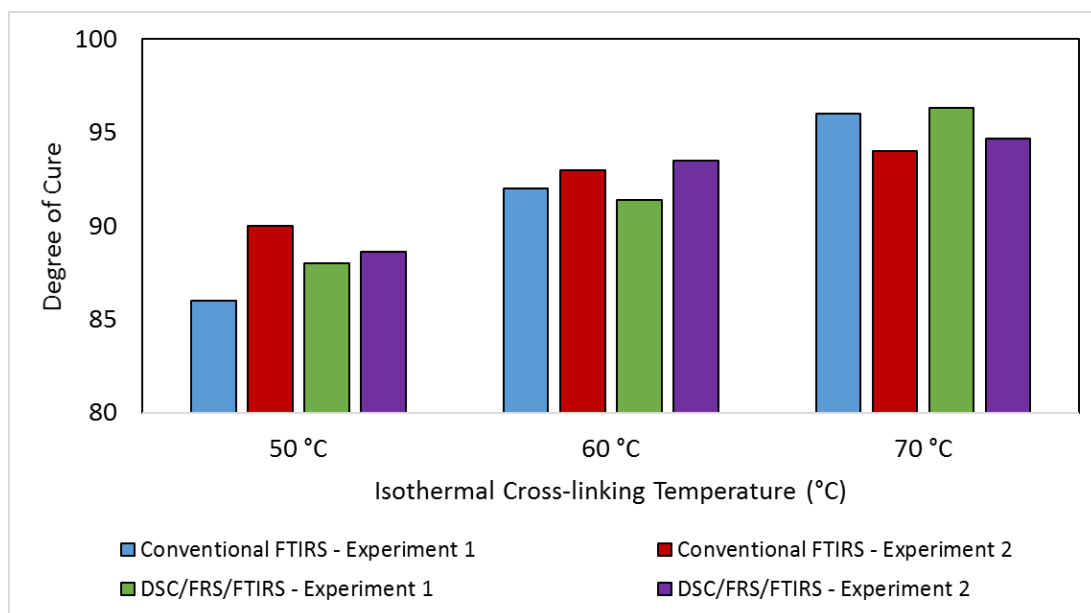


Figure 7.11 Degree of cure after 600 minutes of cross-linking of LY3505/XB3403 using DSC/FRS/FTIRS and conventional FTIRS at specified temperatures.

### 7.2.3 Fresnel Reflection Sensor Data

The normalised FRS data obtained during DSC/FRS/FTIRS for the cross-linking of LY3505/XB3403 at 50, 60 and 70 °C is shown in Figures 7.12 (a) and (b). Upon heating to the desired isothermal cross-linking temperature, a decrease in the signal is due to the reduction of the resin refractive index. Upon reaching the desired isothermal cross-linking temperature, an increase in the FRS signal is observed due to cross-linking. The initial rate of reaction was determined by calculating the gradient of the initial linear slope shown in Figures 7.12 (a) and (b) and presented in Table 7.3. As expected, the initial rate of reaction increased with cross-linking temperature. The data showed a close comparison with the initial rates reported in Chapter 5 during the cross-linking of LY3505/XB3403 under similar conditions using DSC/FRS. A greatly reduced rate of reaction was observed toward the end of the isothermal cross-linking and is also quantified by the gradient of the signal as

presented in Table 7.3. Lower rates of reaction were determined at higher temperatures indicating more extensive cross-linking.

During isothermal cross-linking, a larger increase in the Normalised FRS signal occurred at higher temperatures. This trend has previously been reported during the cross-linking of epoxy resin systems by Crosby *et al.* (1996) and Harris (2011), although these investigations were not conducted within a DSC heating chamber. The magnitude of the signal increase correlated closely to that obtained during DSC/FRS, as discussed in Chapter 5 and presented in Table 7.3.

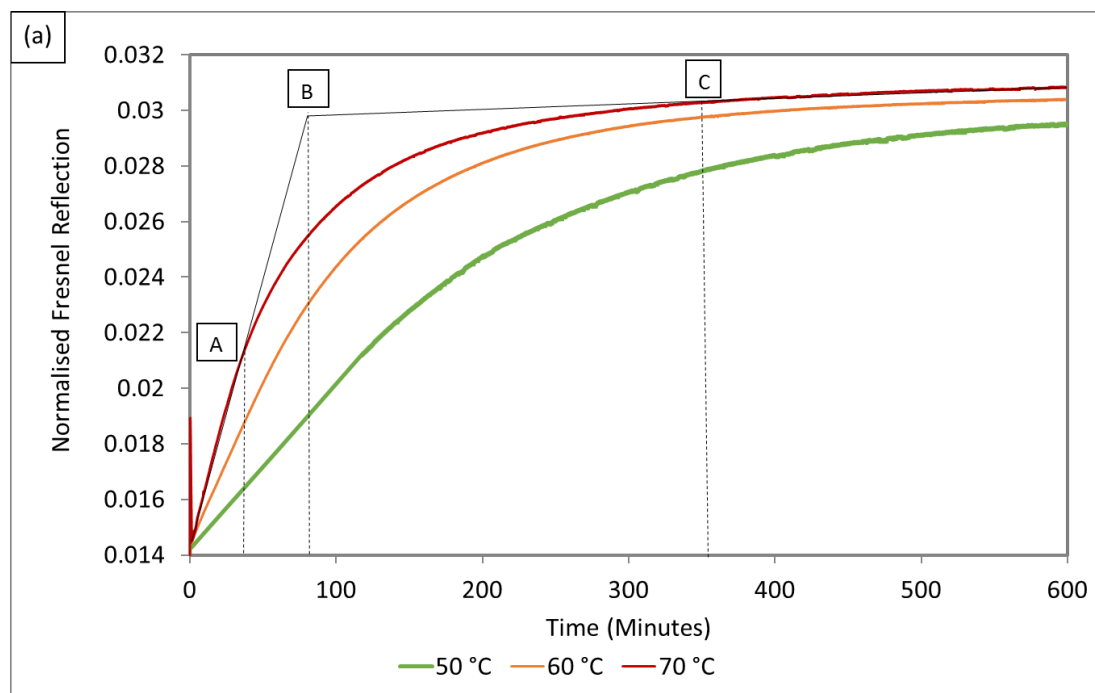


Figure 7.12 FRS signals during isothermal cross-linking of LY3505/XB3403 at 50, 60 and 70 °C: (a) Experiment 1.

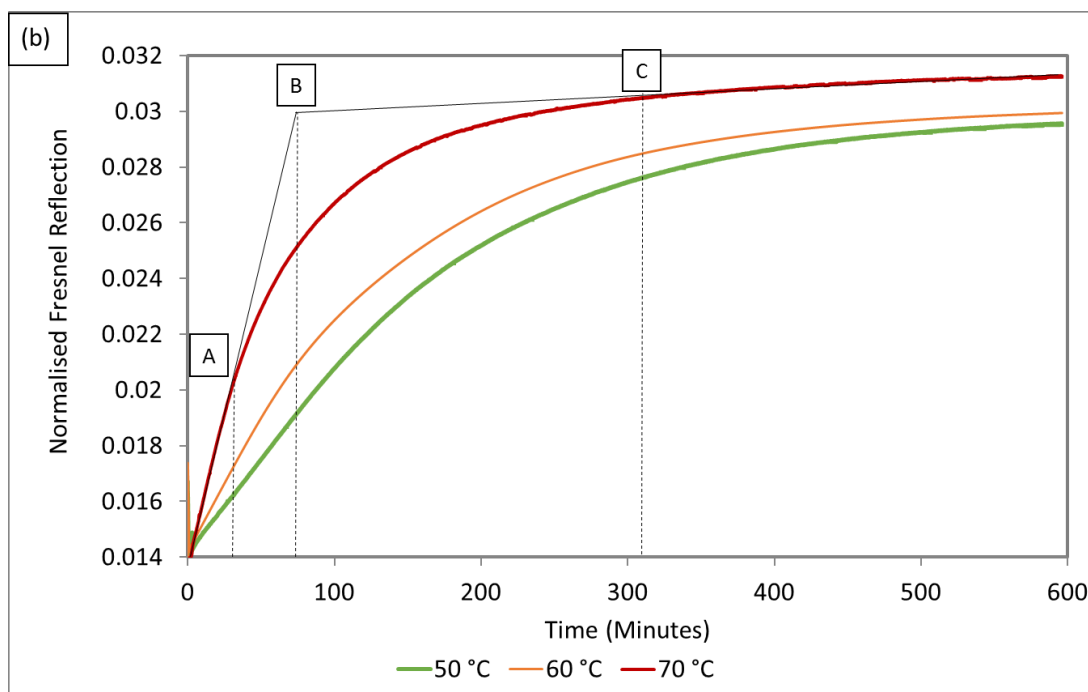


Figure 7.12 (continued) FRS signals during isothermal cross-linking of LY3505/XB3403 at 50, 60 and 70 °C: (b) Experiment 2.

Table 7.3 Values from FRS at various points during the isothermal cross-linking of LY3505/XB3403 using hyphenated DSC/FRS/FTIRS.

Isothermal Cross-linking	Normalised Fresnel Reflection (Arbitrary Units)					
	Initial rate		Rate towards End of Cross-linking (550-600 Minutes)		Increase during Isothermal Cross-linking	
	DSC/FRS/FTIRS	DSC/FRS	DSC/FRS/FTIRS	DSC/FRS	DSC/FRS/FTIRS	DSC/FRS
50 °C - Experiment 1	0.00040	0.0005	3.E-06	2.E-07	0.0147	0.0174
50 °C - Experiment 2	0.00050	0.0006	2.E-06	3.E-07	0.0153	0.0178
60 °C - Experiment 1	0.00012	0.0010	1.E-06	3.E-07	0.0163	0.0188
60 °C - Experiment 2	0.00080	0.0009	1.E-06	2.E-07	0.0159	0.0179
70 °C - Experiment 1	0.00020	0.0018	1.E-06	6.E-07	0.0168	0.0190
70 °C - Experiment 2	0.00021	0.0018	1.E-06	9.E-07	0.0172	0.0187

Points A, B and C, which were previously defined in Chapter 5 and shown in Figures 5.9 and 5.10, were determined for the FRS data during DSC/FTIRS/FRS to compare the datasets. Figure 7.13 compares the time of each point at 50, 60 and 70 °C from the FRS data obtained in Chapter 5 and chapter 7. A similar trend is observed for each point at each temperature indicating a close correlation between the datasets.

Figures 7.14, 7.15 and 7.16 present the normalised FRS data with the degree of cure measured simultaneously from the FTIRS and DSC data. In each Figure, the close correlation between the data sets

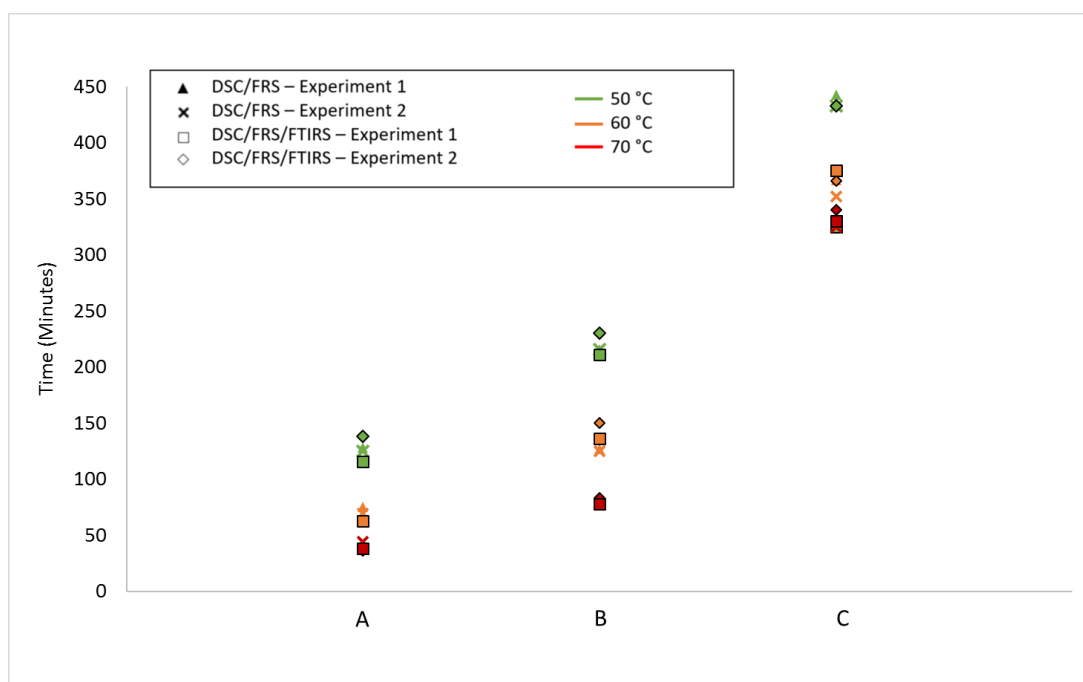


Figure 7.13 Time to reach points A, B and C (see Figure 7.12) during the cross-linking of LY3505/XB3403 at 50, 60 and 70 °C during DSC/FRS and DSC/FRS/FTIRS. A = Deviation of plot from initial linear region; B = Intersection of extrapolation of initial and final linear regions; C = Deviation of plot from final linear region.

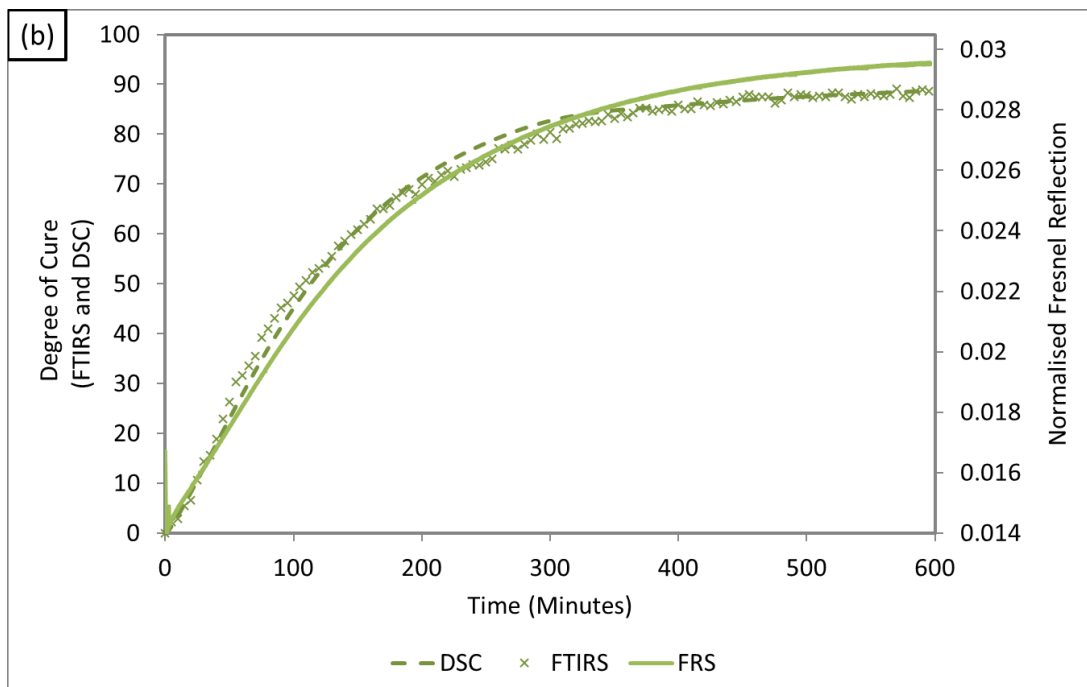
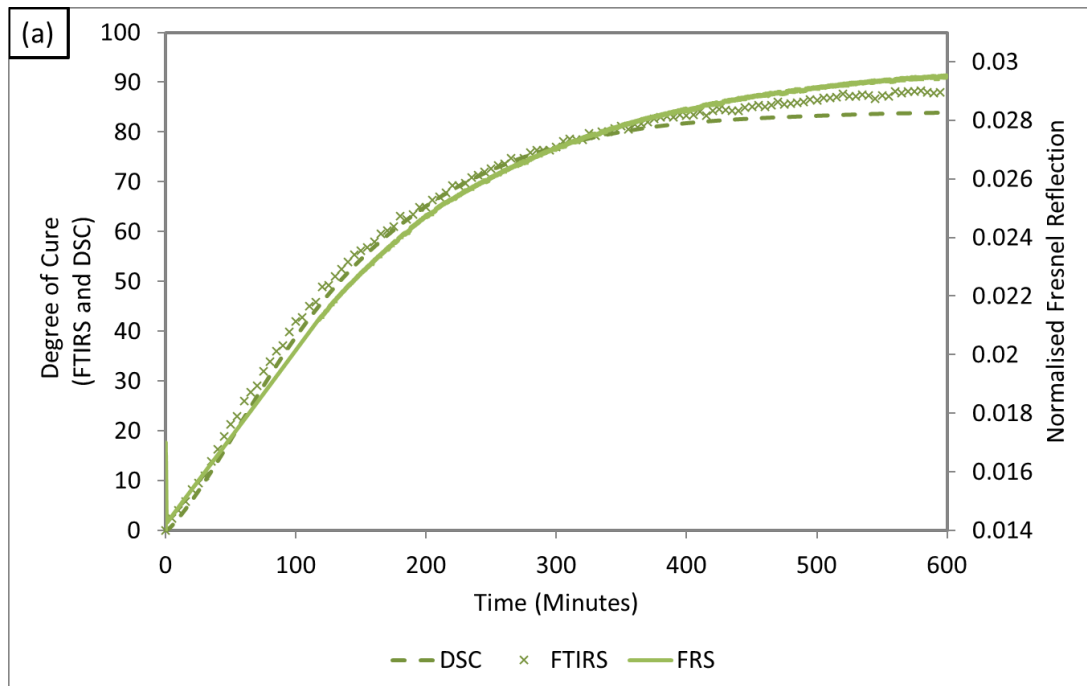


Figure 7.14 Degree of cure of LY3505/XB3403 obtained from DSC and FTIRS alongside normalised Fresnel reflection using the hyphenated DSC/FRS/FTIRS technique at 50 °C: (a) Experiment 1; and (b) Experiment 2.

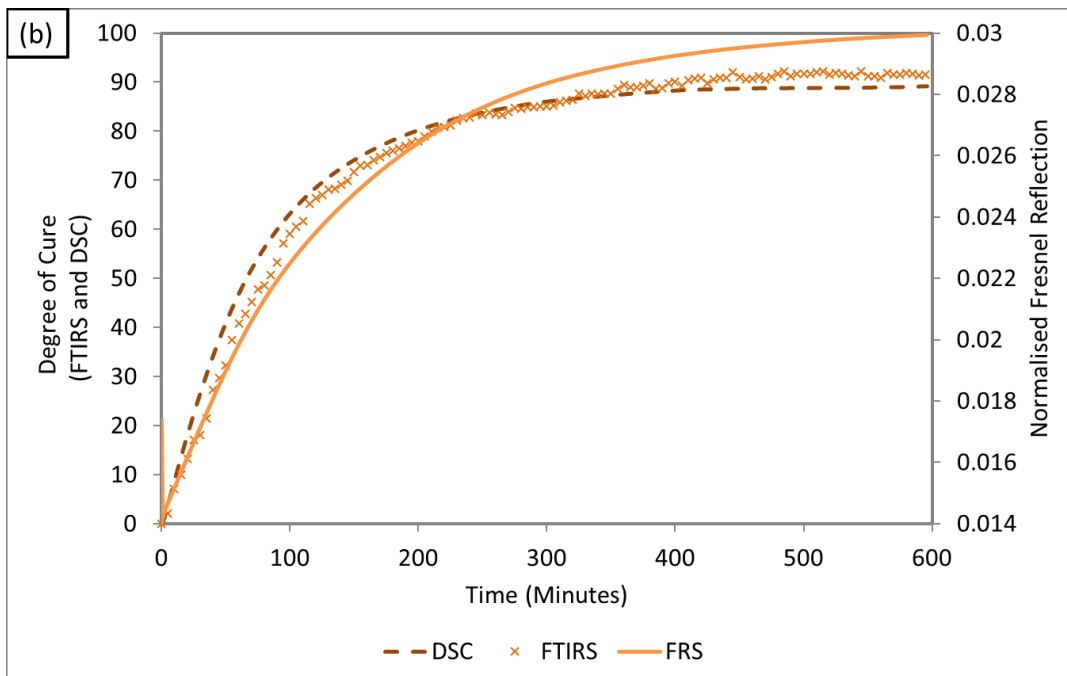
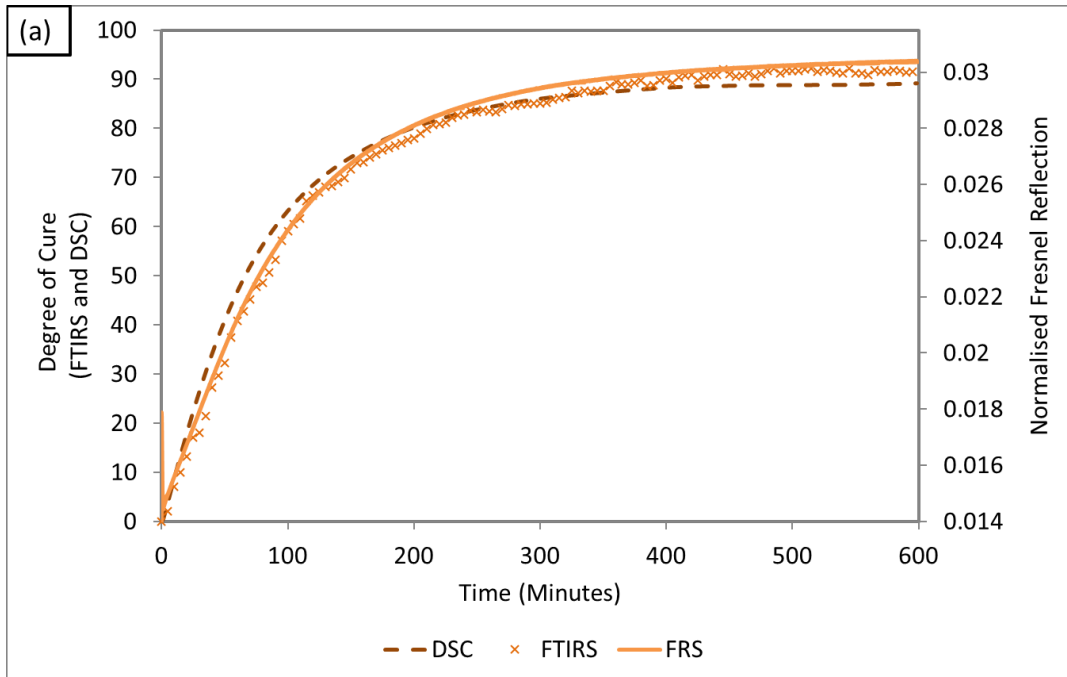


Figure 7.15 Degree of cure of LY3505/XB3403 obtained from DSC and FTIRS alongside normalised Fresnel reflection using the hyphenated DSC/FRS/FTIRS technique at 60 °C: (a) Experiment 1; and (b) Experiment 2.



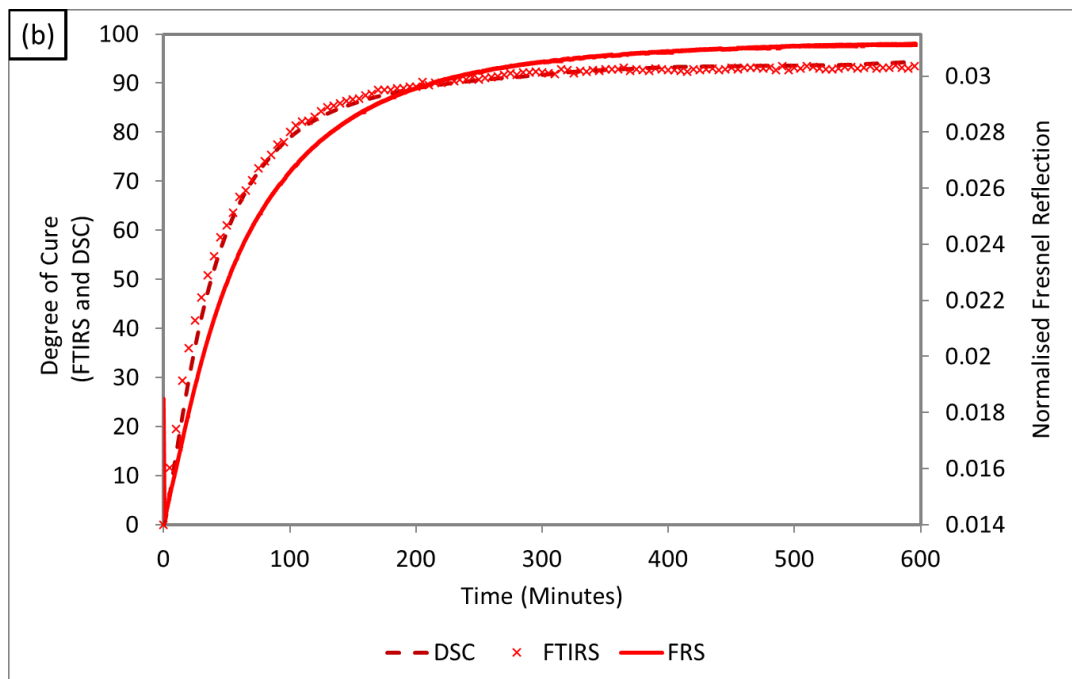
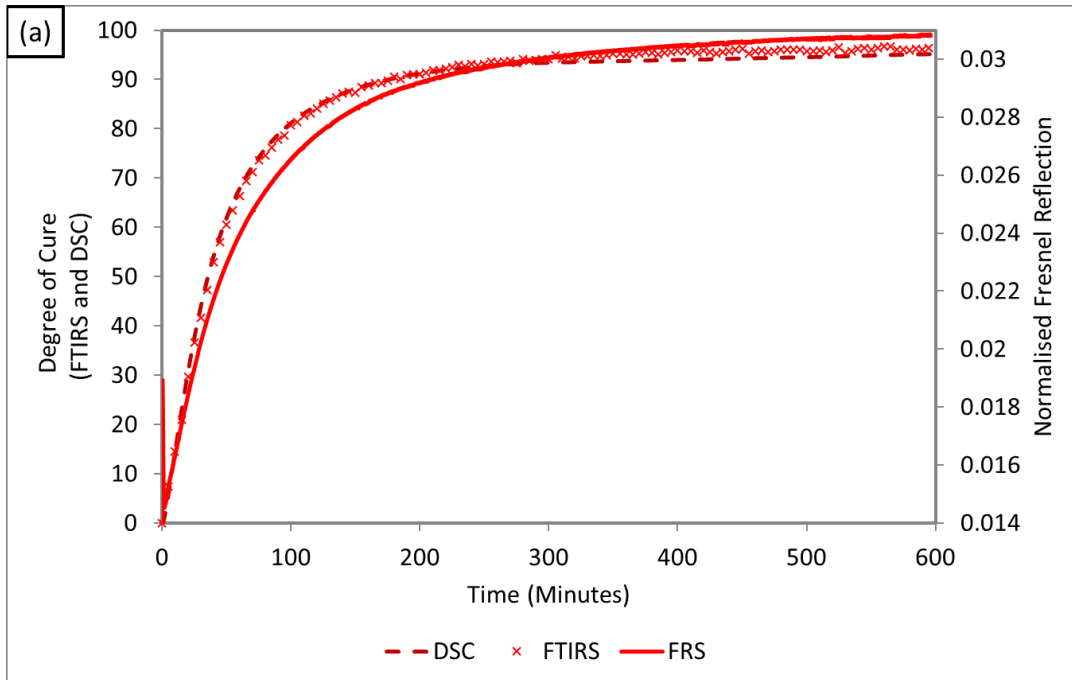


Figure 7.16 Degree of cure of LY3505/XB3403 obtained from DSC and FTIRS alongside normalised Fresnel reflection using the hyphenated DSC/FRS/FTIRS technique at 70 °C: (a) Experiment 1; and (b) Experiment 2.

#### 7.2.4 Kinetic Data

The autocatalytic model (Equation 4.1) was plotted alongside the DSC and FTIRS data acquired during DSC/FRS/FTIRS. Error bars of 5% were added to the predictive model values and are shown in Figures 7.17, 7.18 and 7.19 for experiments conducted at 50, 60 and 70 °C, respectively. At each temperature, the model showed a good correlation with the DSC data. A deviation was observed between the model at the data at 50 and 60 °C after approximately 80% conversion. This mismatch has previously been reported between the autocatalytic model and epoxy-amine resin systems as discussed in Section 4.1.5 and reported by Montserrat and Cima (1999), Teil *et al.* (2004) and Garschke *et al.* (2013). Comparable with conventional DSC experiments, the model predicted a higher conversion after approximately 80% degree of cure. The rate constants of each measurement are shown in Table 7.4 and Figure 7.20, showing a close correlation with the data from conventional DSC and DSC/FRS.

The autocatalytic model also shows an excellent correlation with the FTIRS data; the rate constants are similar to those obtained during the conventional FTIRS experiments (Table 7.4 and Figure 7.20) and DSC data.

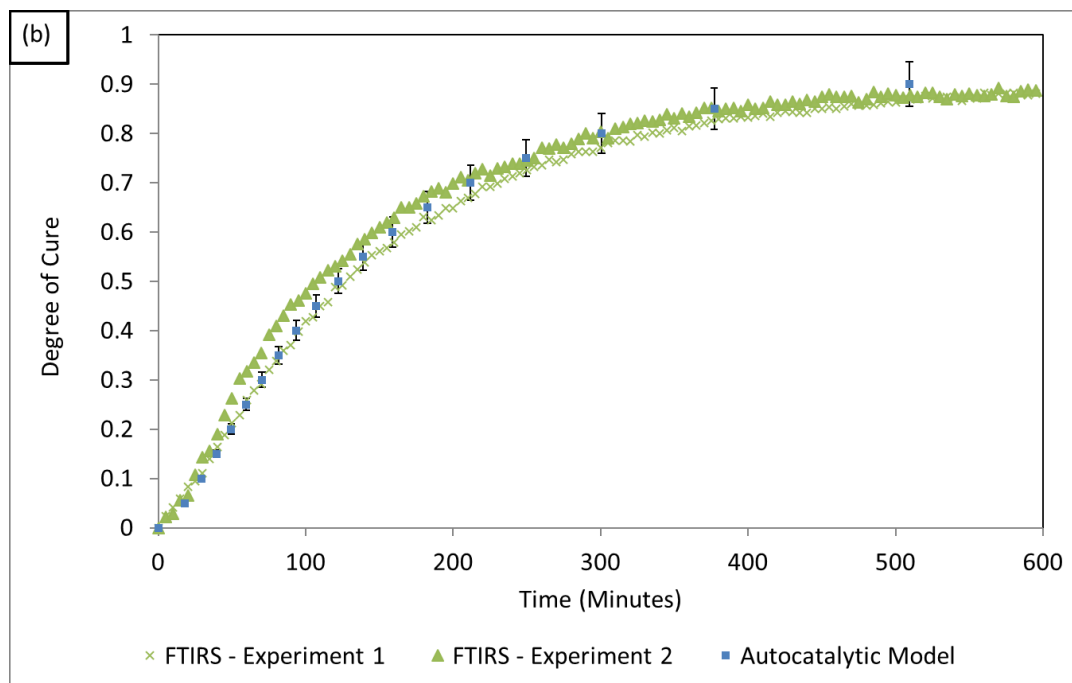
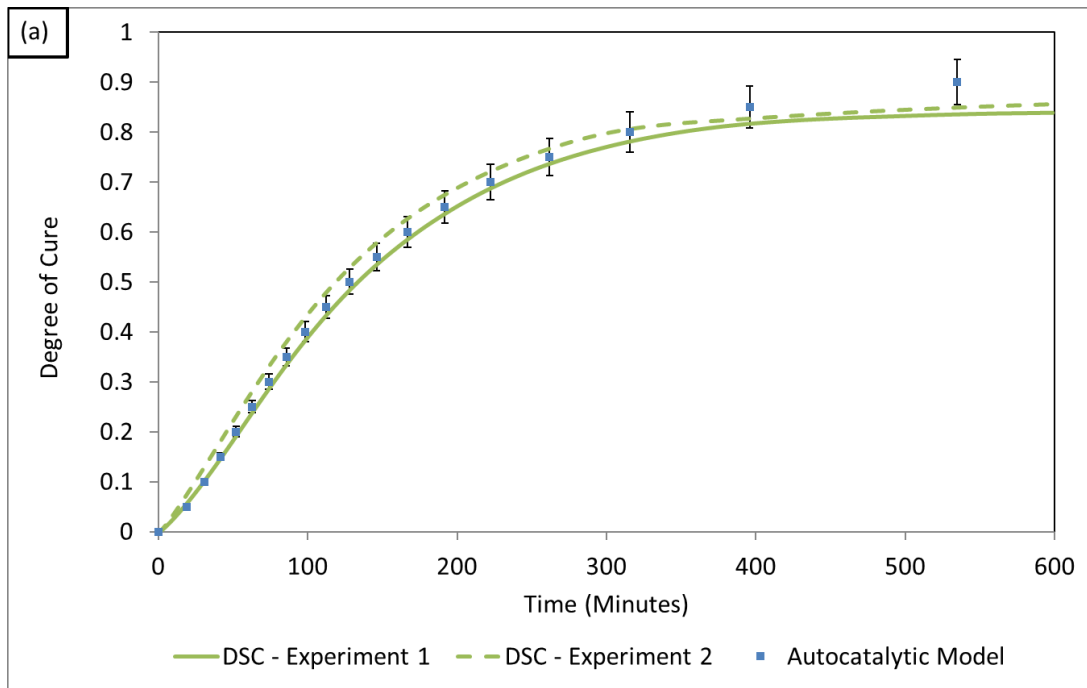


Figure 7.17 Comparison between the degree of cross-linking and the autocatalytic model at 50 °C: (a) DSC data; and (b) FTIRS data.

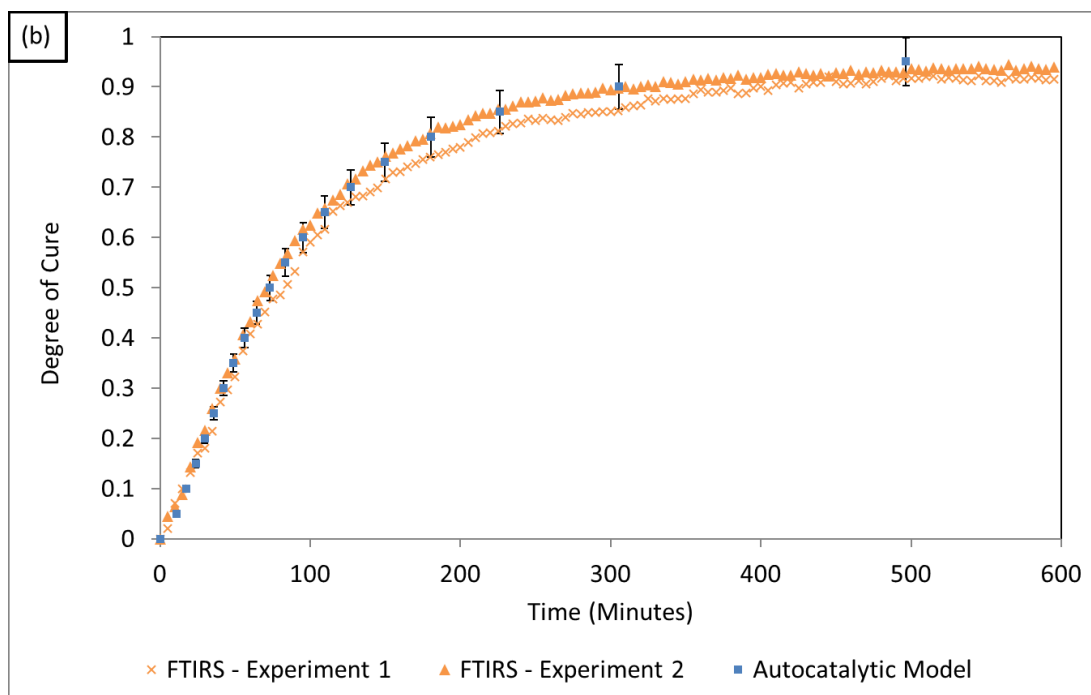
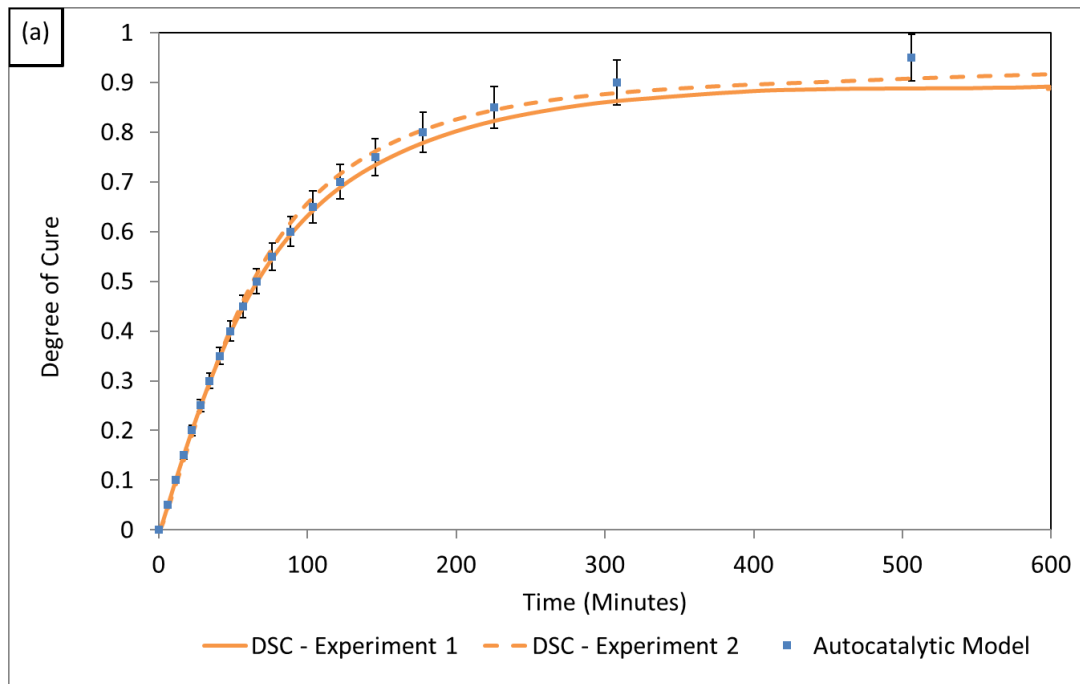


Figure 7.18 Comparison between the degree of cross-linking and the autocatalytic model at 60 °C: (a) DSC data; and (b) FTIRS data.

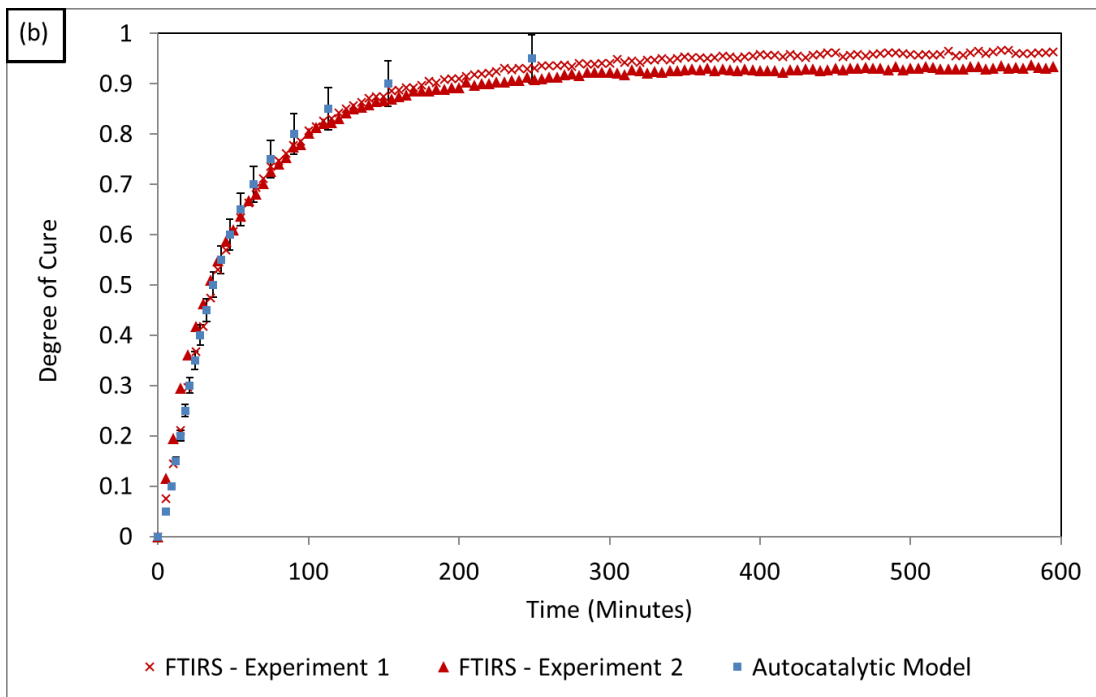
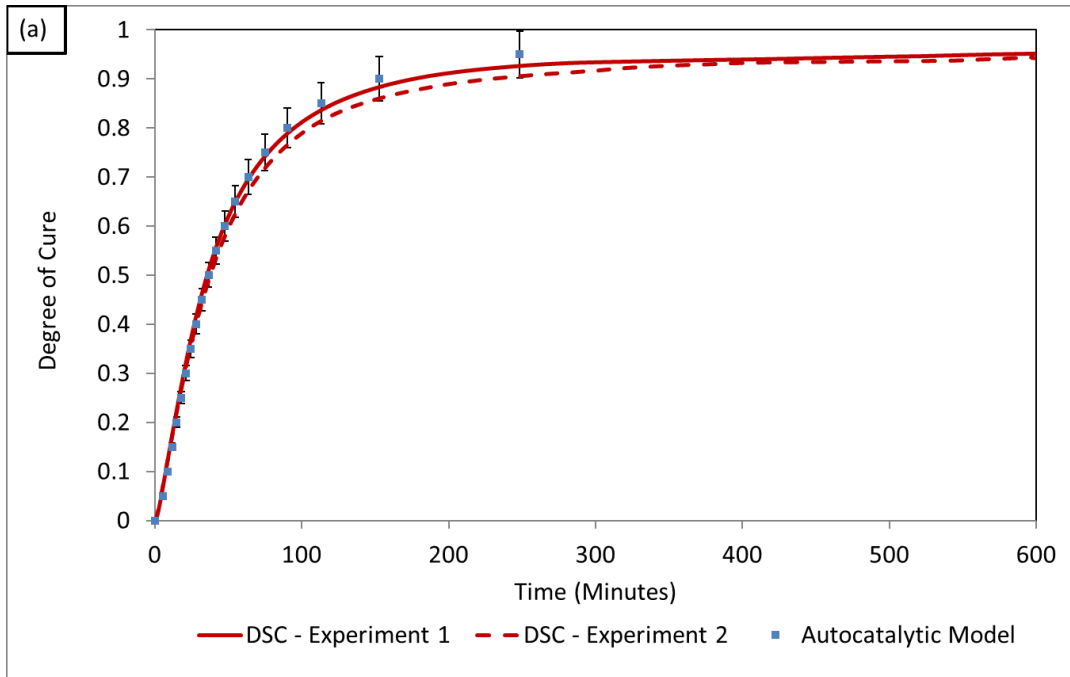


Figure 7.19 Comparison between the degree of cross-linking and the autocatalytic model at 70 °C during simultaneous DSC/FRS/FTIRS:  
 (a) DSC data; and (b) FTIRS data.

Table 7.4 Average rate constants for autocatalytic model from conventional methods compared to hyphenated DSC/FTIRS/FRS.

	DSC/FRS/FTIRS		DSC/FRS	Conventional	
	DSC k (s <sup>-1</sup> )	FTIRS k (s <sup>-1</sup> )	DSC k (s <sup>-1</sup> )	DSC k (s <sup>-1</sup> )	FTIRS k (s <sup>-1</sup> )
<b>50 °C - Experiment 1</b>	0.00020	0.00020	0.00016	0.00018	0.00020
<b>50 °C - Experiment 2</b>	0.00022	0.00023	0.00017	0.00017	0.00021
<b>60 °C - Experiment 1</b>	0.00034	0.00036	0.00029	0.00029	0.00033
<b>60 °C - Experiment 2</b>	0.00033	0.00035	0.00027	0.00032	0.00032
<b>70 °C - Experiment 1</b>	0.00070	0.00070	0.00053	0.00059	0.00068
<b>70 °C - Experiment 2</b>	0.00069	0.00070	0.00056	0.00058	0.00069
<b>Activation Energy (kJ/mol<sup>-1</sup>)</b>	<b>55.03</b>	<b>54.38</b>	<b>54.95</b>	<b>55.54</b>	<b>55.43</b>

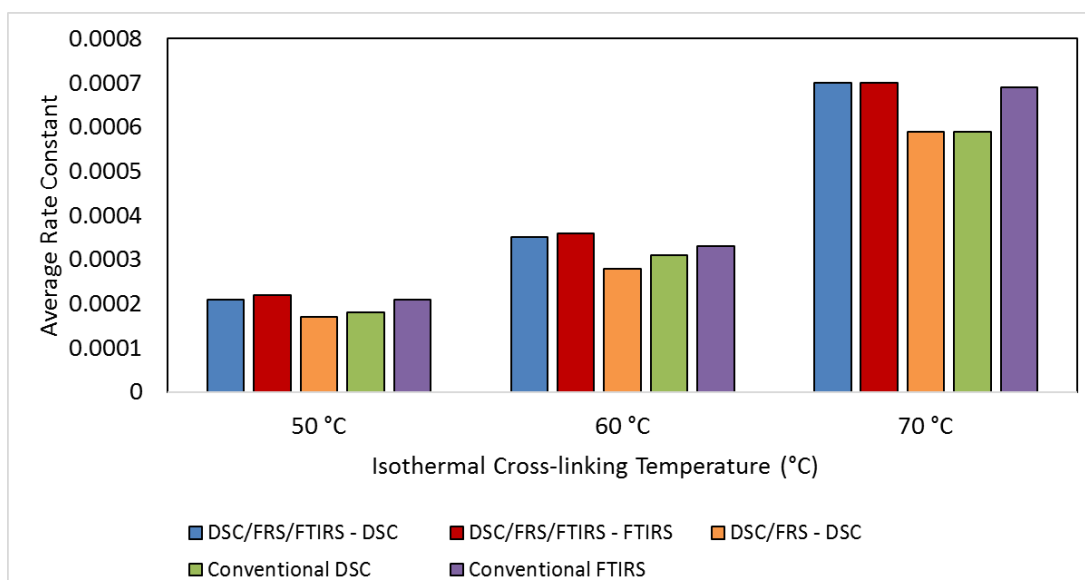


Figure 7.20 Histogram showing the average rate constants obtained for the autocatalytic model during DSC, FTIRS, DSC/FRS and DSC/FRS/FTIRS at 50, 60 and 70 °C.

### **7.2.5 Correlation of Isothermal Differential Scanning Calorimetry, Fourier Transform Infrared Spectroscopy and Fresnel Reflection Sensor Data**

The data from the DSC, FRS, FTIRS and the autocatalytic model is shown in Figures 7.21, 7.22 and 7.23 for experiments conducted at 50, 60 and 70 °C respectively. Equation 4.1 was plotted using the average rate constants assigned to the respective DSC and FTIRS data. A close correlation was observed between the simultaneously conducted data sets and with previous experiments.

At 50 °C, an excellent correlation was observed between the data until approximately 400 minutes, where the FRS and FTIRS increase at an accelerated rate relative to the DSC data. A stronger correlation between the final degree of conversion was observed between the DSC and FTIRS data during the hyphenated DSC/FRS/FTIRS than for the cross-correlation of independent conventional experiments. This is reflected in the correlation of the autocatalytic model rate constants shown in Figure 7.20 and listed in Table 7.4.

Upon increasing the cross-linking temperature to 60 and 70 °C, the initial rate of cross-linking and extent of cross-linking increased. The evolution of the FRS showed a good correlation with the DSC and FTIRS data. Similarly, the FRS signal continued to increase after approximately 400 to 600 minutes whilst the DSC and FTIRS data remain relatively consistent. The correlation between the DSC and FTIRS was stronger than the cross-correlation of the independently performed conventional experiments which were presented in Chapter 4. This is reflected by the rate constants for each experiment.

The following factors were cited to explain the correlations.

- (i) Thermal environment: During the simultaneous DSC/FRS/FTIRS, the same thermal environment guarantees identical cross-linking conditions for the resin. During conventional DSC and FTIRS cross-linking experiments, differing insulation, sample sizes and thermal management systems were employed which affect the sample temperature and therefore the cross-linking conditions. In this study, the DSC/FRS/FTIRS experiments harness the excellent thermal management of the DSC to regulate the sample temperature to  $\pm 0.01$  °C whilst ensuring identical sample conditions during the acquisition of DSC and FTIRS data.
- (ii) Common analyte: Using a common sample eliminates the effect of any intrinsic variability within the resin formulation.

A stronger correlation between the spectral and thermal data sets was achieved when performing simultaneous DSC/FRS/FTIRS, although discrepancies were still observed toward the end of cross-linking, which may be explained by the following reasons:

- (i) DSC data: Due to suspected vitrification, a relatively low reaction rate produced a low magnitude of heat evolved by the exothermic cross-linking reaction. This may have fallen below the 0.2 mW sensitivity of the DSC and caused the relatively stable reading. The modifications to the DSC may have exacerbated this, despite the steps taken to insulate the system.
- (ii) The FTIRS data shows a larger increase during the later stages of cross-linking upon comparison with the DSC data, where the largest discrepancy of 5% was observed at 50 °C. This may be attributed to the previously discussed limitations of DSC, where quantities of heat below the detection limit (0.2  $\mu$ W) can go undetected during the later stages of cross-linking. FTIRS obtains quantitative



data on the strength of functional groups within the resin system and can detect minor changes in cross-linking (Degamber and Fernando, 2004).

- (iii) The FRS signal continued to increase throughout the cross-linking experiments. It is postulated that the increase was due to a combination of cross-linking and enthalpic relaxation of the resin. The FRS signal continued to increase from approximately 400 to 600 minutes during experiments completed at 60 and 70 °C whilst the quantitative FTIRS data remained relatively stable, indicating cross-linking density was not responsible for the refractive index change. Prolonged heating below a resin's glass transition temperature can cause enthalpic relaxation (Hay, 1995) which causes a volume decrease and an increase in the refractive index; (Robertson and Wilkes, 1998). This has previously been shown to be applicable for thermoset materials (Montserrat, 2000).

The optical, thermal and spectral cross-linking data during simultaneous DSC/FRS/FTIRS showed an excellent correlation with the autocatalytic model. The kinetic data also correlated with data reported using conventional DSC and FTIRS analysis in the current study and data from previous publications. The unique probe design allowed for the integration of refractive index and spectral sensors into the platinum lids of the DSC. The simultaneous acquisition of optical, thermal and spectral data allows for direct comparison.

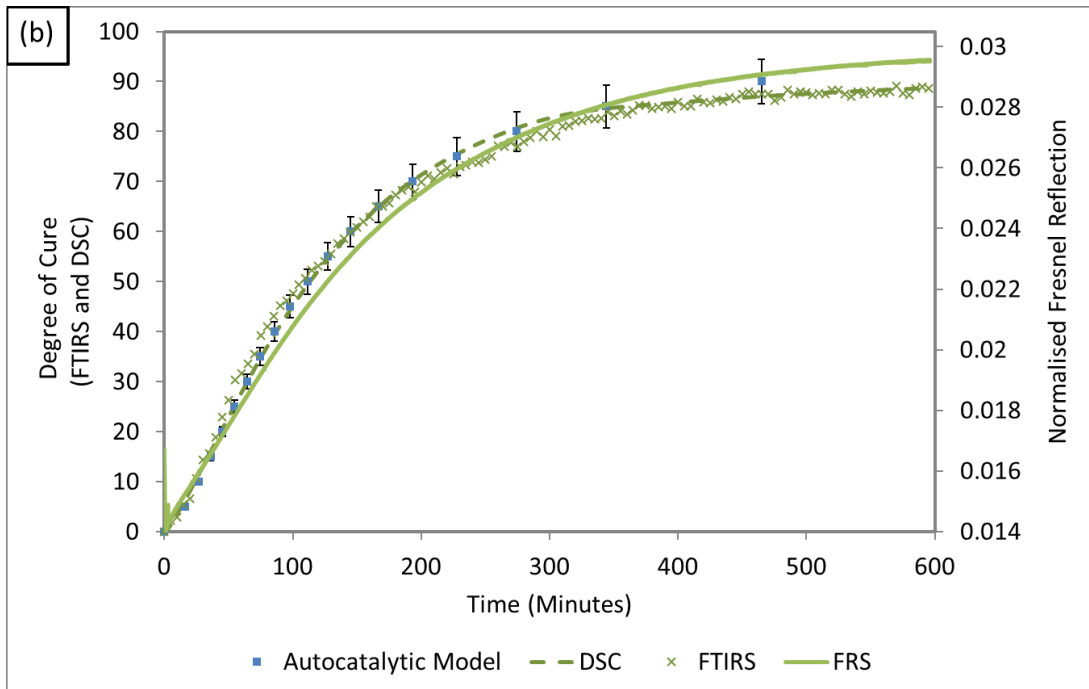
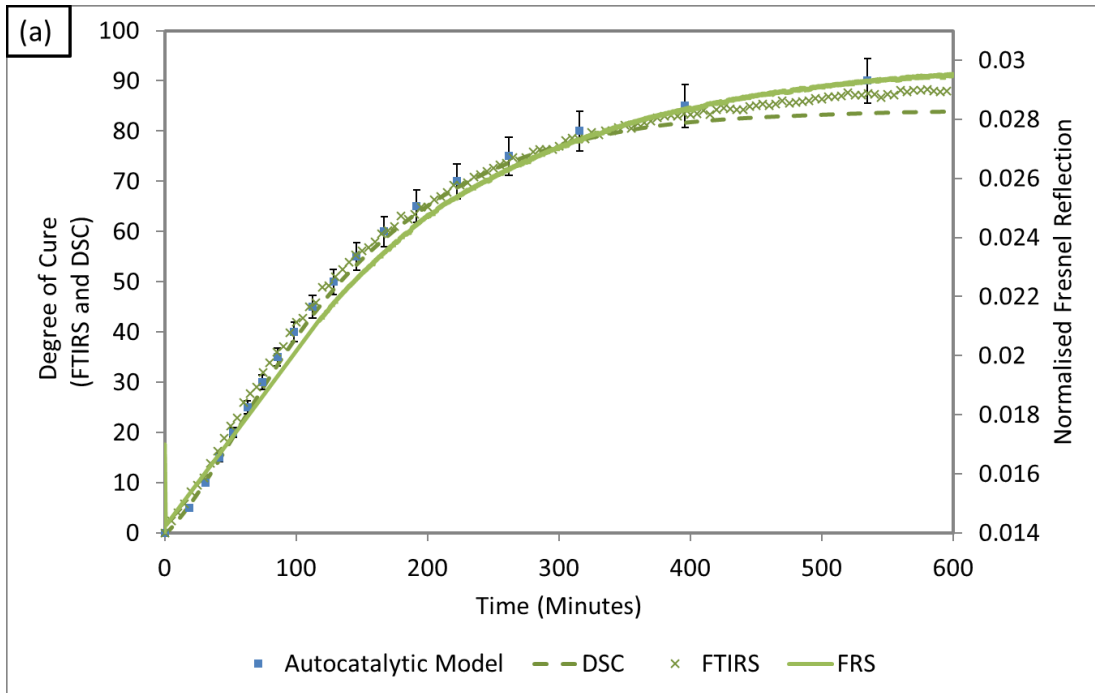


Figure 7.21 DSC, FRS and FTIRS data alongside the autocatalytic model during simultaneous DSC/FRS/FTIRS of LY3505/XB3403 at 50 °C:

(a) Experiment 1; and (b) Experiment 2.

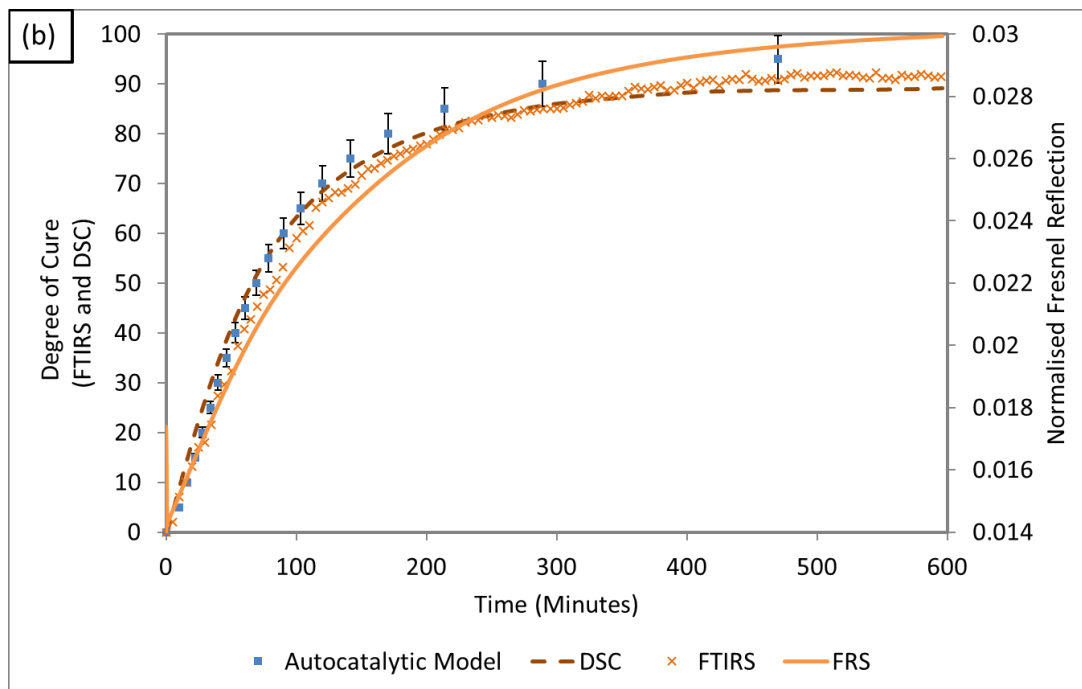
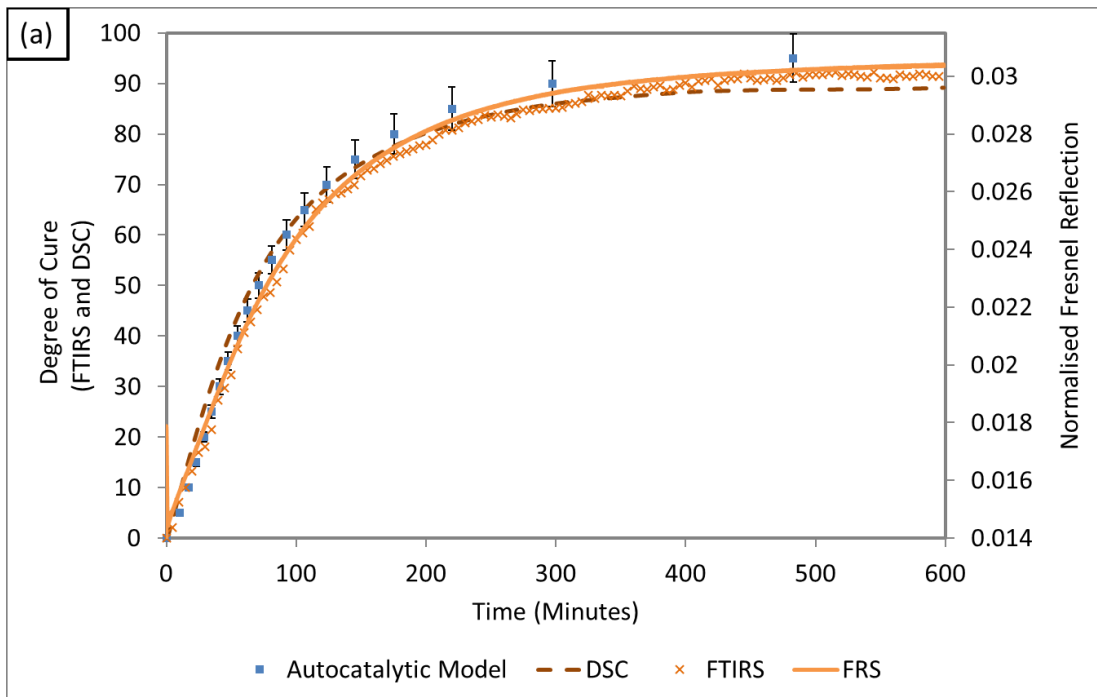


Figure 7.22 DSC, FRS and FTIRS data alongside the autocatalytic model during simultaneous DSC/FRS/FTIRS of LY3505/XB3403 at 60 °C:

(a) Experiment 1; and (b) Experiment 2.

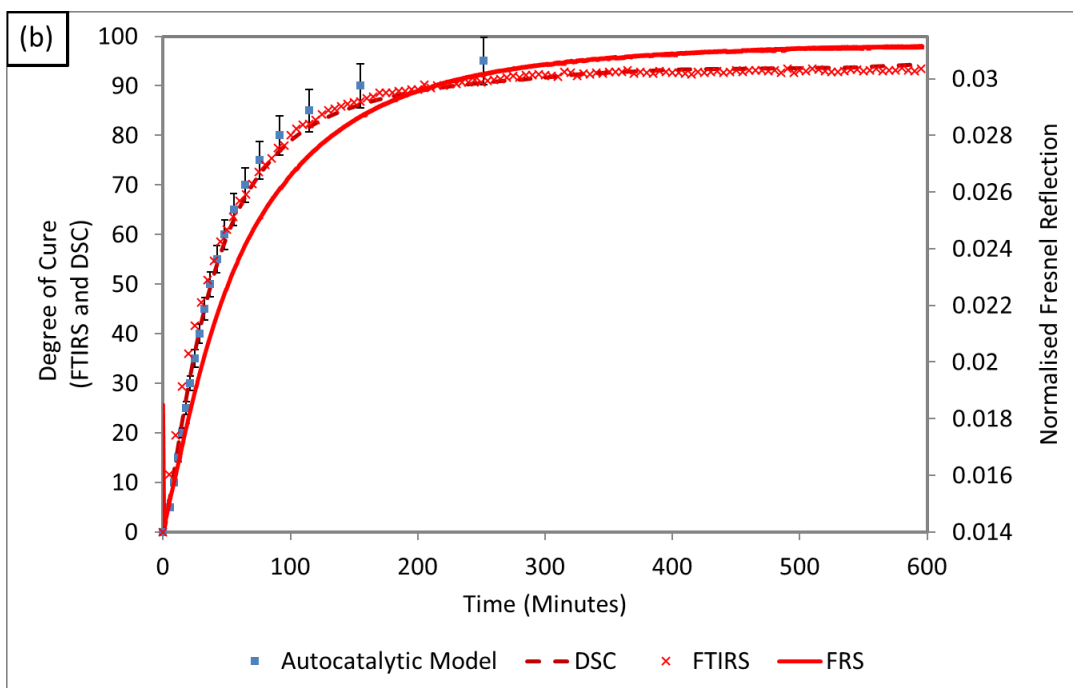
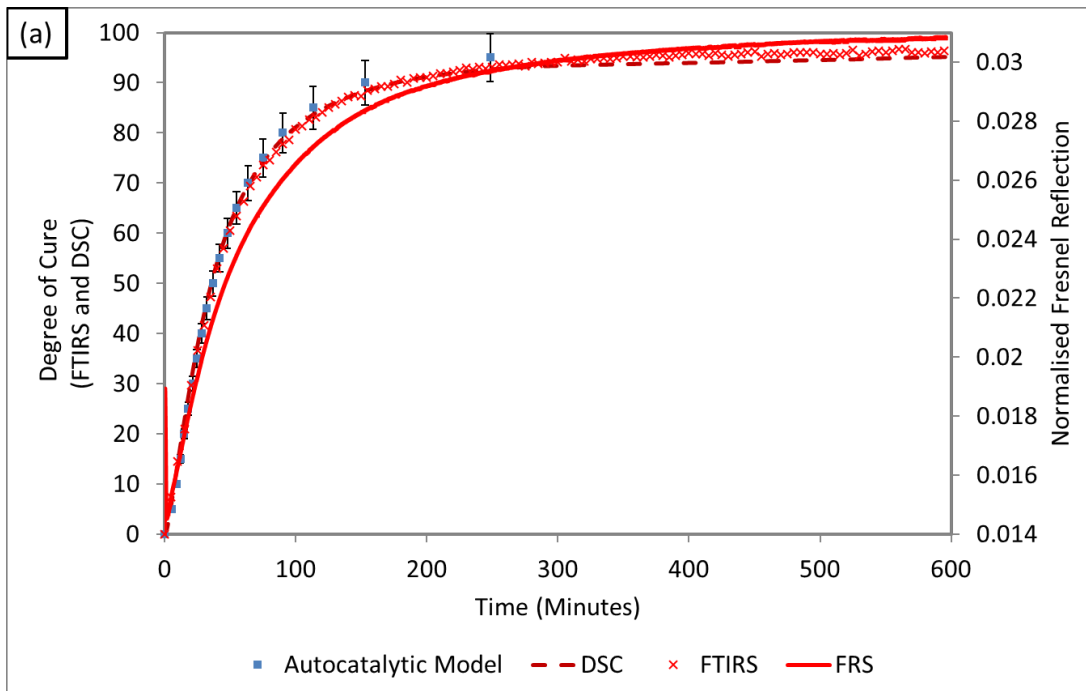


Figure 7.23 DSC, FRS and FTIRS data alongside the autocatalytic model during simultaneous DSC/FRS/FTIRS of LY3505/XB3403 at 70 °C:

(a) Experiment 1; and (b) Experiment 2.

### 7.3 Non-isothermal Differential Scanning Calorimetry Experiments

The glass transition temperatures were measured using the methods as discussed in Section 5.3. A typical DSC/FRS dataset is shown in Figures 7.24 (a) to (c) and the complete datasets are displayed in Table 7.5. A lower ramped temperature range of 30 to 100 °C was used to prevent degradation of the probe. In the previous experiments the temperature range used was 30 to 150 °C. Thus, only the first glass transition temperatures are reported. The average glass transitions temperatures were within  $\pm 2$  °C of those obtained during conventional DSC and simultaneous DSC/Fresnel.

During the temperature ramp, an endothermic event was superposed on the glass transition region as shown in Figure 7.24 (a). This is suspected to be due to the release of enthalpic relaxation. This observation was made during conventional DSC and Hay (1995) has previously reported this to be due to physical ageing of the resin system. The observation supports the previous notion that the increase in the FRS signal during the later stages of isothermal heating is in-part due to enthalpic relaxation.

A change in the thermo-optic coefficient closely correlated with the glass transition temperature measured using the DSC. This was shown during DSC/FRS in Section 5.2.3 and has previously been reported during ramped FRS experiments by Giordano *et al.* (2004), Machavaram *et al.* (2014) and Robert and Dusserre (2014). As discussed previously in Section 5.2.3, it was shown that physical changes such as the glass transition should not affect the refractive index, as there is no change in the chemical nature of the molecules. The change in the thermo-optic coefficient indicates

a change in the relationship of the resin density with temperature in the glassy and gel state.

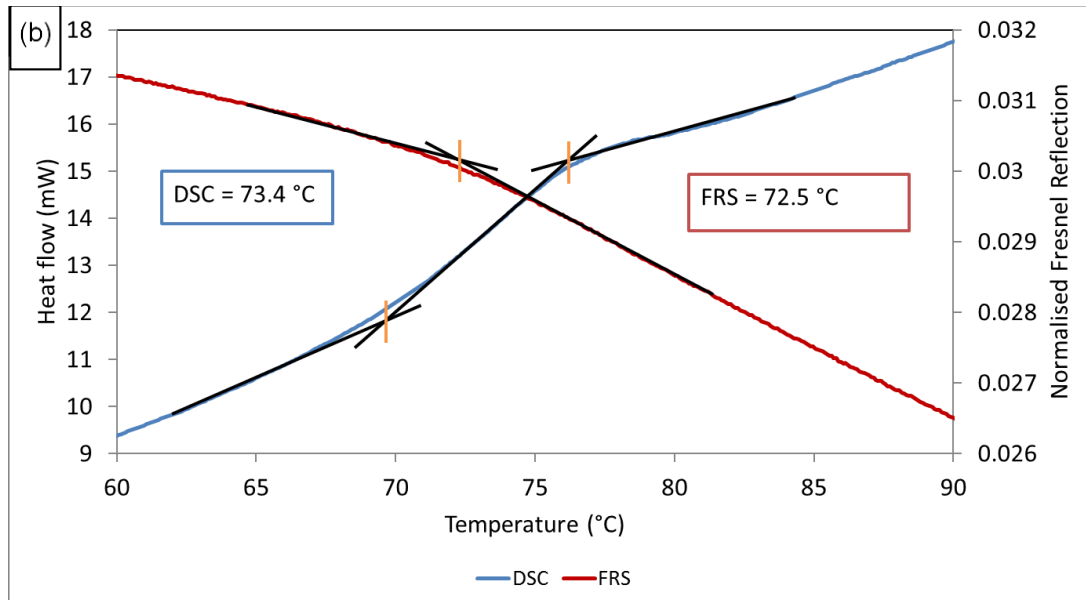
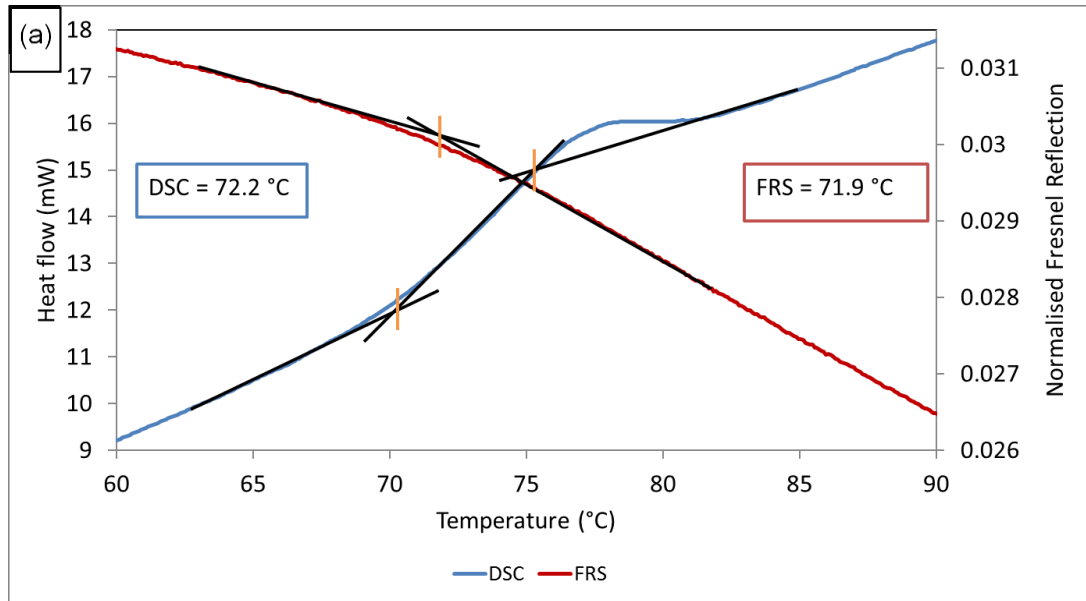


Figure 7.24 Thermogram obtained from DSC during a non-isothermal heating through the glass transition temperature for the LY3505/XB3403 resin system along with data obtained from the Fresnel reflection sensor using DSC/FRS/FTIR technique: (a) Temperature ramp 1; and (b) Temperature ramp 2.

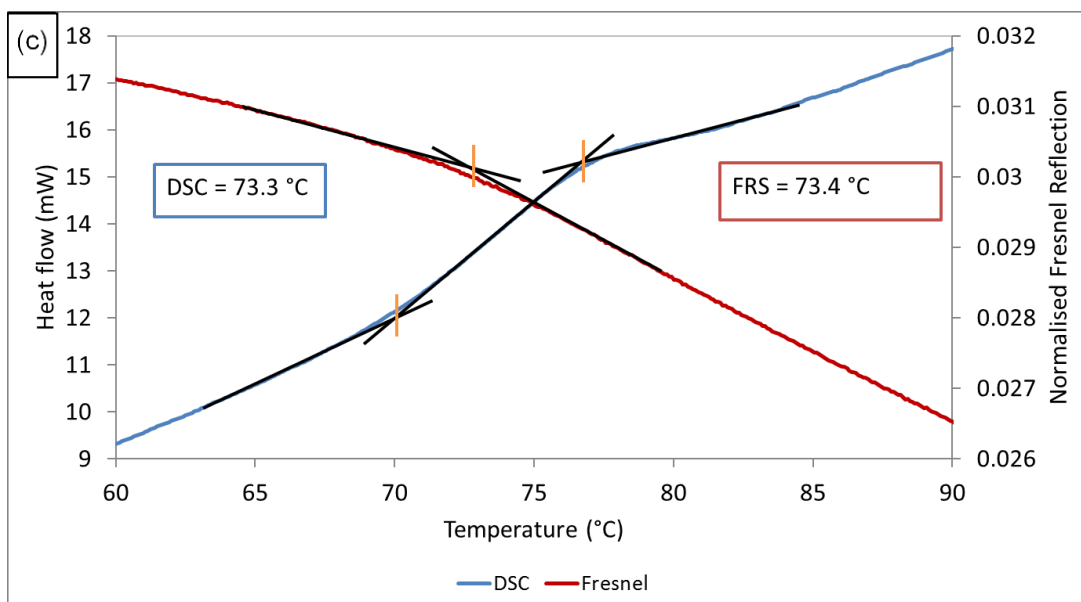


Figure 7.24 (continued) Thermogram obtained from DSC during a non-isothermal scan through the glass transition temperature for the LY3505/XB3403 resin system along with data obtained from the Fresnel reflection sensor using DSC/FRS/FTIR technique: (c) Temperature ramp 3.

Table 7.5 Glass transition temperature values during temperature ramps from 30-100 °C following isothermal cross-linking of LY3505/XB3403 during DSC/FRS/FTIRS.

<b>Isothermal Cross-linking Temperature</b>	<b>DSC/Fresnel T<sub>g</sub> (°C)</b>
<b>50 °C - Experiment 1</b>	<b>55.8/53.8</b>
<b>50 °C - Experiment 2</b>	<b>55.5/55.2</b>
<b>Average</b>	<b>55.7/54.5</b>
<b>60 °C - Experiment 1</b>	<b>67.0/67.5</b>
<b>60 °C - Experiment 2</b>	<b>66.2/65.8</b>
<b>Average</b>	<b>66.6/66.6</b>
<b>70 °C - Experiment 1</b>	<b>73.3/73.9</b>
<b>70 °C - Experiment 2</b>	<b>71.9/72.2</b>
<b>Average</b>	<b>72.6/73.1</b>

## 7.4 Summary

The development of the simultaneous DSC/FRS/FTIRS analytical technique has been demonstrated by the introduction of a fibre optic probe into a DSC instrument. The probe housed a FRS and a bundle of IR transmitting fibres to enable FTIRS. DSC pans were modified to have reflective and non-reflective sections for transmission/reflection FTIRS and Fresnel refractometry, respectively.

Prior to integrating the fibre optic probe into the DSC, the cross-linking of the LY3505/XB3403 resin system was tracked using the FRS/FTIR probe and a hot-plate. Spectral data, comparable to that using conventional FTIRS were acquired. The FRS signal increased as cross-linking proceeded. A good correlation between the data were present. The temperature fluctuations caused by the mode of operation of the hot-plate were detected by the FRS. This was manifested as spikes in the FRS signal when the temperature controller in the hot-plate switched on and off.

The probe was then integrated into the DSC instrument and the calibration was carried out in the conventional manner. The modified-pan arrangement enabled adequate calibration.

Cross-linking of LY3505/XB3403 was then demonstrated at 50, 60 and 70 °C. A good correlation between the thermal, spectral and optical data existed at each temperature. The FTIRS data showed an increased degree of cross-linking when compared to the DSC data, where a maximum increase of 5% was observed at



50 °C. Between 400 and 600 minutes, the FRS signal showed an upward increase whilst the DSC and FTIRS data remained relatively consistent. It is suspected that the FRS detected an optical event related to enthalpic relaxation (also known as physical ageing), which manifested as an endothermic peak superposed on the glass transition during ramped experiments. The cross-linking kinetics were studied, the rate constants and activation energies correlated with previous data.

Ramped heating revealed comparable glass transition values for the resin system using DSC and the FRS probe. Similar to previous experiments in Chapter 4, a close correlation was observed between the change in the thermo-optic coefficient and the stepwise change in the heat-flow.

## **8. CONCLUSIONS AND RECOMMENDATIONS FOR FUTURE RESEARCH**

The focus of this research was to develop the integration of a FRS into a DSC instrument to allow for a direct comparison between thermal and optical properties during isothermal and non-isothermal cross-linking of commercially available epoxy resin systems. The development of two novel hyphenated analytical techniques was demonstrated to track the cross-linking of an epoxy resin system. During DSC/FRS and DSC/FRS/FTIRS the FRS data correlated closely with thermal and spectral data demonstrating its performance to track cross-linking kinetics.

This chapter includes a synopsis of the results presented in previous chapters and demonstrates compliance with the aims and objectives outlined in Chapter 1. Each section is summarised with the experimental outcomes and conclusions. The last part of this chapter proposes recommendations for future research.

### **8.1 Conclusions**

#### **8.1.1 Conventional Analytical Techniques**

The cross-linking kinetics of the LY3505/XB3403 resin system was investigated using differential scanning calorimetry (DSC) and Fourier transform infrared spectroscopy (FTIRS) at 50, 60 and 70 °C. The average degree of cure increased by approximately 3% during FTIRS experiments.

The autocatalytic model (see Equation 2.13) showed a good correlation and fit to the experimentally derived cross-linking data. The activation energy was calculated to be 55.58 kJ mol<sup>-1</sup> and 55.08 kJ mol<sup>-1</sup> during DSC and FTIRS experiments, respectively. The isothermal rate constants and activation energy correlated to within 10% of previous research into the resin system.

A conventional parallel plate rheometer was used to characterise the viscosity of the resin system as a function of temperature. The evolution of the storage (G') and loss modulus (G'') were determined. The cross-over point between the two was then taken as an indication of gelation. The rheometer-based gelation times at 50, 60 and 70 °C were 223, 112 and 61 minutes respectively.

The FRS was integrated into the Abbe refractometer to demonstrate calibration of the sensor.

### **8.1.2 Differential Scanning Calorimetry/Fresnel Reflection Sensor**

The DSC that was used for conventional thermal analysis was modified using a custom-made top-lid, accommodating two micrometer translation stages to allow a FRS sensor to be lowered into the DSC sample chamber.

Isothermal cross-linking of the LY3505/XB3403 resin system at 50, 60 and 70 °C revealed an excellent correlation between the degree of cross-linking and the increase in the FRS signal. The extent of conversion and the activation energies remained within 5% of the conventional data and indicated that the introduction of the optical fibre did not significantly compromise the sensitivity of the DSC.

Ramped heating, following the isothermal cross-linking in the DSC was used to determine the  $T_g$ . A change in the thermo-optic coefficient was also observed from the FRS in the glass transition region.

The simultaneous DSC/FRS was used to detect phase separation in a resin system of interest to the sponsor (Cytec/Solvay) and detect the glass transition temperature in non-stoichiometric systems.

### **8.1.3 LY3505/XB3403 Resin system with Graphene Nano-particles**

The introduction of GNP into the resin system was seen to generate significant fluctuations in the FRS signal, during the early stages of cross-linking. The fluctuations increased in frequency and intensity with increasing GNP concentration and dissipated as cross-linking commenced.

LY3505/GNP samples without the hardener also exhibited fluctuations. It was suspected that the stochastic movement of particles around the cleaved end-face of the optical fibre was responsible for the fluctuations. Freezing a sample of LY3505/GNP in liquid nitrogen caused the fluctuations to cease. Permitting the liquid nitrogen to evaporate naturally led to the fluctuations reappearing.

The hyphenated FRS/rheometer technique was used to investigate if the fluctuations ceased after gelation. The time taken to achieve a linear FRS signal decreased with increasing temperature and this time correlated to the gelation time ( $G'/G''$ ). It can be concluded that the FRS can be used to estimate the gelation time.

#### **8.1.4 First Demonstration of Simultaneous Differential Scanning Calorimetry /Fresnel Reflection Sensor /Fourier Transform Infrared Spectroscopy**

A probe was designed to house a bundle of near-infrared transmitting optical fibres and a demountable FRS. The platinum lids were drilled to create an orifice to allow for insertion into the DSC. In order to prevent specular reflection interfering with the FRS signal, half of an aluminium DSC pan was sprayed with graphite. The FRS was aligned over the non-reflective side of the pan with the NIR bundle of optical fibres aligned over the reflective part of the DSC pan.

The probe was then introduced into the DSC to study the isothermal cross-linking of LY3505/XB3403 at 50, 60 and 70 °C. Excellent agreement was observed throughout the cross-linking process between the three data sets. Discrepancies observed during conventional DSC and FTIRS were reduced significantly when performing the experiments simultaneously.

The autocatalytic model rate constants and glass transition temperatures following cross-linking compared with conventionally performed experiments.

The simultaneous DSC/FRS/FTIRS was demonstrated in this study for the first time.

## 8.2 Recommendations for Future Research

The research presented highlights the use of the FRS measurements for '*in situ*' cure monitoring, by incorporating the sensor into a DSC. This section suggests research to further understand the sensor response.

During the cross-linking of the phase separating resins using the DSC/FRS system, signal fluctuations appeared to be due to phase separation. Experiments where a FRS probe is incorporated into a heated microscopic cell may enable any observable microstructure changes to be directly linked to any optical phenomena.

Fluctuations in the FRS response, when immersed in LY3505/GNP systems, were believed to be due to the stochastic effect of particles, although it was unclear what affected the intensity of the peaks. Experiments designed to investigate the impact of particle size, shape and orientation could be explored to further understand the effect of each upon the signal.

Combined DSC/FRS/FTIRS is a powerful technique that could be utilized for cross-linking analysis of resins demonstrating phase separation. The combination of the three measurement techniques can provide qualitative and quantitative cross-linking information in addition to information regarding phase separation.

## LIST OF REFERENCES

- ABDALLA, M., DEAN, D., ROBINSON, P. & NYAIRO, E. (2008) Cure behavior of epoxy/MWCNT nanocomposites: the effect of nanotube surface modification. *Polymer*, 49, 3310-3317.
- ADURIZ, X. A., LUPI, C., BOYARD, N., BAILLEUL, J. L., LEDUC, D., SOBOTKA, V., LEFÈVRE, N., CHAPELEAU, X., BOISROBERT, C. & DELAUNAY, D. (2007) Quantitative control of RTM6 epoxy resin polymerisation by optical index determination. *Composites Science and Technology*, 67, 3196-3201.
- AFROMOWITZ, M. A. (1988) Fiber optic polymer cure sensor. *Lightwave Technology, Journal of*, 6, 1591-1594.
- AFROMOWITZ, M. A. & LAM, K.-Y. (1990) The optical properties of curing epoxies and applications to the fiber-optic epoxy cure sensor. *Sensors and Actuators A: Physical*, 23, 1107-1110.
- AGRAWAL, G. P. (2013) *Nonlinear Fiber Optics*, Academic Press.
- AL-AZZAWI, A. (2006) *Fiber Optics: Principles and Practices*, Taylor & Francis.
- AMPUDIA, J., LARRAURI, E., GIL, E., RODRIGUEZ, M. & LEÓN, L. (1999) Thermal scanning rheometric analysis of curing kinetic of an epoxy resin. I. An anhydride as curing agent. *Journal of applied polymer science*, 71, 1239-1245.
- ANTONUCCI, V., GIORDANO, M., CUSANO, A., NASSER, J. & NICOLAIS, L. (2006) Real time monitoring of cure and gelification of a thermoset matrix. *Composites Science and Technology*, 66, 3273-3280.
- ASTM-D3418 (2015) Standard Test Method for Transition Temperatures and Enthalpies of Fusion and Crystallization of Polymers by Differential Scanning Calorimetry.
- ASTM-E967 (2014) Standard Test Method for Temperature Calibration of Differential Scanning Calorimeters and Differential Thermal Analyzers. ASTM International.
- ASTM-E968 (2014) Standard Practice for Heat Flow Calibration of Differential Scanning Calorimeters. ASTM International.
- ASTM-E1356 (2014) Standard Test Method for Assignment of the Glass Transition Temperatures by Differential Scanning Calorimetry. ASTM International.
- AVADHANULU, M. N. (1992) *A Textbook of Engineering Physics*, S Chand & Company.
- AZADEH, M. (2009) *Fiber Optics Engineering*, Springer US.
- BAGAD, V. S. (2007) *Optical Fiber Communications*, Technical Publications.
- BAIR, H. E. (1981) CHAPTER 9 - Thermal Analysis of Additives in Polymers. In: TURI, E. A. (ed.) *Thermal Characterization of Polymeric Materials*. Academic Press.
- BALANDIN, A. A., GHOSH, S., BAO, W., CALIZO, I., TEWELDEBRHAN, D., MIAO, F. & LAU, C. N. (2008) Superior thermal conductivity of single-layer graphene. *Nano letters*, 8, 902-907.
- BARTOLOMEO, P., CHAILAN, J. F. & VERNET, J. L. (2001) Curing of cyanate ester resin: a novel approach based on FTIR spectroscopy and comparison with other techniques. *European Polymer Journal*, 37, 659-670.
- BARTON, J. M. (1983) An Improved Method for the Use of Dsc in the Isothermal Mode to Monitor Exothermic Reactions. *Thermochemica Acta*, 71, 337-344.
- BARTON, J. M., GREENFIELD, D. C. & HODD, K. (1992) Some effects of structure on the cure of glycidylether epoxy resins. *Polymer*, 33, 1177-1186.

- BARTON, J. M. & WRIGHT, W. W. (1985) A Study of the Cure Characteristics of an Epoxy-Resin System by Differential Scanning Calorimetry and Torsional Braid Analysis. *Thermochimica Acta*, 85, 411-414.
- BERNATH, A., KÄRGER, L. & HENNING, F. (2016) Accurate Cure Modeling for Isothermal Processing of Fast Curing Epoxy Resins. *Polymers*, 8, 390.
- BERTOLAZZI, S., BRIVIO, J., RADENOVIC, A., KIS, A., WILSON, H., PRISBREY, L., MINOT, E., TSELEV, A., PHILIPS, M. & VIANI, M. (2013) Exploring flatland: AFM of mechanical and electrical properties of graphene, MoS<sub>2</sub> and other low-dimensional materials.
- BILLAUD, C., VANDEUREN, M., LEGRAS, R. & CARLIER, V. (2002) Quantitative Analysis of Epoxy Resin Cure Reaction: A Study by Near-Infrared Spectroscopy. *Applied Spectroscopy*, 56, 1413-1421.
- BILYEU, B. & BROSTOW, W. (2002) Separation of gelation from vitrification in curing of a fiber-reinforced epoxy composite. *Polymer Composites*, 23, 1111-1119.
- BILYEU, B., BROSTOW, W. & MENARD, K. (1999) Evaluation of the curing process in a reinforced epoxy by dynamic DSC (TMDSC) and DMA. *Antec '99: Plastics Bridging the Millennia, Conference Proceedings, Vols I-III*, 2724-2726.
- BILYEU, B., BROSTOW, W. & MENARD, K. P. (2000) Epoxy thermosets and their applications II. Thermal analysis. *Journal of Materials Education*, 22, 107-130.
- BLANCO, I. et al. (2004) Influence of a selected hardener on the phase separation in epoxy/thermoplastic polymer blends. *Journal of Applied Polymer Science* 94(1): 361-371.
- BLANCO, M., CORCUERA, M. A., RICCARDI, C. C. & MONDRAGON, I. (2005) Mechanistic kinetic model of an epoxy resin cured with a mixture of amines of different functionalities. *Polymer*, 46, 7989-8000.
- BOEY, F. Y. C. & QIANG, W. (2000) Experimental modeling of the cure kinetics of an epoxy-hexaaminohydro-4-methylphthalicanhydride (MHPA) system. *Polymer*, 41, 2081-2094.
- BOLL, D., SCHUBERT, K., BRAUNER, C. & LANG, W. (2014) Miniaturized flexible interdigital sensor for in situ dielectric cure monitoring of composite materials. *IEEE Sensors Journal*, 14, 2193-2197.
- BOYARD, N. (2016) *Heat Transfer in Polymer Composite Materials: Forming Processes*, Wiley.
- BOYES, W. (2002) *Instrumentation Reference Book*, Elsevier Science.
- BROCK, T., GROTEKLAES, M. & MISCHKE, P. (2000) *European Coatings Handbook*, Vincentz.
- BROSTOW, W., GOODMAN, S. H. & WAHRMUND, J. (2014) Epoxies. 191-252.
- BROWN, M. E. (2012) *Introduction to Thermal Analysis: Techniques and applications*, Springer Netherlands.
- BUGGY, S. J., CHEHURA, E., JAMES, S. W. & TATAM, R. P. (2007) Optical fibre grating refractometers for resin cure monitoring. *Journal of Optics A: Pure and Applied Optics*, 9, S60.
- BUIST, G. J., BARTON, J. M., HOWLIN, B. J., JONES, J. R. & PARKER, M. J. (1996) Chemical models for the cure of epoxy resins: the influence of hydrogen bonding. *Journal of Materials Chemistry*, 6, 911-915.
- CADENATO, A., SALLA, J. M., RAMIS, X., MORANCHO, J. M., MARROYO, L. M. & MARTIN, J. L. (1997) Determination of gel and vitrification times of thermoset curing process by means of TMA, DMTA and DSC techniques - TTT diagram. *Journal of Thermal Analysis*, 49, 269-279.



- CALABRESE, L. & VALENZA, A. (2003) Effect of CTBN rubber inclusions on the curing kinetic of DGEBA–DGEBF epoxy resin. *European Polymer Journal*, 39, 1355-1363.
- CAMPBELL, F. C. (2010) *Structural composite materials*, ASM international.
- CHAMBON, F. 1987. Linear Viscoelasticity at the Gel Point of a Crosslinking PDMS with Imbalanced Stoichiometry. *Journal of Rheology*, 31, 683.
- CHANDRASEKARAN, S., SATO, N., TÖLLE, F., MÜLHAUPT, R., FIEDLER, B. & SCHULTE, K. (2014) Fracture toughness and failure mechanism of graphene based epoxy composites. *Composites Science and Technology*, 97, 90-99.
- CHANG-BONG, K. & CHIN, B. S. (2004) Measurement of the refractive index of liquids at 1.3 and 1.5 micron using a fibre optic Fresnel ratio meter. *Measurement Science and Technology*, 15, 1683.
- CHARSLEY, E. L., LAYE, P. G., MARKHAM, H. M. & LE GOFF, T. (2010) Calibration of differential scanning calorimeters: A comparison between indium and diphenylacetic acid. *Thermochimica Acta*, 497, 72-76.
- CHATTERJEE, S., WANG, J., KUO, W., TAI, N., SALZMANN, C., LI, W., HOLLERTZ, R., NÜESCH, F. & CHU, B. (2012) Mechanical reinforcement and thermal conductivity in expanded graphene nanoplatelets reinforced epoxy composites. *Chemical Physics Letters*, 531, 6-10.
- CHEN, J. H., HUANG, X. G., HE, W. X. & TAO, J. (2011) A parallel-multipoint fiber-optic temperature sensor based on Fresnel reflection. *Optics and Laser Technology*, 43, 1424-1427.
- CHENG, K. C., CHIU, W. Y., HSIEH, K. H. & MA, C. C. M. (1994) Chemorheology of epoxy resin. *Journal of Materials Science*, 29, 887-893.
- CHENG, S. Z. D. (2002) *Handbook of Thermal Analysis and Calorimetry: Applications to Polymers and Plastics*, Elsevier Science.
- CHOMYCZ, B. (2000) *Fiber Optic Installer's Field Manual*, McGraw-Hill Education.
- CRISP, J. 2005. *Introduction to Fiber Optics*, Elsevier Science.
- CROSBY, P. A., POWELL, G. R., FERNANDO, G. F., FRANCE, C. M., SPOONCER, R. C. & WATERS, D. N. (1996a) In situ cure monitoring of epoxy resins using optical fibre sensors. *Smart Materials & Structures*, 5, 415-428.
- CROSBY, P. A., POWELL, G. R., LIU, T., WU, X. & FERNANDO, G. F. In-situ cure monitoring of an epoxy/amine resin system using an optical fiber transmission sensor. (1996b) 109-115.
- CUSANO, A., BREGLIO, G., GIORDANO, M., CALABRO, A., CUTOLO, A. & NICOLAIS, L. (2001) Optoelectronic characterization of the curing process of thermoset-based composites. *Journal of Optics a-Pure and Applied Optics*, 3, 126-130.
- CUSANO, A., CUTOLO, A., GIORDANO, M. & NICOLAIS, L. (2003) Optoelectronic refractive index measurements: Application to smart processing. *Ieee Sensors Journal*, 3, 781-787.
- CYSNE BARBOSA, A. P., P. FULCO, A. P., S.S. GUERRA, E., K. ARAKAKI, F., TOSATTO, M., B. COSTA, M. C. & D. MELO, J. D. (2017) Accelerated aging effects on carbon fiber/epoxy composites. *Composites Part B: Engineering*, 110, 298-306.
- DALY, J. C. (1984) *Fiber Optics*, Taylor & Francis.
- DANIELS, C. A. (1989) *Polymers: Structure and Properties*, Taylor & Francis.
- DANNENBERG, H. & HARP, W. R. (1956) Determination of Cure and Analysis of Cured Epoxy Resins. *Analytical Chemistry*, 28, 86-90.
- DE BAKKER, C. J., ST JOHN, N. A. & GEORGE, G. A. (1993) Simultaneous differential scanning calorimetry and near-infra-red analysis of the curing of

- tetraglycidyl-diaminodiphenylmethane with diaminodiphenylsulphone. *Polymer*, 34, 716-725.
- DE BOER, J., VISSER, R. J. & MELIS, G. P. (1992) Time-resolved determination of volume shrinkage and refractive index change of thin polymer films during photopolymerization. *Polymer*, 33, 1123-1126.
- DEALY, J. M. & WISSBRUN, K. F. (2012) *Melt Rheology and Its Role in Plastics Processing: Theory and Applications*, Springer Netherlands.
- DEGAMBER, B. & FERNANDO, G. F. (2002) Process monitoring of fiber-reinforced polymer composites. *Mrs Bulletin*, 27, 370-380.
- DEGAMBER, B. & FERNANDO, G. F. (2004) Process monitoring of a thermosetting resin using optical-fiber sensors in a microwave environment. *Ieee Sensors Journal*, 4, 713-721.
- DEGAMBER, B. & FERNANDO, G. F. (2006) Fibre optic dilato-spectroscopic sensor: Simultaneous thermal, spectral, and physical analyses of materials. *Smart Materials & Structures*, 15, 1054-1062.
- DEGAMBER, B., TETLOW, J. & FERNANDO, G. F. (2004a) Design and development of low-cost optical-fiber sensors for temperature metrology: Process monitoring of an epoxy resin system. *Journal of Applied Polymer Science*, 94, 83-95.
- DEGAMBER, B., WINTER, D., TETLOW, J., TEAGLE, M. & FERNANDO, G. F. (2004b) Simultaneous DSC/FTIRS/TMA. *Measurement Science & Technology*, 15, L5-L10.
- DELAWA, U. (1990) *Delaware Composites Design Encyclopedia: Processing and Fabrication Technology*, Taylor & Francis.
- DIMOPOULOS, A., BUGGY, S. J., SKORDOS, A. A., JAMES, S. W., TATAM, R. P. & PARTRIDGE, I. K. (2009) Monitoring Cure in Epoxies Containing Carbon Nanotubes with an Optical-Fiber Fresnel Refractometer. *Journal of Applied Polymer Science*, 113, 730-735.
- DON, T. M. & BELL, J. P. (1998) Fourier transform infrared analysis of polycarbonate/epoxy mixtures cured with an aromatic amine. *Journal of Applied Polymer Science*, 69, 2395-2407.
- DOWNING, J. (2004) *Fiber Optic Communications*, Cengage Learning.
- DOYLE, C., MARTIN, A., LIU, T., WU, M., HAYES, S., CROSBY, P. A., POWELL, G. R., BROOKS, D. & FERNANDO, G. F. (1998a) In-situ process and condition monitoring of advanced fibre-reinforced composite materials using optical fibre sensors. *Smart Materials and Structures*, 7, 145.
- DOYLE, C., MARTIN, A., LIU, T., WU, M., HAYES, S., CROSBY, P. A., POWELL, G. R., BROOKS, D. & FERNANDO, G. F. (1998b) In-situ process and condition monitoring of advanced fibre-reinforced composite materials using optical fibre sensors. *Smart Materials & Structures*, 7, 145-158.
- DÜMICHEN, E., JAVDANITEHRAN, M., ERDMANN, M., TRAPPE, V., STURM, H., BRAUN, U. & ZIEGMANN, G. (2015) Analyzing the network formation and curing kinetics of epoxy resins by in situ near-infrared measurements with variable heating rates. *Thermochimica Acta*, 616, 49-60.
- DUMITRESCU, O. R. (2003a) Simultaneous differential scanning calorimetry : Fourier Transform infrared spectroscopy.
- DUMITRESCU, O. R. C. U. (2003b) *Simultaneous differential scanning calorimetry : Fourier Transform infrared spectroscopy*, Silsoe, Cranfield University.
- EHLERS, J.-E., RONDAN, N. G., HUYNH, L. K., PHAM, H., MARKS, M. & TRUONG, T. N. (2007) Theoretical study on mechanisms of the epoxy-amine curing reaction. *Macromolecules*, 40, 4370-4377.
- ELIAS, H. G. & VOHWINKEL (1986) *Neue Polymere Werkstoffe Für Die Industrielle Anwendung. 2. Folge*, Gordon and Breach Science Publishers.

- ELLIS, B. (2015) *Chemistry and technology of epoxy resins*.
- ERDOĞAN, B., SEYHAN, A., OCAK, Y., TANOĞLU, M., BALKÖSE, D. & ÜLKÜ, S. (2008) Cure kinetics of epoxy resin-natural zeolite composites. *Journal of thermal analysis and calorimetry*, 94, 743-747.
- FAVA, R. A. (1968) Differential scanning calorimetry of epoxy resins. *Polymer*, 9, 137-151.
- FERNANDEZ, B., CORCUERA, M., MARIETA, C. & MONDRAGON, I. (2001) Rheokinetic variations during curing of a tetrafunctional epoxy resin modified with two thermoplastics. *European polymer journal*, 37, 1863-1869.
- FERNANDO, G. F. & DEGAMBER, B. (2006) Process monitoring of fibre reinforced composites using optical fibre sensors. *International Materials Reviews*, 51, 65-106.
- FIORE, V. & VALENZA, A. (2013) *Advanced fibre-reinforced polymer (FRP) composites for structural applications: 5. Epoxy resins as a matrix material in advanced fiber-reinforced polymer (FRP) composites*, Elsevier Science.
- FLORY, P. J. (1941) Molecular size distribution in three dimensional polymers. I. Gelation1. *Journal of the American Chemical Society*, 63, 3083-3090.
- FOUCHAL, F., KNIGHT, J. & DICKENS, P. M. (2004) Monitoring the polymerization of a diglycidyl ether bisphenol-A/2, 2'-dimethyl-4, 4'-methylenebis (cyclohexylamine) matrix with a Fourier transform infrared optical fibre sensor. *Proceedings of the Institution of Mechanical Engineers, Part L: Journal of Materials: Design and Applications*, 218, 331-342.
- FRAGA, F., BURGO, S. & NUNEZ, E. R. (2001) Curing kinetic of the epoxy system BADGE n=0/1,2 DCH by Fourier Transform Infrared Spectroscopy (FTIR). *Journal of Applied Polymer Science*, 82, 3366-3372.
- FRAGA, I., MONTSERRAT, S. & HUTCHINSON, J. M. (2008) Vitrification during the Isothermal Cure of Thermosets: Comparison of Theoretical Simulations with Temperature-Modulated DSC and Dielectric Analysis. *Macromolecular Chemistry and Physics*, 209, 2003-2011.
- FRANCIS B. ET AL. (2007) Diglycidyl ether of bisphenol-A epoxy resin modified using poly(ether ether ketone) with pendent tert-butyl groups. *Journal of Polymer Science Part B: Polymer Physics* 45(17): 2481-2496.
- FRUSHOUR, B. & SABATELLI, D. (1988) Simultaneous measurement of light transmission and heat flow in a modified differential scanning calorimeter. *Journal of applied polymer science*, 36, 1453-1465.
- GALPAYA, D. G., FERNANDO, J. F., RINTOUL, L., MOTTA, N., WACLAWIK, E. R., YAN, C. & GEORGE, G. A. (2015a) The effect of graphene oxide and its oxidized debris on the cure chemistry and interphase structure of epoxy nanocomposites. *Polymer*, 71, 122-134.
- GALPAYA, D. G. D., FERNANDO, J. F. S., RINTOUL, L., MOTTA, N., WACLAWIK, E. R., YAN, C. & GEORGE, G. A. (2015b) The effect of graphene oxide and its oxidized debris on the cure chemistry and interphase structure of epoxy nanocomposites. *Polymer*, 71, 122-134.
- GARSCHKE, C., PARLEVLIT, P. P., WEIMER, C. & FOX, B. L. (2013) Cure kinetics and viscosity modelling of a high-performance epoxy resin film. *Polymer Testing*, 32, 150-157.
- GEISLER, J., BEAVEN, G. & BOUTRUCHE, J. P. (2014) *Optical Fibres: EPO Applied Technology Series*, Elsevier Science.
- GEORGE, G. A., CASH, G. A. & RINTOUL, L. (1996) Cure monitoring of aerospace epoxy resins and prepregs by Fourier transform infrared emission spectroscopy. *Polymer International*, 41, 169-182.
- GILLEN, G. D., GILLEN, K. & GUHA, S. (2013) *Light Propagation in Linear Optical Media*, Taylor & Francis.

- GILLHAM, J. K. (1986) The Time-Temperature-Transformation (Ttt) Cure Diagram of Thermosetting Polymeric Systems. *Abstracts of Papers of the American Chemical Society*, 191, 2-Pmse.
- GIORDANO, M., NICOLAIS, L., CALABRO, A. M., CANTONI, S., CUSANO, A., BREGLIO, G. & CUTOLO, A. (2000) A fiber optic thermoset cure monitoring sensor. *Polymer Composites*, 21, 523-530.
- GIORDANO, M., LAUDATI, A., RUSSO, M., NASSER, J., PERSIANO, G. V. & CUSANO, A. (2004) Advanced cure monitoring by optoelectronic multifunction sensing system. *Thin Solid Films*, 450, 191-194.
- GMELIN, E. & SARGE, S. (1995) Calibration of differential scanning calorimeters. *Pure and Applied Chemistry*, 67(11), pp. 1789-1800.
- GOLDSTEIN, D. H. (2016) *Polarized Light, Third Edition*, CRC Press.
- GONZÁLEZ, M. G., BASELGA, J. & CABANELAS, J. C. (2012) *Applications of FTIR on epoxy resins-identification, monitoring the curing process, phase separation and water uptake*, INTECH Open Access Publisher.
- GROENEWOUD, W. M. (2001) *Characterisation of Polymers by Thermal Analysis*, Elsevier Science.
- GUAN, L.-Z., WAN, Y.-J., GONG, L.-X., YAN, D., TANG, L.-C., WU, L.-B., JIANG, J.-X. & LAI, G.-Q. (2014) Toward effective and tunable interphases in graphene oxide/epoxy composites by grafting different chain lengths of polyetheramine onto graphene oxide. *Journal of Materials Chemistry A*, 2, 15058-15069.
- GUDE, M., ET AL. (2011) Effect of the epoxy/amine stoichiometry on the properties of carbon nanotube/epoxy composites. *Journal of thermal analysis and calorimetry* 108(2): 717-723.
- GUPTA, B. D. & GUPTA, B. D. (2006) *Fiber Optic Sensors: Principles and Applications*, New India Publishing Agency.
- GUPTA, R. K. (2000) *Polymer and Composite Rheology, Second Edition*, Taylor & Francis.
- HAINES, P. J., (2002) *Principles of Thermal Analysis and Calorimetry*, Royal Society of Chemistry.
- HAINES, P. J. & SKINNER, G. A. (1982) Simultaneous differential scanning calorimetry and reflected light intensity measurement. *Thermochimica Acta*, 59, 343-359.
- HAMERTON, I. (1996) *Recent Developments in Epoxy Resins*, Rapra Technology Limited.
- HARDIS, R., JESSOP, J. L. P., PETERS, F. E. & KESSLER, M. R. (2013) Cure kinetics characterization and monitoring of an epoxy resin using DSC, Raman spectroscopy, and DEA. *Composites Part a-Applied Science and Manufacturing*, 49, 100-108.
- HARRIS, D. & FERNANDO, G. (2009) Simultaneous acquisition of data on refractive index, strain, temperature and cross-linking kinetics.
- HARRIS, D. (2011) Design and development of a hyphenated technique for monitoring the cure of epoxy-amine resin systems, University of Birmingham.
- HARSCH, M., KARGER-KOCSIS, J. & HERZOG, F. (2008) Monitoring of cure-induced strain of an epoxy resin by fiber Bragg grating sensor. *Journal of Applied Polymer Science*, 107, 719-725.
- HAY, J. N. (1995) The physical ageing of amorphous and crystalline polymers. *Pure and Applied Chemistry*.
- HECHT, E. (2016) *Optics, Global Edition*, Pearson Education, Limited.
- HECHT, J. (1984) *Understanding Fibre Optics*, BPB Publications.

- HEMMINGER, W. F. & SARGE, S. M. (1991) The baseline construction and its influence on the measurement of heat with differential scanning calorimeters. *Journal of thermal analysis*, 37, 1455-1477.
- HEWA-GAMAGE, G. & CHU, P. (2002) A multiplexed point temperature fibre sensor array using OTDR technique and TDM mechanism. *Sensors. Proceedings of IEEE*, 2002. IEEE, 111-115.
- HÖHNE, G., HEMMINGER, W. & FLAMMERSHEIM, H. J. (1996) *Differential Scanning Calorimetry: An Introduction for Practitioners*, Springer-Verlag.
- HÖHNE, G., HEMMINGER, W. F. & FLAMMERSHEIM, H. J. (2013) *Differential Scanning Calorimetry*, Springer Berlin Heidelberg.
- HUANG, Y. & PAUL, D. R. (2004) Physical aging of thin glassy polymer films monitored by gas permeability. *Polymer*, 45, 8377-8393.
- HUNTSMANN (2017) LY3505/XB3403 MSDS.
- İDE, C. & YÜKSEL, K. (2016) *A comparative study of optical fiber sensors for refractive index measurement*. 2016 National Conference on Electrical, Electronics and Biomedical Engineering (ELECO).
- ISHIDA, H. & AGAG, T. (2011) *Handbook of benzoxazine resins*, Elsevier.
- JANKOVIĆ, B. (2010) The kinetic analysis of isothermal curing reaction of an unsaturated polyester resin: estimation of the density distribution function of the apparent activation energy. *Chemical Engineering Journal*, 162, 331-340.
- KAMAL, M. R. (1974) Thermoset characterization for moldability analysis. *Polymer Engineering & Science*, 14, 231-239.
- KAMAL, M. R. A. K., S (1972) The injection molding of thermoplastics part I: Theoretical model.
- KARKANAS, P. I., PARTRIDGE, I. K. & ATTWOOD, D. (1996) Modelling the cure of a commercial epoxy resin for applications in resin transfer moulding. *Polymer International*, 41, 183-191.
- KEIRL, A. & CHRISTIE, C. (2007) *Clinical Optics and Refraction: A Guide for Optometrists, Contact Lens Opticians and Dispensing Opticians*, Baillière Tindall Elsevier/Butterworth-Heinemann.
- KEISER, G. (2003) *Optical Communications Essentials*, McGraw-Hill Education.
- KELLY, A. & ZWEBEN, C. H. (2000) *Comprehensive Composite Materials*, Elsevier.
- KEMMISH, D. J. & HAY, J. N. (1985) The effect of physical ageing on the properties of amorphous PEEK. *Polymer*, 26, 905-912.
- KENKEL, J. (2010) *Analytical Chemistry for Technicians, Third Edition*, CRC Press.
- KIM, H., ABDALA, A. A. & MACOSKO, C. W. (2010) Graphene/polymer nanocomposites. *Macromolecules*, 43, 6515-6530.
- KIM, J. S. (1996) Analysis of dielectric sensors for the cure monitoring of resin matrix composite materials. *Sensors and Actuators B: Chemical*, 30, 159-164.
- KIM, S. S., MURAYAMA, H., KAGEYAMA, K., UZAWA, K. & KANAI, M. (2012) Study on the curing process for carbon/epoxy composites to reduce thermal residual stress. *Composites Part A: Applied Science and Manufacturing*, 43, 1197-1202.
- KING, J. A., KLIMEK, D. R., MISKIOGLU, I. & ODEGARD, G. M. (2013) Mechanical properties of graphene nanoplatelet/epoxy composites. *Journal of Applied Polymer Science*, 128, 4217-4223.
- KUANG-AN, C., HO-JOON, L. & CHIN, B. S. (2002) A fibre optic Fresnel ratio meter for measurements of solute concentration and refractive index change in fluids. *Measurement Science and Technology*, 13, 1962.
- LACHENAL, G. (1995) Dispersive and Fourier Transform near-infrared spectroscopy of polymeric materials. *Vibrational Spectroscopy*, 9, 93-100.
- LALAUZE, R. (2012) *Chemical Sensors and Biosensors*, Wiley.

- LAM, K. Y. & AFROMOWITZ, M. A. (1995a) Fiberoptic epoxy composite cure sensor. 1. Dependence of refractive index of an autocatalytic reaction epoxy system at 850nm on temperature and extent of cure. *Applied Optics*, 34, 5635-5638.
- LAM, K. Y. & AFROMOWITZ, M. A. (1995b) Fiberoptic epoxy composite cure sensor. 2. Performance characteristics. *Applied Optics*, 34, 5639-5644.
- LANGE, J., ALTMANN, N., KELLY, C. T. & HALLEY, P. J. (2000) Understanding vitrification during cure of epoxy resins using dynamic scanning calorimetry and rheological techniques. *Polymer*, 41, 5949-5955.
- LANGE, J., EKELÖF, R. & GEORGE, G. A. (1999a) Indications of micro-vitrification during chainwise cross-linking polymerisation. *Polymer*, 40, 3595-3598.
- LANGE, J., JOHANSSON, M., KELLY, C. T. & HALLEY, P. J. (1999b) Gelation behaviour during chainwise crosslinking polymerisation of methacrylate resins. *Polymer*, 40, 5699-5707.
- LEE, J. Y., CHOI, H. K., SHIM, M. J. & KIM, S. W. (2000) Kinetic studies of an epoxy cure reaction by isothermal DSC analysis. *Thermochimica Acta*, 343, 111-117.
- LEE, S. M. (1989) *Reference Book for Composites Technology*, Taylor & Francis.
- LI, L., ZENG, Z., ZOU, H. & LIANG, M. (2015) Curing characteristics of an epoxy resin in the presence of functional graphite oxide with amine-rich surface. *Thermochimica Acta*, 614, 76-84.
- LI, Q., LI, X. & MENG, Y. (2012) Curing of DGEBA epoxy using a phenol-terminated hyperbranched curing agent: Cure kinetics, gelation, and the TTT cure diagram. *Thermochimica Acta*, 549, 69-80.
- LI, W., DICHIARA, A. & BAI, J. (2013) Carbon nanotube–graphene nanoplatelet hybrids as high-performance multifunctional reinforcements in epoxy composites. *Composites Science and Technology*, 74, 221-227.
- LIU, F., MING, P. & LI, J. (2007) Ab initio calculation of ideal strength and phonon instability of graphene under tension. *Physical Review B*, 76, 064120.
- LIU, Q., ZHOU, X., FAN, X., ZHU, C., YAO, X. & LIU, Z. (2012a) Mechanical and Thermal Properties of Epoxy Resin Nanocomposites Reinforced with Graphene Oxide. *Polymer-Plastics Technology and Engineering*, 51, 251-256.
- LIU, T. & FERNANDO, G. F. (2001) Processing of polymer composites: an optical fibre-based sensor system for on-line amine monitoring. *Composites Part a- Applied Science and Manufacturing*, 32, 1561-1572.
- LIU, Y. M., GANESH, C., STEELE, J. P. H. & JONES, J. E. (1997) Fiber optic sensor development for real-time in-situ epoxy cure monitoring. *Journal of Composite Materials*, 31, 87-102.
- LIU, Z., XIAO, J., BAI, S. & ZHANG, W. (2012b) Study on phenomenological curing model of epoxy resin for prediction of degree of cure. *Journal of Thermal Analysis and Calorimetry*, 109, 1555-1561.
- MA, J., MENG, Q., ZAMAN, I., ZHU, S., MICHELMORE, A., KAWASHIMA, N., WANG, C. H. & KUAN, H.-C. (2014) Development of polymer composites using modified, high-structural integrity graphene platelets. *Composites Science and Technology*, 91, 82-90.
- MACHAVARAM, V. R., WANG, L., PANDITA, S. D., HELLMANN, S., BOGONEZ, F. N. & FERNANDO, G. F. (2014) Multi-point monitoring of cross-linking reactions. *Journal of Applied Polymer Science*, 131, n/a-n/a.
- MACKINNON, A.J., JENKINS, S.D., MCGRAIL, P.T. & PETHRICK, R.A. (1993) Dielectric, mechanical and rheological studies of phase separation and cure of a thermoplastic modified epoxy resin: incorporation of reactively terminated polysulphones. *Polymer*, 34, Issue 15, 3252-3263.

- MAHENDRAN, R., *et al.* (2009) Fiber-optic sensor design for chemical process and environmental monitoring. *Optics and Lasers in Engineering* 47(10): 1069-1076.
- MAHENDRAN, RAMANI SALMALEE (2010) Characterisation of cross-linking and moisture ingress detection in an epoxy/amine resin using fibre-optic sensors. Ph.D. thesis, University of Birmingham.
- MANI, P., RALLAPALLI, A., MACHAVARAM, V. R. & SIVARAMAKRISHNA, A. (2016) Monitoring phase changes in supercooled aqueous solutions using an optical fiber Fresnel reflection sensor. *Optics Express*, 24, 5395-5410.
- MARTIN-GALLEGO, M., BERNAL, M. M., HERNANDEZ, M., VERDEJO, R. & LOPEZ-MANCHADO, M. A. (2013) Comparison of filler percolation and mechanical properties in graphene and carbon nanotubes filled epoxy nanocomposites. *European Polymer Journal*, 49, 1347-1353.
- MATĚJKA, L. (1991) Rheology of epoxy networks near the gel point. *Polymer Bulletin*, 26, 109-116.
- MCADAMS, L. V. G. J. A. (1986) In Encyclopedia of Polymer Science and Engineering; Mark, H. F., Bikales N. M., Overberger, C. G., Kroschwitz, J. I., Eds.; John Wiley and Sons: New York, 1986; Vol. 6, p 322.
- MCCOY, J. D., ANCIPIK, W. B., CLARKSON, C. M., KROPKA, J. M., CELINA, M. C., GIRON, N. H., HAILESILASSIE, L. & FREDJ, N. (2016) Cure mechanisms of diglycidyl ether of bisphenol A (DGEBA) epoxy with diethanolamine. *Polymer*, 105, 243-254.
- MCHUGH, J., FIDEU, P., HERRMANN, A. & STARK, W. (2010) Determination and review of specific heat capacity measurements during isothermal cure of an epoxy using TM-DSC and standard DSC techniques. *Polymer Testing*, 29, 759-765.
- MENARD, K. P. (2008) *Dynamic Mechanical Analysis: A Practical Introduction, Second Edition*, CRC Press.
- MENCZEL, J. D. & PRIME, R. B. (2014) *Thermal analysis of polymers: fundamentals and applications*, John Wiley & Sons.
- METTLER-TOLEDO (2001) DSC Calibration.
- MEYER, F., ET AL. (1995) The effect of stoichiometry and thermal history during cure on structure and properties of epoxy networks. *Polymer* 36(7): 1407-1414.
- MIJOVIC, J. & ANDJELIC, S. (1995) A study of reaction kinetics by near-infrared spectroscopy. 1. Comprehensive analysis of a model epoxy/amine system. *Macromolecules*, 28, 2787-2796.
- MIJOVIĆ, J. & ANDJELIĆ, S. (1996) Monitoring of reactive processing by remote mid infra-red spectroscopy. *Polymer*, 37, 1295-1303.
- MILLER, R. L. & OEBSER, M. A. (1980) Determination of cure times and activation energies of one-container epoxy resin systems by isothermal DSC. *Thermochemica Acta*, 36, 121-131.
- MIN, B. G., STACHURSKI, Z. H. & HODGKIN, J. H. (1993a) Cure kinetics of elementary reactions of a DGEBA/DDS epoxy resin: 1. Glass transition temperature versus conversion. *Polymer*, 34, 4908-4912.
- MIN, B. G., STACHURSKI, Z. H. & HODGKIN, J. H. (1993b) Cure Kinetics of Elementary Reactions of a Diglycidyl Ether of Bisphenol-a Diaminodiphenylsulfone Epoxy-Resin .2. Conversion Versus Time. *Polymer*, 34, 4488-4495.
- MIN, B. G., STACHURSKI, Z. H., HODGKIN, J. H. & HEATH, G. R. (1993c) Quantitative analysis of the cure reaction of DGEBA/DDS epoxy resins without and with thermoplastic polysulfone modifier using near infra-red spectroscopy. *Polymer*, 34, 3620-3627.

- MIRABELLA, F. M. (1986) Simultaneous differential scanning calorimetry (DSC) and infrared spectroscopy using an infrared microsampling accessory (IRMA) and FT-IR. *Applied spectroscopy*, 40, 417-420.
- MONTSERRAT, S. & CIMA, I. (1999) Isothermal curing of an epoxy resin by alternating differential scanning calorimetry. *Thermochimica Acta*, 330, 189-200.
- MONTSERRAT, S. (2000) Enthalpy relaxation of an epoxy–anhydride resin by temperature-modulated differential scanning calorimetry. *Journal of Polymer Science Part B: Polymer Physics* 38(17): 2272-2284.
- MOSIEWICKI, M. A., MARCOVICH, N. E. & ARANGUREN, M. I. (2011) 4 - Characterization of fiber surface treatments in natural fiber composites by infrared and Raman spectroscopy A2 - Zafeiropoulos, Nikolaos E. *Interface Engineering of Natural Fibre Composites for Maximum Performance*. Woodhead Publishing.
- MRAVLJAK, M. & SERNEK, M. (2011) The influence of curing temperature on rheological properties of epoxy adhesives. *Drvna Industrija*, 62, 19-25.
- NAIDU, S. M. & MANI, N. S. (2009) *Applied Physics*, Pearson Education.
- NAIR, A. K., MACHAVARAM, V. R., MAHENDRAN, R. S., PANDITA, S. D., PAGET, C., BARROW, C. & FERNANDO, G. F. (2015) Process monitoring of fibre reinforced composites using a multi-measurand fibre-optic sensor. *Sensors and Actuators B: Chemical*, 212, 93-106.
- NIKOLIC, G., ZLATKOVIC, S., CAKIC, M., CAKIC, S., LACNJEVAC, C. & RAJIC, Z. (2010) Fast Fourier Transform IR Characterization of Epoxy GY Systems Crosslinked with Aliphatic and Cycloaliphatic EH Polyamine Adducts. *Sensors*, 10, 684-696.
- NISHIKIDA, (1996) Selected Applications of Modern FT-IR Techniques. *Taylor & Francis*.
- NORRIS, J.O.W. (2000) Optical Fiber Chemical sensors: Fundamentals and Applications in GRATTAN, L. & MEGGITT, B. (eds.) (2000) Optical fiber sensor technology: advanced applications-Bragg gratings and distributed sensors, *Springer Science & Business Media*.
- O'BRIEN, D. J., MATHER, P. T. & WHITE, S. R. (2001) Viscoelastic properties of an epoxy resin during cure. *Journal of composite materials*, 35, 883-904.
- PANDA, H. (2016) *Epoxy Resins Technology Handbook (Manufacturing Process, Synthesis, Epoxy Resin Adhesives and Epoxy Coatings)*.
- PANDITA, S. D., WANG, L., MAHENDRAN, R. S., MACHAVARAM, V. R., IRFAN, M. S., HARRIS, D. & FERNANDO, G. F. (2012) Simultaneous DSC-FTIR spectroscopy: Comparison of cross-linking kinetics of an epoxy/amine resin system. *Thermochimica Acta*, 543, 9-17.
- PARK, S. J. (2014) *Carbon Fibers*, Springer Netherlands.
- PASCAULT, J. P. & WILLIAMS, R. J. J. (2009) *Epoxy Polymers: New Materials and Innovations*, Wiley.
- PERKIN-ELMER (2003) Diamond DSC Specifications.
- PERKIN-ELMER (2014) *Guide to Selection of Differential Scanning Calorimetry (DSC) Sample Pans*.
- PERKIN-ELMER (2016) DSC Beginners Guide.
- PHILIPP, M., GERVAIS, P.-C., SANCTUARY, R., MÜLLER, U., BALLER, J., WETZEL, B. & KRÜGER, J.-K. (2008) Effect of mixing sequence on the curing of amine-hardened epoxy/alumina nanocomposites as assessed by optical refractometry.
- POISSON, N., LACHENAL, G. & SAUTEREAU, H. (1996) Near- and mid-infrared spectroscopy studies of an epoxy reactive system. *Vibrational Spectroscopy*, 12, 237-247.



- POWELL, G. R., CROSBY, P. A., WATERS, D. N., FRANCE, C. M., SPOONCER, R. C. & FERNANDO, G. F. (1998) In-situ cure monitoring using optical fibre sensors - a comparative study. *Smart Materials & Structures*, 7, 557-568.
- PRIME, R. B. (1981) Chapter 5 - Thermosets. In: TURI, E. A. (ed.) *Thermal Characterization of Polymeric Materials*. Academic Press.
- PRITCHARD, G. (2012) *Developments in Reinforced Plastics—4*, Springer Science & Business Media.
- PROLONGO, M., SALOM, C., ARRIBAS, C., SÁNCHEZ-CABEZUDO, M., MASEGOSA, R. & PROLONGO, S. (2016) Influence of graphene nanoplatelets on curing and mechanical properties of graphene/epoxy nanocomposites. *Journal of Thermal Analysis and Calorimetry*, 125, 629-636.
- PROLONGO, S. G., MORICHE, R., JIMÉNEZ-SUÁREZ, A., SÁNCHEZ, M. & UREÑA, A. (2014) Advantages and disadvantages of the addition of graphene nanoplatelets to epoxy resins. *European Polymer Journal*, 61, 206-214.
- QIN, Q. & YE, J. (2015) *Toughening mechanisms in composite materials*, Elsevier.
- QIU, S. L., WANG, C. S., WANG, Y. T., LIU, C. G., CHEN, X. Y., XIE, H. F., HUANG, Y. A. & CHENG, R. S. (2011) Effects of graphene oxides on the cure behaviors of a tetrafunctional epoxy resin. *Express Polymer Letters*, 5, 809-818.
- R. BAUER, E. M., M. WATKINS (1995) *Epoxy Resins in Coatings*, <https://books.google.co.uk/books?id=ri6FkY2xvgcC&pg=PA74&dq=types+of+epoxy+resins&hl=en&sa=X&ved=0ahUKEwjwku7ImODTAhVIQBoKHTmdBDcQ6AEIMjAD#v=onepage&q=types%20of%20epoxy%20resins&f=false>.
- RABEARISON, N., JOCHUM, C. & GRANDIDIER, J. C. (2011) A cure kinetics, diffusion controlled and temperature dependent, identification of the Araldite LY556 epoxy. *Journal of Materials Science*, 46, 787-796.
- RAFIEE, M. A., RAFIEE, J., WANG, Z., SONG, H., YU, Z.-Z. & KORATKAR, N. (2009) Enhanced mechanical properties of nanocomposites at low graphene content. *ACS nano*, 3, 3884-3890.
- RAGHUVANSHI (2011) *Engineering Physics*, Prentice-Hall Of India Pvt. Limited.
- RÄTY, J. A., PEIPONEN, K. E. & ASAKURA, T. (2013) *UV-Visible Reflection Spectroscopy of Liquids*, Springer Berlin Heidelberg.
- RAZA, M. A., WESTWOOD, A. & STIRLING, C. (2016) Graphite nanoplatelet-based epoxy composites as adhesives and pads for thermal interface applications.
- RICHARDSON, M. J. (1992) Characterization of the cure of resins by differential scanning calorimetry (Technical Report). *Pure and Applied Chemistry*.
- RICHARDSON, M. J. & SAVILL, N. G. (1975) Derivation of accurate glass transition temperatures by differential scanning calorimetry. *Polymer*, 16, 753-757.
- RIGAIL-CEDEÑO, A. & SUNG, C. S. P. (2005) Fluorescence and IR characterization of epoxy cured with aliphatic amines. *Polymer*, 46, 9378-9384.
- ROBERT, L. & DUSSERRE, G. (2014) Anisothermal thermosetting resin cure monitored by optical fiber refractometer. *Polymer Engineering and Science*, 54, 626-635.
- ROBERTSON, C. G. & WILKES, G. L. (1998) Refractive index: A probe for monitoring volume relaxation during physical aging of glassy polymers. *Polymer*, 39, 2129-2133.
- ROMÁN, F., CALVENTUS, Y., COLOMER, P. & HUTCHINSON, J. M. (2013) Isothermal curing of polymer layered silicate nanocomposites based upon epoxy resin by means of anionic homopolymerisation. *Thermochimica acta*, 574, 98-108.

- ROȘU, D., CAȘCAVAL, C. N., MUSTAȚĂ, F. & CIOBANU, C. (2002) Cure kinetics of epoxy resins studied by non-isothermal DSC data. *Thermochimica Acta*, 383, 119-127.
- RUIZ, E., WAFFO, F., OWENS, J., BILLOTTE, C. & TROCHU, F. (2006) Modeling of resin cure kinetics for molding cycle optimization. Proceedings of the International Conference in Flow Processes in Composite Materials (FPCM'06), 2006.
- RUSLI, A., COOK, W. D. & SCHILLER, T. L. (2014) Blends of epoxy resins and polyphenylene oxide as processing aids and toughening agents 2: Curing kinetics, rheology, structure and properties. *Polymer International*, 63, 1414-1426.
- RYAN, M. & DUTTA, A. (1979) Kinetics of epoxy cure: a rapid technique for kinetic parameter estimation. *Polymer*, 20, 203-206.
- RYU, S. H., SIN, J. H. & SHANMUGHARAJ, A. M. (2014) Study on the effect of hexamethylene diamine functionalized graphene oxide on the curing kinetics of epoxy nanocomposites. *European Polymer Journal*, 52, 88-97.
- SAMPATH, U., KIM, H., KIM, D.-G., KIM, Y.-C. & SONG, M. (2015) In-Situ Cure Monitoring of Wind Turbine Blades by Using Fiber Bragg Grating Sensors and Fresnel Reflection Measurement. *Sensors (Basel, Switzerland)*, 15, 18229-18238.
- SARGE, S. M., HEMMINGER, W., GMELIN, E., HÖHNE, G. W. H., CAMMENGA, H. K. & EYSEL, W. (1997) Metrologically based procedures for the temperature, heat and heat flow rate calibration of DSC. *Journal of thermal analysis*, 49, 1125-1134.
- SBIRRAZZUOLI, N., VYAZOVKIN, S., MITITELU, A., SLADIC, C. & VINCENT, L. (2003) A Study of Epoxy-Amine Cure Kinetics by Combining Isoconversional Analysis with Temperature Modulated DSC and Dynamic Rheometry. *Macromolecular Chemistry and Physics*, 204, 1815-1821.
- SCHUBEL, P. J., CROSSLEY, R. J., BOATENG, E. K. G. & HUTCHINSON, J. R. (2013) Review of structural health and cure monitoring techniques for large wind turbine blades. *Renewable Energy*, 51, 113-123.
- SENIOR, J. (2009) *Optical Fiber Communications: Principles and Practice*, Financial Times/Prentice Hall.
- SICHINA, W. (2000) Measurement of T<sub>g</sub> by DSC.
- SIMMONS, J. H. & POTTER, K. S. (2000) *Optical Materials*, Academic Press.
- SINGH, D. (2015) *Applied Optics*, PHI Learning.
- SMITH, B. C. (2011) *Fundamentals of Fourier Transform Infrared Spectroscopy, Second Edition*, CRC Press.
- SMITH, M. E. & ISHIDA, H. (1999) Critical gel phenomena in the rheology of epoxide network formation. *Journal of Applied Polymer Science*, 73, 593-600.
- SOUROUR, S. & KAMAL, M. R. (1976) Differential scanning calorimetry of epoxy cure: isothermal cure kinetics. *Thermochimica Acta*, 14, 41-59.
- SPILLER, E. (1994) *Soft X-ray Optics*, SPIE Optical Engineering Press.
- ST JOHN, N. A. & GEORGE, G. A. (1992) Cure kinetics and mechanisms of a tetraglycidyl-4,4'-diaminodiphenylmethane/diaminodiphenylsulphone epoxy resin using near i.r. spectroscopy. *Polymer*, 33, 2679-2688.
- STANKOVICH, S., DIKIN, D. A., DOMMETT, G. H. B., KOHLHAAS, K. M., ZIMNEY, E. J., STACH, E. A., PINER, R. D., NGUYEN, S. T. & RUOFF, R. S. (2006) Graphene-based composite materials. *Nature*, 442, 282-286.
- STANLEY, B. (2017) Digital Refractometers and Polarimeters.

- STARK, W. (2013) Investigation of the curing behaviour of carbon fibre epoxy prepreg by Dynamic Mechanical Analysis DMA. *Polymer Testing*, 32, 231-239.
- STREHMEL, V. & SCHERZER, T. (1994) Structural investigation of epoxy amine networks by mid- and near-infrared spectroscopy. *European Polymer Journal*, 30, 361-368.
- SU, C. AND WOO, E. (1995) Chemical interactions in blends of bisphenol A polycarbonate with tetraglycidyl-4, 4'-diaminodiphenylmethane epoxy. *Macromolecules* 28(20): 6779-6786.
- SWIER, S. AND VAN MELE, B. (1999) Reaction-induced phase separation in polyethersulfone-modified epoxy-amine systems studied by temperature modulated differential scanning calorimetry.
- TEIL, H., PAGE, S. A., MICHAUD, V. & MANSON, J. A. E. (2004) TTT-cure diagram of an anhydride-cured epoxy system including gelation, vitrification, curing kinetics model, and monitoring of the glass transition temperature. *Journal of Applied Polymer Science*, 93, 1774-1787.
- TENG, C.-C., MA, C.-C. M., LU, C.-H., YANG, S.-Y., LEE, S.-H., HSIAO, M.-C., YEN, M.-Y., CHIOU, K.-C. & LEE, T.-M. (2011) Thermal conductivity and structure of non-covalent functionalized graphene/epoxy composites. *Carbon*, 49, 5107-5116.
- TERCJAK, A., ET AL. (2005). Phase separation and rheological behavior during curing of an epoxy resin modified with syndiotactic polystyrene. *Polymer Engineering & Science* 45(3): 303-313.
- THOMAS, S. & ZAIKOV, G. (2010) *Recent Advances in Polymer Nanocomposites: Synthesis and Characterisation*, CRC Press.
- THORLABS (2017) 0.22 NA Standard Glass-Clad, Silica Core Multimode Fiber Datasheet.
- TSUDA, H. & LEE, J. R. (2007) Strain and damage monitoring of CFRP in impact loading using a fiber Bragg grating sensor system. *Composites Science and Technology*, 67, 1353-1361.
- TUNG, C.-Y. M. & DYNES, P. J. (1982) Relationship between viscoelastic properties and gelation in thermosetting systems. *Journal of Applied Polymer Science*, 27, 569-574.
- TURI, E. A. (1997) *Thermal characterization of polymeric materials*, Academic Press.
- VAN ASSCHE, G., VAN HEMELRIJCK, A., RAHIER, H. & VAN MELE, B. (1997) Modulated temperature differential scanning calorimetry: Cure, vitrification, and devitrification of thermosetting systems. *Thermochimica Acta*, 304-305, 317-334.
- VACHER, S., MOLIMARD, J., GAGNAIRE, H. & VAUTRIN, A. (2004) A Fresnel's reflection optical fiber sensor for thermoset polymer cure monitoring. *Polymers & Polymer Composites*, 12, 269-276.
- VARLEY, R. J., ET AL. (1996). Toughening of a trifunctional epoxy system. II. Thermal characterization of epoxy/amine cure. *Journal of Applied Polymer Science* 60(12): 2251-2263.
- VELAZQUEZ, P., GONZÁLEZ-ALVAREZ, A., GONZÁLEZ-ROMERO, V. & ARELLANO, M. (2000) Rheological monitoring of curing reaction of an epoxy system: effect of heating rate. *Polymer Bulletin*, 43, 519-526.
- VODICKA, R. (1997) Cure monitoring techniques using embedded sensors. DTIC Document.
- VYAZOVKIN, S. & SBIRRAZZUOLI, N. (1996) Mechanism and kinetics of epoxy-amine cure studied by differential scanning calorimetry. *Macromolecules*, 29, 1867-1873.

- WAN, Y.-J., TANG, L.-C., GONG, L.-X., YAN, D., LI, Y.-B., WU, L.-B., JIANG, J.-X. & LAI, G.-Q. (2014) Grafting of epoxy chains onto graphene oxide for epoxy composites with improved mechanical and thermal properties. *Carbon*, 69, 467-480.
- WANG, L., TOMLIN, A., PANDITA, S. D., GUPTA, B. D., MALIK, S. A., HUDSON, M., CURTIS, P. T. & FERNANDO, G. F. (2016) In-situ monitoring of cross-linking reactions using E-glass fibres and evanescent wave spectroscopy. *Sensors and Actuators B: Chemical*, 236, 358-366.
- WANG, P., MOLIMARD, J., DRAPIER, S., VAUTRIN, A. & MINNI, J. C. (2012) Monitoring the resin infusion manufacturing process under industrial environment using distributed sensors. *Journal of Composite Materials*, 46, 691-706.
- WANG, X. R. & GILLHAM, J. K. (1991) Competitive Primary Amine Epoxy and Secondary Amine Epoxy Reactions - Effect on the Isothermal Time-to-Vitrify. *Journal of Applied Polymer Science*, 43, 2267-2277.
- WEATHERHEAD, R. (2012) *FRP Technology: Fibre Reinforced Resin Systems*, Springer Netherlands.
- WEIK, M. H. (1989) *Fiber optics standard dictionary*, Van Nostrand Reinhold.
- WEIK, M. H. (2013) *Fiber Optics Standard Dictionary*, Springer US.
- WINTER, H. H. (1987) Evolution of rheology during chemical gelation. *Permanent and Transient Networks*. Darmstadt: Steinkopff.
- WISSBRUN, K. (2013) *Melt Rheology and Its Role in Plastics Processing: Theory and Applications*, Springer US.
- WUNDERLICH, B. (1981) Chapter 2 - The Basis of Thermal Analysis. In: TURI, E. A. (ed.) *Thermal Characterization of Polymeric Materials*. Academic Press.
- XIA, L. J., ZUO, L., ZHA, S. W., JIANG, S. F., GUAN, R. & LU, D. P. (2014) Kinetic research on low-temperature cure of epoxy adhesive. *International Journal of Adhesion and Adhesives*, 50, 255-264.
- XIE, H., LIU, B., SUN, Q., YUAN, Z., SHEN, J. & CHENG, R. (2005) Cure kinetic study of carbon nanofibers/epoxy composites by isothermal DSC. *Journal of applied polymer science*, 96, 329-335.
- XU, L., FU, J. H. & SCHLUP, J. R. (1994) In-situ near-infrared spectroscopic investigation of epoxy-resin aromatic amine cure mechanisms. *Journal of the American Chemical Society*, 116, 2821-2826.
- XU, W., HUANG, X. G. & PAN, J. S. (2013) Simple Fiber-Optic Refractive Index Sensor Based On Fresnel Reflection and Optical Switch. *Ieee Sensors Journal*, 13, 1571-1574.
- YAMANAKA, K. & INOUE, T. (1989) Structure development in epoxy resin modified with poly(ether sulphone). *Polymer* 30(4): 662-667.
- YAMASAKI, H. & MORITA, S. (2012) Two-Step Curing Reaction of Epoxy Resin Studied by Thermal Analysis and Infrared Spectroscopy. *Applied Spectroscopy*, 66, 926-933.
- YAMASAKI, H. & MORITA, S. (2014) Identification of the epoxy curing mechanism under isothermal conditions by thermal analysis and infrared spectroscopy. *Journal of Molecular Structure*.
- YANG, H., SHAN, C., LI, F., ZHANG, Q., HAN, D. & NIU, L. (2009) Convenient preparation of tunably loaded chemically converted graphene oxide/epoxy resin nanocomposites from graphene oxide sheets through two-phase extraction. *Journal of Materials Chemistry*, 19, 8856-8860.
- YILGÖR, I., YILGÖR, E., BANTHIA, A., WILKES, G. & MCGRATH, J. (1981) A DSC kinetic study of the epoxy network system bisphenol-A diglycidylether-bis (4-aminocyclohexyl) methane. *Polymer Bulletin*, 4, 323-327.

- YOUNG, M. (2013) *Optics and Lasers: Including Fibers and Optical Waveguides*, Springer Berlin Heidelberg.
- YU, H., MHAISALKAR, S. G. & WONG, E. H. (2005) Observations of gelation and vitrification of a thermosetting resin during the evolution of polymerization shrinkage. *Macromolecular Rapid Communications*, 26, 1483-1487.
- YU, J.-W. & SUNG, C. S. P. (1995) Cure characterization in diamine-cured epoxy and polyimide by UV reflection spectroscopy. *Macromolecules*, 28, 2506-2511.
- YU, Y., SU, H. & GAN, W. (2009) Effects of storage aging on the properties of epoxy prepregs. *Industrial & Engineering Chemistry Research*, 48, 4340-4345.
- YUE, L., PIRCHERAGHI, G., MONEMIAN, S. A. & MANAS-ZLOCZOWER, I. (2014) Epoxy composites with carbon nanotubes and graphene nanoplatelets– Dispersion and synergy effects. *Carbon*, 78, 268-278.
- ZAMAN, I., KUAN, H.-C., DAI, J., KAWASHIMA, N., MICHELMORE, A., SOVI, A., DONG, S., LUONG, L. & MA, J. (2012) From carbon nanotubes and silicate layers to graphene platelets for polymer nanocomposites. *Nanoscale*, 4, 4578-4586.
- ZHANG, S. & ZHAO, D. (2016) *Aerospace Materials Handbook*, CRC Press.
- ZHANG, W. W., CHEN, X. P., GAO, Y. Q., HE, X. D. & IEEE (2012) A fiber optic sensor for real time monitoring of the curing/cured state of adhesives. *Proceedings of the 2012 Second International Conference on Instrumentation & Measurement, Computer, Communication and Control (Imccc 2012)*, 1278-1280.